FUSION OF HIGH SPATIAL RESOLUTION MULTISPECTRAL & OBJECT HEIGHT DATA FOR URBAN ENVIRONMENTAL MONITORING

METHODS & APPLICATIONS

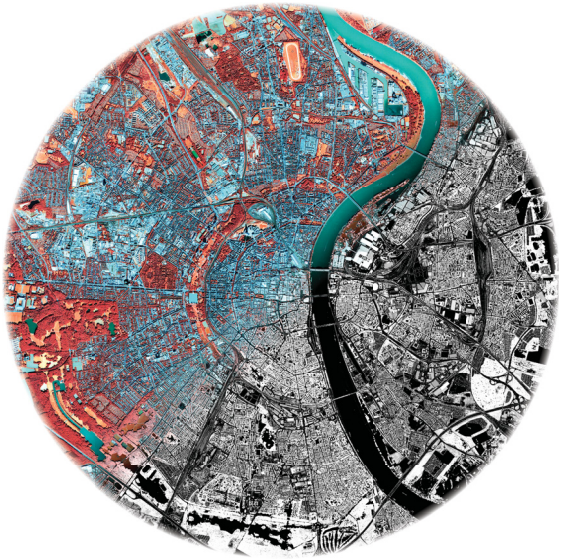

DISSERTATION

CHRISTIAN BERGER

Fusion of High Spatial Resolution Multispectral & Object Height Data for Urban Environmental Monitoring

Methods & Applications

Dissertation

(kumulativ)

zur Erlangung des akademischen Grades
doctor rerum naturalium
(Dr. rer. nat.)

vorgelegt dem Rat der Chemisch-Geowissenschaftlichen Fakultät der
Friedrich-Schiller-Universität Jena

von Christian Berger, M.Sc.
geboren am 03. Mai 1985 in Pößneck

Gutachter:

1. PD Dr. Sören Hese (FSU Jena)
2. Prof. Dr. Christiane Schmullius (FSU Jena)
3. Dr. Hannes Taubenböck (DLR Oberpfaffenhofen)

Tag der öffentlichen Verteidigung: 14. Juni 2017

Acknowledgements

Nobody said it was easy, and I would have been the last person to doubt or even deny that. But now that it's done, I must admit that it could not have been any harder. Without the tremendous help and continuous support of so many delightful people, none of this would've been possible.

I would like to express my gratitude to Prof. Dr. Christiane Schmullius for her general trust in my abilities and for giving me a gentle nudge towards the finish line. I am also deeply indebted to PD Dr. Sören Hese, who has guided me as an understanding and encouraging thesis supervisor. It is my belief that we share the same passion for high spatial resolution urban remote sensing.

Special thanks go to Dr. Michael Voltersen for being the best office mate I could have possibly imagined. His calm and prudent nature often kept me focused and his diverse inputs to the present work are highly appreciated. PD Dr. Christian "CJ" Thiel was both one of the strongest and most critical supporters of my research. I thank him very much for proof-reading the early drafts of each chapter. His constructive criticism has significantly contributed to the final document version.

There are still many more who deserve credit. In this sense, I would like to thank all my colleagues and companions that have made work and life in Jena so enjoyable over the past couple of years. Among the closest friends that have escorted me on my scientific journey are Robs and Nes, The True Colors, as well as Mecki and ☙ Jessi, and I apologize to anybody I may have overlooked.

Above all, I would like to express my heartfelt thanks to my beloved kids and my dear parents and family, who saw me a little less frequently since I have spent so much time in the office.

Jena, New Year's Eve 2016
Christian Berger

Abstract

Human settlements are complex and dynamic systems having diverse and profound impacts on environmental factors and processes. Given the high degree of heterogeneity found in cities, urban environmental monitoring and decision making requires high spatial resolution (HSR) geospatial data and information products derived thereof. Thanks to recent technological advancements, reduced production costs, and loosened data policies, this requirement is fulfilled by a growing number of adequate satellite and airborne sensors. HSR multispectral imagery and object height data (e.g., 3D point clouds) are becoming increasingly available in the urbanized regions of the world. The synergistic utilization of these data sources holds a large potential for the fine-scale characterization of a city because they are of high descriptive power and non-redundant. However, despite this promising development, detailed, area-wide, and consistent maps of important settlement parameters like urban land cover (LC), urban site characteristics (USCs), and urban structure types (USTs) are still lacking in many municipalities. One reason for this observation is the methodological challenge of turning the wealth of geospatial data into reliable thematic information. Accordingly, there is a strong need for accurate, transferable, and automated software solutions being able to produce some of the key data sets for human settlement monitoring from HSR multispectral and object height data. The present work aims at addressing this need.

The overall goal of this dissertation was to develop methods for the fusion of HSR multispectral imagery and object height data as well as to showcase their utility in the context of different urban environmental mapping and monitoring applications. It therefore intended to make both a technical and an applied research contribution to the field of urban remote sensing. Particular emphasis was put on mapping urban LC, USCs, and USTs, as well as the usage of USCs to study urban land surface temperature (LST) and the surface urban heat island (UHI) effect. These settlement parameters were chosen because they are thematically connected, difficult to obtain from other data sources, and of high relevance for urban planning. In order to meet the above goal, a comprehensive literature review was conducted in advance. The review helped identifying current deficits within the chosen fields of research and led to the formulation of specific thesis objectives. The latter determined the practical agenda of this work, comprising an overall number of four studies.

In the first study, a robust geographic object-based image analysis (GEOBIA) approach was developed to extract detailed and accurate urban LC information from HSR multispectral imagery and object height data. Special attention was paid to the critical evaluation of the proposed method with regard its performance for and applicability to different test sites and various sets of HSR

multisensor data. For this purpose, the experimental setup of the study included three cities featuring different physical structures, four sets of HSR optical and light detection and ranging (LiDAR) data, as well as statistical measures to enable the assessment of classification accuracies and methodological transferability. The study results highlight the great potential of the described approach for accurate, robust, and large-area mapping of urban environments. User's and producer's accuracies observed for all maps were almost consistently above 80%, and in many cases even above 90%. Only few larger class-specific errors occurred mainly due to the rather simple (yet effective) assumptions on which the method is based. The presented feature extraction workflow can therefore be used as a template for or starting point of future urban LC mapping efforts.

In the second study, a new spatial indicator was designed and implemented. The aim was to integratively assess urban density by taking into account some of the 2D and 3D key characteristics of a city. To this end, fusion of the WorldView-2 and LiDAR data provided in the framework of the 2012 IEEE GRSS Data Fusion Contest was performed. In a first step, basic urban LC information was extracted from the preprocessed input data sets using the GEOBIA approach developed before. The LC map was then utilized in combination with the object height information provided by the LiDAR data to infer urban density. The resulting map and statistics underscore the plausibility and qualification of the proposed metric as a useful measure to evaluate human settlement density and its distinct spatial patterns for different types of urban land use (LU). By taking into account all three spatial dimensions of the urban environment, an integrated and more holistic assessment of the "builtscape" is enabled. To further enhance the transparency of the study, a dedicated geoportal was set up that visualizes all input data, final results, by-products, and ancillary information.

In the third study, a generic GEOBIA system was developed for an area-wide and automated derivation of USTs. Synergistic use was made of HSR multispectral and object height data acquired by the airborne UltraCamX sensor over the city of Berlin, Germany. Initially, urban LC information was extracted from the preprocessed input data by means of the classification scheme presented in the first study. The LC map was then employed together with the UltraCamX object heights to infer a comprehensive set of 2D, 3D, and integrated 2D/3D USCs. In a third step, the importance of the generated features was evaluated by the random forest (RF) machine learning algorithm. Finally, the experiences gained from the assessment were used to build improved UST class descriptions. The latter were based on both well-established as well as more recently introduced USCs, such as the urban density metric proposed in the second study. The analysis results and the produced map emphasize the suitability of the described method with regard to classification accuracy, workflow automation, and preparedness in the context of future UST mapping and monitoring tasks.

In the fourth study, the relationship between USCs and LST was investigated. Focus was laid on an extensive comparison of 2D, 3D, and integrated 2D/3D USCs as potential predictors of urban LST as well as potential indicators of the surface UHI effect. In addition to the comparison of USCs, the spatio-temporal dependencies of their relation to LST were examined. For this purpose, the experimental setup included two study areas, 26 USCs, and 16 LST scenes covering four

seasons. The results of the study demonstrate that the linkage between USCs and LST sensed at small scan angles is not stronger when 3D or integrated 2D/3D parameters are considered. Even though they may offer more holistic representations of the urban landscape, they were consistently outperformed by some of the most widely-used 2D metrics. The analysis of spatial dependencies revealed that the USC–LST interplay does not only differ between, but also within the two test sites. This is due to their distinct geographies, with urban form and compactness, green spaces and street trees, and the structural composition of LC elements being some of the determining factors. The examination of temporal dependencies yielded that the association between USCs and LST is fairly stable over time, but can be subject to larger inter- and intra-season variations for different reasons, including the season of acquisition, vegetation phenology, and meteorological conditions. Since previous research was based on the analysis of a single test site, a limited number of (mainly 2D) USCs, and/or only few LST scenes acquired in specific seasons, the findings of the study provide researchers and practitioners with a more complete picture of the USC–LST relation.

With the first three studies, the present thesis has introduced a suite of GEOBIA approaches that build on top of each other. These methods exploit the synergies among HSR multisource data and proved to be suitable for an accurate, yet robust characterization of different settlement parameters, including urban LC, USCs, and USTs. From a geographical perspective, much of the work has concentrated on test sites located in Germany. However, the described classification and analysis schemes are expected to work well for any other Western culture city as long as the available multispectral imagery, object height data, and ancillary geospatial information meet some basic requirements. Since their preparedness for (semi-) automated observation tasks was successfully demonstrated, the proposed set of procedures can be considered as a useful complement to already operational urban monitoring systems as well as to more experimental technical solutions. Within the final study of the thesis, use was made of all map types produced by the methods developed to examine the complex spatio-temporal relationship between USCs and LST. This investigation was exemplary for showing that the multilevel information products generated by the fusion of HSR multispectral and object height data can be reutilized in the context of different follow-up applications. It also illustrates that an individual or joint integration of these maps into other experiments holds the potential for advancing urban research at comparable, coarser, or finer spatial scales. In this sense, the dissertation has provided a continuous and consistent methodological framework for local to regional mapping and monitoring of urban environmental phenomena.

Keywords — Urban, remote sensing, data fusion, synergy, high spatial resolution, multispectral imagery, 3D point clouds, LiDAR, thermal, Landsat, ETM+, object-based, classification, accuracy, robustness, mapping, monitoring, land surface temperature, urban heat island, environment.

Kurzfassung

Städte sind komplexe, dynamische Systeme, welche vielfältige und tiefgreifende Auswirkungen auf Umweltfaktoren und -prozesse haben. Aufgrund ihrer ausgeprägten Heterogenität werden für stadtumweltbezogene Fragestellungen räumlich hochaufgelöste Geodaten und darauf basierende Informationen benötigt. Dank technologischer Fortschritte, verringerter Produktionskosten und dem Trend hin zu einer offenen Datenpolitik werden diese Anforderungen zunehmend erfüllt. Konkret nimmt die Verfügbarkeit von räumlich hochaufgelösten Multispektralbildern und Objekthöhendaten (z.B. 3D-Punktwolken) für urbane Gebiete stetig zu. Die synergetische Verknüpfung solcher Daten birgt ein großes Potential zur genauen Beschreibung von Städten, da diese Daten einen hohen Informationsgehalt aufweisen und redundanzfrei sind. Trotz dieser positiven Entwicklung fehlt es in vielen Städten an detaillierten, flächendeckenden und konsistenten Karten, welche Aufschluss über planungsrelevante Siedlungsparameter, wie die Landbedeckung und Stadtstrukturtypen, geben. Ein Grund für diese Beobachtung ist die methodische Herausforderung, die Fülle an zugänglichen Fernerkundungsdaten in verlässliche thematische Informationen zu überführen. Demzufolge besteht ein großer Bedarf an akkuraten, übertragbaren und weitestgehend automatisierten Auswertungsverfahren, welche sich das Synergiepotential von räumlich hochaufgelösten Multispektralbildern und Objekthöhendaten für ein verbessertes Stadtumweltmonitoring zunutze machen. Die vorliegende Arbeit zielt darauf ab, diesen Bedarf zu decken.

Das übergeordnete Ziel der Dissertation war, Methoden zur Fusion von räumlich hochaufgelösten Multispektralbildern und Objekthöhendaten zu entwickeln und deren Nutzen im Rahmen stadtumweltbezogener Fragestellungen zu demonstrieren. Folglich sollte die Arbeit sowohl einen technischen als auch einen angewandten Forschungsbeitrag auf dem Gebiet der urbanen Fernerkundung leisten. Das Hauptaugenmerk lag auf einer genauen und robusten Kartierung der Landbedeckung und Stadtstruktur. Darüber hinaus wurden verschiedene urbane Bewertungsindikatoren extrahiert und zu einem neuen Dichtemaß verknüpft. Die abgeleiteten Karten und Indikatoren kamen im Zuge einer abschließenden Analyse zum Einsatz, welche sich mit den Ursprüngen städtischer Wärmeinseln befasste. Um das obige Ziel zu erreichen, wurde im Vorfeld eine umfangreiche Literaturrecherche vorgenommen. Diese ermöglichte die Identifikation derzeitiger Forschungsdefizite und führte zur Formulierung spezifischer Arbeitsziele. Nach den Zielen richtete sich der praktische Teil der kumulativen Dissertation, welcher insgesamt vier Studien umfasste.

In der ersten Studie wurde ein Klassifikationsansatz entwickelt, welcher auf dem Prinzip der objekt-basierten Bildverarbeitung beruht. Der Ansatz zielte auf die robuste Extraktion feinskali-

ger Landbedeckungsinformationen aus räumlich hochaufgelösten Multispektral- und Objekthöhendaten ab. Im Fokus stand die kritische Bewertung des vorgestellten Verfahrens in Bezug auf Klassifikationsgenauigkeit und methodische Übertragbarkeit. Zu diesem Zweck umfasste der Versuchsaufbau drei Testgebiete mit unterschiedlichen strukturellen Merkmalen, vier verschiedene Eingangsdatensätze sowie statistische Maße. Die Studienergebnisse verdeutlichen das große Potential des beschriebenen Ansatzes zur akkuraten, robusten und großflächigen Kartierung urbaner Räume. Die Nutzer- und Herstellergenauigkeiten der abgeleiteten Karten lagen fast ausnahmslos über 80% und überschritten in vielen Fällen sogar 90%. Nur für wenige Klassen wurden größere Fehlerraten nachgewiesen. Diese lassen sich durch den relativ einfachen Aufbau der Methode begründen. Nichtsdestotrotz lässt sich schlussfolgern, dass sich das präsentierte Verfahren sehr gut als Vorlage oder Ausgangspunkt für zukünftige Landbedeckungsklassifikationen eignet.

In der zweiten Studie wurde ein neuer Bewertungsindikator entworfen und implementiert. Ziel war es, eine integrierte Abschätzung der Stadtdichte unter Berücksichtigung von 2D- und 3D-Siedlungsmerkmalen vornehmen zu können. Hierzu wurden die im Rahmen des IEEE GRSS Data Fusion Contest (2012) bereitgestellten WorldView-2 und Laserdaten fusioniert. In einem ersten Schritt wurden urbane Landbedeckungsinformationen aus den vorprozessierten Eingangsdaten extrahiert. Hierfür fand das zuvor entwickelte Klassifikationsverfahren Verwendung. Die Landbedeckungskarte wurde anschließend mit den Objekthöhen im Laserdatensatz kombiniert, um das angestrebte Dichtemaß zu erhalten. Im Ergebnis lagen eine Karte sowie Statistiken vor, welche die Plausibilität des vorgeschlagenen Indikators suggerieren. Der Index ist in der Lage, die charakteristischen Dichtemuster verschiedener urbaner Landnutzungstypen wiederzugeben. Durch die Betrachtung von 2D- und 3D-Aspekten wird eine ganzheitliche Bewertung der Stadtdichte ermöglicht. Um die Transparenz der geschilderten Untersuchungen zu erhöhen, wurden alle Eingangsdaten, Neben- und Endprodukte in einem zugehörigen Geoportal visualisiert.

In der dritten Studie wurde ein generisches, objekt-basiertes Klassifikationsschema entwickelt, welches der flächendeckenden und automatisierten Ableitung von Stadtstrukturtypen dient. Das Schema baute auf das Synergiepotential von räumlich hochaufgelösten Multispektral- und Objekthöhendaten auf, welche mit dem flugzeuggetragenen UltraCamX-Sensor über Berlin akquiriert wurden. Anhand der aufbereiteten Eingangsdaten sowie dem in der ersten Studie dargelegten Verfahren wurde zunächst Berlins urbane Landbedeckung ausgewiesen. Danach wurde das erzeugte Datenprodukt mit den UltraCamX-Objekthöhen verschnitten, um eine Vielzahl an 2D-, 3D- und kombinierten 2D/3D-Indikatoren zu berechnen. In einem dritten Schritt wurde der Informationsgehalt der so generierten Klassifikationsmerkmale mit Methoden des maschinellen Lernens quantifiziert. Die Erkenntnisse aus diesem Vergleich wurden schließlich verwendet, um eine verbesserte Charakterisierung von Stadtstrukturtypen zu gewährleisten. Die finalen Klassenbeschreibungen beruhen auf sowohl etablierten als auch neuen Siedlungsparametern. Ein Beispiel für Letztere ist das zuvor entworfene Dichtemaß. Die Analyseergebnisse demonstrieren die Eignung des entwickelten Ansatzes in Bezug auf Genauigkeit, Übertragbarkeit und Automatisierung.

In der vierten Studie wurde der Zusammenhang zwischen urbanen Bewertungsindikatoren und Landoberflächentemperaturen untersucht. Besondere Aufmerksamkeit wurde einem umfangreichen Vergleich von 2D-, 3D- und kombinierten 2D/3D-Metriken zuteil, um deren Potential als Indikatoren des städtischen Wärmeinseleffekts zu eruieren. Zusätzlich wurden die raum-zeitlichen Abhängigkeiten der untersuchten Zusammenhänge beleuchtet. Aus diesem Grund umfasste der Versuchsaufbau zwei Testgebiete, 26 Indikatoren und 16 Temperaturkarten aus allen vier Jahreszeiten. Die Ergebnisse des Experiments zeigen, dass die Korrelation zwischen Siedlungsparametern und Landoberflächentemperaturen nicht stärker ist, wenn 3D- oder kombinierte 2D/3D-Maße berücksichtigt werden. Obwohl Letztere eine ganzheitliche Betrachtung von Stadtlandschaften gestatten, wurden diese nahezu ohne Ausnahme von 2D-Metriken übertroffen. Die Analyse räumlicher Abhängigkeiten ergab, dass sich die beobachteten Korrelationen nicht nur zwischen, sondern auch innerhalb von Städten unterscheiden. Dieser Umstand ist auf die individuellen Geographien urbaner Gebiete zurückzuführen. Ausschlaggebende Faktoren sind unter anderem die Morphologie und Kompaktheit sowie die Grünflächen und Straßenbäume einer Stadt. Die Überprüfung zeitlicher Abhängigkeiten führte zu dem Schluss, dass die analysierten Zusammenhänge relativ stabil sind. Dennoch können auch sie größeren temporalen Schwankungen zwischen und innerhalb von Jahreszeiten unterliegen. Als Ursachen solcher Variationen wurden verschiedene Umstände, wie beispielsweise der Zeitraum der Datenakquisition, die Phänologie der Vegetation sowie spezifische meteorologische Bedingungen, ausgemacht. Bisherige Forschungsergebnisse basieren oftmals auf der Untersuchung eines einzelnen Testgebiets, einer begrenzten Anzahl an Indikatoren und/oder nur wenigen Temperaturkarten aus spezifischen Jahreszeiten. Entsprechend bietet das hier angeführte Experiment einen umfassenderen empirischen Blick auf den statistischen Zusammenhang zwischen urbanen Bewertungsindikatoren und Landoberflächentemperaturen.

Mit den ersten drei Studien hat diese Arbeit eine Reihe objekt-basierter Klassifikationsansätze vorgestellt, welche aufeinander aufbauen. Diese Methoden machen sich das Synergiepotential von räumlich hochaufgelösten Fernerkundungs- bzw. Geodatentypen zunutze und eignen sich für die genaue und robuste Erfassung verschiedener Siedlungsparameter, einschließlich urbaner Landbedeckung und Stadtstrukturtypen. Aus geographischer Sicht konzentrierte sich das Gros der Untersuchungen auf Testgebiete in Deutschland. Jedoch ist zu erwarten, dass die beschriebenen Verfahren auch auf andere Städte im westlichen Kulturraum problemlos anwendbar sind. Voraussetzung hierfür ist allerdings, dass die verwendeten Multispektralbilder, Objekthöhendaten und zusätzlichen Informationsebenen einige wenige Anforderungen erfüllen. Da das präsentierte Repertoire an Klassifikatoren einen hohen Automatisierungsgrad aufweist, kann es als sinnvolle Ergänzung an der Schnittstelle zwischen bereits operationellen Anwendungen und eher experimentellen Lösungen zur Kartierung städtischer Umweltparameter angesehen werden.

In der finalen Studie dieser Arbeit wurde der komplexe raum-zeitliche Zusammenhang zwischen urbanen Bewertungsindikatoren und Landoberflächentemperaturen untersucht. Zu diesem Zweck kamen alle Karten zum Einsatz, welche zuvor mit den hier entwickelten Verfahren erstellt wur-

den. Die Studie dient folglich als Beispiel für die vielseitigen Einsatzmöglichkeiten der erzeugten Datenprodukte. Darüber hinaus impliziert diese, dass die Verwendung der generierten Karten in zukünftigen Experimenten über ein erhebliches Potential verfügt, die Erfassung und Erforschung von Städten auf ähnlichen, gröberen oder feineren räumlichen Skalen voranzubringen. In diesem Sinne hat die vorliegende Dissertation ein kontinuierliches und konsistentes Methodenspektrum für ein verbessertes Stadtumweltmonitoring auf lokaler und regionaler Ebene bereitgestellt.

Schlüsselwörter — Stadt, Fernerkundung, Datenfusion, Synergie, hochaufgelöst, multispektral, 3D, Punktwolke, Laser, thermal, Landsat, ETM+, objekt-basiert, Klassifikation, Genauigkeit, Robustheit, Kartierung, Monitoring, Landoberflächentemperatur, Wärmeinsel, Umwelt.

Outline

Contents

Figures

Tables

Acronyms

2D	Two-dimensional 4
3D	Three-dimensional 4
ABI	Advanced Baseline Imager 13
ACP	Annual cycle parameter 12
ALS	Airborne laser scanning 5
ALTM	Airborne Laser Terrain Mapper 12
ANN	Artificial neural network 14
AOI	Area of interest 27
ASTER	Advanced Spaceborne Thermal Emission and Reflection Radiometer 13
ATKIS	Amtliches Topographisch-Kartographisches Informationssystem 24
AVHRR	Advanced Very High Resolution Radiometer 13
BAR	Biotope area ratio 28
BCI	Biophysical composition index 28
BCR	Building coverage ratio 28
BI	Bare soil index 28
CAR	Complete aspect ratio 30
CBD	Central business district 17
CBERS	China-Brazil Earth Resources Satellite 13
CIR	Color infrared 24
DEM	Digital elevation model 12
DN	Digital number 10
DSM	Digital surface model 12
DTM	Digital terrain model 12
EARSeL	European Association of Remote Sensing Laboratories 7
EBBI	Enhanced built-up and bareness index 27
ETM+	Enhanced Thematic Mapper Plus 13
FAI	Frontal area index 30
FAR	Floor area ratio 29
FSV	Fraction of surrounding vegetation 28

NDBaI	Normalized difference bareness index	28
NDBI	Normalized difference built-up index	27
NDISI	Normalized difference impervious surface index	27
nDSM	Normalized DSM	12
nDTM	Normalized DTM	12
NDVI	Normalized difference vegetation index	10
NDWI	Normalized difference water index	28
NIR	Near infrared	11
NN	Nearest neighbor	23
NOAA	National Oceanic and Atmospheric Administration	13
NPOESS	National Polar-orbiting Operational Environmental Satellite System	13
OBIA	Object-based image analysis	15
OSM	OpenStreetMap	9
PCI	Park cool island	22
RF	Random forest	23
RTE	Radiative transfer equation	12
SAM	Spectral angle mapper	23
SAR	Synthetic aperture radar	9
SAVI	Soil-adjusted vegetation index	28
SEE	French Society for Electricity and Electronics	7
SIG	Special interest group	7
SLEUTH	Slope, land use, exclusion, urban, transportation, hillshade	114
SLSTR	Sea and Land Surface Temperature Radiometer	13
SVF	Sky view factor	20
SVM	Support vector machine	14
SWIR	Shortwave infrared	10
TES	Temperature/emissivity separation	12
TIR	Thermal infrared	9
TIRS	Thermal Infrared Sensor	13
TM	Thematic Mapper	13

Chapter 1

Introduction

Over the past decades, the world has faced a continuous and increasingly dynamic urbanization. While in 1950 city dwellers made up 30% of the total human population, more than half of the people on this planet are residing in urban areas today. By absolute numbers, the global urban population has risen from 746 million to 3.9 billion people within the last 65 years (UN 2014). The current rates of urbanization are twice as fast as just 30 years from now, with the Earth gaining one billion more urban residents every 13 years (Solecki et al. 2013). According to official estimations, 6.4 billion townsmen are expected until 2050, meaning that 66% of all human beings will live an urban life by then (UN 2014). Based on these demographic developments, there is no doubt that the future of humankind will be urban (Taubenböck et al. 2009b).

1.1 Problem statement

The ever-growing percentage of global urban population comes at a high price. Many cities all over the world are sprawling rapidly, and their spread is associated with alarming rates of land consumption (Angel et al. 2011b; Taubenböck et al. 2012). Between 1970 and 2000, the global urban extent has quadrupled and comprises now about 3.7 million km² (or 2.8%) of the Earth's land surface (Hooke & Martín-Duque 2012; Seto et al. 2011). For 2030, it is predicted to be three times larger than it was in 2000 (Seto et al. 2012). If the latest projections hold true, human settlements will consume an additional area of "29 000 soccer fields" ($\hat{=}$ 207 km²) – every day for the next 15 years (Solecki et al. 2013:13). On average, cities around the globe are growing twice as fast as their population does (Angel et al. 2011a). But even in regions where there is little demographic pressure (e.g., in Europe), urban expansion is in full swing (Artmann 2014; EEA 2002; UN 2014). This is because additional socio-economic and environmental factors contribute to urban development as well. These include micro- and macro-economic activities, housing preferences, inner city problems and urban quality of life, aspects related to the transportation and mobility of people, as well as land policies and other regulatory frameworks (EEA 2006). Overall, urban growth is a global phenomenon that is becoming more expansive than compact (Seto et al. 2011), and there are no signs for a slow-down or even stopping of this process in the near future.

Tab. 1–1: Impacts of urban development on environmental parameters.

	Parameters	Impact
Climate[1]	• Temperature; Clouds; Fog; Precipitation; Contaminants; Greenhouse gases	▲
	• Solar radiation; Sunshine duration; Relative humidity; Wind speed; Gusts	▼
Hydrology[2]	• Surface runoff; Storm water discharge; Flash floods; Water pollution	▲
	• Soil permeability; Soil filtering; Water infiltration; Ground water recharge	▼
Biota[3]	• Plant damage; Growing season length; Habitat fragmentation; Species extinction	▲
	• Biodiversity; Natural resources; Ecosystem services (e.g., carbon uptake by plants)	▼

[1] Arnfield (2003); Bereitschaft & Debbage (2013); Changnon (1992); Grimmond (2007); Huizhi et al. (2002); Kuttler (2008); Landsberg (1981); Lowry (1998); Svirejeva-Hopkins et al. (2004).

[2] Arnold & Gibbons (1996); Grimm et al. (2008); Haase & Nuissl (2007); Niemczynowicz (1999); Pauleit & Breuste (2011); Scalenghe & Marsan (2009); Shaver et al. (2007[2]); Tang et al. (2005).

[3] Grimm et al. (2008); Haas et al. (2015); Hahs et al. (2009); Mandal (2006); McKinney (2008); Neil & Wu (2006); Pauleit & Breuste (2011); Roetzer et al. (2000); Seto et al. (2000); Vitousek et al. (1997).

Urban development represents one of the most irreversible forms of land transformation (Seto et al. 2011). In the course of this process, the natural "skin" of the Earth is successively replaced by man-made objects and surfaces with distinct physical properties. Therefore, building construction as well as the sealing and compaction of soils have diverse and profound impacts on the environment (Tab. 1–1). It is commonly agreed that urban areas and their expansion affect the micro- and mesoscale climate (Landsberg 1981). A prominent example of this human-induced climate modification is the urban heat island (UHI) effect (Arnfield 2003). It refers to the observation that cities often feature higher temperatures than their surroundings (Howard 1833[2]; Oke 1973). Besides climate, the presence and intensity of development are also known to impact hydrology. Due to the isolation of the land surface by impervious materials, soil permeability and water infiltration rates are significantly reduced in urban environments. As a result, groundwater tables are forced to decrease while, at the same time, surface runoff increases (Niemczynowicz 1999; Scalenghe & Marsan 2009). Furthermore, the filtering function of the soil is lost so that pollutants can accumulate on urban ground and get easily transported to receiving waters in the case of heavy rain events (Arnold & Gibbons 1996; Shaver et al. 2007[2]). In consequence of the specific conditions within and around cities, the local flora and fauna is subject to change as well (Grimm et al. 2008; Vitousek et al. 1997), with issues of plant damage (Berry 2008), habitat fragmentation (Seto et al. 2011), and biodiversity loss (McKinney 2008; Seto et al. 2012) being frequently reported. Other environmental problems caused by cities are the degradation of ecosystem services and the depletion of natural resources for food and industry (Haas et al. 2015; Hooke & Martín-Duque 2012; Seto et al. 2000). Apart from their local and regional effects on biotic and abiotic systems, human settlements are also responsible for the bulk of global greenhouse gas emissions through, amongst others, energy consumption, industrial activities, and transportation demands (Brown 2001; IEA 2008). Thus, they have to be understood as key drivers of environmental change at all spatial scales (Grimm et al. 2008; Miller & Small 2003).

Urbanization and its environmental consequences have manifold and far reaching implications for urban planning and management. As a matter of fact, they are considered to be the main challenges of the 21st century (Miller & Small 2003; Taubenböck 2011). In a more provocative sense, urban sprawl is also called "the ignored challenge" (EEA 2006). This description refers to the problems encountered by policy makers and town planners when dealing with such a complex issue. The chief difficulty is that all actors need to account for at least as many socio-economic factors as there are environmental ones. For instance, urban infill may seem like a good idea to reduce land consumption (environmental dimension) and infrastructure costs (economic dimension), but may also lead to a decrease in urban quality of life (social dimension) due to densification and the loss of open spaces for recreational purposes (EEA 2006; Pauleit et al. 2005; UBA 2004). In addition, the reutilization of derelict city sites and the concomitant sealing of the soil usually entail a loss of local wildlife habitats and a decline of ecosystem services (Bolund & Hunhammar 1999; Gibson 1998; Harrison & Davies 2002), thereby canceling out some of the environmental advantages of introversive urban growth. In other words, every decision for the environment, society, or economy might as well be a decision against one or more of these domains, and the conflicts of interest arising from the strong interconnectedness of each sphere have to be carefully evaluated in the decision-making process (Artmann 2014; Foley et al. 2005).

Given that urban expansion and the associated modification of the environment are expected to accelerate while more and more people will be exposed to the living conditions within the cities of tomorrow (Miller & Small 2003; Seto et al. 2011), the question that emerges from the above considerations is how officials can get a handle on environmentally, socially, and economically sustainable urban development. While no magic bullet exists to resolve all the known trade-offs, there is a general consensus that only holistic approaches constitute a suitable means to achieve this goal (Pauleit & Duhme 2000; UN 2014; UN-Habitat 2010). Most importantly, a concerted action of all involved parties, including politicians, urban planners, resource managers, industry, science, and people is mandatory to make progress towards sustainability in all of its facets (Solecki et al. 2013; Taubenböck 2011). At the heart of such integrative solutions are geospatial data covering the various environmental and socio-economic aspects of the complex urban system. They form an integral part of all stages within those schemes, from the identification of unsolved problems and the execution of subsequent urban analyses to the development of dedicated management strategies and the assessment of their impact (Taubenböck 2011). A successful implementation of problem-oriented, holistic frameworks therefore stands and falls with the availability of data and the tools ready to exploit them. To plan and manage smart city growth, area-wide, up-to-date, and reliable information on urban environments are a basic prerequisite (Heinonen et al. 2015; Taubenböck et al. 2010a). Unfortunately, it is often difficult to obtain these information in practice, which is partly owing to the high expenditure of labor and time needed when traditional ways of data collection (e.g., field surveys or manual interpretation of aerial photos) are employed to produce them (Heiden et al. 2012; Jensen & Cowen 1999).

Remote sensing represents an alternative approach to data acquisition. It is defined as a measurement principle to gather information about distant phenomena without making physical contact with them (Lillesand et al. 2008[6]). In the geosciences, it mainly refers to satellite and airborne sensor technology used to detect and characterize features on Earth by quantifying the electromagnetic radiation they reflect or emit (Albertz 2009[4]; Campbell & Wynne 2011[5]; Schowengerdt 2007[3]). The diverse types of available Earth observation data are frequently described as being spatially explicit, synoptic, up-to-date, repetitive, consistent, unobtrusive, and cost-efficient (Longley 2002; Miller & Small 2003; Patino & Duque 2013). Thus, remote sensing is generally capable of providing the measurements required for urban monitoring. Since the first experiments have been conducted over human settlements (e.g., Tuyahov et al. 1973), numerous books (Bhatta 2010; Donnay et al. 2001; Gamba & Herold 2009; Jensen et al. 2007[2]; Rashed & Jürgens 2010; Soergel 2010; Taubenböck & Dech 2010; Weng & Quattrochi 2007; Weng 2008; Weng 2014; Yang 2011) and reviews (Du et al. 2014; Gallo et al. 1995; Gamba et al. 2005; Gamba 2013; Gamba 2014; Heldens et al. 2011; Henderson & Xia 1997; Jensen & Cowen 1999; Longley 2002; Mesev 1997; Miller & Small 2003; Ngie et al. 2014; Nichol et al. 2007; Patino & Duque 2013; Slonecker et al. 2001; Stathopoulou & Cartalis 2007; Tomlinson et al. 2011; Voogt & Oke 2003; Wang et al. 2013; Wang 2013; Weng 2009; Weng 2012; Wentz 2012; Wentz et al. 2014; Yan et al. 2015) have appeared demonstrating the unique and manifold opportunities offered by this technique.

With remote sensing, many kinds of settlement parameters can be derived and studied (Tab. 1–2). It is particularly well-suited to make direct estimates of key urban environmental features. These include, but are not limited to, urban extents and their spatio-temporal growth, land cover (LC) and surface materials, urban site characteristics (USCs) like biophysical proxies, landscape patterns, or two-dimensional (2D) and three-dimensional (3D) morphology, as well as land surface temperature (LST) and UHIs. Based on one or more of these information layers and by incorporating ancillary geospatial data, it is possible to indirectly assess further important variables such as land use (LU), urban structure types (USTs), and socio-economic attributes like energy efficiency, population distribution, and urban quality of life, to name a few. This brief overview highlights that remote sensing can serve as a common basis for multi-, inter-, and transdisciplinary research (Longley 2002; Miller & Small 2003), thereby supporting holistic thinking in urban planning and management. However, while many global and regional Earth observation data, methods, and products are already well-established (e.g., CIESIN 2011; EEA 2013; Esch et al. 2013), fine-scale urban remote sensing is still at a more experimental stage and stakeholders remain skeptic about its practical utility (Donnay 1999; Miller & Small 2003; Reiss-Schmidt 2010).

For investigations at the local level, high spatial resolution (HSR) data (≤5 m) are usually required to properly capture common urban LC objects like buildings or trees (Jensen & Cowen 1999; Konecny et al. 1982; Welch 1982). Thanks to recent technological advancements, reduced production costs, and loosened data policies, this requirement is fulfilled by a growing

Tab. 1–2: Typical applications of remote sensing for urban monitoring.

Application type	Case studies
Environmental	
Urban footprints	Esch et al. (2014); Pesaresi et al. (2011a); Schneider et al. (2009)
Urban expansion	Bhatta et al. (2010); Taubenböck et al. (2012); Ward et al. (2000)
Urban LC mapping	Lu et al. (2010); O'Neil-Dunne et al. (2013); Walker & Blaschke (2008)
Surface materials	Berger et al. (2015); Franke et al. (2009); Heiden et al. (2007)
Urban LU/Function	Barnsley et al. (2001); Herold et al. (2003b); Mesev (2010)
USTs/Biotope types	Banzhaf & Höfer (2008); Bochow et al. (2010a); Heiden et al. (2012)
Biophysical proxies	Esch et al. (2009); Schöpfer et al. (2005); Zhang et al. (2009b)
Landscape patterns	Besussi et al. (2010); Huang et al. (2007); Ji et al. (2006)
2D/3D morphology	Fina et al. (2014); González-Aguilera et al. (2013); Yu et al. (2010)
LST retrieval/UHIs	Weng et al. (2004); Xian & Crane (2006); Yuan & Bauer (2007)
Socio-economic	
Energy efficiency	Geiss et al. (2011); Hay et al. (2011); Zhou et al. (2012)
Solar potential	Jakubiec & Reinhart (2013); Jochem et al. (2009); Voegtle et al. (2005)
Signal obstruction	Li et al. (2008); Lohani & Kumar (2008); Parrish & Nowak (2009)
Economic activities	Chen & Nordhaus (2011); Doll et al. (2006); Henderson et al. (2012)
Population distribution	Li & Weng (2005); Liu et al. (2006); Lo (1995); Wu & Murray (2005)
Social vulnerability	Ebert et al. (2009); Rashed et al. (2007); Taubenböck et al. (2008)
Poverty hot spots	Baud et al. (2010); Kit & Lüdeke (2013); Taubenböck & Kraff (2014)
Human well-being	Beck et al. (2000); Dousset et al. (2011); Liu & Weng (2009)
Urban quality of life	Jensen et al. (2004); Lo (1997); Weber & Hirsch (1992)

number of sensors (Benediktsson et al. 2012; Ehlers 2009; Weng et al. 2014). HSR data are becoming increasingly available in the urbanized regions of the world. This is especially true for multispectral imagery (IGN 2015; NLS 2015; NOAA 2015; USDA 2015) and object height data (IGN 2015; Lidar Online 2014; OpenTopography 2014; Sugarbaker et al. 2014) derived from photogrammetric principles or light detection and ranging (LiDAR), also known as airborne laser scanning (ALS) (Baltsavias 1999; Wehr & Lohr 1999). Since these data sources are of high descriptive power and non-redundant (Wentz et al. 2014; Yan et al. 2015), their joint usage within dedicated data fusion frameworks holds a large potential for urban area characterization and is therefore considered to be "the new frontier of urban remote sensing" (Gamba et al. 2005; Gamba 2014:10). Despite these promising developments, area-wide and detailed maps of the above settlement parameters are still lacking in many urban areas. The main reason for this observation is the methodological challenge of turning the wealth of geospatial data into reliable thematic information (Longley et al. 2001; O'Neil-Dunne et al. 2013). Mapping cities is arguably one of the most complex remote sensing tasks (Griffiths et al. 2010; Mesev 1997). In order to meet the high expectations of practitioners and to overcome some of the existing skepticism, there is a strong need for accurate, transferable, and automated software solutions being able to produce key data sets for human settlement monitoring from HSR multispectral and object height data. Accordingly, it is necessary to develop and evaluate appropriate fusion techniques that fully exploit the synergistic potential of those HSR multisource data becoming available for more and more urban areas (Benediktsson et al. 2012). The present work aims at addressing this need.

1.2 Scope of this work

Based on the above considerations, *the overall goal of this thesis is to develop methods for the fusion of HSR multispectral imagery and object height data as well as to showcase their utility in the context of different urban environmental mapping and monitoring applications*. The thesis therefore aims at making both a technical ("Methods") and an applied research contribution ("Applications") to the field of urban remote sensing (Fig. 1–1). At the interface of these individual contributions are urban environmental maps produced by the methods to be developed and employed within the framework of a predefined case study. Particular emphasis is put on mapping urban LC, USCs, and USTs, as well as the usage of USCs to study urban LST and surface UHIs[1]. These settlement parameters were chosen because they are thematically connected (cf. Fig. 3–1), difficult to obtain from other data sources, and of high importance for urban planning and environmental management (Chrysoulakis et al. 2014; Jensen & Cowen 1999; Longley 2002; Nichol et al. 2007; Pauleit & Breuste 2011; Wentz et al. 2014). Moreover, they can serve as a starting point to extract further layers of information or to conduct subsequent analyses. From a methodological perspective, much of the work presented in the following concentrates on geographic object-based image analysis (GEOBIA) (Blaschke et al. 2008; Blaschke 2010; Blaschke et al. 2014) to achieve the above goal. In addition, the bulk of investigations focuses on test sites in Germany.

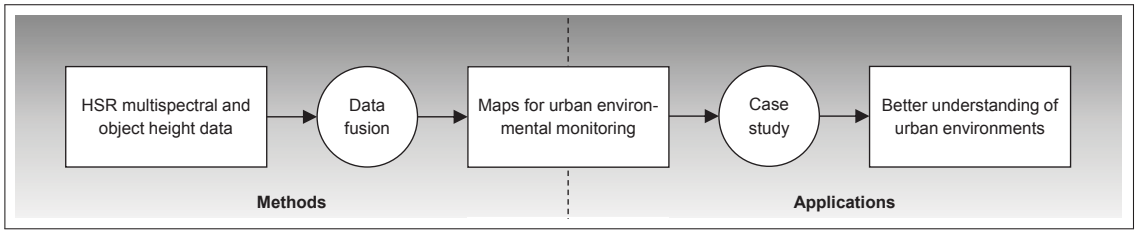

Fig. 1–1: Scope of this work.

The remainder of the thesis is structured as follows. Chapter 2 presents the state of the art related to this study. It provides the reader with the necessary theoretical background and a concise review of the most relevant scientific publications in the field. In Chapter 3, the objectives of this work are deduced from existing research needs and the interconnection between the individual research contributions is introduced by illustrating the practical workflow of the thesis. Chapter 4 represents the core of the dissertation. It contains the manuscripts submitted to and accepted by internationally renowned publication organs with independent review system to conform to the doctoral regulations imposed by the University of Jena. A tabular overview of the journal articles can be found in the Appendix (page 141ff.). Chapter 5 synthesizes the thesis outcomes. It summarizes the obtained results, puts the scientific contributions into the context of the current state of the art, reflects on their implications, and outlines potential avenues for future research.

[1] A definition and differentiation of key terms used in this thesis is provided in Section 2.1.4.

Chapter 2

State of the art

The present chapter shall allow the reader to better comprehend the research conducted in the framework of this thesis (cf. Chap. 3 and 4). To this end, Section 2.1 contains a selection of important background information and necessary theoretical considerations related to the chosen topics of work. These include descriptions of (1) the data fusion concept, (2) HSR and complementary data sets for urban studies, (3) the GEOBIA paradigm, (4) terminologies in urban environmental monitoring, and (5) the UHI effect. Note that the structure of this section directly refers to the explicit and some implicit keywords found in the title of this dissertation. After that, Section 2.2 presents the scientific basis of the research undertaken. It provides a concise review of the most relevant publications in the field. The survey is split up into a mapping and monitoring component, with each covering two of the four selected work topics at a time. While the former addresses (1) studies on the extraction of HSR urban LC and UST information, the latter is dedicated to (2) a summary of existing USCs as well as their applications in urban LST and UHI investigations.

2.1 Theoretical background

2.1.1 Data fusion: Definition, applications, and levels

According to Wang et al. (2005:1391), the rationale of data fusion "goes back to the 1950's and 1960's, with the search for practical methods of merging images from various sensors to provide a composite image which could be used to better identify natural and manmade objects". Since then, several terms expressing more or less the same concept have found their way into the scientific literature. Amongst them are, to mention only few, synonyms such as combination, integration, and merging as well as phrases such as combined, complementary, or synergistic data analysis (Pohl & Van Genderen 1998). However, the problem with these expressions is that their precise meaning is often interpreted differently (Wald 1999). As a consequence of the growing need for terms of reference in data fusion, a special interest group (SIG) set up by the European Association of Remote Sensing Laboratories (EARSeL) and the French Society for Electricity and Electronics (SEE), finally proposed a general definition in the late 1990's which is now widely

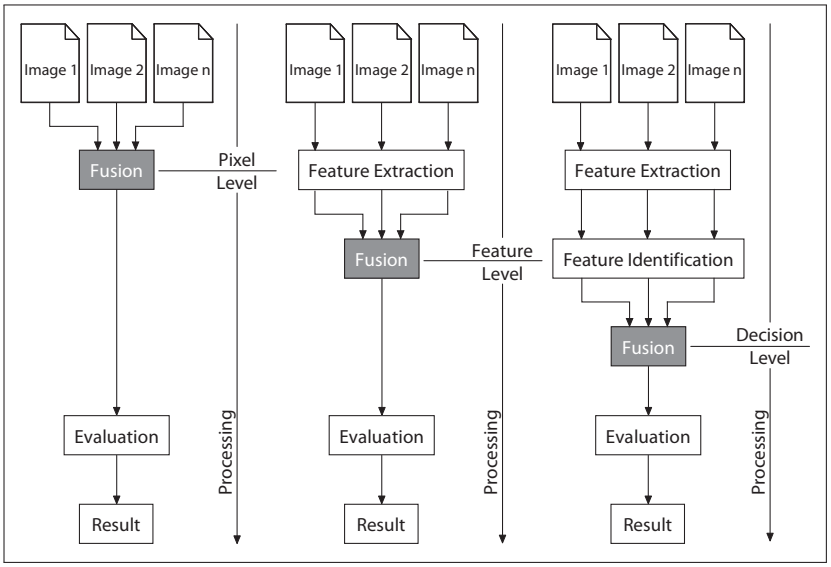

Fig. 2–1: Processing levels of image fusion (redrawn from Pohl & Van Genderen 1998).

adopted: "Data fusion is a formal framework in which are expressed means and tools for the alliance of data originating from different sources. It aims at obtaining information of greater quality; the exact definition of greater quality will depend upon the application" (Wald 1999:1191).

The above definition clearly puts its focus on the framework and principles of data fusion rather than the tools and methods that may be used. But even more importantly, it is kept generic: The improvement of quality depends on the type of application. In this sense, the objectives of data fusion can be manifold. Pohl & Van Genderen (1998:827) find that data fusion is applied to digital imagery from multiple sources in order to: "sharpen images" (i.e., pansharpening); "improve geometric corrections"; "provide stereo-viewing capabilities"; "enhance certain features not visible in either of the single data alone"; "complement data sets for improved classification"; "detect changes using multitemporal data"; "substitute missing information […] in one image with signals from another image"; or "replace defective data". Besides, data assimilation is a special form of data fusion. It aims at the analysis and prediction of the behavior of a system by integrating measured data into numerical models (Wald 1999). For the achievement of all the respective goals, a successful fusion scheme may involve the combination of data coming from different sensors (multisensor), the combination of data having different spatial resolutions (multiscale) and/or the combination of data sensed at different dates of acquisition (multitemporal) (Gamba et al. 2005).

In dependence of application and data basis, image fusion can be performed at three different processing stages, called levels. According to the processing stage at which fusion takes place, existing approaches are classified into (1) fusion at pixel level, also referred to as iconic image fusion, (2) fusion at feature level, also referred to as symbolic image fusion and (3) fusion at decision level, also referred to as interpretation or knowledge fusion (Pohl & Van Genderen 1998; Ehlers et al. 2008). As shown in Figure 2–1, the pixel level constitutes the lowest processing stage at which multisource data can be integrated. It involves the merging of measured physical

parameters as represented by individual pixels. On this account, the complementary data sets need to be at least coregistered. The feature level is considered as an intermediate stage of data processing. It requires the a priori extraction of scene characteristics from the input images. These features are then fused for further analysis. The decision level denotes the highest processing stage in image fusion and necessitates the existence of value-added data. For this purpose, the original images are processed separately for the extraction and identification of scene features. Subsequently, the resulting thematic information layers are combined by applying predefined decision rules in order to enhance interpretability and to gain a better understanding of the image objects under consideration (Pohl & Van Genderen 1998). The choice of an appropriate processing stage for image fusion depends upon the application as well the data available for a specific task. In fact, one may explore the benefits from more than one fusion approach at the same time so that the boundaries between the presented categories can be flawless in practice (Wald 1999).

In conclusion to this section, the present work primarily deals with data fusion at feature level. That is, the complementary information contained in HSR multispectral and object height data are combined within a GEOBIA framework to map urban LC, USCs, and USTs. Besides, fusion at pixel level (i.e., pansharpening) is performed during the preprocessing stage of each classification task to increase the spatial resolution of the multispectral images at hand (cf. Sect. 2.1.2).

2.1.2 HSR and complementary data sets for urban studies

Urban environments are complex systems comprising a diverse set and arrangement of fine-scale LC and LU elements. An area-wide, detailed, and accurate characterization of these features necessitates HSR remote sensing data with a pixel spacing of 0.5 to 5 m (Ehlers 2009; Jensen & Cowen 1999; Konecny et al. 1982; Steinnocher et al. 2001; Welch 1982). Thanks to recent technological advancements, reduced production costs, and loosened data policies, this requirement is met by an ever-growing number of space- and airborne sensors (Benediktsson et al. 2012; Ehlers 2009; Weng et al. 2014). Most notably, HSR multispectral imagery (NLS 2015; NOAA 2015; USDA 2015) and object height data (i.e., 3D point clouds; IGN 2015; Lidar Online 2014; OpenTopography 2014; Sugarbaker et al. 2014) are becoming increasingly available in the urbanized regions of the world. At the same time, thermal infrared (TIR) satellite images of coarser resolution as well as ancillary geospatial information (e.g., those distributed by the OpenStreetMap (OSM) project) are already at hand in many places (Geofabrik GmbH 2015; USGS 2015). These additional data sources complement the latest generation remote sensing products and are often ready to be explored in the context of urban environmental monitoring applications at the local scale. Since they form the basic building blocks of the practical research conducted within this thesis, a brief overview of the above data types is provided in the following[1].

[1] Note that other types of HSR data, like hyperspectral and synthetic aperture radar (SAR) data, are not covered in this summary as their availability over urban areas is still quite limited apart from a few exceptions (Cook et al. 2013; Dell'Acqua 2009; JPL 2015a). Besides, HSR SAR imagery of human settlements suffers from geometric distortions,

Tab. 2–1: Overview of common HSR multispectral satellite systems (after Ehlers 2009; eoPortal 2015b; EUSI 2015; Satellite Imaging Corporation 2015a; Satellite Imaging Corporation 2015b; Weng et al. 2014).

Satellite sytem	Operating company	Data avail. since/from	Pixel spacing [m][1]	Bit depth	Spectral bands
GeoEye-1	DigitalGlobe[2]	2008	0.41/1.65	11 bit	Pan, Blue, Green, Red, NIR
Ikonos-2	DigitalGlobe[2]	1999	1.00/4.00	11 bit	Pan, Blue, Green, Red, NIR
KOMPSAT-2	KARI	2006	1.00/4.00	10 bit	Pan, Blue, Green, Red, NIR
KOMPSAT-3	KARI	2012	0.70/2.80	14 bit	Pan, Blue, Green, Red, NIR
QuickBird-2	DigitalGlobe	2001–2014	0.61/2.44	11 bit	Pan, Blue, Green, Red, NIR
WorldView-2	DigitalGlobe	2009	0.46/1.84	11 bit	Pan, Coastal, Blue, Green, Yellow, Red, Red Edge, NIR-1, NIR-2
WorldView-3[3]	DigitalGlobe	2014	0.31/1.24	11 bit	Pan, Coastal, Blue, Green, Yellow, Red, Red Edge, NIR-1, NIR-2
WorldView-4	DigitalGlobe	2016[4]	0.34/1.36	11 bit	Pan, Blue, Green, Red, NIR

[1] The notation refers to the spatial resolution of the panchromatic (pan) and multispectral bands, respectively.

[2] Satellites originally operated by GeoEye Inc. before it was acquired by DigitalGlobe (DigitalGlobe 2013).

[3] WorldView-3 also features eight shortwave infrared (SWIR) bands at 3.7 m spatial resolution (EUSI 2015).

[4] The anticipated launch date of WorldView-4 (GeoEye-2) is 2016 (Satellite Imaging Corporation 2015a).

HSR multispectral sensors detect the sunlight reflected from the Earth's surface by up to eight spectral channels operating in the visible and infrared regions of the electromagnetic spectrum (Albertz 2009[4]; Ehlers 2009). They are therefore sensitive to the chemical composition and biophysical properties of urban elements (Herold et al. 2004; Weng et al. 2014). The data provided by these scanners allow for the extraction of various scene features that can be used for human settlement characterization and urban environmental monitoring. Among others, these include: spectral signatures; vegetation indices like the normalized difference vegetation index (NDVI) (Kriegler et al. 1969; Rouse et al. 1973; Tucker 1979); band ratios such as visual brightness (O'Neil-Dunne et al. 2014); principal components (Richards & Jia 2008[4]); as well as measures of image texture (e.g., those after Haralick et al. 1973). Prior to feature extraction, HSR multispectral imagery needs to be preprocessed. Data preparation usually comprises three steps. First, to correct the scene for illumination and atmospheric effects and to convert the digital numbers (DNs) to reflectance values, a radiometric normalization is applied (e.g., with ATCOR-2/3; Richter & Schläpfer 2014). Second, to obtain a multispectral data set at the (higher) spatial resolution of its panchromatic band, image fusion at pixel level (i.e., pansharpening) is performed (Dahiya et al. 2013). Third, to define its exact geographic coordinates and to spatially match it to any additional geospatial information, an orthorectification and/or coregistration of the multispectral data stack is conducted (cf. Schowengerdt 2007[3]). Today, a wide range of HSR multispectral sensors is

shadow effects, and an overall lack of clarity (Brenner & Roessing 2008; Dong et al. 1997; Raney 1998[3]; Soergel 2010). Accordingly, its interpretation is complicated and its suitability for detailed urban investigations is restricted (Gamba 2013; Weng et al. 2014). For the sake of brevity, the subsequent review instead focuses on HSR multispectral and 3D point cloud data, spaceborne TIR imagery, and supplementary geospatial information.

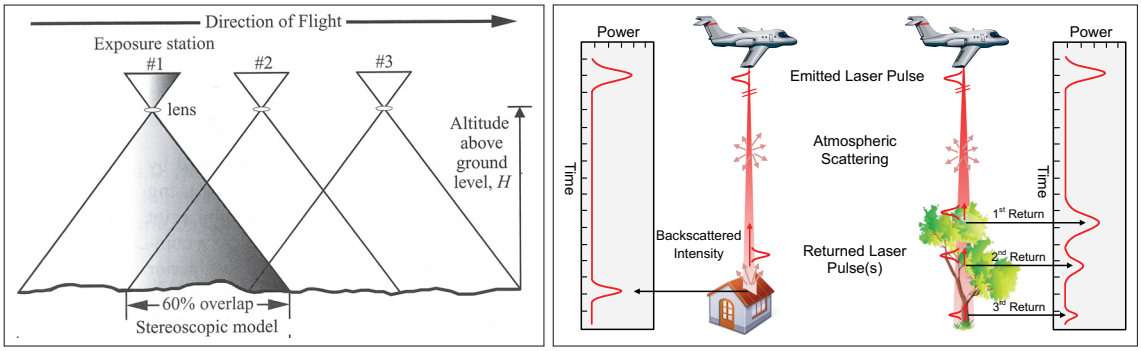

Fig. 2–2: Principles of (l) stereophotogrammetry (Jensen 2006[2]) and (r) topographic LiDAR (Yan et al. 2015).

either already available or planned for the near future. The optical data they (will) deliver typically contain four lower spatial resolution spectral channels (i.e., blue, green, red, near infrared (NIR)) and a higher spatial resolution panchromatic band representing mean reflectance values in the visible and NIR domain (Weng et al. 2014). The spatial resolution ratio between the multispectral and panchromatic images is almost exclusively 4:1, making them particularly well-suited for pansharpening tasks (Ling et al. 2008). Common spaceborne missions and airborne sensors with such a system design are GeoEye-1, Ikonos-2, KOMPSAT-2/3, QuickBird-2, and WorldView-4 (Tab. 2–1) as well as ADS40, DMC, HRSC-AX, and UltraCamX, respectively (Ehlers 2009; Weng et al. 2014). Only the current WorldView-2/3 satellites carry an extended number of multispectral channels with a releasable spatial resolution below 5 m (EUSI 2015).

3D point clouds at fine spatial resolution, i.e., dense networks of georeferenced elevation points, are either obtained from stereophotogrammetric techniques or topographic LiDAR (Fig. 2–2). Stereophotogrammetry is a measurement principle that relies on the joint analysis of two or more overlapping optical images taken from different viewing angles to recover the x-, y-, and z-coordinates of real-world objects (Campbell & Wynne 2011[5]; Lillesand et al. 2008[6]; Schowengerdt 2007[3]). The same approach is called radargrammetry when SAR data are employed (Meric et al. 2009). Topographic LiDAR is an active sensor technology that emits intense, high frequency beams of NIR light to illuminate the terrain. It makes use of the time difference between the emitted and returned laser pulses, the angle at which these are sent out, and the absolute location of the scanner to retrieve the exact position of points on the Earth's surface (Heritage & Large 2009; NOAA 2012; Raber & Cannistra 2005; Shan & Toth 2009). While most LiDAR sensors are only able to record discrete returns of laser pulses, some systems provide enhanced capabilities and capture the full waveform of the reflected light beams, making it possible to better decompose the received signal and to relate it to the vertical structure of the target objects (Mallet & Bretar 2009; Yan et al. 2015). The features and products that can be derived from 3D point clouds are diverse, of high descriptive power, and non-redundant, which is why their fusion with HSR multispectral imagery holds a large potential for urban analyses (Gamba et al.

2005; Wentz et al. 2014). They span from basic point cloud statistics (e.g., the mean, minimum, maximum, and standard deviation of height values within a resolution cell) to readily usable information layers such as digital elevation models (DEMs), digital surface models (DSMs), digital terrain models (DTMs) (all of which are created with specific interpolation techniques; Maune 2007[2]), normalized DSMs (nDSMs), normalized DTMs (nDTMs) as well as more advanced attributes like LiDAR intensity, waveform amplitude, the mean number of discrete LiDAR returns, echo width, the nDSM–nDTM difference, and the slope of the nDSM (O'Neil-Dunne et al. 2014; Yan et al. 2015). Whereas most of the space- and airborne multispectral systems mentioned in the preceding paragraph provide stereo viewing capabilities (e.g., GeoEye-1, WorldView-2, HRSC-AX, and UltraCamx), past and current LiDAR sensors generating HSR point clouds exclusively operate on airborne platforms. Well-known production series are ALTM by Optech (Canada), ALS by Leica Geosystems (Switzerland), LMS by Riegl (Austria), and LiteMapper by IGI (Germany) (Heritage & Large 2009; Raber & Cannistra 2005; Shan & Toth 2009).

TIR remote sensors measure the spectral radiance emitted from the Earth's surface in the mid- and longwave infrared region of the electromagnetic spectrum (Albertz 2009[4]; Kuenzer & Dech 2013). They are therefore sensitive to completely different site characteristics than HSR multispectral scanners. In particular, it is possible to infer LST from TIR imagery (Cheng & Ren 2012; Li et al. 2013). LST has long been recognized by the International Geosphere–Biosphere Program (IGBP) as a high-priority parameter (Townshend et al. 1994). But even more importantly, it is an indicator of the surface UHI (cf. Sect. 2.1.4 and 2.1.5) and, thus, of great relevance to the study of urban climates (Arnfield 2003; Voogt & Oke 2003; Weng et al. 2014). Besides single-date LST maps, TIR time series enable the calculation of an extended set of features describing urban thermal environments. These include annual cycle parameters (ACPs) like the mean annual surface temperature (MAST), the yearly amplitude of surface temperature (YAST), the phase shift relative to equinox, and the principal components of the multitemporal data stack (Bechtel 2011; Bechtel 2012a; Bechtel 2012b; Weng & Fu 2014). To retrieve LST, three major processing steps are necessary. First, the DNs of a thermal image are translated to at-sensor spectral radiance using band-specific lookup tables. Second, spectral radiance is converted to at-sensor brightness temperature by the inversion of Planck's law. Third, brightness temperature is corrected for land surface emissivity (LSE) and atmospheric effects to finally obtain LST (Voogt & Oke 2003). Depending on the TIR data at hand, the implementation of the third step is achieved by different approaches. If only one thermal band is available, the radiative transfer equation (RTE) method (Sobrino et al. 2004) as well as the single-channel (Jiménez-Muñoz & Sobrino 2003) and mono-window algorithms (Qin et al. 2001) come into question. If more than one thermal band is available, split-window and multi-angle techniques or the temperature/emissivity separation (TES) algorithm, to name a few, are suitable candidates to derive LST (cf. Cheng & Ren 2012; Gillespie et al. 1998; Li et al. 2013). Common to all these options is that the emissivity

Tab. 2–2: Technical specifications of selected spaceborne TIR sensors (after Abrams et al. 2002; Abrams & Hook 2013; Arvidson et al. 2013; Barsi et al. 2014; Chander et al. 2009; Cheng & Ren 2012; eoPortal 2015a; JPL 2015b; Kramer 2002[4]; Kuenzer et al. 2013; Reuter et al. 2015; Tomlinson et al. 2011; Weng et al. 2014).

TIR sensor	Satellite mission	Data avail. since/from	Pixel spacing [m]	Repeat cycle [d]	Equatorial crossing time	Band number	Spectral range [µm]
ASTER	Terra	1999	90	16	~10:30 am	10	8.125–8.475
						11	8.475–8.825
						12	8.925–9.275
						13	10.25–10.95
						14	10.95–11.65
IRS	CBERS-4	2014	80	26	~10:30 am	4	10.40–12.50
TM[1]	Landsat 4	1982–1993	120	16	~09:45 am	6	10.42–11.66
TM[1]	Landsat 5	1984–2011	120	16	~09:45 am	6	10.45–12.42
ETM+[1,2]	Landsat 7	1999	60	16	~10:00 am	6	10.31–12.36
TIRS[1]	Landsat 8	2013	100	16	~10:00 am	10	10.60–11.20
						11	11.50–12.50
TIR[3]	HyspIRI	TBD	60	5	~11:00 am	1	3.938–4.022
						2	7.190–7.510
						3	8.110–8.450
						4	8.455–8.805
						5	8.890–9.250
						6	10.26–10.80
						7	11.06–11.60
						8	11.79–12.31

[1] Landsat TIR data products are now resampled to 30 m spatial resolution before delivery (USGS 2010).

[2] ETM+ imagery acquired after May 2003 is affected by data gaps and anomalies (Chander et al. 2009).

[3] Spectral ranges of the TIR bands may shift based on ongoing science studies (Abrams & Hook 2013).

of the land surface needs to be known. There are various ways to compute LSE and among them, classification- and NDVI-based approaches are widely used (cf. Cheng & Ren 2012; Li et al. 2013; Valor & Caselles 1996). While HSR airborne thermal imagery of human settlements is relatively rare, coarser resolution spaceborne TIR data are available for most regions of the world and, in part, also freely accessible (e.g., Landsat data; USGS 2015). In addition, the existing data archives are comprehensive and continuously growing thanks to the long legacy of dedicated satellite missions and their comparably short revisit times. Thermal imagery with 3 to 5 km spatial resolution is currently provided by geostationary satellites such as GOES, MSG, and MTSAT. Data with up to 1 km pixel spacing are delivered by low Earth orbiters like MetOp and NOAA AVHRR, Terra/Aqua MODIS as well as the future GOES-R ABI, NPOESS VIIRS, and Sentinel-3 SLSTR, amongst others (cf. Cheng & Ren 2012; Tomlinson et al. 2011; Weng et al. 2014). Most relevant to the present thesis are Sun-synchronous space systems including Terra ASTER, CBERS-4 IRS, Landsat TM/ETM+/TIRS, and the anticipated HyspIRI. The TIR images they record feature ground sampling distances (GSDs) between 60 and 120 m (Tab. 2–2).

Ancillary geospatial information refer to all kinds of vector data that are readily usable within a geographical information system (GIS) to further characterize urban areas. Especially for non-commercial purposes, such information are often provided free of charge by the offices, agencies, and authorities of a city, state or country. Besides, some of them are simply available through the internet (e.g., Geofabrik GmbH 2015). Because they are scalable and can relate to environmental, socio-economic, and/or administrative properties of human settlements, vector layers hold the potential to complement fine-scale urban analyses with the latest HSR remote sensing data. Typical representatives of such information are: (cadastral) building footprints (Belgiu et al. 2014; Ural et al. 2011); point-based building height and use data (Mesev 2007; Salehi et al. 2012); road networks (Geiss et al. 2011; Wurm et al. 2011); borders of tax parcels, LU entities, and census blocks (Heiden et al. 2012; Ural et al. 2011; Wu et al. 2007; Yu et al. 2010; Zhou & Troy 2008); climate records (Gál et al. 2009; Wong & Nichol 2013), demographic figures (Aubrecht et al. 2009; Mesev 1998; Qiu et al. 2010); and social media contents (Crooks et al. 2014).

2.1.3 GEOBIA: An advanced concept to exploit HSR data

Over the past decades, a considerable amount of research has been directed towards the development and evaluation of pixel-based classifiers taking advantage of the complementary information in multisensor remote sensing data. Statistical approaches, like the maximum likelihood (ML) method, and non-parametric techniques, like artificial neural networks (ANNs) or support vector machines (SVMs), have proven to be successful in the context of urban mapping applications (Huang et al. 2012; Pacifici et al. 2008; Paola & Schowengerdt 1995). However, when it comes to the extraction of features from HSR data, the performance of algorithms based on a pixel-by-pixel analysis may not be sufficient. Real-world objects are made up of several pixels in HSR data (Blaschke 2010). At this scale, the variability of spectral and other features within a given LC class is high, whereas the radiometric variations between different LC types are low (Ouma et al. 2006; Schiewe et al. 2001; Woodcock & Strahler 1987). Therefore, if a classifier solely relies on information derived at the pixel level of HSR data, it is likely that the mapping result will be compromised by increased error rates due to the similarity between different target classes in feature space (Barnsley & Barr 1996; Schiewe & Ehlers 2005) as well as by the so-called "salt and pepper" noise (Baraldi & Boschetti 2012:2719; Blaschke 2000; Yu et al. 2006). This is particularly true for pixel-based LC classifications of urban areas, which are well-known for their spectral and spatial heterogeneity (Forster 1993; Herold et al. 2003a; Weng & Lu 2007). Other drawbacks of traditional approaches are their sensitivity to registration errors between multimodal inputs (Salehi et al. 2012; Zhou et al. 2008; Zhou et al. 2009), the computational effort that comes along with a per-pixel analysis of HSR data (Baatz et al. 2008; Thomas et al. 2003), the unreliability of single pixel values because of the influence of the pixel neighborhood on the signal (Dell'Acqua et al. 2006; Townshend et al. 2000), and the missing ability to infer

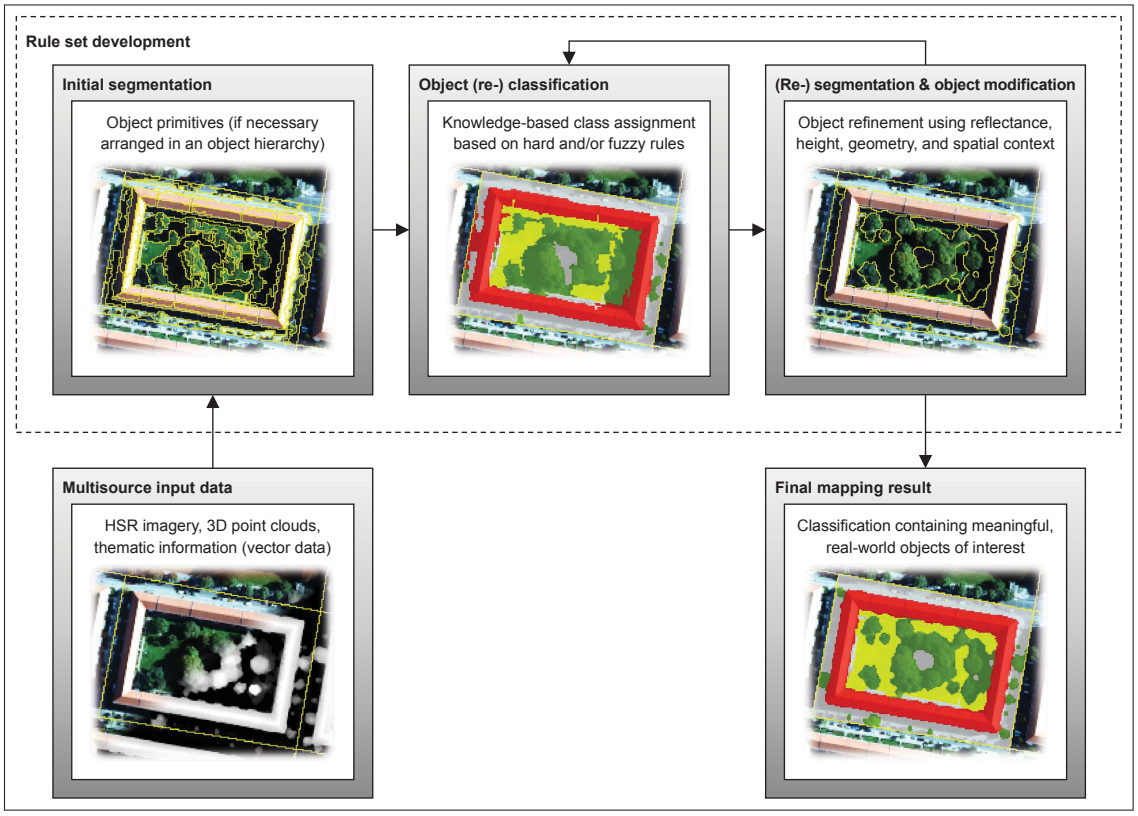

Fig. 2–3: A typical GEOBIA workflow to infer real-world objects from HSR multisource data.

meaningful objects corresponding to the visual perception of humans (Koch et al. 2003). Furthermore, spatial information, like image texture or morphological measures (Haralick et al. 1973; Soille 2004[2]), are usually calculated using a moving window, which causes borders between LC classes to become blurred (Barnsley & Barr 2000). For these reasons, it is worthwhile to consider alternative methods for the classification of HSR multisensor Earth observation data.

GEOBIA, often simply referred to as object-based image analysis (OBIA) (Blaschke et al. 2008), holds the potential to overcome the above problems with pixel-based approaches. In contrast to traditional algorithms, GEOBIA relies on the classification of image segments (objects), i.e., topologically connected, non-overlapping regions in scene space (Schiewe 2002), rather than individual pixels (Fig. 2–3). These segments are initially created by grouping adjacent pixels of an input data set according to predefined criteria of spectral and shape-related homogeneity (Blaschke 2010), thereby reducing the radiometric variability in HSR data (Salehi et al. 2012). It is possible to generate several segmentation levels with varying degrees of pixel aggregation and to arrange them in an object hierarchy. This allows for a multiscale exploration of image content, which is often necessary to model the complexity of (urban) landscapes (Burnett & Blaschke 2003). After segmentation, the resulting object primitives are subjected to an iterative process of (re-) classification, (re-) segmentation and morphological modification to ultimately obtain objects of interest (Baatz et al. 2008; Burnett & Blaschke 2003). Thus, during this

stage of the analysis task, image objects can constantly change their class membership, spatial geometry, and mutual relations until the mapping requirements are met (Benz et al. 2004). For the refinement of object primitives, not only their spectral characteristics (e.g., object mean, min, max, and variance value per input band), but also their geometry (e.g., shape and size), texture (e.g., second-order statistics after Haralick et al. 1973), and spatial context (e.g., positions, distances, and topologies) can be employed (Evans et al. 2010; Meinel et al. 2001; Taubenböck et al. 2010b). Especially the latter features gain importance as the iterative process progresses, meaning that classification gradually moves from utilizing basic object attributes (i.e., reflectance, height, geometry, texture) to the use of contextual information defined by spatial relationships (O'Neil-Dunne et al. 2014). GEOBIA can be regarded as a knowledge-based feature extraction approach in which temporary and final object classes and geometries are inferred by a series of user-defined, hard or fuzzy rules and conditions (Benz et al. 2004). All necessary image processing steps and class descriptions are stored in process sequences called rule sets. They enable the (re-) application of a developed workflow to other study areas and data sets. In the context of urban mapping with HSR imagery, GEOBIA methods are considered to be superior to pixel-based approaches (Bhaskaran et al. 2010; Linde & Kirstein 2004; Platt & Rapoza 2008), partly because the large variety of available image features and processing tools is well-suited to properly capture the complex urban system (Blaschke & Strobl 2001). However, in the light of this thesis, some of the most important advantages of GEOBIA are its capability to incorporate a diversity of input data (Hay & Castilla 2008; Kim et al. 2010; Zhang 2010) and the possibility to reuse rule sets (Flanders et al. 2003; Schöpfer & Möller 2006; Taubenböck et al. 2010b).

2.1.4 Terminologies in urban environmental monitoring

In this dissertation, each of the four chosen research topics either covers a specific urban environmental phenomenon or a set of settlement parameters belonging together (cf. Fig. 3–1). The variables are thematically connected and comprise urban LC, USTs, USCs, and LST. For the sake of clarity, a definition and differentiation of these and related terms is given in the following. Furthermore, the concept behind the expression of urban environmental monitoring is explained.

Urban environmental monitoring is conceived here as an umbrella term for mapping, tracking, analyzing, and understanding the diverse environmental aspects of a city. As these include, but are not limited to, urban LC, USTs, USCs, and LST, the expression provides an overarching framework to unify the four subjects of research selected in this work.

Land cover (LC) is the observed (bio-) physical material at and cover on the Earth's surface (Di Gregorio 2005; Fisher et al. 2005). Typical examples of (urban) LC elements are buildings, impervious surfaces, trees or tree canopy, short vegetation like grass and shrubs, bare soil areas, and water bodies (cf. Comber et al. 2008). LC information are either obtained from field surveys or remote sensing data. If the latter are employed, the above definition can be extended: "LC is

the material which we see and which directly interacts with electromagnetic radiation and causes the level of reflected energy which we observe as the tone or the digital number at a location in an aerial photograph or satellite image" (Comber et al. 2008:187). This emphasizes that, for instance, buildings represent higher-level LC classes since they are composed of different materials (e.g., slate, tile, asphalt, lead, tin, steel, wood, or thatch) that interact individually with electromagnetic radiation (Fisher et al. 2005). In any way, an exact definition of LC is crucial because LC is often erroneously confused with LU (Di Gregorio 2005). Although both concepts are certainly related, they are quite distinct from each other and should not be intertwined (Barnsley & Barr 2000; Comber 2008; Fisher et al. 2005; GLP 2005; Di Gregorio 2005; Loveland 2012; Veldkamp & Verburg 2004). To use the two terms correctly, meaningfully, and to the best advantage (Giri 2012), the next paragraph distinguishes LU from LC.

Land use (LU) is "characterized by the arrangements, activities and inputs people undertake in a certain land cover type to produce, change or maintain it" (Di Gregorio 2005:3). Residential, industrial, and commercial areas, parks, sports grounds, and other recreational sites are all common LU types (cf. Comber et al. 2008). As LU refers to the way the land is used by people (i.e., function), LC can be considered as the "visible evidence" of LU (i.e., form; Giri 2012:9). Both concepts are therefore closely, but not directly linked. What makes their mutual connection rather complex is that a given LU may be associated with several LC elements and vice versa (Fisher et al. 2005; Giri 2012; Jansen & Di Gregorio 2003; Loveland 2012). For example, single-family homes are LU entities that typically comprise multiple LC classes, including buildings, impervious ground, and trees. Conversely, buildings are LC categories that can belong to different LUs, such as single-family homes, industrial estates, or theme parks. It is because of these so-called "many-to-many relationships" (Fisher et al. 2005:88) that remote sensing approaches are best suited for direct assessments of LC whereas LU maps can often only be inferred indirectly or by the use of ancillary geospatial data (Barnsley et al. 2001; Loveland 2012; Mesev 2010).

Urban structure types (USTs) are an ecological concept to divide cities into spatial units of homogenous environmental conditions. Accordingly, units of the same UST feature comparable biophysical properties while units belonging to different USTs do not (Böhm et al. 2001a). The UST concept is realized in the form of maps. A widely-known UST map legend is presented in Böhm et al. (2001b) for the City of Leipzig, Germany. It comprises both main USTs (e.g., residential areas) as well as their subclasses (e.g., central business district (CBD), block development, and (semi-) detached houses). Main USTs are primarily defined according to the predominant type of LU (i.e., function). In contrast, their subclasses relate to the physiognomy of developed and open land (i.e., form), including the arrangement and density of buildings, impervious surface area (ISA), and vegetation structure (Böhm et al. 2001a; Böhm et al. 2001c). This is why USTs are sometimes also called urban morphology types (UMTs) (Gill et al. 2008). A standardized UST classification system does not exist yet (Banzhaf & Höfer 2008; Wurm & Taubenböck 2010c). Mapping schemes vary slightly from city to city and usually incorporate a mixture of LU

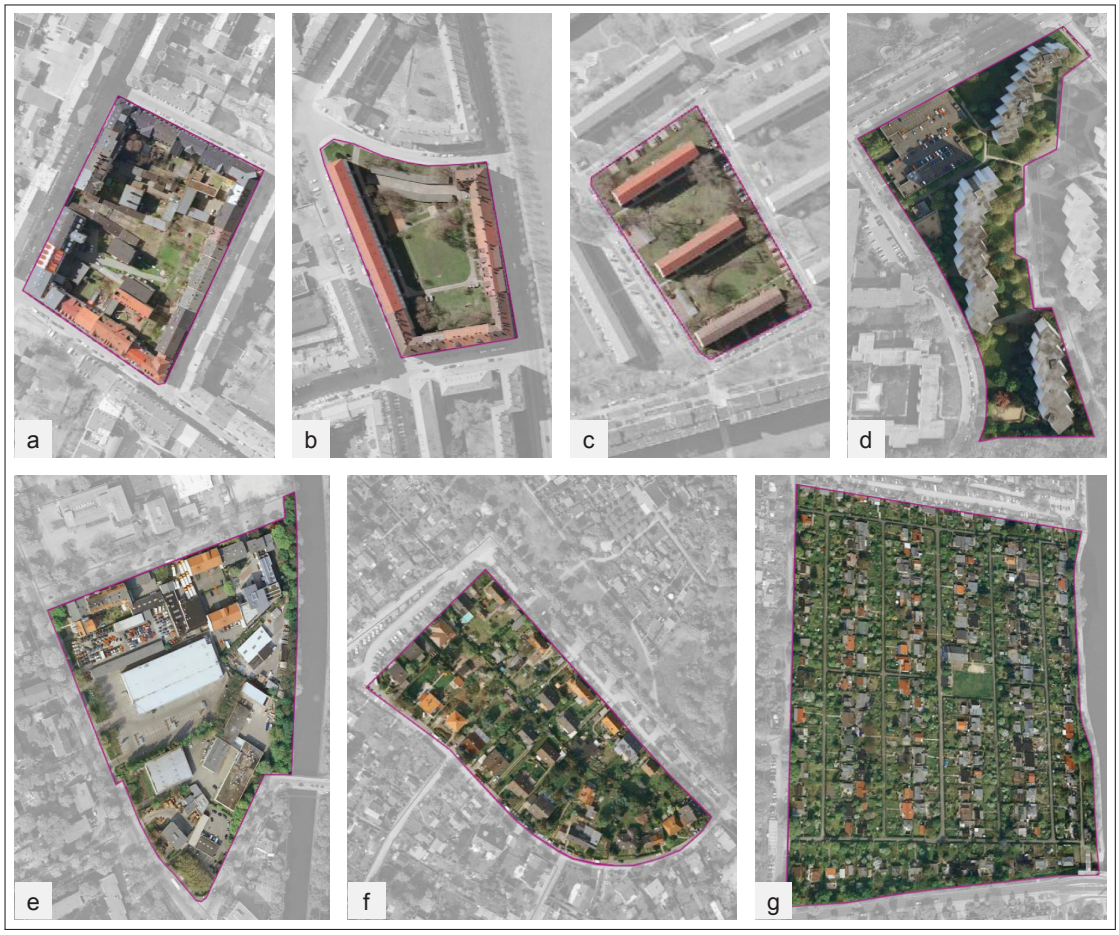

Fig. 2–4: Visual examples of selected UST categories: (a) block development, (b) perimeter block development, (c) row development, (d) high-rise districts, (e) industrial and commercial parks, (f) detached and semi-detached homes, and (g) allotment gardens. Block geometries are highlighted in purple (modified after Bochow 2010).

and LC classes with specific connotations (Fig. 2–4). However, since UST maps aim at supporting decision makers with geospatial information needed to plan and manage sustainable urban development, their class descriptions are strongly connected to official land development plans (Pauleit 2011). Apart from that, UST legends also resemble classifications of urban biotope types and local climate zones (LCZs) (Bochow et al. 2010a; Bechtel et al. 2015; Schulte & Sukopp 2000; Stewart & Oke 2012; Sukopp & Weiler 1988). The spatial delimitation of individual UST entities is based on block geometries, i.e., the streets, railways, and/or topographic features surrounding a block of buildings (cf. Geiss et al. 2011). In this way, USTs integrate seamlessly into the hierarchical physical and administrative organization of urban areas. The block concept therefore allows to make both site-specific evaluations as well as more general assessments of urban environmental performance on an aggregated scale (e.g., at the census level; Meinel et al. 2007). Furthermore, the transferability of the UST approach is ensured because block geometries can be found in basically any human settlement. Some German cities (e.g., Berlin, Halle, Leipzig, and Munich) have already adopted UST maps to support urban planning and management (BSDUDE 2015; Pauleit & Duhme 2000; Wickop et al. 1998; Zierdt & Dippmann 1995).

Urban site characteristic (USC) is a hypernym specifically defined within this thesis. The term refers to all kinds of quantitative descriptors that help to map, monitor, and evaluate human settlements. These include, among others, biophysical proxies like vegetation fraction (VF) and ISA (Esch et al. 2009; Ridd 1995; Schöpfer et al. 2005), landscape patterns (Besussi et al. 2010; Huang et al. 2007; Ji et al. 2006), 2D and 3D morphology (Fina et al. 2014; González-Aguilera et al. 2013; Yu et al. 2010), and LST (Weng et al. 2004; Xian & Crane 2006; Yuan & Bauer 2007). In a broader sense, categorical data, such as LC (Lu et al. 2010; O'Neil-Dunne et al. 2013; Walker & Blaschke 2008), surface materials (Berger et al. 2015; Franke et al. 2009; Heiden et al. 2007), as well as LU and USTs (Banzhaf & Höfer 2008; Barnsley et al. 2001; Heiden et al. 2012; Mesev 2010) can also be considered as USCs since they complement urban analyses with continuous parameters (cf. Sect. 4.4). USCs are either based on spectral reflectance values (Chen et al. 2006; Small 2006; Xian & Crane 2006) or information previously extracted from remotely sensed imagery (e.g., LC; Heiden et al. 2012; Walde et al. 2014; Wurm & Taubenböck 2010c). Ancillary geospatial data can also be employed to obtain further USCs, with socioeconomic attributes like population density being quite common (Buyantuyev & Wu 2010; Huang et al. 2011). Once they have been derived, it is straightforward to use USCs in the context of various applications. In the present work, for instance, a set of USCs is utilized to map urban LC and USTs as well as to investigate urban LST patterns and surface UHIs (cf. Sect. 4).

Land surface temperature (LST) is the "average temperature of an element of the exact surface of the Earth calculated from measured radiance" (Gillespie 2014). Therefore, it is often referred to as radiometric or skin temperature (Li et al. 2013). LST can either be measured locally by the use of dedicated thermometers or remotely with data acquired by air- and spaceborne TIR sensors (cf. Sect. 2.1.2). It is an essential parameter in urban climate research, where it serves as an indicator of surface UHI (cf. Sect. 2.1.5; Roth et al. 1989). Comprehensive information on LST, including in-depth definitions, measurement principles, scale issues, and related problems, can be found in Becker & Li (1995), Cheng & Ren (2012), Li et al. (2013), and Norman & Becker (1995).

2.1.5 The UHI effect: Overview, formation, and types

Human settlements have radiative, thermal, aerodynamic, and hydraulic properties that are much different from those of natural landscapes (Landsberg 1981). This fact gives rise to what is arguably the most well-documented example of anthropogenic climate modification – the UHI effect (Arnfield 2003). It refers to the observation that cities, towns, and even villages often experience higher air and surface temperatures than their rural surroundings (Oke 1973). Urban warming is usually strongest during longer periods of fine weather, i.e., clear skies and no or very light winds (Oke 1982). Under these circumstances, the air and surface temperature difference between a large city (population ≥ 100 000) in the mid-latitudes and its environs can be as much as 12 respectively 17 K (cf. Oke & East 1971; Price 1979). The first scientific record of an UHI

Tab. 2–3: Summary of the controllable determinants of UHI formation and their impact on energy balance terms (after EPA 2008; Grimmond 2007; Oke 1981; Oke 1982; Rizwan et al. 2008).

Factor	Impact	
Urban geometry	Increased surface area, increased multiple reflection	▸ Increased absorption of shortwave radiation
	Decreased sky view factor (SVF)	▸ Decreased loss of longwave radiation
	Increased surface roughness, decreased wind speeds	▸ Decreased total turbulent heat transport
Surface materials	Decreased albedo	▸ Increased absorption of shortwave radiation
	Increased thermal inertia	▸ Increased sensible heat storage
	Increased "waterproofing", decreased vegetation fraction	▸ Decreased evapotranspiration
Human activities	Increased energy use, increased combustion	▸ Increased anthropogenic heat discharge
	Increased emission of dust, air pollutants and water vapor	▸ Increased absorption of shortwave radiation, increased emission of longwave radiation from sky

dates back to Howard (1833[2]) and, since its discovery, the phenomenon has been demonstrated beyond doubt (Oke 1982) and studied extensively (Arnfield 2003; Landsberg 1981; Oke 1987[2]; Rizwan et al. 2008; Stewart 2010) so that some generalizations can be drawn.

The formation of UHIs is caused by a complex interplay of many different factors operating at various spatio-temporal scales. In general, the scientific literature differentiates between uncontrollable and controllable determinants of urban warming (Rizwan et al. 2008). To the former group belong factors such as the weather (e.g., cloud cover, wind speed, synoptic weather type), geographic location (e.g., climate zone, topography, wind systems, proximity to water bodies, soil and vegetation types), and timing (e.g., season of year, solar angle, plant phenology, moisture availability, fuel use, time of day) (EPA 2008; Kuttler 2004; Oke 1982; Shahmohamadi et al. 2010). The factors of the latter group are listed in Table 2–3. They are related to the 3D geometry of urban environments, the properties of urban surface materials, and human activities. Urban geometry refers to the height, width, and spacing of buildings (Grimmond 2007). Special cases of urban geometry are street canyons, which are formed by "the walls and ground […] between two adjacent buildings" (Nunez & Oke 1977:11). They have several impacts on a city's climate. For instance, "the visible area of the sky from a given point on a surface", the so-called SVF, is reduced within street canyons (EPA 2008:12; Unger 2004). This leads to a trapping of the absorbed solar energy emitted from urban surfaces. The decreased loss of longwave radiation from street canyons therefore attenuates the cooling of urban infrastructure at night (Grimmond 2007; Oke 1981). Construction materials have distinct physical properties and contribute to UHI genesis as well. As one example, their heat capacity and, consequently, their thermal inertia is higher than that of rural soils and vegetation. This means that urban surfaces are able to take up and store greater amounts of energy from the Sun and that they slowly release this energy in the form of sensible heat at night, when rural surfaces have already cooled down (Keramitsoglou 2014; Oke 1982). Finally, urban warming is also driven by anthropogenic activities. The increased use of energy,

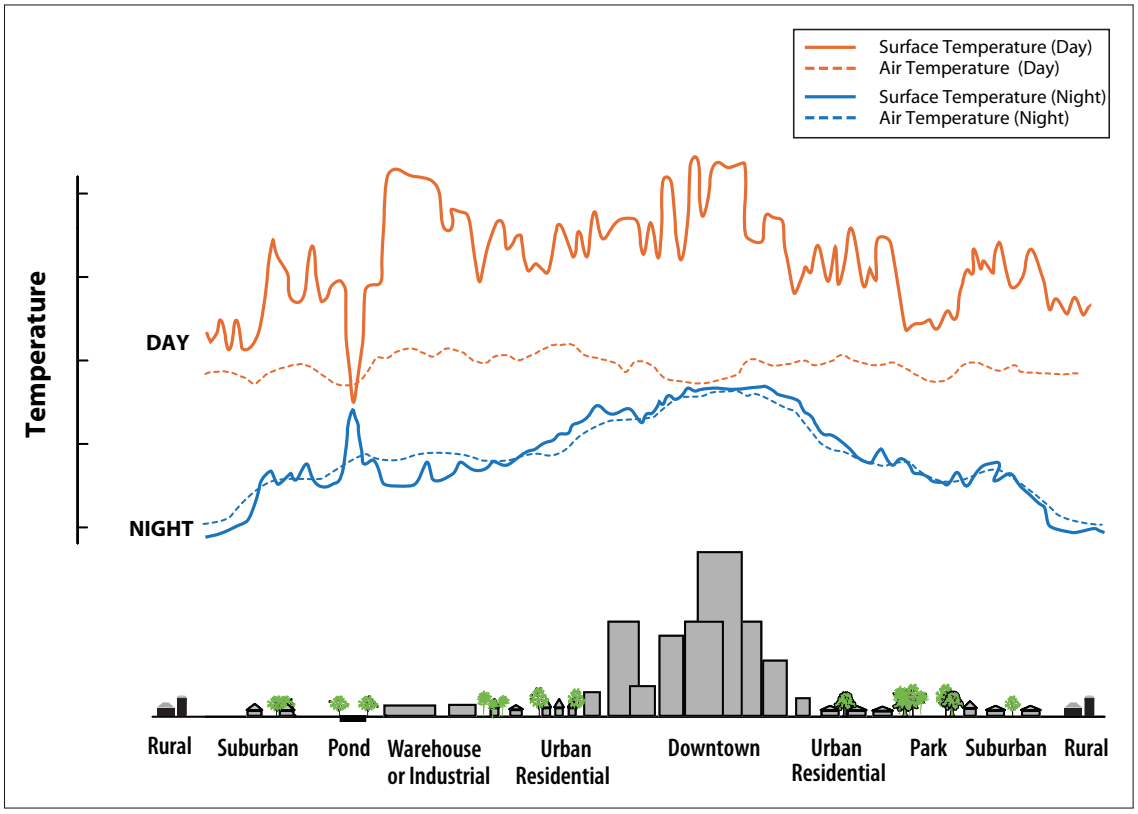

Fig. 2–5: Idealized air and surface temperature profiles along a rural–urban transect comprising different types of LU (EPA 2008; after Voogt 2002). The graphs highlight the spatio-temporal similarities and differences between surface and atmospheric UHIs. Note that the displayed temperatures do not refer to absolute but relative values.

combustion of fossil fuels, and emission of air contaminants in the urban domestic, traffic, and industry sectors determine an increased heat discharge as well as a greater absorption and (re-) emission of longwave radiation from the sky (EPA 2008; Grimmond 2007).

Depending on their evolution, impact, and measurement, two major types of urban warming can be differentiated: Atmospheric and surface UHIs (Oke 1976; Voogt & Oke 2003). While the former refer to the differences in air temperature between developed and rural areas, the latter relate to the thermal anomaly of urban surfaces (Fig. 2–5). Atmospheric UHIs are directly measured either through a network of fixed meteorological stations or by the use of automobile traverses recording ambient temperatures (Landsberg 1981; Oke 1973). They are often weak or even non-existent from late morning to early afternoon and become most pronounced a few hours after sunset, especially in winter (Grimmond 2007; Pickett et al. 2011; Shahmohamadi et al. 2010). This is because urban infrastructure releases absorbed solar energy with much lower efficiency at night than the countryside (Oke 1982). Moreover, anthropogenic heat can significantly contribute to atmospheric UHI formation in the cold season (EPA 2008). A feature that becomes evident from Figure 2–5 is that atmospheric UHIs exhibit relatively small variations over space and time. The reason for this observation is that air masses constantly mix within the atmosphere, thereby reducing existing temperature gradients (EPA 2008). On average, the daytime and nocturnal air

temperatures of settlements in the temperate zones are 1 to 3 K respectively 6 to 11 K higher than those of its hinterland (cf. Botkin & Beveridge 1997; Oke 1973; Oke 1997).

Surface UHIs are of particular relevance to this work as their detection and quantification is accomplished using thermal remote sensing. By applying some specific corrections to TIR imagery (cf. Sect. 2.1.2), LST maps can be obtained as indicators of urban surface warming (Roth et al. 1989). In contrast to atmospheric UHIs, the latter is observable day and night throughout the year. At daytime and in the summer, however, it tends to be strongest due to the presence and intensity of sunlight (EPA 2008; Roth et al. 1989). Figure 2–5 reveals that while surface temperatures are more constant and match the ambient temperatures overnight, they fluctuate widely across different types of urban LU by day (Prashad 2014). This shows that surface UHIs are very closely connected to the immediate site character, i.e., the biophysical properties of each individual urban element (Roth et al. 1989; Small 2006; Xian & Crane 2006). For instance, on a sunny and calm summer day, an industrial area with flat metal roofs and a large, asphalted parking site is likely to become a thermal hot spot (cf. Fig. 2–5) whereas the trees and lawns of a nearby park provide the necessary shading and evaporative cooling to form a local heat sink, also termed park cool island (PCI) (Ren et al. 2013). The magnitude of urban surface warming typically ranges between 10 to 15 K during the day and 5 to 10 K in the night (cf. Price 1979; Voogt & Oke 2003). Besides the temporal aspect, these numbers highlight that the differences between urban and rural areas are much higher when surface temperatures instead of air temperatures are considered.

2.2 Literature review

2.2.1 Mapping of urban LC and USTs with HSR data

Urban LC — From a historical point of view, surveying from the ground or the manual interpretation of analogue aerial imagery have long been the only ways to obtain detailed (urban) LC maps (Woodcock et al. 1983). It was not until the first HSR digital cameras became available that scientists of different backgrounds began working on the development of computer-aided methods to produce such information (Guindon 1997). In this context, the launch of Ikonos-2 in September 1999 is often referred to as having ushered in a new era of urban remote sensing (Aguilar et al. 2013; EUSI 2015; Sawaya et al. 2003). Ikonos-2 was the first commercial Earth observation satellite to collect HSR multispectral and, at the same time, publicly accessible data (cf. Tab. 2–1). The system therefore opened up a whole range of new opportunities to an extended community of users from industry, government, and research (Ehlers 2009; Zanoni & Goward 2003). Driven by the need to adequately process the latest generation space- and airborne optical imagery, an ever growing number of dedicated studies has appeared over the years (see below). A similar, but more recent trend goes along with the advent and open distribution of 3D point clouds and HSR object height data acquired over human settlements (Sect. 2.1.2; Yan et al. 2015).

The introductory paragraph already indicates that, to date, fine-scale urban LC information is mainly extracted from HSR multispectral scenes (Fauvel et al. 2006; Johnson 2013; Shackelford & Davis 2003; Taubenböck et al. 2010b; Walker & Blaschke 2008). Only a small number of investigations solely relies on 3D point clouds (Alexander et al. 2011; Zhu & Toutin 2013), and just a few more combine imagery and object heights (Kim & Kim 2014; Salehi et al. 2012; Wurm et al. 2011). This is contrary to the observation that both data types are of high descriptive power and non-redundant, making them particularly well-suited for fusion at feature level (cf. Sect. 2.1.1; Gamba et al. 2005; Weng et al. 2014; Wentz et al. 2014; Yan et al. 2015). In fact, using LiDAR or photogrammetric information in addition to optical images is known to improve urban area characterization (Haala & Brenner 1999; Herold & Roberts 2006; Priestnall et al. 2000). Some authors even argue that height data are the key to accurate mapping, given that their quality (e.g., LiDAR point cloud density) meets the requirements of the intended application (O'Neil-Dunne et al. 2013; O'Neil-Dunne et al. 2014; MacFaden et al. 2012).

The methods employed for the classification task are diverse. They include, but are not limited to: traditional supervised and (non-) parametric techniques like the pixel-based ANN (La Rosa & Wiesmann 2013), ML (Herold & Roberts 2006), nearest neighbor (NN) (Yokoya et al. 2014), and spectral angle mapper (SAM) classifiers (Forzieri et al. 2013); more recent machine learning procedures such as decision trees (Alexander et al. 2011), random forests (RFs) (Niemeyer et al. 2014), and SVMs (Tuia & Camps-Valls 2011); Bayesian networks (Qian et al. 2015); ensemble decision fusion (Thoonen et al. 2012); Dempster-Shafer and graph theory (Cao et al. 2012; Liao et al. 2015); genetic algorithms (Pahlavani et al. 2015); random fields (Cai & Liu 2013; Zhong et al. 2014b); multi-agent systems (Zhong et al. 2014a); regression models (Okujeni et al. 2014); and hybrid approaches (Novack et al. 2011). However, by far the most popular way of deriving detailed urban LC maps is GEOBIA (Chen et al. 2009; O'Neil-Dunne et al. 2013; Hamedianfar et al. 2014; Wurm et al. 2011), underscoring its suitability to exploit HSR data.

The image features used for class discrimination are as varied as the methods taking advantage of them. They comprise, for instance, typical multispectral and object height data characteristics (cf. Sect. 2.1.2; MacFaden et al. 2012; Zhou et al. 2014), the comprehensive set of attributes available through GEOBIA processing environments (cf. Sect. 2.1.3; O'Neil-Dunne et al. 2014; Salehi et al. 2012), filtering outputs like morphological profiles (MPs) (Liao et al. 2015; Luo & Zhang 2014), geostatistics from semi-variogram analyses (Yue et al. 2013), shape indices (Han et al. 2012; Zhang et al. 2013), and class probabilities (Cao et al. 2012; Fauvel et al. 2006).

Most of the results achieved with the above data, methods, and features are promising. It is not uncommon that observed overall accuracies are above 85, 90, or even 95% (Chen et al. 2009; O'Neil-Dunne et al. 2014; Pahlavani et al. 2015; Wurm et al. 2011; Xu et al. 2014; Zhou et al. 2014). As indicated earlier, this is not exclusively, but especially true for studies integrating HSR optical imagery and 3D point clouds as well as investigations incorporating GEOBIA expert systems or advanced machine learning routines that leverage contextual image information and

the spatial relationships between pixels and objects. Only the traditional pixel-based techniques unsurprisingly tend to be less appropriate for urban LC classifications from HSR data (cf. Sect. 2.1.3; Chen et al. 2009; Hamedianfar et al. 2014; Herold & Roberts 2006; Kim & Kim 2014).

As a summary of the above paragraphs, the usage of HSR multispectral imagery and 3D point clouds within a GEOBIA environment holds the largest potential for detailed urban LC mapping. This is because of two reasons. First, both of the above data types are of high descriptive power and non-redundant, which makes them particularly well-suited for fusion at feature level (Gamba et al. 2005; Weng et al. 2014; Wentz et al. 2014; Yan et al. 2015). Second, GEOBIA approaches are markedly versatile. They can incorporate a diversity of input data (Hay & Castilla 2008; Kim et al. 2010; Zhang 2010), offer a large variety of image features and processing tools (Blaschke & Strobl 2001), and enable the reutilization of developed rule sets (Flanders et al. 2003; Schöpfer & Möller 2006; Taubenböck et al. 2010b). Besides further advantages, this makes them superior to pixel-based methods (Bhaskaran et al. 2010; Linde & Kirstein 2004; Platt & Rapoza 2008) and highly appropriate for feature extraction from HSR multisensor inputs.

USTs — In comparison to existing LC mapping efforts, significantly less research has been directed towards the characterization of USTs and urban LU at the parcel level. This is certainly related to the fact that such inventories are a rather new and specific field within urban remote sensing that only recently gained increased attention (cf. Banzhaf & Höfer 2008; Meinel et al. 2007). At the same time, this already gives an indication of the challenges associated with deriving these information (cf. Sect. 2.1.4; Barnsley et al. 2001; Loveland 2012; Wentz et al. 2014).

The literature reveals that there are two general approaches to UST mapping: Manual interpretation (e.g., Gill et al. 2008; Pauleit & Duhme 2000) and computer-aided classification (e.g., Walde et al. 2014; Wurm & Taubenböck 2010c). Both strategies always rely on some kind of HSR imagery, including color infrared (CIR) aerial photos (Banzhaf & Höfer 2008; Zierdt & Dippmann 1995), multispectral satellite scenes (Aubrecht et al. 2009; Meinel & Heber 1998), or even hyperspectral (Bochow et al. 2010a; Heiden et al. 2012), thermal (Böhm et al. 2001b; Wickop et al. 1998), and SAR acquisitions (Geiss et al. 2011; Lindner et al. 2011). They also make consistent use of ancillary geospatial data, such as land development plans (BSDUDE 2015) or maps of urban zones (Steinnocher et al. 2001), biotope types (Wickop et al. 1998), and topographic features (Steiniger et al. 2008). However, only computer-assisted analyses (are able to) take full advantage of height information inferred from LiDAR or photogrammetric principles (Hermosilla et al. 2014; Wurm et al. 2009). Another interesting point is that almost none of the reviewed studies takes a pass on block geometries and instead presents an own attempt to spatially divide cities into units of homogeneous physiognomy (cf. Lackner & Conway 2008; Taubenböck et al. 2006). Although this would surely contribute to methodological independence and transferability, it is obviously not a trivial task and may also not be desired by the map end user. Thus, UST surveys generally require remote sensing and complementary data sets to be successful.

Tab. 2–4: Key features of the UST studies most relevant to this work (OA = overall accuracy).

Reference(s)	Study area(s)	Input data	Method(s)	Class #	OA [%]
Banzhaf & Höfer (2008)	Leipzig, DE[1];	Multispectral imagery (CIR orthoimages);	GEOBIA	9	93.40
	Leipzig, DE[1]	GIS data (block boundaries, LU map (ATKIS))		14	73.15
Bochow et al. (2010b)	Berlin, DE[1];	Multi-/hyperspectral imagery (Ikonos-2/HyMap scenes);	GEOBIA; Machine learning	10	81.00
	Dresden, DE[1];	Object height data (nDSMs/3D city model);	(fuzzy logic modeling); Manual	6	83.00
	Padang, ID[1]	GIS data (block boundaries)	digitization	5	83.00
Heiden et al. (2012)	Munich, DE[1]	Hyperspectral imagery (HyMap scene); Object height data (nDSM)	Separability analysis	10	—.—
Hermosilla et al. (2012);	Sagunto, ES	Multispectral imagery (CIR orthoimages);	Machine learning (decision tree	8	93.50
Hermosilla et al. (2014)		Object height data (nDSM); GIS data (block boundaries)	classifier); Graph theory	8	81.10
Hu & Wang (2013)	Austin, TX[1]	Multispectral imagery (CIR orthoimages); Object height data (DSM) GIS data (block boundaries, LU map)	Machine learning (decision tree classifier)	4	61.61
Lackner & Conway (2008)	Mississauga, CA[1]	Multispectral imagery (Ikonos-2 scene);	GEOBIA	6	90.00
		GIS data (road network)		10	86.00
Meinel et al. (2007);	Bonn, DE;	GIS data (LU maps (ATKIS), topographic maps)	Filter operations (morphology);	8	76.60
Meinel et al. (2008)	Dresden, DE		GEOBIA; Pattern recognition	8	76.00
Puissant et al. (2012)	Strasbourg, FR[1];	Multispectral imagery (QuickBird-2/SPOT-5 scenes);	GEOBIA	9	76.60
	Toulouse, FR[1]	GIS data (block boundaries)		9	93.35
Steiniger et al. (2008)	Zurich, CH[1];	GIS data (block boundaries, building footprints)	Machine learning	5	75.00
	Southampton, UK[1]		(discriminant analysis)	5	74.00
Steinnocher et al. (2001)	Vienna, AT[1]	Multispectral imagery (Ikonos-2 scene); GIS data (LU map)	GEOBIA; Graph theory	11	—.—
Walde et al. (2014)	Rostock, DE	Multispectral imagery (QuickBird-2 scene); Object height data (nDSM); GIS data (LU map (ATKIS))	GEOBIA; Graph theory; Machine learning (RF classifier)	5	87.00
Wurm et al. (2009)	Cologne, DE[1];	Multispectral imagery (Ikonos-2 scenes); Object height	GEOBIA	15	—.—
	Dresden, DE[1]	data (DSM); GIS data (LU boundaries/maps (ATKIS))		15	—.—
Wurm & Taubenböck (2010c)	Munich, DE[1]	Multispectral imagery (Ikonos-2 scene); Object height data (DSM); GIS data (LU map)	GEOBIA	6	80.00

[1] A spatial subset of the mentioned study area is investigated in the corresponding publication(s).

The digital mapping methods employed to assign USTs are not as diverse as those to extract urban LC (Tab. 2–4). Among them are machine learning algorithms like AdaBoost (Steiniger et al. 2008), decision trees (Hermosilla et al. 2012), and RFs (Walde et al. 2014), but also some hybrid procedures (Bochow et al. 2010a; Meinel et al. 2007). Nevertheless, the bulk of publications focuses on the development of GEOBIA techniques (Banzhaf & Höfer 2008; Lackner & Conway 2008; Wurm & Taubenböck 2010c). This is probably not least because of their ability to process HSR data from multiple sources (cf. Sect. 2.1.3; Hay & Castilla 2008).

Many different features, or USCs, have been proposed to describe USTs [1]. They can be divided into object- and block-level parameters. While the former refer to attributes of individual urban elements within a block, the latter summarize data and LC properties of an entire land lot (Bochow et al. 2010a; Hermosilla et al. 2012; Meinel et al. 2008). Typical object- and block-level characteristics are therefore building size (in m^2) and density (in %), respectively. The above definitions imply that detailed urban LC maps are central to any UST classification and that their accuracy has a large impact on the quality of the final product. Indeed, LC data collection or extraction is an integral preparatory part of any study in the field (e.g., Aubrecht et al. 2009; Geiss et al. 2011; Hermosilla et al. 2012). Based on these information, a variety of queries can be made to create USCs related to, for example, the morphology, abundance, proportion, spatial arrangement, and distribution of LC within city blocks (Bochow et al. 2010b; Lackner & Conway 2008). Moreover, the set of usable morphological features is greatly enhanced when the LC layer is jointly analyzed with 3D data. This enables the computation of LC-specific quantities of volume and height (cf. Hermosilla et al. 2012). The implementation of the above queries can be realized on the basis of different concepts, including Gestalt theory for morphological features (Steiniger et al. 2008), landscape metrics and graph measures for topological relationships (Baud et al. 2010; Walde et al. 2014), and GEOBIA for all kinds of USCs (Wurm & Taubenböck 2010c).

The mapping results reported for the presented investigations are satisfying, but still leave room for improvement. Overall accuracies are often below 85 or even 80% and span from 61.6 to 93.5% (Hu & Wang 2013; Wu et al. 2007). Higher performances are mainly reached on relatively small test sites (Banzhaf & Höfer 2008; Hermosilla et al. 2012; Lackner & Conway 2008) or for a limited number of UST classes (Geiss et al. 2011; Graesser et al. 2012; Walde et al. 2014).

In conclusion to this section, the characterization of USTs and LU at parcel level is a relatively young and small field in urban remote sensing. For a long time, manual interpretation was the predominating mapping strategy (Böhm et al. 2001b; Meinel & Heber 1998; Pauleit & Duhme 2000; Wickop et al. 1998; Zierdt & Dippmann 1995). In contrast to that, computer-aided classifications have only recently gained more interest (starting with Banzhaf & Höfer 2008; Meinel et al. 2007; Steinnocher et al. 2001). However, despite just a few years of research, one particular trend can already be deduced from the scientific literature. More specifically, Table 2–4

[1] For an overview of specific USCs, the reader is referred to Section 2.2.2 and Table 2–5.

reveals that GEOBIA systems are most popular for generating UST maps. This is because of several key features they offer. First, GEOBIA can integrate HSR data from multiple sources within a single software environment (Hay & Castilla 2008; Kim et al. 2010; Zhang 2010). Since almost all of the reviewed studies rely on a combination of imagery, object heights, and/or ancillary geospatial information (e.g., block geometries), this ability is of crucial importance. Second, because GEOBIA works at the interface of remote sensing and GIS (Blaschke & Strobl 2001), it provides a lot of options to explore the different input data sets, to make use of their synergistic potential, and to implement existing and new USCs for improved UST descriptions. Third, GEOBIA enables an accurate extraction of fine-scale urban LC information and allows for their comprehensive analysis within UST mapping projects. Considering the central role of LC inventories in UST classifications (Aubrecht et al. 2009; Geiss et al. 2011; Hermosilla et al. 2012), this is another big quality. Together with the possibility to reuse developed rule sets, these advantages highlight the suitability of GEOBIA approaches for the derivation of USTs from HSR multisource data.

2.2.2 Monitoring of surface UHIs with 2D/3D USCs

USCs — A variety of USCs has been suggested for human settlement mapping and monitoring. These indicators either refer to properties of individual urban LC elements (e.g., buildings and trees) or a predefined reference area of interest (AOI). The latter can be a single pixel, a grid cell, or a moving window (kernel) summarizing groups of classified pixels (Pesaresi et al. 2011b; Taubenböck et al. 2009a). It can also be a circle of a certain radius around specific urban LC objects (Lang et al. 2008; Tompalski & Wężyk 2012), one or more stretches of roads (Hermosilla et al. 2014), or an administrative area like a tax parcel, land lot, city block, zoning district, or a census unit (Hermosilla et al. 2012; Pan et al. 2008; Santos et al. 2012; Wu et al. 2007; Yu et al. 2010). If the AOI is a single pixel, the desired parameter is computed by analyzing the proportion of different LC classes at the sub-pixel level using spectral unmixing techniques (Esch et al. 2009; Leinenkugel et al. 2011; Weng 2012; Xian & Crane 2006; Yuan & Bauer 2007).

Besides the scale or level of inference, USCs can be subdivided into 2D and 3D descriptors (Tab. 2–5). 2D USCs are sometimes based on spectral reflectance values, but mainly rely on LC information previously collected or extracted from remote sensing imagery. Most of the spectral indicators are band ratios like the enhanced built-up and bareness index (EBBI) (Assyakur et al. 2012), index-based built-up index (IBI) (Xu 2008), normalized difference built-up index (NDBI) (Zha et al. 2003), normalized difference impervious surface index (NDISI) (Xu 2010), and NDVI (Rouse et al. 1973). 2D USCs based on LC address many different features of urban object and surface types within the AOI, including their area and perimeter (Heinzel & Kemper 2015; Hermosilla et al. 2012; Qiu et al. 2010; Ural et al. 2011; Yu et al. 2010), shape and geometry (Chen 2011; Hermosilla et al. 2012), frequency and proportion (Heiden et al. 2012; Lang et al. 2008; Pan et al. 2008; Pesaresi et al. 2011b; Schöpfer et al. 2005), as well as topology

Tab. 2–5: Compilation of USCs frequently used for urban monitoring.

Type	Focus	Examples[1]
2D	Spectral reflectance	
	Natural features	BCI (Deng & Wu 2012); BI (Assyakur et al. 2012); NDBaI (Zhao & Chen 2005); NDVI (Kriegler et al. 1969; Rouse et al. 1973; Tucker 1979); NDWI (Gao 1996); SAVI (Huete 1988)
	Man-made features	EBBI (Assyakur et al. 2012); IBI (Xu 2008); NDBI (Zha et al. 2003); NDISI (Xu 2010); UI (Kawamura et al. 1996)
	Urban LC elements	
	Area and perimeter	Building area (Aguilar et al. 2013; Heinzel & Kemper 2015; Hermosilla et al. 2012; Ural et al. 2011; Yu et al. 2010); Building perimeter (Hermosilla et al. 2012; Yu et al. 2010); Road surface area (Chun & Guhathakurta 2016; Hermosilla et al. 2014)
	Shape and geometry	Circularity, compactness, ellipticity, elongation, fractal dimension, radial shape, rectangular fit of cities, blocks, and buildings (Chen 2011; de Souza & Giunta 2011; Hermosilla et al. 2012)
	Frequency and proportion	BAR (Lakes & Kim 2012); BCR (de Souza & Giunta 2011; Fina et al. 2014; González-Aguilera et al. 2013; Heiden et al. 2012; Hermosilla et al. 2012; Pan et al. 2008; Salomons & Berghauser Pont 2012; Yoshida & Omae 2005; Yu et al. 2010); Building number (Yu et al. 2010); Edge density (Pesaresi et al. 2011b); FSV (Lang et al. 2008; Moeller & Blaschke 2006); GI (Hofmann et al. 2011b; Lang et al. 2008; Schöpfer et al. 2005); ISA (Esch et al. 2009; Heiden et al. 2012; Pesaresi et al. 2011b; Yuan & Bauer 2007); Road network density (Salomons & Berghauser Pont 2012); Vegetation to building ratio (Heinzel & Kemper 2015); VF (Gupta et al. 2012; Scarano & Sobrino 2015; Weng et al. 2004; Wurm et al. 2011; Yuan & Bauer 2007)
	Topology and arrangement	Adjacency between and proximity to LC objects (Gupta et al. 2012; Hermosilla et al. 2012); Lacunarity (Greenhill et al. 2003)
3D	Height	Height of urban LC objects (Chun & Guhathakurta 2016; González-Aguilera et al. 2013; Heiden et al. 2012; Hermosilla et al. 2012; Qiu et al. 2010; Santos et al. 2012; Yu et al. 2010); Percentage of high- and low-rise buildings (Gupta et al. 2012)
	Volume	Volume of urban LC objects (Chun & Guhathakurta 2016; González-Aguilera et al. 2013; Heiden et al. 2012; Hermosilla et al. 2014; Lwin & Murayama 2009; Rafiee et al. 2016; Santos et al. 2012; Yu et al. 2010); Volumetric density (Fina et al. 2014; Heiden et al. 2012; Santos et al. 2012); Volumetric homogeneity (Santos et al. 2012); VV2BV (Tompalski & Wężyk 2012)
	Area	CAR (Srivanit & Kazunori 2011); FAI (Wong & Nichol 2013); FAR (de Souza & Giunta 2011; Krehl et al. 2016; Giridharan & Kolokotroni 2009; González-Aguilera et al. 2013; Salomons & Berghauser Pont 2012; Yoshida & Omae 2005; Yu et al. 2010); GPR (Ong 2003); LAI (Nichol 1994)
	View	Enclosure index (Susaki et al. 2013); SVF (Chun & Guldmann 2014; Eliasson 1992; Gál et al. 2009; Krüger et al. 2011; Nassar et al. 2016; Scarano & Sobrino 2015; Svensson 2004)

[1] Please refer to page xxi for definitions of abbreviated USCs.

and arrangement (Gupta et al. 2012; Hermosilla et al. 2012). Some of them are implemented through landscape metrics (Greenhill et al. 2003; Herold et al. 2002; McGarigal 2014).

In contrast to the bulk of 2D parameters, 3D USCs do not only draw from LC inventories but also incorporate urban object height data. They can be further differentiated into height-, volume-, area-, and view-related indices. Typical representatives of the former group are building and vegetation height (González-Aguilera et al. 2013; Lwin & Murayama 2009; Poznanska et al. 2013), but also the percentage of high- and low rise buildings within the AOI (Gupta et al. 2012). Common examples of the second group are the volume of man-made objects and trees (Hermosilla et al. 2012; Qiu et al. 2010; Yu et al. 2010), the vegetation volume to built-up volume (VV2BV) ratio (Tompalski & Wężyk 2012), and volumetric density (Fina et al. 2014; Heiden et al. 2012; Santos et al. 2012). To the third group belong measures like the floor area ratio (FAR), green plot ratio (GPR), and leaf area index (LAI) (de Souza & Giunta 2011; Ong 2003; Salomons & Berghauser Pont 2012; Yoshida & Omae 2005; Yu et al. 2010). The last group comprises the enclosure index and SVF (Chun & Guldmann 2014; Gál et al. 2009; Scarano & Sobrino 2015; Susaki et al. 2013). All of the above 2D and 3D quantities are often statistically summarized (e.g., by computing their mean, minimum, and maximum values per AOI) or normalized (Heiden et al. 2012; Hermosilla et al. 2014; Wurm & Taubenböck 2010c). Besides, many of them are related to the density or compactness of urban environments (e.g., Fina et al. 2014; González-Aguilera et al. 2013; Krehl et al. 2016; Pan et al. 2008; Yu et al. 2010).

Surface UHIs — Numerous studies have investigated the linkage between USCs and surface UHIs. In general, the scientific literature can be grouped into several categories according to the USCs considered. Biophysical descriptors of human settlements, like surface albedo, VF, and ISA, are among the most frequently used USCs. They are usually obtained from spectral indices (Chen et al. 2006; Liu & Zhang 2011; Ogashawara & da Silva Brum Bastos 2012; Xian 2008), spectral unmixing (Small 2006; Weng et al. 2004; Yuan & Bauer 2007), or subpixel classification techniques (Lazzarini et al. 2013; Xian & Crane 2006; Zhang et al. 2009b). Discrete representations of urban LC and LU are of similar popularity as biophysical descriptors. They are often utilized to study intra-urban temperature differences, the magnitude of surface UHIs, and their changes over space and time (Chen et al. 2006; Lazzarini et al. 2013; Li et al. 2011; Mallick et al. 2013; Weng 2001; Xiao et al. 2008). A special form of LC representations are urban surface material maps, which have been compared to LST patterns as part of some studies (Ben-Dor & Saaroni 1997; Heldens et al. 2013; Quattrochi & Ridd 1994).

On the basis of LC and LU products, it is possible to extract further USCs, including landscape and settlement density metrics. Respective research has demonstrated that the composition and configuration of LC elements as well as the intensity of urban development can be closely connected to the thermal characteristics within cities (Li et al. 2011; Li et al. 2016; Liu & Weng 2008; Liu et al. 2016; Maimaitiyiming et al. 2014; Myint et al. 2013; Ren et al. 2013; Weng et al. 2008; Xiao et al. 2008; Yue et al. 2012; Zhang et al. 2009a; Zhou et al. 2011). A few investigations have dealt with 3D USCs like building or tree height and volume (Coseo & Larsen

2014; Ivajnšič et al. 2014; Nassar et al. 2016; Rafiee et al. 2016; Weber et al. 2014b), complete aspect ratio (CAR) (Srivanit & Kazunori 2011), frontal area index (FAI) (Wong & Nichol 2013), FAR (Giridharan & Kolokotroni 2009; Srivanit & Kazunori 2011), LAI (Nichol 1994), and SVF (Chun & Guldmann 2014; Chun & Guhathakurta 2016; Eliasson 1992; Gál et al. 2009; Krüger et al. 2011; Nassar et al. 2016; Scarano & Sobrino 2015; Svensson 2004). In most cases, it was found that these quantities have a strong impact on the genesis of UHIs because they were able to explain many of the variations in measurements of both urban LST as well as air temperature (e.g., Eliasson 1992; Nichol 1994; Srivanit & Kazunori 2011; Svensson 2004; Weber et al. 2014b). Besides remotely-sensed USCs, ancillary geospatial data are sometimes used to analyze the origins of surface UHI formation. Typical layers of information are socioeconomic attributes, with population density being a quite common one (Buyantuyev & Wu 2010; Huang et al. 2011; Li et al. 2016; Weng et al. 2008; Xiao et al. 2008).

Chapter 3

Scientific rationale

The current state of the art in the field of urban environmental monitoring with HSR multispectral and object height data helps identifying past as well as more recent topics of research (cf. Sect. 2.2). But even more importantly, it provides a means to infer those scientific aspects that have gained only little attention so far. The present chapter describes some of the research needs arising from the above literature review and uses them to formulate the specific objectives of this study (Sect. 3.1f.).

3.1 Research needs

Urban LC — Section 2.2.1 has shown that many studies have already been successful at applying GEOBIA approaches to characterize fine-scale urban LC on the basis of HSR data. However, in spite of previous mapping efforts, only little research in the field has been devoted to building and evaluating robust methods that are capable of processing different sets of HSR multispectral and object height data. So far, existing GEOBIA systems are frequently reported to work well on small spatial subsets (Lu et al. 2010; Salehi et al. 2012) or for one entire study area (>100 km^2) only (Platt & Rapoza 2008; Walker & Blaschke 2008). A closer look at the review statistics presented in Table 3–1 supports this statement. In addition, GEOBIA algorithms often rely on monosensor imagery (Taubenböck et al. 2010b) or even data acquired by one specific sensor (Schöpfer & Möller 2006; Platt & Rapoza 2008; Lu et al. 2010; Walker & Blaschke 2008). In order to exploit the full synergistic potential of those HSR multisource data that become increasingly available, suitable fusion techniques and effective practical solutions still need to be developed and rigorously tested. The latter requires an in-depth assessment of their performance with regard to classification accuracy as well as spatial, temporal, and sensor-related transferability. An adequate experimental setup should therefore comprise large volumes of HSR data acquired at varying sensing schemes and covering different urban areas with distinct physical structures.

USCs — Due to the 3D nature of human settlements, urban environmental monitoring should rely on information sources that account not only for the horizontal spatial dimensions of a city, but also for its vertical spatial dimension. This enables an integrated and more holistic assessment

Tab. 3–1: Selected research deficits arising from the literature review.

Research topic	Review criterion	Number	Percentage
Urban LC	Studies with at least one test site >100 km^2	15/115	13.04
	Studies with more than one test site >100 km^2	2/115	1.74
	Studies with more than two test sites >100 km^2	1/115	0.87
USCs	Studies proposing and/or using 2D USCs	78/96	81.25
	Studies proposing and/or using 3D USCs	31/96	32.29
	Studies proposing integrated 2D/3D USCs	4/96	4.17
USTs	Studies defining UST classes suitable for area-wide mapping	20/38	52.63
	Studies defining UST classes suitable for transferable mapping	12/38	31.58
	Studies defining UST classes for gap-free and robust mapping	1/38	2.63
Surface UHIs	Studies comparing LST against 2D USCs	119/125	95.20
	Studies comparing LST against 3D USCs	19/125	15.20
	Studies analyzing integrated 2D/3D USCs	0/125	0.00

of the "builtscape" (Gamba et al. 2004). In order to meet these requirements, various 2D and 3D USCs have been proposed and used to date (cf. Tab. 2–5). As detailed in Section 2.2.2, this holds especially true for the field of urban density mapping by means of remote sensing data and methods. However, despite these developments, it has to be kept in mind that each of the available USCs covers different and distinct features of a city and therefore addresses only specific aspects of human settlement density. This implies that there is a lack of comprehensive USCs being able to interrelate existing and possibly new spatial indicators for a more holistic assessment of density patterns in urban environments. Exceptions to this observation are limited. As Table 3–1 shows, only four out of 96 reviewed studies (i.e., ca. 4%) put a focus on developing these advanced metrics. Examples include the fuzzy urban index (Gopal et al. 2016), the Spacematrix (Berghauser Pont & Haupt 2010; Salomons & Berghauser Pont 2012), and a few indices related to urban green (Gupta et al. 2012; Liu et al. 2015; Tompalski & Wężyk 2012). Apart from these exceptions, there is still a need for integrated spatial indicators taking full advantage of a combination of 2D and 3D USCs to estimate urban density in its entirety. Their implementation would be straightforward provided that detailed urban LC information as well as HSR object height data are available.

USTs — The review in Section 2.2.1 has revealed that GEOBIA holds the largest potential for characterizing USTs. Accordingly, object-based approaches have already proven to be successful in the context of several independent UST studies (cf. Tab. 2–4). However, they are part of a relatively young field of science (starting with Steinnocher et al. 2001) so that there are still some research aspects deserving more attention. First, existing class hierarchies and definitions are insufficient. To date, investigations are often restricted to a limited number of map categories (Hu & Wang 2013; Steiniger et al. 2008; Walde et al. 2014; Wurm & Taubenböck 2010c) or a small spatial subset of the city under consideration (Bochow et al. 2010b; Heiden et al. 2012; Hu & Wang 2013; Lackner & Conway 2008; Steiniger et al. 2008; Steinnocher et al. 2001; Wurm et al. 2009). Furthermore, even though some of the earlier works deal with an extended set

of classes, they rely on site-specific UST legends (e.g., by referring to historic functional use) that are not applicable to other urban areas (cf. Banzhaf & Höfer 2008; Geiss et al. 2011; BSDUDE 2015). Table 3–1 reflects the above conceptual issues. More specifically, it highlights that there is only one relevant publication (Wurm & Taubenböck 2010c) in which UST classes are defined and derived that meet the requirements of map completeness and standardization (cf. Banzhaf & Höfer 2008; Breuste 2010; Heldens 2010). In order to enable the generation of area-wide (gap-free) and comparable (uniform) UST maps, there is a need for improved class hierarchies with greater depth, enhanced transferability, and, thus, broader applicability. The development of a comprehensive, yet generic UST map key is a prerequisite for the operational monitoring of cities and should therefore be an integral preparatory step within any future study in the field.

Second, the potential of many USCs remains unknown. Based on the form and function of the desired UST categories, a qualitative description and parametrization of all target classes is frequently performed in advance. As a consequence, the majority of existing classification schemes focuses on the extraction of features that have been subjectively predefined and are assumed to be effective according to the conceptual model for each UST of interest (Banzhaf & Höfer 2008; Meinel et al. 2007; Meinel et al. 2008; Wurm et al. 2009; Wurm & Taubenböck 2010c). Such an approach suffers from several drawbacks. One of them is that only a small fraction of potentially useful USCs is considered. Those site properties with no obvious link to any of the anticipated USTs are neglected. Another disadvantage is that the individual and combined descriptive power of all theoretically available USCs is not systematically assessed. Rather, an isolated examination and utilization of apparent physiognomic urban block characteristics takes place. This is one of the reasons why a lot of methods are fairly successful at deriving morphologically distinct USTs but less appropriate for an accurate differentiation of the more common and structurally similar USTs (cf. Wurm & Taubenböck 2010c). To overcome these limitations, the proposed strategies for extracting and selecting USCs need to be reconsidered. For this purpose, a promising approach is to systematically retrieve all kinds of land surface parameters known from the urban remote sensing literature (cf. Sect. 2.2.2) without making specific assumptions about their avail. While some of them may already be established, others, like landscape metrics (e.g., patch density) and several 3D USCs (e.g., VV2BV), may have never been used before in the context of UST mapping. After the derivation of these variables, it is crucial to statistically evaluate their suitability in the framework of a dedicated, importance-based assessment. The latter facilitates the identification of their individual potential as well as their synergies. In summary, the above suggestion would ensure a comprehensive analysis and objective comparison of USCs for a better characterization of USTs. Its implementation would help compiling a new set of UST features, developing more sophisticated class descriptions, and improving previously achieved mapping accuracies.

Surface UHIs — The compilation of studies in Section 2.2.2 shows that a considerable amount of research has already been directed towards understanding the interactions between USCs and LST.

Most notably, a lot of emphasis has been placed on the 2D features of a city. Table 3–1 confirms this tendency by indicating that 119 out of 125 publications (i.e., ca. 95%) deal with 2D metrics. In contrast to that, 3D (15%) and integrated 2D/3D USCs (0%) still remain largely unexplored although their impact on the urban climate is unquestioned (Oke 1981; Roth et al. 1989; Unger 2004) and their area-wide calculation has become feasible thanks to the increased availability of appropriate remote sensing data (Cook et al. 2013; Ehlers 2009; Gamba et al. 2005; IGN 2015; Lidar Online 2014; O'Neil-Dunne et al. 2013). Except for a few cases (Chun & Guldmann 2014; Chun & Guhathakurta 2016; Nassar et al. 2016; Scarano & Sobrino 2015; Weber et al. 2014b; Wong & Nichol 2013), there is still a lack of studies relating 2D, 3D, and integrated 2D/3D USCs to LST (cf. Mallick et al. 2013; Ngie et al. 2014; Voogt & Oke 2003). Moreover, previous research findings are often based on the analysis of a single study area, a limited number of USCs, and/or only a few LST scenes acquired within specific seasons (e.g., Huang et al. 2011; Liu & Zhang 2011; Maimaitiyiming et al. 2014; Myint et al. 2013; Ogashawara & da Silva Brum Bastos 2012; Ren et al. 2013; Weng et al. 2004; Xiao et al. 2008; Yue et al. 2012; Zhang et al. 2009a; Zhang et al. 2009b). In order to obtain a more complete picture of the connection between USCs and LST, more comprehensive investigations still need to be undertaken.

3.2 Study objectives

In accordance with the overall goal of the present thesis (cf. Sect. 1.2) and motivated by the four above research needs, the specific objectives of this study are defined as follows:

1. *Robust extraction of urban LC information*, including the
    - development and application of a robust GEOBIA approach to extract detailed and accurate urban LC information from HSR multispectral and object height data;
    - critical evaluation of the proposed method with regard to its performance for and transferability to different study areas and various sets of HSR multisensor data.
2. *Integrated assessment of 2D and 3D USCs*, including the
    - design and implementation of a new spatial indicator to integratively assess urban density by taking into account the horizontal and vertical key characteristics of a city;
    - critical evaluation of the proposed metric's plausibility and qualification to estimate human settlement density and its distinct spatial patterns for different urban LU types.
3. *Automated derivation of UST maps*, including the
    - development and application of a generic GEOBIA approach for an area-wide and automated derivation of USTs from HSR multispectral and object height data;

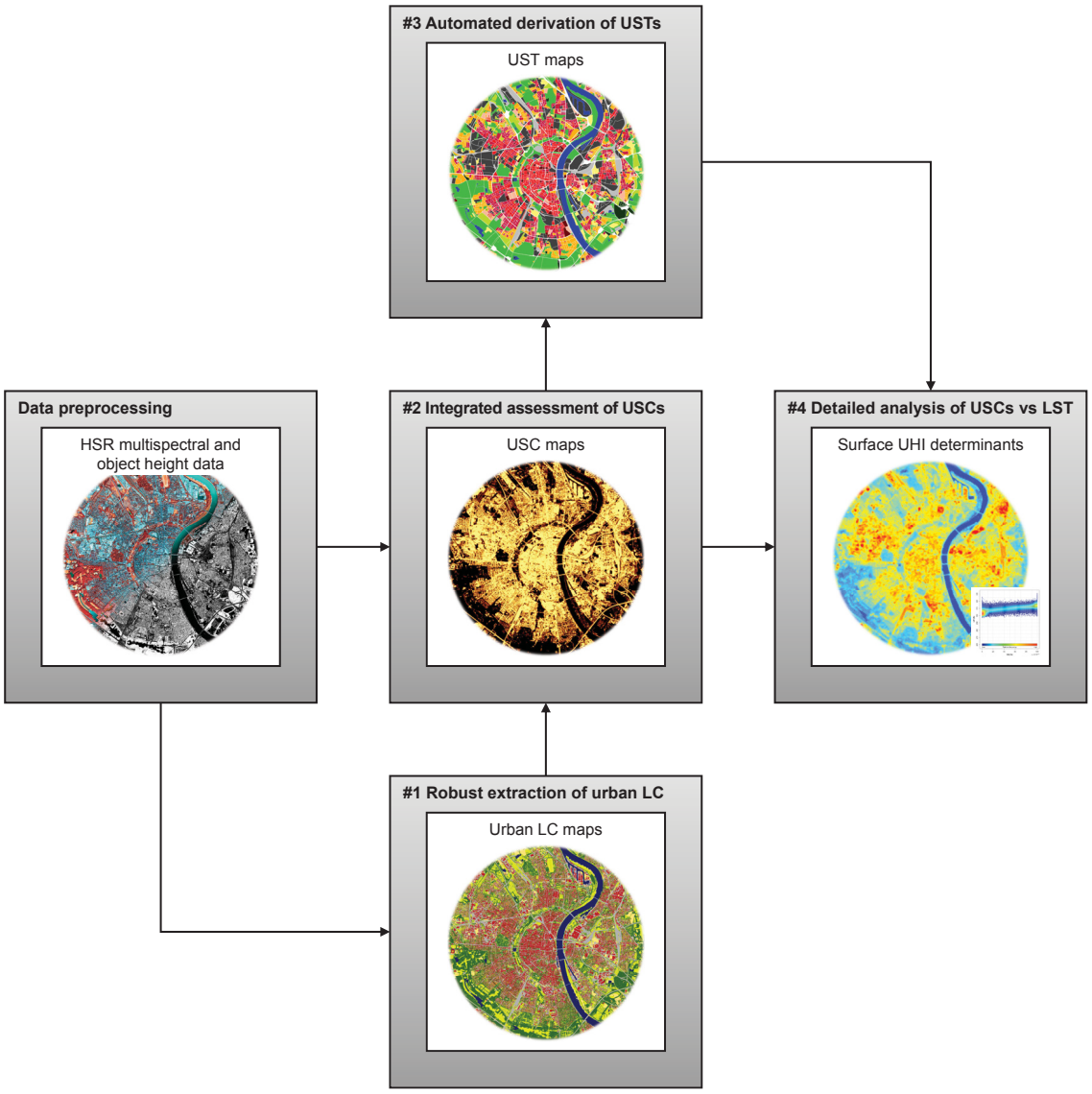

Fig. 3–1: Practical workflow of the dissertation and links between the four chosen research topics.

- critical evaluation of the proposed method regarding classification accuracy, workflow automation, and preparedness for future UST mapping and monitoring tasks.

4. *Detailed analysis of USC–LST links*, including the
   - calculation and analysis of 2D, 3D, and integrated 2D/3D USCs as potential predictors of urban LST as well as potential indicators of the surface UHI phenomenon;
   - detailed inspection of the observed relationships as well as their spatio-temporal dependencies by designing and implementing a comprehensive experimental setup.

Figure 3–1 provides an overview of the four chosen research topics and shows their thematic interconnection. At the same time, it illustrates the conceptual workflow of the practical investigations to be conducted within this thesis and outlines the research agenda for the next chapter.

Chapter 4

Research contributions

4.1 Robust extraction of urban LC information

This section is based on the manuscript entitled
"Robust extraction of urban land cover information from HSR multi-spectral and LiDAR data".

The manuscript was authored by
Berger C, Voltersen M, Hese S, Walde I & Schmullius C (2013)

and published in
IEEE J Sel Top Appl Earth Obs Remote Sens 6(5): 2196–2211;
doi: 10.1109/jstars.2013.2252329.

2196 IEEE JOURNAL OF SELECTED TOPICS IN APPLIED EARTH OBSERVATIONS AND REMOTE SENSING, VOL. 6, NO. 5, OCTOBER 2013

Robust Extraction of Urban Land Cover Information From HSR Multi-Spectral and LiDAR Data

Christian Berger, Michael Voltersen, Sören Hese, Irene Walde, and Christiane Schmullius

***Abstract*—This paper focuses on the description and demonstration of a simple, but effective object-based image analysis (OBIA) approach to extract urban land cover information from high spatial resolution (HSR) multi-spectral and light detection and ranging (LiDAR) data. Particular emphasis is put on the evaluation of the proposed method with regard to its generalization capabilities across varying situations. For this purpose, the experimental setup of this work includes three urban study areas featuring different physical structures, four sets of HSR optical and LiDAR input data, as well as statistical measures to enable the assessment of classification accuracies and methodological transferability. The results of this study highlight the great potential of the developed approach for accurate, robust and large-area mapping of urban environments. User's and producer's accuracies observed for all maps are almost consistently above 80%, in many cases even above 90%. Only few larger class-specific errors occur mainly due to the simple assumptions on which the method is based. The presented feature extraction workflow can therefore be used as a template or starting point in the framework of future urban land cover mapping efforts.**

***Index Terms*—Accuracy, data fusion, land cover, multi-sensor, object-based image analysis (OBIA), transferability, urban.**

I. Introduction

LAND COVER is an important characteristic for monitoring, describing, and analyzing the environment. According to Di Gregorio [1], it is defined as "the observed (bio)-physical cover on the earth's surface". Information about land cover are of substantial relevance to a broad range of fields, including climate change research and mitigation, sustainable development, resource management, biodiversity conservation, and biogeochemical cycling [2]. Besides these fields, land cover observations are of particular importance for urban planning.

Human settlements are complex and dynamic systems having both diverse and profound impacts on environmental factors and processes [3]. Because of the isolation of the land surface by impervious materials, soil permeability in urban areas is significantly reduced. As a result, groundwater tables are forced to decrease while, at the same time, surface runoff increases [4], [5]. The hydrological cycle is therefore highly affected by the presence and intensity of urban development. Human settlements do also influence energy fluxes between soil and atmosphere. Especially during longer periods of heat stress, a phenomenon called urban heat island (UHI) is observable [6]–[8]. Because construction materials store thermal energy longer than natural land cover types, cities often feature higher air temperatures at night than their surroundings. Since the knowledge about the physical properties of the land surface is crucial for a better understanding and assessment of these ecological conditions and relationships [9], urban land cover datasets represent a valuable source of information which city planners can incorporate into decision-making processes to foster effective management and to safeguard sustainability.

Urban cadastral maps, as a product of the land survey, may be regarded as a proper source of urban land cover information. However, these datasets only feature some of the land cover classes (e.g., buildings) that make up an urban area. Other classes, like vegetation or tree canopy, are typically not mapped [10], even though they are at least equally important for many applications (e.g., [11]). In addition, the production of area-wide cadastral maps is time-consuming and labor-intensive. As a consequence, it is not possible to update an entire map within short time intervals, which, in turn, makes cadastral maps less attractive for urban land cover monitoring. For these reasons, alternative ways of data collection need to be explored.

Remote sensing data provide an excellent basis for cost-effective, up-to-date, and large-area mapping and monitoring of urban land cover at multiple scales. At the regional to global scale, a number of land cover and urban extent maps has already been derived from remote sensing data [12]–[20]. While these maps are inarguably of great value for a broad range of users, they also suffer from certain limitations that may prevent authorities and practitioners from considering them in the context of local urban planning applications. In this regard, one of the most relevant limitations is the rather coarse spatial resolution ($\geq$300 m) of those maps [21]–[25].

For urban analyses at the local scale, high spatial resolution (HSR) data ($\leq$5 m) are usually required to properly capture common land cover objects like buildings or trees [26]–[31]. Thanks to recent technological advancements, this requirement is fulfilled by a growing number of satellite-based and airborne sensors [32]. HSR multi-spectral and light detection and ranging (LiDAR) data are becoming increasingly available in the urbanized areas of the world [33]. Despite this development, detailed

Manuscript received August 13, 2012; revised February 04, 2013; accepted February 27, 2013. Date of publication July 02, 2013; date of current version September 20, 2013. This work was supported in part by the ENVILAND 2 research project, which is funded by the Space Agency of the German Aerospace Center (DLR) with financial support of the German Federal Ministry of Economics and Technology (BMWi) on the basis of legislation by the German Parliament Grant 50EE0844-50EE0847.

The authors are with the Department for Earth Observation, Institute of Geography, Friedrich-Schiller-University Jena, 07743 Jena, Germany (e-mail: christian.berger@uni-jena.de; michael.voltersen@uni-jena.de; soeren.hese@uni-jena.de; irene.walde@uni-jena.de; c.schmullius@uni-jena.de).

Color versions of one or more of the figures in this paper are available online at http://ieeexplore.ieee.org.

Digital Object Identifier 10.1109/JSTARS.2013.2252329

land cover maps are still missing in many of these areas. The main reasons for this observation are the methodological challenges and computational difficulties associated with turning the wealth of geospatial data into accurate thematic information [10], [34]. Hence, there is a need for practical solutions being able to produce urban land cover from large amounts of HSR data acquired at different sensing schemes.

This paper focuses on the description and demonstration of a robust object-based image analysis (OBIA) approach to extract urban land cover information from HSR multi-spectral and LiDAR data. Particular emphasis is put on the evaluation of the proposed method with regard to its generalization capabilities across varying situations. For this purpose, the experimental setup of this study includes the analysis of

- three urban areas with different physical structures,
- four sets of multi-spectral and LiDAR input data, and
- statistical measures

to enable the assessment of mapping accuracies and methodological transferability. The paper is structured as follows. Section II provides information on the theoretical background and work related to this study. In Section III and Section IV, the data and methods used to achieve the above goal are presented. Section V and Section VI follow with the description and discussion of the study results. And finally, Section VII concludes the findings of this investigation.

II. Related Work

Over the past decades, a considerable amount of research has been directed towards the development and evaluation of pixel-based classifiers taking advantage of the complementary information in multi-sensor remote sensing data. Statistical approaches, like the maximum likelihood (ML) or minimum distance (MD) method, and non-parametric techniques, like artificial neural network (ANNs) or support vector machine (SVMs), have proven to be successfull in the context of various applications, including change detection [35], agricultural classifications [36]–[41], tree/vegetation type identification [42]–[48], and, most relevantly, land cover/land use mapping [39], [49]–[56]. However, when it comes to the extraction of features from HSR data, the performance of methods based on a pixel-by-pixel analysis may not be sufficient.

In HSR data, real-world objects are made up of several pixels [57]. At this scale, the variability of spectral and other features within a given land cover class is high, whereas the radiometric variations between different land cover types are low [28], [58]–[64]. Therefore, if a classifier solely relies on information derived at the pixel level of HSR data, it is likely that the mapping result will be compromised by increased error rates due to the similarity between different target classes in feature space [58], [65] as well as by the so-called "salt and pepper" noise [55], [57], [64], [66]–[71]. This is particularly true for pixel-based land cover classifications in urban areas, which are well-known for their spectral and spatial heterogeneity [33], [72]–[75]. Other drawbacks of traditional approaches are their sensitivity to registration errors between multi-modal inputs [64], [76], [77], the computional effort that comes along with a per-pixel analysis of HSR data [78], [79], the unreliability of single pixel values because of the influence of the pixel neighborhood on the signal [80], [81], and the missing ability to infer objects of interest corresponding to the visual perception of humans [82]. Furthermore, spatial information, like image texture or morphological measures [83], [84], are usually calculated using a moving window, which causes borders between land cover classes to become blurred [85]. For these reasons, it is worthwhile to consider alternative methods for the classification of HSR multi-sensor Earth observation data.

OBIA [57], [86] holds the potential to overcome the above problems with pixel-based approaches. In contrast to traditional algorithms, OBIA relies on the classification of image segments, rather than single pixels. These segments are initially created by grouping adjacent pixels of an input dataset according to one or more predefined criteria of homogeneity [57], thereby reducing the radiometric variability in HSR data [64]. After segmentation, the resulting object primitives are subjected to an iterative process of (re-)classification and (re-)segmentation to ultimately obtain objects of interest [79], [87]. Thus, during this stage of the analysis task, image objects can constantly change their class membership, spatial geometry, and mutual relations until the mapping requirements are met [88].

For the refinement of the object primitives, not only their spectral characteristics (e.g., object mean, median, minimum, maximum, and variance value per band), but also their morphology (e.g., shape and size), texture, and spatial context (e.g., distances, neighborhoods, and topologies) can be employed [57], [64], [88]–[93]. All necessary processing steps and class descriptions are stored in so-called rulesets, which enable the reapplication of a developed workflow to other study areas and datasets. In the context of (urban) mapping with HSR imagery, OBIA methods are considered to be superior to pixel-based approaches [68], [89], [94]–[98], partly because the large variety of available image features and processing tools is well-suited to model the complexity of urban landscapes [99]. However, with regard to this study, the most important advantage of OBIA is its capability to incorporate a diversity of input data [64], [77], [88], [91], [92], [100]–[102] and the possibility to reuse rulesets [90].

Given its distinct amenities, numerous studies have employed OBIA for land cover mapping. Taubenböck *et al.* [93] extracted urban features using Ikonos imagery of Istanbul, Turkey, and transfered their workflow with some adaptations to QuickBird data of Hyderabad, India. The maps had an overall accuracy of 85% and 82%, respectively. A land use and land cover classification was presented by Schöpfer & Möller [103]. Their results were produced from two Advanced Spaceborne Thermal Emission and Reflection Radiometer (ASTER) acquisitions over Phoenix, Arizona, and Las Vegas, Nevada, and suggested accuracies similar to [93]. Wurm *et al.* [104] utilized Ikonos data in combination with a LiDAR digital surface model (DSM) to derive urban structures for two German test sites, namely Munich and Cologne. With overall accuracies exceeding 90%, the outcome of this study highlighted the great potential of DSMs for urban land cover mapping. In a recent work by O'Neil-Dunne *et al.* [10], an object-based data fusion system, supported by manual interpretations, was built to infer high-resolution land cover from aerial imagery, LiDAR, and

TABLE I
STUDY AREAS AND DATA BASIS

	Multi-Spectral Imagery				LiDAR Data			
Study Area	Sensor	Date	Spectral Bands	GSD	Sensor	Date	Products	GSD
Rostock, MV, Germany	QuickBird	2009-09-19, 12:25 CEST	Blue, Green, Red, NIR, Pan	2.4 m (MS), 0.6 m (Pan)	Optech ALTM 3100	2006-10	DEM, DSM	2.0 m
	RapidEye	2010-07-09, 13:12 CEST	Blue, Green, Red, Red Edge, NIR	5.0 m (MS)	Optech ALTM 3100	2006-10	DEM, DSM	2.0 m
Erfurt, TH, Germany	WorldView-2	2011-09-26, 12:48 CEST	Coastal Blue, Blue, Green, Yellow, Red, Red Edge, NIR-1, NIR-2, Pan	2.0 m (MS), 0.5 m (Pan)	Optech ALTM 1225	2003-03	DEM, DSM	2.0 m
San Francisco, CA, USA	WorldView-2	2011-10-09, 12:36 PDT	Coastal Blue, Blue, Green, Yellow, Red, Red Edge, NIR-1, NIR-2, Pan	2.0 m (MS), 0.5 m (Pan)	Optech ALTM 3100	2010-06	DEM, DSM	0.5 m

vector data. The methodology was developed on small spatial subsets and then applied to the complete data basis of Philadelphia, Pennsylvania, yielding very high mapping accuracies. Salehi *et al.* [64] developed an object-based classification scheme analyzing a small subset of QuickBird data and Spot Height information. Imagery of the city of Fredericton, Canada, was used to derive five land cover classes for the pilot image. After transferring the method to another subset of QuickBird and Ikonos data, the overall classification accuracies yielded were 92% and 86%, respectively. Platt & Rapoza [96] compared the performances of a pixel-based classifier and OBIA for an Ikonos scene covering the urban-agricultural landscape surrounding Gettysburg, Pennsylvania. The classification output obtained using OBIA showed a 14% higher agreement with the reference than that of the pixel-based classifier. After a comparison of different methods, Lu *et al.* [105] came to a similar conclusion. With an overall accuracy of 88%, OBIA improved the classification performance for all target classes. The study area was a relatively small town in Brazil, for which QuickBird data were available. A generic mapping scheme was developed by Walker & Blaschke [106]. A two-level segmentation was implemented to analyze aerial images of the Phoenix metropolitan area. The validation statistics, reported for an optimized and generalized ruleset, underline the trade-off between performance and robustness.

The above selection of papers shows that many studies have already successfully applied OBIA to extract urban land cover from HSR data. However, in spite of previous mapping efforts, only little research in the field was directed towards building and evaluating robust methods that are capable of processing different sets of HSR multi-sensor inputs (e.g., optical and LiDAR data) covering large areas. So far, existing OBIA algorithms are frequently reported to work well on small spatial subsets [64], [105], or for one entire study area only [96], [106]. In addition, these algorithms often rely on mono-sensor imagery [93], or even data acquired by one specific sensor [96], [103], [105], [106]. To exploit the full potential of the HSR multi-source data available for more and more urban areas, suitable data fusion techniques still need to be developed and rigorously tested. The present study aims at addressing this need.

III. MATERIALS

The method described in this paper is applied to different constellations of HSR multi-spectral and LiDAR data. The available datasets were acquired over three urban areas in Germany and the USA, respectively. An overview of the study areas and data basis is given in Table I.

A. Study Areas

The City of Rostock is located in the north-east of Germany ($54°7'41''\mathrm{N}$, $12°6'40''\mathrm{E}$) and belongs to the federal state of Mecklenburg-Western Pomerania (MV). It has more than 200,000 inhabitants and comprises an administrative area of about 181 km^2 [107]. The City of Erfurt is located in Central Germany ($50°59'20''\mathrm{N}$, $11°1'23''\mathrm{E}$) and belongs to the federal state of Thuringia (TH). It also has 200,000 inhabitants, but comprises an official area of about 269 km^2 [107]. The City of San Francisco is located at the west coast of the USA ($37°45'7''\mathrm{N}$, $122°23'6''\mathrm{W}$) and belongs to the federal state of California (CA). It has more than 800,000 inhabitants and comprises a land area of about 121 km^2 [108]. Rostock and Erfurt are typical representatives of European cities featuring historically determined, complex structures. In contrast, San Francisco is a modern planned city of North America, where the spatial arrangement of urban land cover elements is frequently constrained by a predefined, grid-like network of streets [109].

B. Data Basis

As shown in Table I, the data basis of this study consists of a variety of multi-spectral satellite imagery. The datasets were acquired at multiple spectral resolutions, small ground sampling distances (GSDs), and at different dates. While QuickBird and RapidEye data are available for Rostock, WorldView-2 data are available for both Erfurt and San Francisco. For each study area, the multi-spectral imagery is complemented by digital elevation models (DEMs) and DSMs derived from airborne LiDAR data. In Erfurt, the LiDAR dataset was recorded prior to leaf emergence and, thus, contains no information on tree canopy heights. Moreover, the data basis for San Francisco covers only a central part of the city and not the entire urban area. Given the

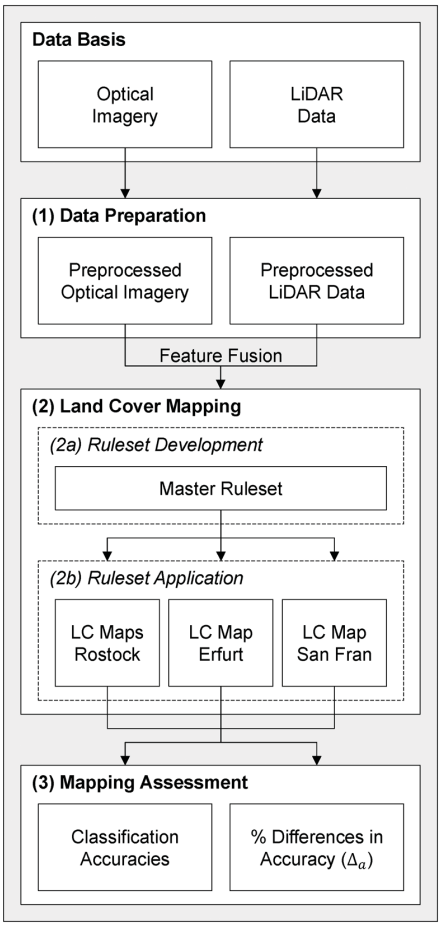

Fig. 1. The conceptual workflow of this study.

availability of four different multi-spectral satellite scences, it is possible to produce four urban land cover maps from the data basis.

IV. Methods

The overall workflow of this study is displayed in Fig. 1. It consists of three consecutive steps, including

1) data preparation,
2) land cover mapping, and
3) mapping assessment.

After data preparation, a single ruleset for land cover mapping is developed that makes use of the complementary information provided by the preprocessed optical and LiDAR data by means of feature fusion [110]. This master ruleset is then applied with slight modifications to the entire data bases of Rostock, Erfurt, and San Francisco. Finally, the accuracies of the resulting land cover maps are assessed, and the proposed method is evaluated with regard to its transferability. In the following sections, the three above-mentioned steps are described in more detail.

A. Data Preparation

A uniform sequence of preprocessing steps is applied to the data basis. Preprocessing of the multi-spectral imagery includes radiometric normalizations using ATCOR [111], pansharpening using the high-pass filter (HPF) fusion [112], and coregistration to the LiDAR datasets using manually selected ground control points (GCPs) and the DEMs. A panfusion is not performed for RapidEye data since they do not feature a panchromatic band. Preprocessing of the LiDAR data comprises two further steps. First, normalized digital surface models (nDSMs) are calculated for each study area by subtracting the available DEMs from the DSMs. They contain the height of urban objects relative to the ground [10]. Second, the nDSMs are smoothed to enable the creation of derivative LiDAR products (e.g., nDSM slope).

With respect to the subsequent classification step, additional features are derived from the input data. Those are brightness, computed as the average reflectance of the blue, green, red, and near infrared (NIR) bands within a multi-spectral dataset, the normalized difference vegetation index (NDVI) [113], and the slope (in percent) of the smoothed nDSMs [114]. The latter is useful for identifying transitions between flat areas and elevated objects such as buildings [115].

B. Land Cover Mapping

The methodology presented in this paper aims at the robust extraction of six urban land cover classes from the data basis: Buildings, impervious, bare soil, trees, grass/shrubs, and water bodies. These cover types, along with a minimum mapping unit (MMU) of 5 m^2, were defined within the research project this study was part of [116]. An object-based approach [57], [86], [88] was chosen for land cover mapping because of its distinct advantages over pixel-based classification techniques with respect to feature extraction from HSR multi-source data [64], [77], [88], [91], [100], [101]. The mapping procedure was implemented as a single ruleset using Trimble eCognition Developer and its cognition network language (CNL) [117]. This master ruleset was initially developed using ten subsets of the QuickBird and LiDAR data available for the City of Rostock. The subsets represented different forms of urban land use including downtown, industrial, and suburban areas as well as (semi-) natural land cover types such as water bodies, forests, and open/agricultural land. After its development, the ruleset was applied with some modifications to the entire data bases of Rostock, Erfurt, and San Francisco (cf. Section VI). For Rostock, two land cover maps were produced using QuickBird and RapidEye data as multi-spectral classification inputs.

The developed ruleset starts off with an initial segmentation of the input data. Goal of the segmentation step was to obtain larger image objects for homogeneous regions, such as water bodies and bare soil areas, and smaller image objects for heterogeneous regions, such as densely built-up areas. For this purpose, a three-stage segmentation approach was selected. After applying a conventional quadtree-based segmentation, the resulting object primitives are fused using the multiresolution segmentation region grow algorithm [117]. Similar segments are then further aggregated by means of the multiple object difference conditions-based fusion, a customizable merging procedure that builds upon the standard image object fusion method

TABLE II
DETAILS OF THE THREE-STAGE SEGMENTATION APPROACH

Stage	Algorithm	Features	Parameter(s)	Value(s)
1	Quadtree-based segmentation	Brightness, NDVI, nDSM slope	Scale	7
2	Multi-resolution segmentation region grow	Brightness, Blue, Green, Red, NIR, NDVI, nDSM	Scale / No. of cycles	50 / 3
3	Multiple object difference conditions-based fusion	Brightness, Blue, Green, Red / NDVI / nDSM	Maximum difference	3 / 0.2 / 1

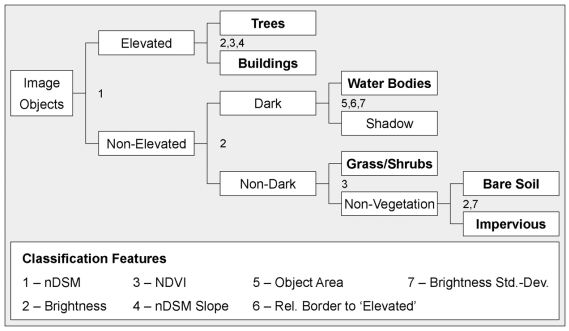

Fig. 2. The proposed urban land cover mapping scheme.

but allows users to define their own merging criteria and thresholds [118]. The image features and parameters used for segmentation and object merging are compiled in Table II. The advantage of the segmentation strategy employed here is its capability to achieve results comparable to those of the commonly used, but computationally demanding multi-resolution segmentation while simultaneously saving a significant amount of processing time. Considering the large volume of HSR multi-source data that were to be processed, this increase in performance was crucial to the feasibility of this study.

After the initial segmentation, a rule-based classification of the created image objects is performed following the scheme depicted in Fig. 2. The numbers at each node of the decision tree indicate the features that are used for class separation. The six target classes are displayed in bold type. To foster the transparency and transferability of the ruleset, the compilation of complex class descriptions was avoided. Instead, use was made of seven basic image object characteristics. The features and corresponding thresholds were chosen based on different separability analyses (Fig. 3) and empirical values gained from several trial runs on the ten training subsets. Another requirement was that the computational cost needed to calculate all features should be low. This was also the reason why second order image texture [83] was not considered for classification. Especially when analyzing large sets of HSR multi-source data containing hundreds of millions of pixels, the integration of these features heavily compromises processing performance. As an alternative, a simple first order texture measure (i.e., the standard deviation of the brightness layer) was employed as part of the proposed urban land cover mapping scheme.

Image segments are first divided into elevated and non-elevated objects using the nDSM. An adaptable object height serves as separation threshold, which was set to $\geq$2 m for the City of Rostock. The height value is chosen to enable the differentiation between small, but elevated objects such as allotment garden cottages, and pseudo-elevated objects such as vehicles [119]–[121]. Subsequently, elevated objects are reclassified as trees or buildings. The main feature used for this purpose is the NDVI. In Fig. 3(a), NDVI values of 50 tree and building objects are summarized as boxplots. As can be seen, an NDVI of roughly 0.25 lies between the extreme values of both classes and is therefore well-suited to make a distinction. The exact approach to characterize trees and buildings is as follows. Initially, elevated objects are reclassified as tree canopy if they feature a relatively high NDVI of $\geq$0.4. The resulting tree canopy objects are then used as seeds which are grown into neighboring pixels belonging to the elevated class if the latter have similar, but not necessarily as distinct, NDVI characterisitcs as the former. This is true for all pixels with NDVI values that are at maximum 25% smaller than those of their respective seed objects. As a second criterion, the brightness of these pixels has to be equal to or even higher than that of their seeds. This is to prevent seed objects from growing into elevated, but shadowed areas. With regard to the building class, seed objects are generated by reclassifying all remaining elevated objects with small nDSM slope values ($\leq$30%). Afterwards, building seeds are grown pixelwise into elevated objects if the latter feature NDVI values that are at minimum 50% smaller than the NDVI threshold used to determine tree object seeds (i.e., $\leq$0.2). The eCognition process used to grow and/or shrink objects according to one or more conditions is called pixel-based object resizing [117].

In a next step, the non-elevated land cover classes are extracted, including water bodies, grass/shrubs, bare soil areas, and impervious surfaces. To this end, ground objects are first labeled as dark if a predefined brightness criterion of $\leq$2 is satisfied. These segments are again treated as seeds which iteratively consume the pixels of adjacent ground objects if the latter are at maximum 2.5 times brighter than their seed objects. In addition, ground objects that are enclosed by dark objects are also reclassified as dark. After this refinement, dark objects are further differentiated into water bodies and shadowed areas by means of their size, relative border to building or tree objects, and brightness standard deviation. Since shadowed areas are usually smaller than water bodies, an area threshold of $\geq 20,000\ \mathrm{m}^2$ is employed to detect most of the larger waters. As can be seen in Fig. 3(b), all shadowed areas are below and 75% of all water bodies are above this value. In order to identify further water bodies, all dark objects that are not larger than a quarter of the original area threshold (i.e., $\leq 5,000\ \mathrm{m}^2$) and do not share a common border with trees or buildings (Fig. 3(c)) are then also assigned to the water class. As part of a last iteration, the standard deviation of image brightness, calculated within a moving window of 25 $\times$ 25 pixels, is used to delineate the remaining water bodies. The assumption behind this approach is

that water objects feature less brightness inhomogeneities than shadows. In Fig. 3(d), this issue is graphically represented. It becomes clear that circa 75% of all water bodies have a brightness standard deviation of ≤ 1. Accordingly, this value was chosen to derive further water seeds, which are grown on a pixel-by-pixel basis into neighboring dark objects having a brightness standard deviation that is at maximum 2 times higher than that of the seeds. All remaining dark objects are then reclassified as shadowed areas.

In a following sequence of processes, ground objects that are neither water nor shadow are split into vegetated and non-vegetated regions. This is satisfactorily accomplished by means of the NDVI. While every non-elevated object with an NDVI ≥ 0.3 is immediately classified as grass/shrubs, the residual objects are treated as non-vegetated areas that, in turn, are further subdivided into bare soils and impervious surfaces. During the first separability analyses, it was found that there are no unique characteristics to discriminate between bare soil and sealed areas. This is because the color, shape, and spatial context of objects of both classes varied greatly accross the entire study area. The only features that led to reasonable results were again image brightness and its standard deviation. As shown in Fig. 3(e), the median brightness of 50 samples of the bare soil class is 11.75, whereas the minimum and maximum values are 7.3 and 27.6, respectively. On the contrary, impervious surfaces are usually darker, have a smaller maximum value (11.8), and a smaller overall range of values (9.05). Based on this observation, and the assumption that built-up areas feature higher brightness standard deviation values than, e.g., more homogeneous patches of arable land or sands, non-vegetated areas with a mean brightness of ≥ 20 and a brightness standard deviation of ≤ 1.5 are first classified as bare soil seed objects. These seeds are then merged with pixels of surrounding non-vegetation objects if the latter show brightness values that are at maximum 5% smaller than the mean brightness of the respective seed object. If, after this process, there are any non-vegetation objects enclosed by bare soil areas, these objects are also labeled as bare soil. Lastly, all residual non-vegetation objects are reassigned to the impervious class. With that, all of the six target classes are derived.

After the extraction of the land cover types, some reshaping algorithms are applied to the thematic objects for the purpose of border optimization. For instance, the shape of tree objects is slightly smoothed and building footprints are generalized. All this is done by calculating a morphological parameter called surface tension [117] and evaluating the result against a predefined criterion of compactness. In this way, the original object primitives are successively transformed into more meaningful objects of interest that better correspond to the visual perception of humans [79], [82], [87], [88]. Finally, all remaining shadow objects are reassigned to the class they share the largest relative common border with.

C. Mapping Assessment

The method and results presented in this paper are evaluated with regard to two aspects: Mapping accuracy and methodological transferability. First, the accuracy of the urban land cover maps is assessed [122]. For this purpose, use is made of a variety of reference datasets. The building class in each map is validated using building footprints provided by the land registry offices of Rostock and Erfurt, and by the City of San Francisco [123]. The remaining land cover classes are validated using digital orthophotos (DOPs) and Jena Airborne Scanner (JAS) imagery [124] for Rostock and Erfurt. Due to the lack of alternatives, the panchromatic band of the WorldView-2 dataset is used in the case of San Francisco. A uniform assessment scheme is applied to the four maps. Since all of the six derived land cover classes are considered as equally important, priority was put on ensuring that the accuracy of each class is assessed using the same number of sample points. To this end, a stratified random sampling design is chosen comprising 50 samples per class (i.e., 300 samples per map). Following this approach, all classes, no matter how small or how large their areal coverage is for a given test site, are equally represented/weighted in the validation scheme. The actual land cover at each sample point location is then extracted from the reference data and compared to the map. Finally, the numeric results of the comparison are transferred to an error matrix to determine overall classification accuracy, errors of commission and omission, and the kappa coefficient of agreement [125], [126].

Second, the transferability of the proposed method is tested. The evaluation is based on a simple comparison between the accuracies a_t of an urban land cover map under test t and the accuracies a_r of a reference map r. While r refers to a map for which a given ruleset is initially developed for, t refers to a map that is produced after applying the developed ruleset to another data basis and/or study area. Since the ruleset presented in this study is originally developed using the QuickBird and LiDAR data available for Rostock, the accuracies of the corresponding urban land cover map (r) serve as reference values a_r. After its development, the ruleset is applied to the remaining data basis. Hence, the accuracies of the urban land cover maps of Rostock (using RapidEye data as multi-spectral input), Erfurt, and San Francisco (t) serve as test values a_t. As a numerical indicator of transferability, the percentage differences in accuracy Δ_a between t and r are expressed by:

$$\Delta_a = \frac{a_t}{a_r} - 1 \tag{1}$$

For $\Delta_a \geq 0.00$, the accuracies of t are the same as, or even higher than those of r. For $\Delta_a < 0.00$, the accuracies of t are lower than those of r. Thus, higher values of Δ_a generally suggest an increased methodological transferability of the ruleset used to produce both maps and vice versa.

V. Results

Using the methodology presented in this study, four urban land cover maps were produced from the data basis (Figs. 4, 5). For this task, an overall volume of 50 gigabyte (GB) of HSR multi-spectral and LiDAR imagery covering roughly 700 km^2 of land area was turned into thematic information. In Fig. 4(a) and Fig. 4(b), the two maps of Rostock are illustrated. Since the QuickBird and the RapidEye data used to produce them were recorded at different dates (cf. Table I), the most obvious difference between both maps is due to the different phenological conditions that were present during the time of data acquisition. In Fig. 5(a) and Fig. 5(b), the maps of Erfurt and San Francisco

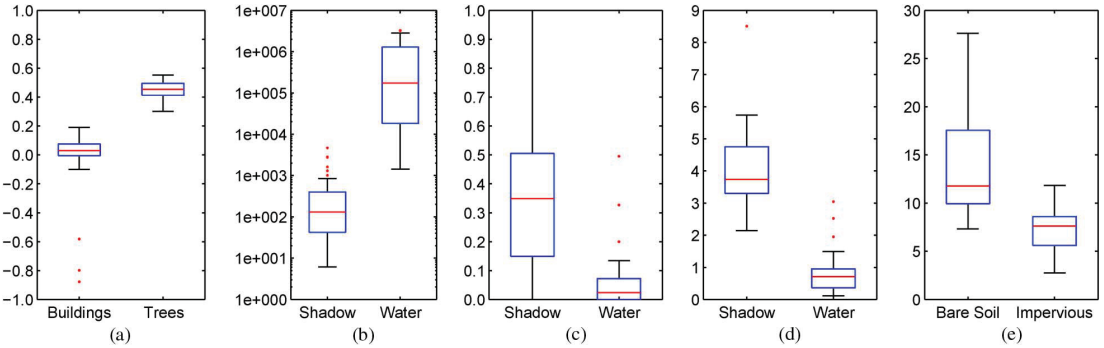

Fig. 3. Boxplots for different class pairs (50 samples per class each) and image features: (a) Mean NDVI, (b) object area [m²], (c) rel. border to 'elevated', (d) std.-dev. of brightness, and (e) mean brightness.

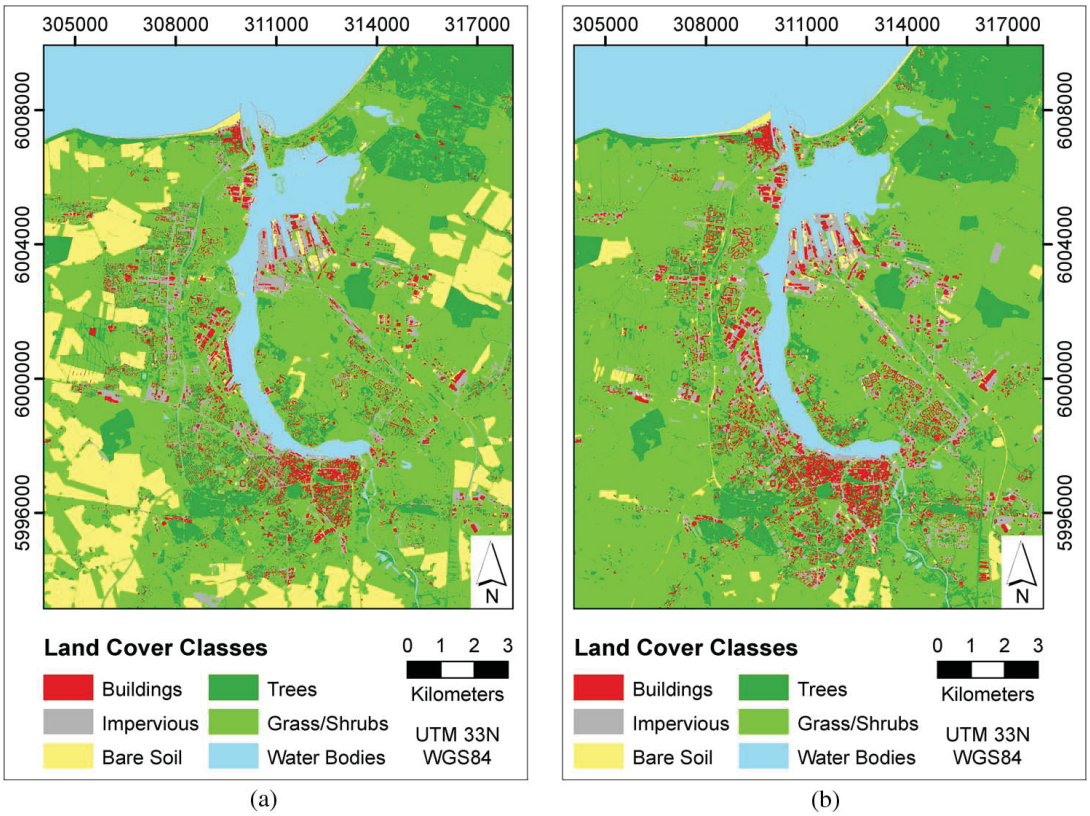

Fig. 4. The urban land cover maps of Rostock derived from two different multi-spectral input data: (a) QuickBird and (b) RapidEye.

are illustrated. As opposed to the other study areas, the map of San Francisco covers only a central part of the city for reasons of data availability. The four urban land cover maps are accompanied by statistics providing information on the achieved classification accuracies, as well as the percentage differences in accuracy (Δ_a). These numerical results are subject to further description in the following paragraphs.

A. Classification Accuracies

The classification accuracies obtained for each of the four urban land cover maps and the corresponding error matrices are compiled in Table III and Table IV. For reasons of visual consistency, all accuracies are displayed as numbers between 0.00 and 1.00 instead of percentages. The map of Rostock (QuickBird) features very high accuracies for almost all classes. Buildings, trees, and water bodies are mapped with user's and producer's accuracies equal to or greater than 0.90. The accuracies of the remaining cover types are still relatively high. While the largest error of commission is observed for impervious surfaces (0.18), the largest error of omission is attributed to bare soils (0.14). The map of Rostock (RapidEye) is of comparable quality. The only significant exception is that confusions between impervious surfaces and bare soil areas occur more frequently, leading to a producer's accuracy of 0.78 for the former,

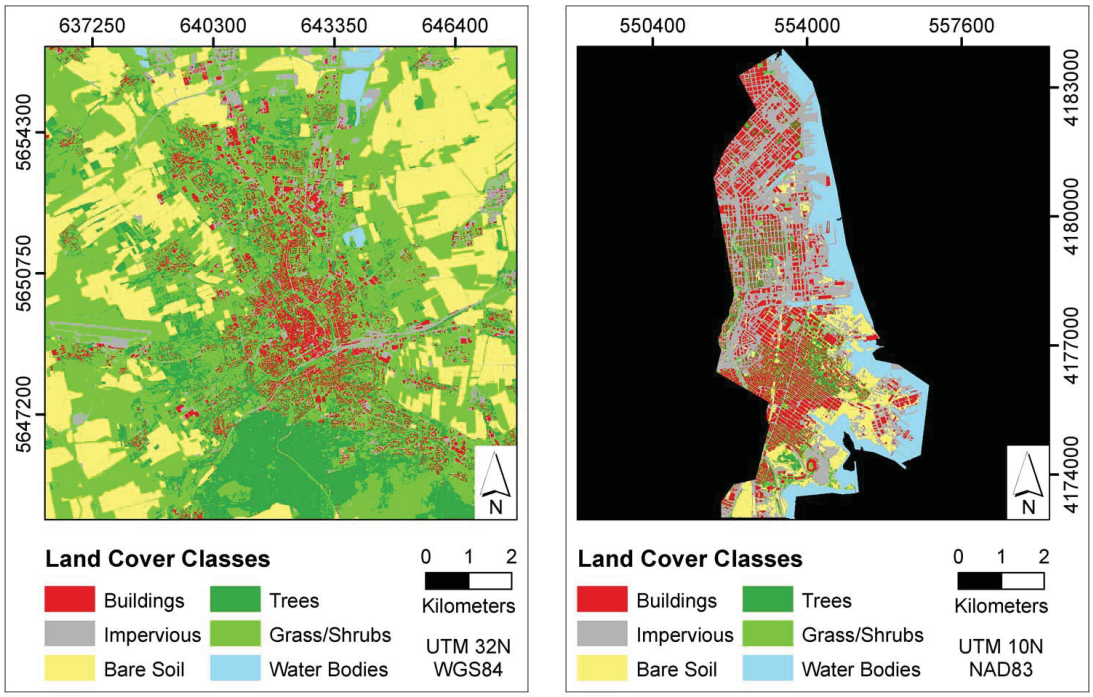

Fig. 5. The urban land cover maps of (a) Erfurt and (b) San Francisco.

and a user's accuracy of 0.84 for the latter class. Higher error rates, and a wider spread in values, are reported for the map of Erfurt. The spread is explained by an increased number of accuracies below 0.85. Larger misclassifications related to the tree and grass/shrubs class are the major cause for this tendency. The map of San Francisco is characterized by accuracies close to those of the urban land cover maps of Rostock. While errors of commission are highest for trees (0.18) and short vegetation (0.20), errors of omission are highest for buildings (0.19) and impervious areas (0.26). Apart from these errors, mapping accuracies are constantly above 0.86. This verifies the quality of the land cover map of San Francisco.

In general, a rather high degree of accuracy is observed for all maps. Except for two respectively three examples, the reported user's and producer's accuracies are consistently above 0.80, in many cases even above 0.90. This is also reflected by the median user's and producer's accuracies, as well as the total accuracies of the maps. With an overall accuracy of 0.91 and a kappa index of 0.89, the map of Rostock (QuickBird) features the highest values within the comparison. This can be expected since the classification ruleset was initially developed using ten representative subsets of the QuickBird and LiDAR data available for Rostock. The maps of Rostock (RapidEye) and San Francisco are of slightly lower overall accuracy (0.90 and 0.88). The corresponding kappa coefficients follow the same trend with values of 0.88 and 0.86, respectively. For the map of Erfurt, the lowest overall accuracy (0.83) and kappa score (0.80) are achieved by the proposed method. The median overall accuracy of all maps is 0.89, and the median kappa coefficient amounts to 0.87. Therefore, and according to other authors [127], [128], the urban land cover maps depicted in Fig. 4 and Fig. 5 are considered as very good.

B. Percentage Differences in Accuracy

The percentage differences in accuracy (Δ_a) between the map of Rostock (Fig. 4(a)), and the remaining urban land cover maps (Fig. 4(b), Fig. 5(a), Fig. 5(b)) are compiled in Table V. These statistics enable a straightforward assessment of the gains and losses in classification accuracy after applying the developed ruleset to another data basis and/or study area. For reasons of visual consistency, all Δ_a values are displayed as numbers between $+1.00$ and -1.00. For the map of Rostock (RapidEye), the obtained accuracies are often close to, the same as, or even higher than those for the map of Rostock (QuickBird). Larger Δ_a values are evident for the user's accuracy of the impervious class ($+0.12$) and the producer's accuracy of buildings ($+0.06$). Relatively small Δ_a values can only be found for the user's accuracy of bare soil areas (-0.13) and the producer's accuracy of sealed surfaces (-0.12). As a result of these observations, both overall accuracy and the kappa coefficient are reduced by only 1% for the map of Rostock (RapidEye). As indicated by a higher number of negative Δ_a values, the validation result for the map of Erfurt features several decreases in classification accuracy as compared to the reference map. Most of these decreases are less or equal -0.08 and are evenly distributed across all land cover types. The smallest Δ_a values are reported for the user's accuracy of the tree class (-0.23) and the producer's accuracy of the

TABLE III
CLASSIFICATION ACCURACIES

Map	User's/Producer's Accuracy						Overall/Kappa
	Buildings	Impervious	Bare Soil	Trees	Grass/Shrubs	Water Bodies	
Rostock (QuickBird)	0.90/0.90	0.82/0.89	0.96/0.86	0.96/0.98	0.84/0.89	1.00/0.96	0.91/0.89
Rostock (RapidEye)	0.90/0.96	0.92/0.78	0.84/0.86	0.94/0.96	0.84/0.88	0.96/1.00	0.90/0.88
Erfurt (WorldView-2)	0.94/0.85	0.82/0.82	0.88/0.80	0.74/0.90	0.72/0.68	0.92/1.00	0.83/0.80
San Francisco (WorldView-2)	0.92/0.81	0.86/0.74	0.90/0.90	0.82/0.98	0.80/0.93	1.00/1.00	0.88/0.86
Median Accuracies	0.91/0.88	0.84/0.80	0.89/0.86	0.88/0.97	0.82/0.88	0.98/1.00	0.89/0.87

TABLE IV
ERROR MATRICES FOR THE URBAN LAND COVER MAPS OF (a) ROSTOCK (QUICKBIRD), (b) ROSTOCK (RAPIDEYE), (c) ERFURT, AND (d) SAN FRANCISCO

		Reference						
		BD	IM	BS	TR	GS	WB	Total
Classification	Buildings	45	4	1	0	0	0	50
	Impervious	3	41	5	0	1	0	50
	Bare Soil	0	0	48	0	2	0	50
	Trees	0	0	0	48	2	0	50
	Grass/Shrubs	2	1	2	1	42	2	50
	Water Bodies	0	0	0	0	0	50	50
	Total	50	46	56	49	47	52	300

(a) ROSTOCK (QUICKBIRD)

		Reference						
		BD	IM	BS	TR	GS	WB	Total
Classification	Buildings	45	2	2	0	1	0	50
	Impervious	1	46	2	1	0	0	50
	Bare Soil	0	6	42	1	1	0	50
	Trees	0	0	0	47	3	0	50
	Grass/Shrubs	1	5	2	0	42	0	50
	Water Bodies	0	0	1	0	1	48	50
	Total	47	59	49	49	48	48	300

(b) ROSTOCK (RAPIDEYE)

		Reference						
		BD	IM	BS	TR	GS	WB	Total
Classification	Buildings	47	2	1	0	0	0	50
	Impervious	3	41	1	1	4	0	50
	Bare Soil	0	1	44	0	5	0	50
	Trees	3	1	1	37	8	0	50
	Grass/Shrubs	2	3	7	2	36	0	50
	Water Bodies	0	2	1	1	0	46	50
	Total	55	50	55	41	53	46	300

(c) ERFURT (WORLDVIEW-2)

		Reference						
		BD	IM	BS	TR	GS	WB	Total
Classification	Buildings	46	4	0	0	0	0	50
	Impervious	1	43	5	0	1	0	50
	Bare Soil	0	3	45	0	2	0	50
	Trees	7	2	0	41	0	0	50
	Grass/Shrubs	3	6	0	1	40	0	50
	Water Bodies	0	0	0	0	0	50	50
	Total	57	58	50	42	43	50	300

(d) SAN FRANCISCO (WORLDVIEW-2)

grass/shrubs class (-0.24). Taken together, these numbers contribute to an overall loss in accuracy of 8%, and a kappa index decline of 9% for the map of Erfurt. The Δ_a statistics for the map of San Francisco are mainly greater than or equal to ± 0.00. In seven out of twelve cases, errors of commission and omission are the same or even less than those for the map of Rostock (QuickBird). However, the magnitude of the remaining negative scores is a bit higher. Minimum Δ_a values of -0.15 and -0.17 are observed for trees (user's accuracy) and impervious surfaces (producer's accuracy), respectively. In consequence, only slight drops in overall accuracy (4%) and the kappa coefficient (3%) are detected for the map of San Francisco.

Besides the individual statistics for Rostock, Erfurt, and San Francisco, the median Δ_a values of all maps suggest that it is possible to apply the developed ruleset to another data basis and/or study area with an almost similar degree of success. In general, the only classes that are affected by decreases in accuracy larger than -0.10 are trees (user's accuracy) and impervious areas (producer's accuracy). For the other land cover types, the error margins are quite stable across all maps and losses in accuracy are only marginal, if they occur at all.

VI. DISCUSSION

The method and results presented in this study are discussed in the following paragraphs. Based on the design and implementation of the classification approach, the resulting urban land cover maps, and the corresponding validation statistics, crucial aspects of the mapping effort are addressed, including major sources of errors and methodological transferability.

A. Major Sources of Errors

Even though the validation result in Table III suggests a high overall degree of accuracy for all urban land cover maps, it also reveals few larger class-specific errors of commission and omission. These errors are mainly because of two reasons: The prop-

erties of the available LiDAR input data, as well as the simplicity of the developed ruleset.

1) Data Properties: An essential requirement for mapping urban land cover using the presented method is that the LiDAR input data should be acquired after leaf emergence to ensure that information on tree canopy heights are available. This is because the classification scheme expects tree objects to be of a certain height (cf. Fig. 2). If an nDSM does not contain these information, the method will almost exclusively rely on the multi-spectral signal in tree-covered areas and, thus, will mistake trees for the class grass/shrubs. In this study, information on tree canopy heights are present in all nDSMs but one. For Erfurt, only the heights of tree stems and larger tree branches are visible in the LiDAR dataset since it was recorded prior to the growing season (cf. Table I). To compensate for this data property, the description of the tree class was slightly modified by decreasing the use of height information and by increasing the importance of the spectral features that were already in use (i.e., brightness and NDVI). However, despite the adaptations made, the impact of missing vegetation height information on classification errors is still significant. For the mapping result of Erfurt, user's and producer's accuracies for trees and grass/shrubs are the lowest of all maps and classes.

Another mapping prerequisite is a sufficient spatial resolution of the LiDAR input data. This is of particular importance for the accurate detection of fine-scale urban land cover objects like allotment garden cottages. These buildings are so small that they are not properly captured by the lower resolution nDSMs of Rostock and Erfurt ($\mathrm{GSD} = 2\,\mathrm{m}$). Because of the incomplete or entirely missing height information, allotment garden cottages in Rostock and Erfurt are often considered as non-elevated by the classifier. In the course of further class assignments, they are finally labeled as impervious, instead of buildings. For the map of San Francisco, the described issue is not of relevance since the available nDSM features an adequate spatial resolution ($\mathrm{GSD} = 0.5\,\mathrm{m}$).

2) Ruleset Simplicity: As the proposed method aims at the robust extraction of urban land cover information, focus was put on keeping the method simple. To avoid overfitting effects and to ensure the reproducibility and the reapplicability of the ruleset, only few basic image object features are used for classification. While being conducive to transferability, this approach has also some limitations that find their expression in reduced mapping accuracies for certain land cover types.

The widely known confusion between impervious surfaces and bare soil areas [129]–[135] is a characteristic example in this regard. Especially for the impervious class, median user's and producer's accuracies of all maps are comparatively low, with values of 0.84 and 0.80, respectively. The main reason for this observation is that the presented method makes only use of two object features, namely image brightness and its standard deviation, to discriminate between these categories. Obviously, more elaborated class descriptions are necessary to increase class separability and, with that, mapping accuracies.

Another typical source of errors is extensive shadowing from buildings. After the assignment of elevated and non-elevated image objects, the decision tree relies on brigthness values and the NDVI to separate between several classes, including trees and buildings, as well as grass/shrubs and non-vegetated land cover. However, these spectral information are usually distorted in overshadowed areas, a problem that is particulary distinct in HSR imagery of urban environments [10], [136], [137]. Since the classifier does not feature a dedicated routine to cover these kind of exceptions, accuracies for shadow-affected patches of land are often below average for all maps.

Further uncertainties are introduced by some of the assumptions on which the ruleset is based on. For instance, according to the structure of the decision tree, image objects cannot be elevated and impervious at the same time. However, some urban elements, like bridges, are both in reality. Such misconceptions lead to systematic errors that propagate through the decision tree hierarchy [138]. With regard to the above instance, bridges are commonly treated as buildings, instead of impervious surfaces, because the description of the building class better suits their real-world properties than that of the impervious class. This issue also demonstrates that the classification features and rules used at the first nodes of the decision tree have a potentially larger impact on mapping accuracies due to the problem of error propagation. For this reason, these features have been selected with great care during ruleset development (cf. Section VI-B-1).

From the provided examples, it becomes clear that most of the larger misclassifications are plausible, as they are a logical consequence of the simplicity of the urban land cover mapping scheme. To further increase the accuracy of the method, the implementation of more sophisticated class paramterizations would be necessary. However, this would also be at the cost of robustness, since a higher degree of methodological complexity is likely to require more individual adaptations to the ruleset if the latter is to be transferred to other input data bases and/or study areas featuring different properties. For this reason, the trade-off between performance and transferability [106], [139] was carefully evaluated during each stage of ruleset development.

B. Methodological Transferability

The numbers in Table V build the foundation from which the strenghts and limitations of the described method are deduced with respect to its transferability. While aspects related to the study areas, the corresponding data bases, and the design and implementation of the approach are part of the discussions on methodological strengths, thoughts on the limitations of the method include issues of ruleset automation and adaptation.

1) Strengths: One strength of the proposed classification scheme is its ability to deal with urban areas that are of different physical property and complexity. Rostock, for example, is a typical European city regarding the diversity of urban structures and elements. It features densely built-up areas, such as its historic city center, as well as regions of less intense development. Furthermore, urban land cover elements are manifold and arranged in a variety of ways. On the contrary, San Francisco is a characteristic North American city, for which the variety and spatial arrangement of urban land cover elements is frequently constrained by a predefined, grid-like network of streets [109]. The resulting blocks of houses create an urban fabric that is less complex and significantly different from that of Rostock. Despite these structural differences, only a slight drop in overall

TABLE V
PERCENTAGE DIFFERENCES IN ACCURACY (Δ_a)

Map	User's/Producer's Accuracy						Overall/Kappa
	Buildings	Impervious	Bare Soil	Trees	Grass/Shrubs	Water Bodies	
Rostock (RapidEye)	±0.00/+0.06	+0.12/−0.13	−0.13/±0.00	−0.02/−0.02	±0.00/−0.02	−0.04/+0.04	−0.01/−0.01
Erfurt (WorldView-2)	+0.04/−0.05	±0.00/−0.08	−0.08/−0.07	−0.23/−0.06	−0.14/−0.24	−0.08/+0.04	−0.08/−0.09
San Francisco (WorldView-2)	+0.02/−0.10	+0.05/−0.17	−0.06/+0.05	−0.15/±0.00	−0.05/+0.04	±0.00/+0.04	−0.04/−0.03
Median Differences	+0.02/−0.05	+0.05/−0.13	−0.08/±0.00	−0.15/−0.02	−0.05/−0.02	−0.04/+0.04	−0.04/−0.03

accuracy ($\Delta_a = -0.04$) and the kappa index ($\Delta_a = -0.03$) is observed after the ruleset, initially developed for Rostock, is transfered to the data basis of San Francisco. This demonstrates that it is possible to apply the proposed method to urban areas featuring different spatial patterns with a similar degree of success.

Another advantage of the presented mapping technique is its capability to successfully incorporate data that were acquired at multiple dates, spatial resolutions, and using different sensing modalities. In this study, four sets of HSR multi-spectral and LiDAR data are used to derive urban land cover products (cf. Table I). By initiating global variables, such as brightness and NDVI thresholds, at the beginning of the ruleset, subsequent processing of optical scenes featuring various illumination and phenological conditions is enabled. Besides this possibility, it should also be noted that the spectral features used for classification (cf. Fig. 2) proved to be rather stable across differing situations. This is thanks to the radiometric normalization applied to the optical data prior to classification. As a consequence, values of the spectral bands and derivative features (i.e., NDVI, brightness, and standard deviation of brightness) become more comparable from scene to scene [111]. Moreover, it is worth mentioning that the NDVI itself represents a quite stable feature because of its formulation as a ratio. The two maps of Rostock, produced using QuickBird and RapidEye data as multi-spectral input (cf. Figs. 4, 5), are exemplary for the method's capability to cope with phenological differences. In addition, the median accuracies and Δ_a values of all maps substantiate that the method generally supports the joint use of optical and LiDAR data having somewhat smaller or larger GSDs than the data for which it was originally developed for.

Some of the distinct amenities of the feature extraction workflow are due to its general concept and its implementation within an OBIA environment. To foster the reproducibility and transferability of the ruleset, the compilation of complex class descriptions is avoided. For this reason, use and reuse is made only of a few basic image object features to perform classification. Moreover, the presented decision tree is deliberately designed to first split the created image segments into elevated and ground objects using the LiDAR nDSM. This is because height and height-related features (like slope) have a very high power of discrimination and are therefore well-suited to make a first and accurate differentiation between urban land cover objects without the risk of causing fundamental classification errors that may propagate through the remaining structure of the decision tree. Hence, these attributes and their specific role in the mapping scheme were carefully selected during ruleset development. After analyzing the results for three entire study areas and four different sets of input data, it was also found that the LiDAR features and thresholds used are broadly applicable. In other words, the values chosen to accurately detect elevated objects (nDSM) and building seeds (nDSM slope) did not have to be altered at all and proved to be robust.

Finally, conducive to robustness is also that optical input data are not required to be of high spectral resolution. Instead, the four spectral bands (blue, green, red, NIR) commonly supported by most of the sensors with increased spatial resolution [32] suffice for the method to work. This is because only two spectral features are employed for classification. Amongst them are brightness, which is computed here as the average reflectance of the blue, green, red, and NIR bands within a multi-spectral dataset, and the NDVI. Therefore, no matter if a given optical image has four (QuickBird), five (RapidEye) or eight (WorldView-2) spectral bands, the brightness values calculated by the proposed method stay comparable. Further strengths of the approach are thanks to the opportunities offered by OBIA. Among others, OBIA enables the creation of modular-structured rulesets [106] that, as opposed to traditional classifiers, allow users to easily pinpoint and correct potential issues of performance and/or robustness. In addition, OBIA is well-suited to transfer and apply developed rulesets to vast amounts of HSR imagery [10] without the need for training data and, thus, fulfills an essential requirement for large-area mapping and monitoring of urban environments.

2) Limitations: Considering methodological transferability, one potential limitation of the proposed method is that it does not work fully-, but semi-automatic. An initial setup of the ruleset, including the definition of the MMU and the specification of thresholds for tree and building heights, brightness, and NDVI, has always to be carried out prior to its application. Depending on the properties of the multi-spectral and LiDAR input data, a number of further modifications may have to be made. In this context, most crucial is the quality of the available LiDAR imagery. As pointed out earlier, the mapping scheme strongly relies on tree canopy height information. However, if a LiDAR acquisition took place prior to leaf emergence, these

information are not contained in the final LiDAR dataset and, thus, may have to be compensated for by alternative classification rules and features. For example, almost 30 changes to the developed ruleset were necessary to extract urban land cover for the City of Erfurt. Most of these changes were due to incomplete or entirely missing tree canopy height information. As opposed to this, only few ruleset adaptations (<10) were sufficient to obtain the maps of Rostock (RapidEye) and San Francisco (WorldView-2), both of which are almost as accurate as the map of Rostock (QuickBird). Therefore, and in general, the additional expenditure of human labor and time needed to produce further land cover maps that are of comparable accuracy is considered to be reasonable.

VII. Conclusions

Detailed urban land cover is an important source of information for a large number of research fields and practical applications. However, despite the increasing availability of HSR multi-source geospatial data, it still lacks in many urban areas. The methodological challenge of turning the wealth of geospatial data into accurate thematic information is one of the main reasons for this observation. As a consequence, suitable data fusion techniques still need to be developed and rigorously tested for their performance and reliability.

The present study aimed at addressing this need by describing and demonstrating a simple, but effective OBIA approach to extract urban land cover from HSR multi-spectral and LiDAR data. Particular emphasis was put on the evaluation of the methodology with regard to its generalization capabilities across varying situations. For this purpose, the experimental setup of this work included three urban areas with different physical structures, four sets of optical and LiDAR input data, as well as statistical measures to enable the assessment of both mapping accuracies and methodological transferability.

The results of this investigation highlight the great potential of the developed approach for accurate and robust urban land cover mapping. The observed user's and producer's accuracies are almost consistently above 80%, in many cases even above 90%. Few larger class-specific errors occur mainly because of the simple assumptions and descriptions on which the ruleset is based. Still, the overall performance of the latter is high, as reflected by the median accuracies of all maps and classes.

From the reported validation statistics, as well as from its qualitative evaluation, it is found that the presented feature extraction workflow is able to successfully

- capture the property of different urban areas,
- integrate various sets of optical and LiDAR inputs,
- deal with changes in illumination and phenology, and
- process vast amounts of HSR data.

Thus, the method fulfills some of the essential requirements for detailed, transferable, and large-area mapping and monitoring of urban environments by exploiting the synergistic potential between those HSR multi-sensor Earth observation data that are becoming increasingly available. The proposed classification scheme can therefore be used as a template or starting point in the framework of future urban land cover mapping efforts.

Acknowledgment

The authors are truly grateful to 1) P. Kotzerke, R. Eckardt, and T. Heyer for their assistance during the preparation of this study; 2) the four anonymous reviewers, whose constructive criticism helped to substantially improve the quality of the manuscript; and 3) the land registry offices of Rostock and Erfurt for the kind provision of building footprints, LiDAR data and DOPs. The JAS imagery is courtesy of Jena-Optronik GmbH. The WorldView-2 and LiDAR data of San Francisco were provided within the framework of the 2012 IEEE Geoscience and Remote Sensing Society (GRSS) Data Fusion Contest. The images are courtesy of DigitalGlobe ©, 2012, and USGS/CLICK ©, 2012.

References

[1] A. Di Gregorio, *Land Cover Classification System (LCCS), Version 2: Classification Concepts and User Manual*, ser. FAO Environment and Natural Resources Service Series. Rome, Italy: FAO, 2005, no. 8.

[2] M. Herold, C. Woodcock, T. Loveland, J. Townshend, M. Brady, C. Steenmans, and C. Schmullius, "Land-cover observations as part of a Global Earth Observation System of Systems (GEOSS): Progress, activities, and prospects," *IEEE Syst. J.*, vol. 2, no. 3, pp. 414–423, Sep. 2008.

[3] R. Scalenghe and F. Marsan, "The anthropogenic sealing of soils in urban areas," *Landscape Urban Planning*, vol. 90, no. 1, pp. 1–10, Mar. 2009.

[4] J. Niemczynowicz, "Urban hydrology and water management—Present and future challenges," *Urban Water*, vol. 1, no. 1, pp. 1–14, Mar. 1999.

[5] Z. Tang, B. Engel, K. Lim, B. Pijanowski, and J. Harbor, "Minimizing the impact of urbanization on long term runoff," *J. Amer. Water Res. Assoc.*, vol. 41, no. 6, pp. 1347–1359, Dec. 2005.

[6] L. Howard, *The Climate of London Deduced From Meteorological Observations Made in the Metropolis and at Various Places Around It*, 2nd ed. London, U.K.: J. Rickerby, 1833, vol. I–III.

[7] T. Oke, "City size and the urban heat island," *Atmosph. Environ.*, vol. 7, no. 8, pp. 769–779, Aug. 1973.

[8] J. Voogt and T. Oke, "Thermal remote sensing of urban climates," *Remote Sens. Environ.*, vol. 86, no. 3, pp. 370–384, Aug. 2003.

[9] S. Pauleit and F. Duhme, "Assessing the environmental performance of land cover types for urban planning," *Landscape Urban Planning*, vol. 52, no. 1, pp. 1–20, Nov. 2000.

[10] J. O'Neil-Dunne, S. MacFaden, A. Royar, and K. Pelletier, "An object-based system for LiDAR data fusion and feature extraction," *Geocarto Int.*, pp. 1–16, May 2012.

[11] D. Locke, J. Grove, J. Lu, A. Troy, J. O'Neil-Dunne, and B. Beck, "Prioritizing preferable locations for increasing urban tree canopy in New York City," *Cities Environment*, vol. 3, no. 1, 2010.

[12] European Environment Agency (EEA). CORINE Land Cover Data [Online]. Available: http://www.eea.europa.eu/data-and-maps, (accessed November 12, 2012).

[13] O. Arino, D. Gross, F. Ranera, L. Bourg, M. Leroy, P. Bicheron, J. Latham, A. Di Gregorio, C. Brockman, R. Witt, P. Defourny, C. Vancutsem, M. Herold, J. Sambale, F. Archard, L. Durieux, S. Plummer, and J.-L. Weber, "GlobCover: ESA service for global land cover from MERIS," in *Proc. IGARSS*, Barcelona, Spain, Jul. 23–28, 2007, pp. 2412–2415.

[14] E. Bartholome and A. Belward, "GLC2000: A new approach to global land cover mapping from Earth observation data," *Int. J. Remote Sens.*, vol. 26, no. 9, pp. 1959–1977, May 2005.

[15] Center for International Earth Science Information Network (CIESIN)/ Columbia University, International Food Policy Research Institute (IFPRI), The World Bank, and Centro Internacional de Agricultura Tropical (CIAT),, Global Rural-Urban Mapping Project, Version 1 (GRUMPv1): Urban Extents Grid. Palisades, NY, NASA Socioeconomic Data and Applications Center (SEDAC) [Online]. Available: http://sedac.ciesin.columbia.edu/data/set/grump-v1-urban-extents, (accessed November 12, 2012).

[16] C. Elvidge, M. Imhoff, K. Baugh, V. Hobson, I. Nelson, J. Safran, J. Dietz, and B. Tuttle, "Night-time lights of the world: 1994–1995," *ISPRS J. Photogrammetry Remote Sensing*, vol. 56, no. 2, pp. 81–99, Dec. 2001.

[17] M. Imhoff, W. Lawrence, D. Stutzer, and C. Elvidge, "A technique for using composite DMSP/OLS "city lights" satellite data to map urban areas," *Remote Sens. Environ.*, vol. 61, no. 3, pp. 361–370, Sep. 1997.

[18] C. Elvidge, B. Tuttle, P. Sutton, K. Baugh, A. Howard, C. Milesi, B. Bhaduri, and R. Nemani, "Global distribution and density of constructed impervious surfaces," *Sensors*, vol. 7, no. 9, pp. 1962–1979, Sep. 2007.

[19] A. Schneider, M. Friedl, D. McKiver, and C. Woodcock, "Mapping urban areas by fusing multiple sources of coarse resolution remotely sensed data," *Photogramm. Eng. Remote Sens.*, vol. 69, no. 12, pp. 1377–1386, Dec. 2003.

[20] A. Schneider, M. Friedl, and D. Potere, "A new map of global urban extent from MODIS satellite data," *Environ. Res. Lett.*, vol. 4, no. 4, pp. 1–11, Oct./Dec. 2009.

[21] D. Potere and A. Schneider, "A critical look at representations of urban areas in global maps," *GeoJournal*, vol. 69, no. 1–2, pp. 55–80, Jun. 2007.

[22] D. Potere, A. Schneider, S. Angel, and D. Civco, "Mapping urban areas on a global scale: Which of the eight maps now available is more accurate?," *Int. J. Remote Sens.*, vol. 30, no. 24, pp. 6531–6558, Dec. 2009.

[23] A. Tatem, A. Noor, and S. Hay, "Assessing the accuracy of satellite derived global and national urban maps in Kenya," *Remote Sens. Environ.*, vol. 96, no. 1, pp. 87–97, May 2005.

[24] G. Hepner, B. Houshmand, I. Kulikov, and N. Bryant, "Investigation of the integration of AVIRIS and IFSAR for urban analysis," *Photogrammetric Eng. Remote Sens.*, vol. 64, no. 8, pp. 813–820, Aug. 1998.

[25] S. Roessner, K. Segl, U. Heiden, and H. Kaufmann, "Automated differentiation of urban surfaces based on airborne hyperspectral imagery," *IEEE Trans. Geosci. Remote Sens.*, vol. 39, no. 7, pp. 1525–1532, Jul. 2001.

[26] G. Konecny, W. Schuhr, and J. Wu, "Untersuchungen über die Interpretierbarkeit von Bildern unterschiedlicher Sensoren und Plattformen für die kleinmaß stäbige Kartierung," *Bildmessung und Luftbildwesen*, vol. 50, pp. 187–200, 1982.

[27] R. Welch, "Spatial resolution requirements for urban studies," *Int. J. Remote Sens.*, vol. 3, no. 2, pp. 139–146, 1982.

[28] C. Woodcock and A. Strahler, "The factor of scale in remote sensing," *Remote Sens. Environ.*, vol. 21, no. 3, pp. 311–332, Apr. 1987.

[29] J. Jensen and D. Cowen, "Remote sensing of urban/suburban infrastructure and socio-economic attributes," *Photogrammetric Eng. Remote Sens.*, vol. 65, no. 5, pp. 611–622, May 1999.

[30] K. Steinnocher, T. Bauer, M. Köstl, and F. Kressler, "Beobachtung von Stadtentwicklung mit Fernerkundung. Applikationen und Innovationen," *Österreichische Zeitschrift für Vermessung und Geoinformation*, vol. 89, no. 3, pp. 145–148, 2001.

[31] C. Small, "High spatial resolution spectral mixture analysis of urban reflectance," *Remote Sens. Environ.*, vol. 88, no. 1–2, pp. 170–186, Nov. 2003.

[32] M. Ehlers, "Future EO sensors of relevance—Integrated perspective for global urban monitoring," in *Global Mapping of Human Settlement*, P. Gamba and M. Herold, Eds. Boca Raton, FL, USA: CRC Press, 2009, pp. 321–337.

[33] P. Gamba, F. Dell'Acqua, and B. Dasarathy, "Urban remote sensing using multiple data sets: Past, present, and future," *Inf. Fus.*, vol. 6, no. 4, pp. 319–326, Dec. 2005.

[34] K. Singh, J. Vogler, D. Shoemaker, and R. Meentemeyer, "LiDAR-Landsat data fusion for large-area assessment of urban land cover: Balancing spatial resolution, data volume and mapping accuracy," *ISPRS J. Photogramm. Remote Sens.*, vol. 74, pp. 110–121, Nov. 2012.

[35] N. Longbotham, F. Pacifici, T. Glenn, A. Zare, M. Volpi, D. Tuia, E. Christophe, J. Michel, J. Inglada, J. Chanussot, and Q. Du, "Multimodal change detection, application to the detection of flooded areas: Outcome of the 2009–2010 data fusion contest," *IEEE J. Sel. Topics Appl. Earth Observ. Remote Sens.*, vol. 5, no. 1, pp. 331–342, Feb. 2012.

[36] T. Lee, J. A. Richards, and P. Swain, "Probabilistic and evidential approaches for multisource data analysis," *IEEE Trans. Geosci. Remote Sens.*, vol. 25, no. 3, pp. 283–293, May 1987.

[37] S. Serpico and F. Roli, "Classification of multisensor remote-sensing images by structured neural networks," *IEEE Trans. Geosci. Remote Sens.*, vol. 33, no. 3, pp. 562–578, May 1995.

[38] K. Chen, W. Huang, D. Tsay, and F. Amar, "Classification of multifrequency polarimetric SAR imagery using a dynamic learning neural network," *IEEE Trans. Geosci. Remote Sens.*, vol. 34, no. 3, pp. 814–820, May 1996.

[39] A. Schistad Solberg, T. Taxt, and A. Jain, "A markov random field model for classification of multisource satellite imagery," *IEEE Trans. Geosci. Remote Sens.*, vol. 34, no. 1, pp. 100–113, Jan. 1996.

[40] X. Song, G. Fan, and M. Rao, "Automatic CRP mapping using nonparametric machine learning approaches," *IEEE Trans. Geosci. Remote Sens.*, vol. 43, no. 4, pp. 888–897, Apr. 2005.

[41] B. Waske and J. Benediktsson, "Fusion of support vector machines for classification of multisensor data," *IEEE Trans. Geosci. Remote Sens.*, vol. 45, no. 12, pp. 3858–3866, Dec. 2007.

[42] J. Benediktsson, P. Swain, and O. Ersoy, "Neural network approaches versus statistical methods in classification of multisource remote sensing data," *IEEE Trans. Geosci. Remote Sens.*, vol. 28, no. 4, pp. 540–552, Jul. 1990.

[43] J. Benediktsson and P. Swain, "Consensus theoretic classification methods," *IEEE Trans. Systems, Man Cybern.*, vol. 22, no. 4, pp. 688–704, Jul./Aug. 1992.

[44] J. Benediktsson and I. Kanellopoulos, "Classification of multisource and hyperspectral data based on decision fusion," *IEEE Trans. Geosci. Remote Sens.*, vol. 37, no. 3, pp. 1367–1377, May 1999.

[45] G. Briem, J. Benediktsson, and J. Sveinsson, "Multiple classifiers applied to multisource remote sensing data," *IEEE Trans. Geosci. Remote Sens.*, vol. 40, no. 10, pp. 2291–2299, Oct. 2002.

[46] M. Hill, C. Ticehurst, J.-S. Lee, M. Grunes, G. Donald, and D. Henry, "Integration of optical and radar classifications for mapping pasture type in Western Australia," *IEEE Trans. Geosci. Remote Sens.*, vol. 43, no. 7, pp. 1665–1681, Jul. 2005.

[47] M. Dalponte, L. Bruzzone, and D. Gianelle, "Fusion of hyperspectral and LIDAR remote sensing data for classification of complex forest areas," *IEEE Trans. Geosci. Remote Sens.*, vol. 46, no. 5, pp. 1416–1427, May 2008.

[48] R. Pouteau and B. Stoll, "SVM selective fusion (SELF) for multisource classification of structurally complex tropical rainforest," *IEEE J. Sel. Topics Appl. Earth Observ. Remote Sens.*, vol. 5, no. 4, pp. 1203–1212, Aug. 2012.

[49] A. Schistad Solberg, A. Jain, and T. Taxt, "Multisource classification of remotely sensed data: Fusion of Landsat TM and SAR images," *IEEE Trans. Geosci. Remote Sens.*, vol. 32, no. 4, pp. 768–778, Jul. 1994.

[50] J. Paola and R. Schowengerdt, "A detailed comparison of backpropagation neural network and maximum-likelihood classifiers for urban land use classification," *IEEE Trans. Geosci. Remote Sens.*, vol. 33, no. 4, pp. 981–996, Jul. 1995.

[51] Y.-L. Chang, L.-S. Liang, C.-C. Han, J.-P. Fang, W.-Y. Liang, and K.-S. Chen, "Multisource data fusion for landslide classification using generalized positive boolean functions," *IEEE Trans. Geosci. Remote Sens.*, vol. 45, no. 6, pp. 1697–1708, Jun. 2007.

[52] I. Farah, W. Boulila, K. Ettaba, B. Solaiman, and M. Ahmed, "Interpretation of multisensor remote sensing images: Multiapproach fusion of uncertain information," *IEEE Trans. Geosci. Remote Sens.*, vol. 46, no. 12, pp. 4142–4152, Dec. 2008.

[53] F. Pacifici, F. Del Frate, W. Emery, P. Gamba, and J. Chanussot, "Urban mapping using coarse SAR and optical data: Outcome of the 2007 GRSS data fusion contest," *IEEE Geosci. Remote Sens. Lett.*, vol. 5, no. 3, pp. 331–335, Jul. 2008.

[54] D. Tuia, G. Camps-Valls, G. Matasci, and M. Kanevski, "Learning relevant image features with multiple-kernel classification," *IEEE Trans. Geosci. Remote Sens.*, vol. 48, no. 10, pp. 3780–3791, Oct. 2010.

[55] B. Huang, H. Zhang, and L. Yu, "Improving Landsat ETM+ urban area mapping via spatial and angular fusion with MISR multi-angle observations," *IEEE J. Sel. Topics Appl. Earth Observ. Remote Sens.*, vol. 5, no. 1, pp. 101–109, Feb. 2012.

[56] V. Turkar, R. Deo, Y. Rao, S. Mohan, and A. Das, "Classification accuracy of multi-frequency and multi-polarization SAR images for various land covers," *IEEE J. Sel. Topics Appl. Earth Observ. Remote Sens.*, vol. 5, no. 3, pp. 936–941, Jun. 2012.

[57] T. Blaschke, "Object-based image analysis for remote sensing," *ISPRS J. Photogramm. Remote Sens.*, vol. 65, no. 1, pp. 2–16, Jan. 2010.

[58] M. Barnsley and S. Barr, "Inferring urban land use from satellite sensor images using kernel-based spatial reclassification," *Photogrammetric Eng. Remote Sens.*, vol. 62, no. 8, pp. 949–958, Aug. 1996.

[59] J. Schiewe, L. Tufte, and M. Ehlers, "Potential and problems of multiscale segmentation methods in remote sensing," *GeoBIT*, vol. 6, pp. 34–39, 2001.

[60] Y. Ouma, T. Ngigi, and R. Tateishi, "On the optimization and selection of wavelet texture for feature extraction from high-resolution satellite imagery with application towards urban-tree delineation," *Int. J. Remote Sens.*, vol. 27, no. 1, pp. 73–104, 2006.

[61] R. Mohapatra and C. Wu, "High resolution impervious surface estimation: An integration of IKONOS and Landsat-7 ETM+ imagery," *Photogrammetric Eng. Remote Sens.*, vol. 76, no. 12, pp. 1329–1341, Dec. 2010.

[62] T. Blaschke, G. Hay, Q. Weng, and B. Resch, "Collective sensing: Integrating geospatial technologies to understand urban systems—An overview," *Remote Sensing*, vol. 3, no. 8, pp. 1743–1776, Aug. 2011.

[63] S. Myint, P. Gober, A. Brazel, S. Grossman-Clarke, and Q. Weng, "Per-pixel versus object-based classification of urban land cover extraction using high spatial resolution imagery," *Remote Sens. Environ.*, vol. 115, no. 5, pp. 1145–1161, May 2011.

[64] B. Salehi, Y. Zhang, M. Zhong, and V. Dey, "Object-based classification of urban areas using VHR imagery and height points ancillary data," *Remote Sens.*, vol. 4, no. 8, pp. 2256–2276, Aug. 2012.

[65] J. Schiewe and M. Ehlers, "A novel method for generating 3-D city models from high resolution and multi-sensor remote sensing data," *Int. J. Remote Sens.*, vol. 26, no. 4, pp. 683–698, 2005.

[66] T. Blaschke, "Ohne Salz und Pfeffer. Objektorientierte Bildanalyse--eine Revolution in der Fernerkundung," *GeoBIT*, vol. 2, pp. 30–32, 2000.

[67] Q. Yu, P. Gong, N. Clinton, G. Biging, M. Kelly, and D. Schirokauer, "Object-based detailed vegetation classification with airborne high spatial resolution remote sensing imagery," *Photogrammetric Eng. Remote Sens.*, vol. 72, no. 7, pp. 799–811, Jul. 2006.

[68] J. Im, J. Jensen, and J. Tullis, "Object-based change detection using correlation image analysis and image segmentation," *Int. J. Remote Sens.*, vol. 29, no. 2, pp. 399–423, Jan. 2008.

[69] S. Lang, "Object-based image analysis for remote sensing applications: Modeling reality—Dealing with complexity," in *Object-Based Image Analysis. Spatial Concepts for Knowledge-Driven Remote Sensing Applications*, T. Blaschke, S. Lang, and G. Hay, Eds. Berlin, Germany: Springer, 2008, pp. 3–28.

[70] A. Tzotsos, C. Iosifidis, and D. Argialas, "A hybrid texture-based and region-based multi-scale image segmentation algorithm," in *Object-Based Image Analysis. Spatial Concepts for Knowledge-Driven Remote Sensing Applications*, T. Blaschke, S. Lang, and G. Hay, Eds. Berlin, Germany: Springer, 2008, pp. 221–236.

[71] A. Baraldi and L. Boschetti, "Operational automatic remote sensing image understanding systems: Beyond geographic object-based and object-oriented image analysis (GEOBIA/GEOOIA). Part 1: Introduction," *Remote Sens.*, vol. 4, no. 9, pp. 2694–2735, Sep. 2012.

[72] B. Forster, "Coefficient of variation as a measure of urban spatial attributes using spot HRV and Landsat TM data," *Int. J. Remote Sens.*, vol. 14, no. 12, pp. 2403–2409, 1993.

[73] M. Herold, M. Gardner, and D. Roberts, "Spectral resolution requirements for mapping urban areas," *IEEE Trans. Geosci. Remote Sens.*, vol. 41, no. 9, pp. 1907–1919, Sep. 2003.

[74] M. Herold, D. Roberts, M. Gardner, and P. Dennison, "Spectrometry for urban area remote sensing—Development and analysis of a spectral library from 350 to 2400 nm," *Remote Sens. Environ.*, vol. 91, no. 3–4, pp. 304–319, Jun. 2004.

[75] Q. Weng and D. Lu, "Subpixel analysis of urban landscapes," in *Urban Remote Sensing*, Q. Weng and D. Quattrochi, Eds. Boca Raton, FL, USA: CRC Press, 2007, pp. 71–90.

[76] W. Zhou, A. Troy, and M. Grove, "Object-based land cover classification and change analysis in the Baltimore Metropolitan Area using multitemporal high resolution remote sensing data," *Sensors*, vol. 8, no. 3, pp. 1613–1636, Mar. 2008.

[77] W. Zhou, G. Huang, A. Troy, and M. Cadenasso, "Object-based land cover classification of shaded areas in high spatial resolution imagery of urban areas: A comparison study," *Remote Sens. Environ.*, vol. 113, no. 8, pp. 1769–1777, Aug. 2009.

[78] N. Thomas, C. Hendrix, and R. Congalton, "A comparison of urban mapping methods using high-resolution digital imagery," *Photogrammetric Eng. Remote Sens.*, vol. 69, no. 9, pp. 963–972, Sep. 2003.

[79] M. Baatz, C. Hoffmann, and G. Willhauck, "Progressing from object-based to object-oriented image analysis," in *Object-Based Image Analysis. Spatial Concepts for Knowledge-Driven Remote Sensing Applications*, T. Blaschke, S. Lang, and G. Hay, Eds. Berlin, Germany: Springer, 2008, pp. 29–42.

[80] J. Townshend, C. Huang, S. Kalluri, R. Defries, and S. Liang, "Beware of per-pixel characterization of land cover," *Int. J. Remote Sens.*, vol. 21, no. 4, pp. 839–843, 2000.

[81] F. Dell'Acqua, P. Gamba, and G. Lisini, "Semi-automatic choice of scale-dependent features for satellite SAR image classification," *Pattern Recogn. Lett.*, vol. 27, no. 4, pp. 244–251, Mar. 2006.

[82] B. Koch, M. Jochum, E. Ivitis, and M. Dees, "Pixelbasierte Klassifizierung im Vergleich und zur Ergänzung zum objektbasierten Verfahren," *Photogrammetrie, Fernerkundung, Geoinformation*, vol. 3, pp. 195–204, 2003.

[83] R. Haralick, K. Shanmugam, and I. Dinstein, "Textural features for image classification," *IEEE Trans. Systems, Man Cybern.*, vol. 3, no. 6, pp. 610–621, Nov. 1973.

[84] P. Soille, *Morphological Image Analysis*, 2nd ed. Berlin, Germany: Springer, 2004, p. 392.

[85] M. Barnsley and S. Barr, "Monitoring urban land use by Earth observation," *Surveys in Geophysics*, vol. 21, no. 2–3, pp. 269–289, 2000.

[86] *Object-Based Image Analysis for Remote Sensing. Spatial Concepts for Knowledge-Driven Remote Sensing Applications*, T. Blaschke, S. Lang, and G. Hay, Eds. Berlin, Germany: Springer, 2008.

[87] C. Burnett and T. Blaschke, "A multi-scale segmentation/object relationship modelling methodology for landscape analysis," *Ecol. Modell.*, vol. 168, no. 3, pp. 233–249, Oct. 2003.

[88] U. Benz, P. Hofmann, G. Willhauck, I. Lingenfelder, and M. Heynen, "Multi-resolution, object-oriented fuzzy analysis of remote sensing data for GIS-ready information," *ISPRS J. Photogramm. Remote Sens.*, vol. 58, no. 3–4, pp. 239–258, Jan. 2004.

[89] G. Meinel, M. Neubert, and J. Reder, "Pixelorientierte versus segmentorientierte Klassifikation von IKONOS-Satellitenbilddaten—ein Methodenvergleich," *Photogrammetrie, Fernerkundung, Geoinformation*, vol. 3, pp. 157–170, 2001.

[90] D. Flanders, M. Hall-Beyer, and J. Pereverzoff, "Preliminary evaluation of eCognition object-based software for cut block delineation and feature extraction," *Can. J. Remote Sens.*, vol. 29, no. 4, pp. 441–452, Aug. 2003.

[91] G. Hay and G. Castilla, "Geographic Object-Based Image Analysis (GEOBIA): A new name for a new discipline," in *Object-Based Image Analysis. Spatial Concepts for Knowledge-Driven Remote Sensing Applications*, T. Blaschke, S. Lang, and G. Hay, Eds. Berlin, Germany: Springer, 2008, pp. 75–89.

[92] T. Evans, M. Costa, K. Telmer, and T. Silva, "Using ALOS/PALSAR and RADARSAT-2 to map land cover and seasonal inundation in the Brazilian Pantanal," *IEEE J. Sel. Topics Appl. Earth Observ. Remote Sens.*, vol. 3, no. 4, pp. 560–575, Dec. 2010.

[93] H. Taubenböck, T. Esch, M. Wurm, A. Roth, and S. Dech, "Object-based feature extraction using high spatial resolution satellite data of urban areas," *J. Spatial Science*, vol. 55, no. 1, pp. 117–132, Jun. 2010.

[94] A. Shackelford and C. Davis, "A hierarchical fuzzy classification approach for high-resolution multispectral data over urban areas," *IEEE Trans. Geosci. Remote Sens.*, vol. 41, no. 9, pp. 1920–1932, Sep. 2003.

[95] L. Linde and W. Kirstein, "Vergleich unterschiedlicher Klassifikationsansätze am Beispiel von hoch auflösenden Satellitenbilddaten im Raum Leipzig," *Photogrammetrie, Fernerkundung und Geoinformation*, vol. 6, pp. 519–526, 2004.

[96] R. Platt and L. Rapoza, "An evaluation of an object-oriented paradigm for land use/land cover classification," *The Professional Geographer*, vol. 60, no. 1, pp. 87–100, 2008.

[97] I. Castillejo-Gonzalez, F. Lopez-Granados, A. Garcia-Ferrer, J. Pena-Barragan, M. Jurado-Exposito, M. de la Ordena, and M. Gonzalez-Audicana, "Object- and pixel-based analysis for mapping crops and their agro-environmental associated measures using QuickBird imagery," *Comput. Electron. Agriculture*, vol. 68, no. 2, pp. 207–215, Oct. 2009.

[98] S. Bhaskaran, S. Paramananda, and M. Ramnarayan, "Per-pixel and object-oriented classification methods for mapping urban features using Ikonos satellite data," *Appl. Geograph.*, vol. 30, no. 4, pp. 650–665, Dec. 2010.

[99] T. Blaschke and J. Strobl, "What's wrong with pixels? Some recent developments interfacing remote sensing and GIS," *GIS Zeitschrift für Geoinformationssysteme*, vol. 14, no. 6, pp. 12–17, 2001.

[100] W. Zhou and A. Troy, "An object-oriented approach for analyzing and characterizing urban landscape at the parcel level," *Int. J. Remote Sens.*, vol. 29, no. 11, pp. 3119–3135, Jun. 2008.

[101] M. Kim, M. Madden, and B. Xu, "GEOBIA vegetation mapping in Great Smoky Mountains National Park with spectral and non-spectral ancillary information," *Photogrammetric Eng. Remote Sens.*, vol. 76, no. 2, pp. 137–149, Feb. 2010.

[102] J. Zhang, "Multi-source remote sensing data fusion: Status and trends," *Int. J. Image Data Fus.*, vol. 1, no. 1, pp. 5–24, Mar. 2010.

[103] E. Schöpfer and M. Möller, "Comparing metropolitan areas—Transferable object-based image analysis approach," *Photogrammetrie, Fernerkundung, Geoinformation*, vol. 10, no. 4, pp. 277–286, Jul./Aug. 2006.

[104] M. Wurm, H. Taubenböck, M. Schardt, T. Esch, and S. Dech, "Object-based image information fusion using multisensor Earth observation data over urban areas," *Int. J. Image Data Fus.*, vol. 2, no. 2, pp. 121–147, Jun. 2011.

[105] D. Lu, S. Hetrick, and E. Moran, "Land cover classification in a complex urban-rural landscape with QuickBird imagery," *Photogrammetric Eng. Remote Sens.*, vol. 76, no. 10, pp. 1159–1168, Oct. 2010.

[106] J. Walker and T. Blaschke, "Object-based land-cover classification for the Phoenix metropolitan area: Optimization versus transportability," *Int. J. Remote Sens.*, vol. 29, no. 7, pp. 2021–2040, Apr. 2008.

[107] Destatis, Städte (Alle Gemeinden mit Stadtrecht) nach Fläche und Bevölkerung am 31.12.2010 [Online]. Available: https://www.destatis.de/DE/ZahlenFakten/LaenderRegionen/Regionales/Gemeindeverzeichnis/Administrativ/Aktuell/05Staedte.html (accessed June 19, 2012).

[108] U.S. Census Bureau, State & County QuickFacts. San Francisco, CA, USA [Online]. Available: http://quickfacts.census.gov/qfd/states/06/0667000.html, (accessed June 19, 2012).

[109] S. Brunn, M. Hays-Mitchell, and D. Zeigler, *Cities of the World—World Regional Urban Development*, 5th ed. Lanham, MD, USA: Rowman & Littlefield, 2012, p. 632.

[110] C. Pohl and J. van Genderen, "Multisensor image fusion in remote sensing: Concepts, methods and applications," *Int. J. Remote Sens.*, vol. 19, no. 5, pp. 823–854, May 1998.

[111] R. Richter, *Atmospheric/Topographic Correction for Satellite Imagery. ATCOR-2/3 User Guide, Version 8.0.2*. Wessling, Germany: Deutsches Zentrum für Luft- und Raumfahrt (DLR), Aug. 2011.

[112] U. Gangkofner, P. Pradhan, and D. Holcomb, "Optimizing the high-pass filter addition technique for image fusion," *Photogrammetric Eng. Remote Sens.*, vol. 74, no. 9, pp. 1107–1118, Sep. 2008.

[113] C. Tucker, "Red and photographic infrared linear combinations for monitoring vegetation," *Remote Sens. Environ.*, vol. 8, no. 2, pp. 127–150, May 1979.

[114] L. Zevenbergen and C. Thorne, "Quantitative analysis of land surface topography," *Earth Surf. Process. Landforms*, vol. 12, no. 1, pp. 12–56, Jan./Feb. 1987.

[115] G. Priestnall, J. Jafaar, and A. Duncan, "Extracting urban features from LiDAR digital surface models," *Computers, Environ. Urban Syst.*, vol. 24, no. 2, pp. 65–78, Mar. 2000.

[116] N. Ackermann, F. Becker, C. Berger, M. Bindel, J. Eberle, I. Elbertzhagen, K.-H. Franke, A. Hecheltjen, T. Koch, T. Kubertschak, G. Menz, T. Riedel, C. Schmullius, M. Schwarz, F. Thonfeld, K. Weise, and B. Wolf, "ENVILAND 2—Von multisensoralen Satellitenbildern zu operationellen Produkten," in *RapidEye Science Archive (RESA). "Vom Algorithmus zum Produkt". Tagungsband zum 4. RESA Workshop, Neustrelitz, 21.–22. März 2012*, E. Borg, H. Daedelow, and R. Johnson, Eds., Berlin, Germany: GITO, 2012, pp. 123–149.

[117] *eCognition Developer 8.7.1. Reference Book*. Munich, Germany: Trimble, Trimble Documentation, 2012.

[118] C. Weise, Customized Algorithm to Generating Meaningful Objects [Online]. Available: http://community.ecognition.com/home/customized&20segmentation zip/view (accessed January 22, 2013).

[119] R. Ma, "DEM generation and building detection from LiDAR data," *Photogrammetric Eng. Remote Sens.*, vol. 71, no. 7, pp. 847–854, Jul. 2005.

[120] B. Yu, H. Liu, J. Wu, and W.-M. Lin, "Investigating impacts of urban morphology on spatio-temporal variations of solar radiation with airborne LiDAR data and a solar flux model: A case study of downtown Houston," *Int. J. Remote Sens.*, vol. 30, no. 17, pp. 4359–4385, 2009.

[121] B. Yu, H. Liu, J. Wu, Y. Hu, and L. Zhang, "Automated derivation of urban building density information using airborne LiDAR data and object-based method," *Landscape Urban Planning*, vol. 98, no. 3–4, pp. 210–219, Dec. 2010.

[122] S. Stehman and R. Czaplewski, "Design and analysis for thematic map accuracy assessment: Fundamental principles," *Remote Sens. Environ.*, vol. 64, no. 3, pp. 331–344, Jun. 1998.

[123] J. Johnson, Building Footprints as of June 2011 [Online]. Available: https://data.sfgov.org/Facilities-and-Structures/Building-Footprints-Zipped-Shapefile-Format-/jezr-5bxm (accessed July 09, 2012), 2012

[124] C. Georgi, R. Strognienko, S. Knuth, and G. Albe, "JAS: The next generation digital aerial scanner," in *Photogrammetric Week '05*, D. Fritsch, Ed., Heidelberg, Germany: Wichmann, 2005, pp. 147–154.

[125] S. Stehman, "Selecting and interpreting measures of thematic classification accuracy," *Remote Sens. Environ.*, vol. 62, no. 1, pp. 77–89, Oct. 1997.

[126] J. Cohen, "A coefficient of agreement for nominal scales," *Educat. Psycholog. Meas.*, vol. 20, no. 1, pp. 37–46, Apr. 1960.

[127] D. Altman, *Practical Statistics for Medical Research*. Boca Raton, FL, USA: Chapman & Hall, 1991, p. 624.

[128] U. Grouven, R. Bender, A. Ziegler, and S. Lange, "The kappa coefficient," *Deutsche Medizinische Wochenschrift*, vol. 132, no. 23, pp. 65–68, 2007.

[129] M. Bauer, B. Loeffelholz, and B. Wilson, "Estimating and mapping impervious surface area by regression analysis of Landsat imagery," in *Remote Sensing of Impervious Surfaces*, Q. Weng, Ed. Boca Raton, FL, USA: CRC Press, 2008, pp. 3–19.

[130] A. Elmore and S. Guinn, "Synergistic use of Landsat Multispectral Scanner with GIRAS land-cover data to retrieve impervious surface area for the Potomac River Basin in 1975," *Remote Sens. Environ.*, vol. 114, no. 10, pp. 2384–2391, Oct. 2010.

[131] T. Esch, V. Himmler, G. Schorcht, M. Thiel, T. Wehrmann, F. Bachofer, C. Conrad, M. Schmidt, and S. Dech, "Large-area assessment of impervious surface based on integrated analysis of single-date Landsat-7 images and geospatial vector data," *Remote Sens. Environ.*, vol. 113, no. 8, pp. 1678–1690, Aug. 2009.

[132] P. Leinenkugel, T. Esch, and M. Gähler, "Settlement detection and impervious surface estimation in the Mekong Delta using optical and SAR remote sensing data," *Remote Sens. Environ.*, vol. 115, no. 12, pp. 3007–3019, Dec. 2011.

[133] L. Luo and G. Mountrakis, "Integrating intermediate inputs from partially classified images within a hybrid classification framework: An impervious surface estimation example," *Remote Sens. Environ.*, vol. 114, no. 6, pp. 1220–1229, Jun. 2010.

[134] Q. Weng, "Remote sensing of impervious surfaces," in *Remote Sens. Impervious Surf.*, Q. Weng, Ed. Boca Raton, FL, USA: CRC Press, 2008, pp. XV–XXVI.

[135] L. Yang, C. Huang, C. Homer, B. Wylie, and M. Coan, "An approach for mapping large-area impervious surfaces: Synergistic use of Landsat-7 ETM+ and high spatial resolution imagery," *Can. J. Remote Sens.*, vol. 29, no. 2, pp. 230–240, Apr. 2003.

[136] P. Dare, "Shadow analysis in high-resolution satellite imagery of urban areas," *Photogramm. Eng. Remote Sensing*, vol. 71, no. 2, pp. 169–177, Feb. 2005.

[137] J. Guo, L. Liang, and P. Gong, "Removing shadows from Google Earth images," *Int. J. Remote Sens.*, vol. 31, no. 6, pp. 1379–1389, Mar. 2010.

[138] S. Safavian and D. Landgrebe, "A survey of decision tree classifier methodology," *IEEE Trans. Systems, Man Cybern.*, vol. 21, no. 3, pp. 660–674, May/Jun. 1991.

[139] Y. Jin and B. Sendhoff, "Trade-off between performance and robustness: An evolutionary multiobjective approach," in *Evolutionary Multi-Criterion Optimization*, ser. Lecture Notes in Computer Science, C. Fonseca, P. Fleming, E. Zitzler, L. Thiele, and K. Deb, Eds. Berlin, Germany: Springer, 2003, vol. 2632, pp. 237–251.

4.2 Integrated assessment of 2D and 3D USCs

This section is based on the manuscript entitled
"Multi-modal and multi-temporal data fusion: Outcome of the 2012 GRSS Data Fusion Contest".

The manuscript was authored by
Berger C, Voltersen M, Eckardt R, Eberle J, Heyer T, Salepci N, Hese S, Schmullius C, Tao J, Auer S, Bamler R, Ewald K, Gartley M, Jacobson J, Buswell A, Du Q & Pacifici F (2013)

and published in
IEEE J Sel Top Appl Earth Obs Remote Sens 6(3): 1324–1340;
doi: 10.1109/jstars.2013.2245860.

1324 IEEE JOURNAL OF SELECTED TOPICS IN APPLIED EARTH OBSERVATIONS AND REMOTE SENSING, VOL. 6, NO. 3, JUNE 2013

Multi-Modal and Multi-Temporal Data Fusion: Outcome of the 2012 GRSS Data Fusion Contest

Christian Berger, Michael Voltersen, Robert Eckardt, Jonas Eberle, Thomas Heyer, Nesrin Salepci, Sören Hese, Christiane Schmullius, Junyi Tao, *Student Member, IEEE*, Stefan Auer, Richard Bamler, *Fellow, IEEE*, Ken Ewald, Michael Gartley, John Jacobson, Alan Buswell, Qian Du, *Senior Member, IEEE*, and Fabio Pacifici, *Member, IEEE*

***Abstract*—The 2012 Data Fusion Contest organized by the Data Fusion Technical Committee (DFTC) of the IEEE Geoscience and Remote Sensing Society (GRSS) aimed at investigating the potential use of very high spatial resolution (VHR) multi-modal/multi-temporal image fusion. Three different types of data sets, including spaceborne multi-spectral, spaceborne synthetic aperture radar (SAR), and airborne light detection and ranging (LiDAR) data collected over the downtown San Francisco area were distributed during the Contest. This paper highlights the three awarded research contributions which investigate (*i*) a new metric to assess urban density (UD) from multi-spectral and LiDAR data, (*ii*) simulation-based techniques to jointly use SAR and LiDAR data for image interpretation and change detection, and (*iii*) radiosity methods to improve surface reflectance retrievals of optical data in complex illumination environments. In particular, they demonstrate the usefulness of LiDAR data when fused with optical or SAR data. We believe these interesting investigations will stimulate further research in the related areas.**

***Index Terms*—Data fusion, LiDAR, multi-modal, multi-temporal, optical, SAR, urban, VHR imagery.**

Manuscript received November 06, 2012; revised January 16, 2013; accepted January 21, 2013. Date of publication March 15, 2013; date of current version June 17, 2013. This work was supported in part by the IEEE Geoscience and Remote Sensing Society (GRSS), DigitalGlobe, Inc., and the National Air and Space Intelligence Center (NASIC) under the Advanced Technical Exploitation Program (ATEP) Contract FA8604-09-D-7976.

C. Berger, M. Voltersen, R. Eckardt, J. Eberle, T. Heyer, N. Salepci, S. Hese, and C. Schmullius are with the Department for Earth Observation, Institute of Geography, Friedrich-Schiller-University Jena, Loebdergraben 32, D-07743 Jena, Germany (corresponding author e-mail: christian.berger@uni-jena.de).

J. Tao is with the Remote Sensing Technology Institute (IMF), German Aerospace Center (DLR), 82234 Oberpfaffenhofen-Wessling, Germany.

S. Auer is with the Chair of Remote Sensing Technology, Technische Universität München, 80333 München, Germany.

R. Bamler is with the Remote Sensing Technology Institute (IMF), German Aerospace Center (DLR), 82234 Oberpfaffenhofen-Wessling, Germany, and also with the Chair of Remote Sensing Technology, Technische Universität München, 80333 München, Germany.

K. Ewald and A. Buswell are with Ball Aerospace and Technologies, Fairborn, OH 45324 USA.

M. Gartley is with the Center for Imaging Science, Rochester Institute of Technology, Rochester, NY 14623 USA.

J. Jacobson is with theNational Air & Space Intelligence Center, Wright Patterson AFB, OH 45433 USA.

Q. Du is with the Department of Electrical and Computer Engineering, Mississippi State University, Mississippi State, MS 39762 USA.

F. Pacifici is with DigitalGlobe Inc., Longmont, CO 80503 USA.

Color versions of one or more of the figures in this paper are available online at http://ieeexplore.ieee.org.

Digital Object Identifier 10.1109/JSTARS.2013.2245860

I. Introduction

THE Data Fusion Contest has been annually organized by the Data Fusion Technical Committee [1] of the IEEE Geoscience and Remote Sensing Society (GRSS) since 2006 [2]–[6]. It is open not only to IEEE members, but to everyone, with the aim of developing new or evaluating existing methodologies at the research or operational level to solve remote sensing problems using data from different sources. It has earned international reputation for providing high-quality data and promoting the cutting-edge research of remote sensing image processing and analysis.

The 2012 Contest was designed to investigate the potential use of very high spatial resolution (VHR) multi-modal/multi-temporal image fusion for various remote sensing applications. Three different types of data sets, including spaceborne multi-spectral (i.e., QuickBird and WorldView-2) and synthetic aperture radar (SAR) data (i.e., TerraSAR-X), and airborne (LiDAR) data, were provided by DigitalGlobe, Astrium Services, and the United States Geological Survey (USGS).

Fusion of multi-source images and data is considered to be the ultimate solution for optimized information exploitation in remote sensing [7]. Passive optical sensors have been widely employed to map horizontal structures like land cover (LC) types at broad scales. SAR complements optical imaging capabilities because of the minimum constraints on time-of-day and atmospheric conditions, and because of the unique responses of terrain and man-made targets to radar frequencies. Airborne LiDAR can provide highly accurate sample measurements (single pulse, multiple pulses, or even full waveform) of vertical structures, but it is currently limited by the high cost of acquisition. Thus, fusion of optical/SAR/LiDAR data can offer additional information for various applications, such as LC mapping [5], forest-related studies [8]–[12], oil slick detection and characterization [13], and accurate digital surface model (DSM) and digital elevation model (DEM) generation [7]. More recently, due to its increased availability, hyperspectral imagery and its fusion with LiDAR data have been of great interest for practical applications [14]–[20].

The data sets distributed during the Contest were acquired over the downtown San Francisco area, covering a number of large buildings, skyscrapers, commercial and industrial structures, a mixture of community parks and private housing, as well as highways and bridges. The composition of the optical, SAR, and LiDAR data sets is shown for a small subset in Fig. 1. As listed in Table I, the QuickBird/WorldView-2/TerraSAR-X data sets were acquired in late 2007 and 2011, while the LiDAR

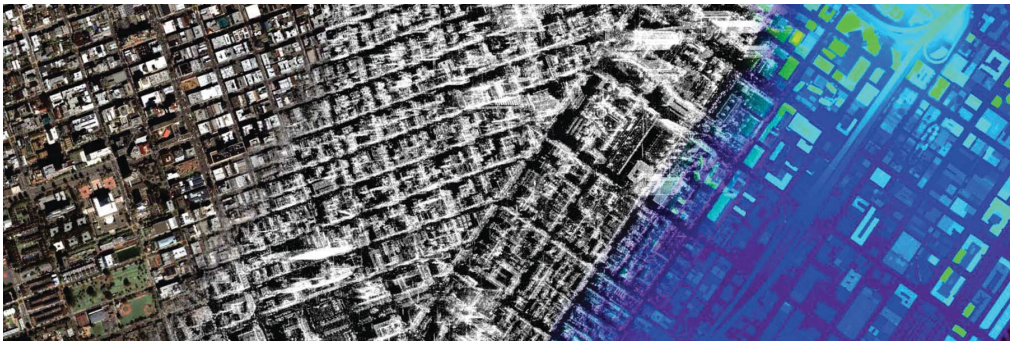

Fig. 1. Composition of the optical, SAR, and LiDAR data sets over the downtown San Francisco area.

TABLE I
SENSORS AND ACQUISITION DATES FOR THE IMAGES DISTRIBUTED DURING THE CONTEST

Sensor	Acquisition 1	Acquisition 2
QuickBird/WorldView-2	11 November 2007	9 October 2011
TerraSAR-X	5 December 2007	2 October 2011
	16 December 2007	13 October 2011
	27 December 2007	24 October 2011
LiDAR	June 2010	

data were collected in June 2010. Three products were derived from the raw LiDAR data in advance, including a DEM, a DSM and an intensity image. For this purpose, the LP360 software for ArcGIS was used. The DEM was created by triangulating elevation only from the bare-earth LiDAR points, while the DSM was created by triangulating elevation only from the first-return LiDAR points. And finally, the intensity layer was generated by triangulating intensity from the first-return LiDAR points.

More than 1150 researchers across the globe registered to the Contest, corresponding to an increase of more than 51% over the previous year. The data sets were downloaded by practitioners from 78 different countries, with a large number from developing and underdeveloped countries. This clearly demonstrates that the Data Fusion Contest is of great interest to the Earth observation research and application community.

To enter the Contest, each participant was asked to submit a paper describing the problem addressed, the method used, and the final results. Several interesting contributions were received, the large majority of which investigated the fusion problem for urban LC classification and change detection, followed by image pansharpening. Other topics included automated road extraction, moving object detection, urban tree inventory, and image superresolution, demonstrating the large variety of applications that multi-modal/multi-temporal remote sensing images can offer.

After rigorous review by the Data Fusion Award Committee, three winning papers were selected, and their authors were awarded IEEE GRSS Certificates of Appreciation during the 2012 IEEE International Geoscience and Remote Sensing Symposium (IGARSS) held in Munich, Germany.

In the remainder of this paper, the contributions proposed by the three winning teams are described in detail. Specifically, Section II presents the work of C. Berger, M. Voltersen, R. Eckardt, J. Eberle, T. Heyer, N. Salepci, S. Hese, and C. Schmullius, from the Friedrich-Schiller-University of Jena, Germany, who fused WorldView-2 and LiDAR data to derive a new metric for the assessment of urban density (UD) by taking into account both horizontal and vertical characteristics of a city. In Section III, a simulation-based method to jointly use TerraSAR-X and LiDAR data for image interpretation and change detection in dense urban areas is proposed by J. Tao, S. Auer, and R. Bamler from the German Aerospace Center and Technische Universität München, Germany. Section IV illustrates the research of K. Ewald and A. Buswell from Ball Aerospace and Technologies Corp., M. Gartley from the Rochester Institute of Technology, and J. Jacobson from the National Air and Space Intelligence Center, United States, on a technique using radiosity methods to improve surface reflectance retrievals from WorldView-2 data in complex illumination environments. Finally, the conclusions and perspectives drawn from this Contest are presented and discussed in Section V.

II. FUSION OF MULTI-SPECTRAL AND LIDAR DATA FOR AN INTEGRATED ASSESSMENT OF URBAN DENSITY (UD)

This section aims at the derivation of a new indicator to assess UD (defined here as the intensity of urban development) that takes into account all three spatial dimensions of a city. In fact, the presence of building objects adds a third dimension to be considered among the environmental relationships found in urban areas. Thus, urban environmental studies should rely on information sources that account not only for the horizontal dimensions, but also for the vertical dimension of a city to enable a more holistic assessment of the *builtscape* [21].

To assess UD, a variety of spatial indicators has been used in the past. In general, these indicators can be subdivided into two groups: (*i*) two-dimensional (2D), and (*ii*) three-dimensional (3D) indicators. While 2D indicators measure the percentage of specific urban LC classes within a predefined area of interest (AOI), 3D indicators quantify information related to the height or volume of objects belonging to specific urban LC classes within the AOI. To calculate the 2D indicators, *a priori* information about urban LC is required. In addition to urban LC, 3D indicators do also require information about the height of urban LC objects. The AOI used to infer those indicators can

be a single pixel, a grid cell, or a moving window (kernel) summarizing groups of classified pixels [22], [23], but can also be a circle of a certain radius around specific urban LC objects [24] or an administrative area like a zoning district, tax parcel or a land lot [25], [26]. If the AOI is a single pixel (2D indicators only), the indicator is computed by analyzing the proportion of specific urban LC classes at the sub-pixel level using spectral unmixing techniques [27]–[31].

A common 2D indicator of UD is the impervious surface area (ISA), also known under various other names [22], [23], [27], [28], [32]. Often provided as percentage [27]–[30], [33], the ISA is defined as the share of impervious surfaces within an AOI. A similar 2D indicator is the building coverage ratio (BCR) [25], [26], [34], [35]. As bare soil areas usually do not cover more than 5% of a city, the abundance of impervious surfaces is found to be inversely related to the abundance of urban vegetation [31], [36]. For this reason, it is also possible to describe UD by the intensity of urban greenery. In this regard, a widely used 2D indicator is the vegetation fraction (VF) [37]–[40]. VF evaluates the percentage of urban green within an AOI. Schöpfer *et al.* [41] extended the VF by introducing additional criteria and weighting factors to its calculation. As a result, VF values depend not only on the amount of urban vegetation, but also on the percentage of high-rise buildings and the distance between buildings found within the AOI.

Only few 3D indicators of UD can be found in the scientific literature. Among them, the floor area ratio (FAR) has been discussed in [25], [26], [35]. It represents the ratio of the gross floor area of one or more buildings within an AOI and the total area of the AOI. For its estimation, a constant value representing the average height of one story of all buildings under consideration has to be specified. Another 3D indicator is the vegetation volume to built-up volume (VV2BV) [24], which describes the relation between the cubic volume of high vegetation and the cubature of buildings within an AOI. The VV2BV was developed to better characterize the living quality in cities. A further 3D indicator related to vegetation is the green plot ratio (GPR) [42]. It is defined as the average leaf area index (LAI) of urban greenery within the AOI. For example, a site with a GPR of 2:1 features vegetation that has a total canopy cover twice that of the site. Because the LAI measures the area of leaves per area of ground, the concept behind the GPR takes into account the area that is covered by multiple, vertically-arranged canopy layers within the AOI.

The above selection of studies shows that various spatial indicators of UD have been proposed and used so far. However, it has to be kept in mind that each of these indicators considers different and distinct characteristics of human settlements and, thus, addresses only specific aspects of UD. Consequently, there is a lack of comprehensive indicators that are able to interrelate existing and possibly new spatial indicators for a more holistic assessment of density patterns in urban environments. An exception to this observation are the Spacematrix and the urban vegetation index (UVI). The Spacematrix is a 3D feature space to describe UD within an AOI [34]. This feature space is spanned by the indicators road network density (N), FAR, and BCR [34], and was successfully used to investigate the relation between traffic noise and UD [35]. The UVI represents the weighted sum of two ratios, namely the VV2BV and the vegetation area to built-up area ratio, and was recently employed for an improved assessment of both urban green spaces and urban quality of life [24]. Apart from these exceptions, there is still a need for integrated approaches making use of a combination of 2D and 3D indicators to estimate UD in its entirety. In the following subsections, this need is addressed by a combined indicator that takes into account four different key features of the urban landscape.

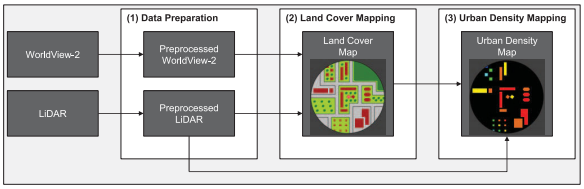

Fig. 2. Conceptual workflow for the assessment of urban density.

A. Proposed Method

The overall workflow of this study consists of three consecutive steps: (*i*) data preparation, (*ii*) LC mapping, and (*iii*) UD mapping. Fig. 2 illustrates the role of the data sets being used in the context of each stage of the data fusion approach. After data preparation, LC is extracted from the preprocessed WorldView-2 and LiDAR data by means of feature fusion [43]. The LC map is then utilized in combination with the object height information provided by the LiDAR data to infer UD.

1) Data Preparation: Preprocessing of the WorldView-2 imagery comprises three separate steps: (*i*) radiometric normalization using ATCOR [44], (*ii*) pansharpening using the high-pass filter (HPF) fusion [45], and (*iii*) co-registration to the LiDAR data using more than 20 well-distributed ground control points (GCPs) and the DEM. A normalized digital surface model (nDSM) is calculated from the LiDAR data by subtracting the DEM from the DSM. It contains the height of urban objects relative to the ground. With respect to the LC classification, additional features are derived from the input data. Amongst those features are the average reflectance of the blue, green, red, and the first near-infrared (NIR) WorldView-2 bands, the normalized difference vegetation index (NDVI) [46] and the slope (in percent) of the nDSM [47]. The latter is useful for identifying transitions between flat areas and elevated objects (e.g., trees or buildings) [48].

2) Extraction of Land Cover (LC) Information: Six LC classes are extracted from the data basis: buildings, impervious surfaces, trees, grass/shrubs, bare soil areas and water bodies. For this purpose, an object-based image analysis (OBIA) approach [49]–[51] is employed for its advantages over traditional, pixel-based classification techniques with respect to feature extraction from VHR multi-source imagery [49], [52]–[56]. A complete description and evaluation of the method (implemented in Trimble eCognition), including a discussion on its robustness with regard to four different multi-spectral and LiDAR input data sets acquired over three urban areas, is provided in Berger *et al.* [57].

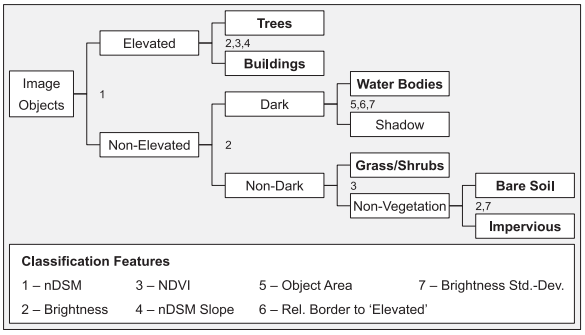

Fig. 3. The land cover mapping scheme applied to the image objects.

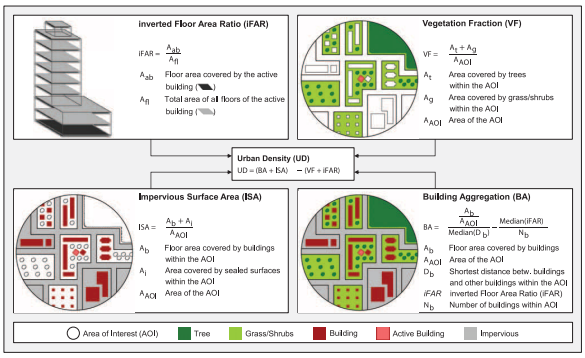

Fig. 4. The four input parameters used to infer urban density.

As a first step, a number of segmentation algorithms is applied to the input data. Subsequently, a rule-based classification of the resulting objects is performed following the scheme in Fig. 3. The numbers at each node of the decision tree indicate the features that are used for class separation. As an example, the tree canopy class is considered. Image segments are first divided into elevated and non-elevated objects using the LiDAR nDSM. To this end, an adjustable object height value serves as threshold for classification. Afterwards, elevated objects are reclassified as tree canopy if they feature a relatively high NDVI. Finally, the resulting tree canopy objects are used as seeds which are grown into adjacent pixels belonging to the elevated class if the latter have similar, but not necessarily as distinct, NDVI and brightness characteristics as the former. In a way similar to the tree canopy class, these so-called pixel-based object resizing operations [58] are also used to grow and/or shrink objects of other LC types. After the extraction of the six target classes, some reshaping algorithms are applied to the thematic objects for the purpose of border optimization. For instance, building footprints are generalized by calculating a morphological parameter called surface tension [58] and evaluating the result against a predefined criterion of compactness. In this way, the original object primitives are successively transformed into more meaningful objects of interest that better correspond to the visual perception of humans [49], [59]–[61]. Finally, all remaining shadow objects are reassigned to the class with which they share the largest relative common border.

To assess mapping accuracy, two data sources are used. The building class is validated using the building footprints provided by the City of San Francisco [62], whereas the remaining LC types are validated using the panchromatic WorldView-2 band. A random sampling design is chosen for validation comprising 50 sample points per LC class to assess overall accuracy, errors of commission and omission, as well as the kappa coefficient of agreement [63], [64].

3) Derivation of Urban Density (UD) Information: UD values are calculated for each single building (referred to as *active* building) in the LC map and within a predefined radius (i.e., the AOI) around the centroid of the respective building. They are the result of a logical combination of four parameters quantifying (*i*) vertical development, (*ii*) urban vegetation, (*iii*) soil sealing, and (*iv*) the clustering of urban structures within the AOI (Fig. 4). Since each of these input variables evaluates a different and distinct aspect of the *builtscape* [21], the resulting information layer enables an integrated and more holistic assessment of local UD patterns.

The parameters used to assess UD are the inverted floor area ratio (iFAR), VF, ISA and building aggregation (BA):

- *iFAR* describes the ratio between the footprint and the gross floor area of an active building [25], [26], [35]. It ranges between 0 and 1. UD decreases with higher values of iFAR.
- *VF* describes the urban green area ratio within the AOI [37]–[40]. It ranges between 0 and 1. UD decreases with higher values of VF.
- *ISA* describes the degree of soil sealing within the AOI [27]–[30], [33]. It ranges between 0 and 1. UD increases with higher values of ISA.
- *BA* describes the arrangement and compactness of buildings within the AOI. For the calculation of BA, the median building distances as well as the median iFAR values of all buildings within the AOI are used. BA is normalized between 0 and 1 to match its values to the range of other input parameters. UD increases with higher values of BA.

Finally, UD represents an example for describing the intensity of urban development in its entirety, i.e., with regard to horizontal and vertical settlement characteristics. It is obtained by linking/integrating the above selected indicators as depicted in Fig. 4. The index is designed in a way that the individual and unique contributions coming from its inputs are mutually reinforced. That is why UD is formulated as the difference between two terms. The left term of the expression is proportional to UD and increases if BA and/or ISA increase, whereas the right term of the expression is inversely proportional to UD and increases if VF and/or iFAR increase. Given the dynamic range of its input parameters, UD ranges between −2 and +2 (from low to high intensity of urban development).

B. Results and Discussion

The resulting LC map is shown in Fig. 5. An overall area of about 30 km^2 has been classified. Since the study area is close to downtown San Francisco, the largest areal coverage is observed for sealed surfaces (43.2%) and buildings (20.6%). Together with the small coverage of the vegetation classes (7.9%), this is a first indicator of the high overall degree of UD found in the area. The user's and producer's accuracies of

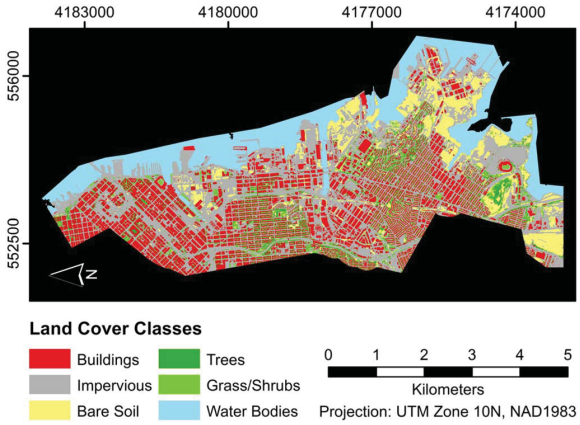

Fig. 5. Land cover map of the study area in San Francisco.

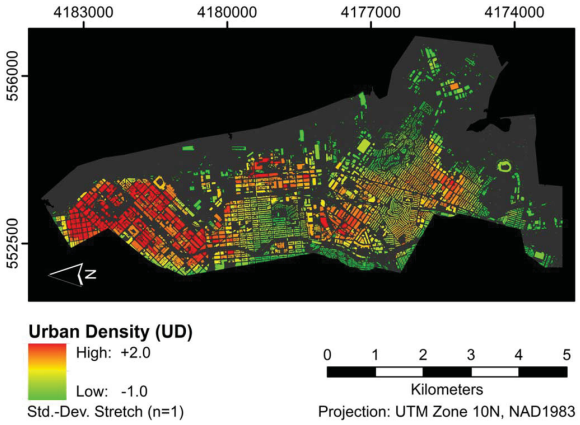

Fig. 6. Urban density map of the study area in San Francisco.

the LC map are consistently above 80.0%, and in many cases even above 90.0%. Smaller errors of commission and omission mainly occur because of the rather simple classification rules applied to the image objects (see Fig. 3). Examples are the misclassification of very high bridges as buildings (instead of impervious) or the confusion between bare soil areas and sealed surfaces [27], [28], [65]–[69]. Apart from these classification errors, the overall accuracy of the LC map is 88.0% and the kappa coefficient amounts to 0.86.

The UD map derived for the study area is shown in Fig. 6. More than 5,000 buildings have been attributed with UD values. While high UD values are indicated by red color, medium, moderate and low UD values are expressed by orange, yellow and green tones, respectively. The AOI used for the calculation of UD corresponds to a radius of 250 m around the centroid of each building object. To compute the area of individual floors of a single building (i.e., to calculate iFAR), a mean floor height of 2.8 m is assumed [25]. The largest patch featuring high to medium UD values (up to +1.9) is located in the north of the scene. Three smaller UD hot spots are distributed across the rest of the area. Moderate to low UD values (as low as −1.0) are found in the western, southern and south-eastern regions of the map. In the north, the high degree of horizontal and vertical development (ISA and iFAR) paired with the large number of buildings (BA) and the small urban green area ratio (VF) lead to the largest UD values for the entire scene, whereas these conditions are inverted for the western, southern and south-eastern regions of the map leading to the smallest UD values.

To further investigate the validity of the UD map, UD box plots for and locations of six selected land use (LU) types [70] are presented in Fig. 7. Since the radius of the AOI used is 250 m, LU polygons that are closer than 250 m to the edge of the study area are excluded from the analysis to obtain error-free UD statistics. A comparison of the median values (red dashes) for each LU class suggests that UD is able to consistently reproduce the increasing degree of urban development that can be expected in dependence of the LU type considered. While the median UD is low for the residential classes (RM, RH), UD steadily rises with actual settlement density in industrial areas (PDR) until it reaches its peak for the downtown classes in the north of the scene (DR, SM, DC). Besides these trends of urban densification, Fig. 7 also shows that UD values are generally high (between 0.2 and 1.9) for all LU classes and no negative values occur at all. This is in good agreement with the fact that the study area covers a central part of San Francisco. In conclusion, these findings underline the validity and suitability of the proposed UD metric as a useful measure to assess density patterns in urban environments. To increase the transparency of this contribution to the Data Fusion Contest, a dedicated geoportal was set up that visualizes all input data, final results, by-products, as well as additional information layers [71].

III. Combination of LiDAR and SAR Data With Simulation Techniques for Image Interpretation and Change Detection

The visual interpretation of SAR images is difficult due to distortion effects related to the SAR imaging concept, whereas the detection of changes may be hampered by missing pre-event SAR data, different SAR acquisition configurations (especially changes of the incidence angle), and revisit time related to subsequent SAR acquisitions.

For SAR image interpretation, raw data simulators [72] and imaging simulators [73]–[76] have been developed. Raw data simulators focus on radiometric correctness and consider dielectric properties and roughness parameters of building materials for the radiometric interpretation [77]. SAR imaging simulators concentrate primarily on geometric correctness when using detailed building CAD-models with simplified surface material information as input. A detailed overview of different concepts for SAR simulation is given in [78]. So far, none of the simulators reported in the literature enables to provide geocoded simulated image for direct comparison with real SAR data. First attempts in the application of simulation techniques for damage assessment using high resolution SAR data are presented in [79] and are based on building parameters extracted manually from optical images. So far, LiDAR data have not been included in SAR simulation applications in a practicable and productive way.

The use of multi-temporal medium-high spatial resolution SAR data has been discussed in [80], [81] for unsupervised change detection methods. For very high spatial resolution SAR

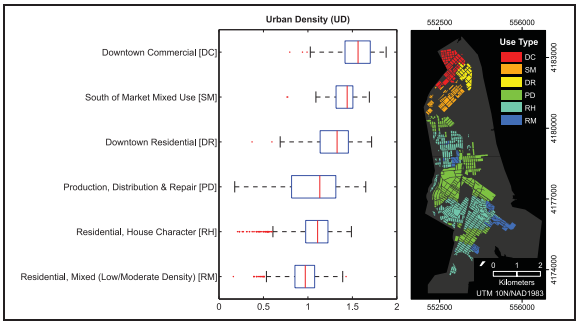

Fig. 7. Urban density box plots for the six selected land use types [70].

images, e.g., TerraSAR-X or COSMO-SkyMed, feature based change detection methods have been proposed in [82], [83]. One condition of all these multi-temporal analysis is that the images should be acquired with the same viewing configuration, in order to avoid high rate of false alarms in the final change detection result.

A. Proposed Method

This section provides the details in three major steps: (*i*) interpret TerraSAR-X images of a dense urban area, (*ii*) detect changes between LiDAR data and TerraSAR-X data, and (*iii*) support an object-based multi-temporal SAR change analysis focusing on façade regularities:

1) Automatic Interpretation of SAR Images Based on Simulation Techniques: The TerraSAR-X product is first projected to a plane with constant height (frame mean height) on the WGS84 ellipsoid. The LiDAR image is converted to a DSM in the WGS-84 coordinate system with ellipsoidal heights. Finally, a DEM and an nDSM are generated from the DSM using the method described in [84]. Successfully, the SAR simulator RaySAR [85] is used to generate a simulated SAR image of the LiDAR DSM. Thereafter, the geoinformation of the DSM as well as the orbit and projection parameters of the real SAR image are used to geocode the simulated image. The generation and geocoding of the simulated SAR image using a DSM is detailed in [86]. Finally, the simulated signals of reflection levels 1 and 2 are combined into one image or are assigned to separate image layers [85] for the DSM, DEM, and nDSM, respectively. The simulated images are: image *A* (double reflections from DSM) and images *B*, *C*, and *D* (sum of all reflection levels for DSM, DEM and nDSM, respectively). Successively, the images are combined to generate five image layers:

- double reflection ($A > 0$)
- layover ($D > 0$)
- shadow ($B = 0$ & $C > 0$)
- background ($B = 0$ & $C = 0$)
- ground ($B > 0$ & $A = 0$ & $D = 0$)

The layer generation flow-chart is illustrated in Fig. 8.

2) Change Detection Between LiDAR and SAR Data: as the simulated images and the real SAR images are geocoded, they can be directly compared. As the focus of the simulation algorithm is on geometrical correctness, no comparison is carried out

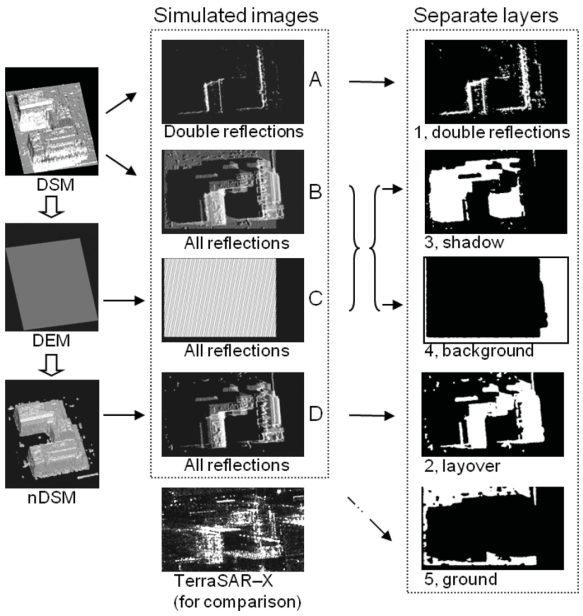

Fig. 8. Simulation of separate layers: from the elevation models (left), four simulated images are generated (center); the combination of them yields five image layers (right).

between simulated and real intensities. Instead, the geometric information provided by the simulated images is used, especially in the shadow and ground layers. If there is no change within the scene between the LiDAR and SAR acquisition dates, SAR image pixels in the shadow and ground layers should be mainly characterized by low intensity. Following this assumption, a pixel based algorithm is performed to detect positive changes of large extent in shadow and ground layers. To this end, an intensity threshold is determined by a statistical analysis of the SAR image for each layer. All pixels in the corresponding layer in the SAR image with intensities higher than the threshold value are considered as candidates of positive changes and will form regions in terms of changes of significant extent (see [87] for a detailed description).

3) Object Based Change Detection Between Two SAR Images With Support of LiDAR Data Simulation: In addition to the pixel based change detection between LiDAR and SAR data, simulation techniques that enable an object based change detection between two SAR images are also investigated.

For the extraction and simulation of single buildings and single walls, isolated parts in the nDSM exceeding a size threshold of 1500 pixels are selected as building of interest (see example in Fig. 9(a)). Similarly to the procedure described previously, three image layers can be generated for each building: layover, double bounce and shadow. As the analysis aims at individual façades, every building model is decomposed into separate wall segments. First, gradient magnitude (Fig. 9(b)) and gradient direction (Fig. 9(c)) maps are calculated and are convolved with a median filter. Second, a height threshold value is calculated in the neighborhood of the pixel with the highest gradient magnitude, using the mean

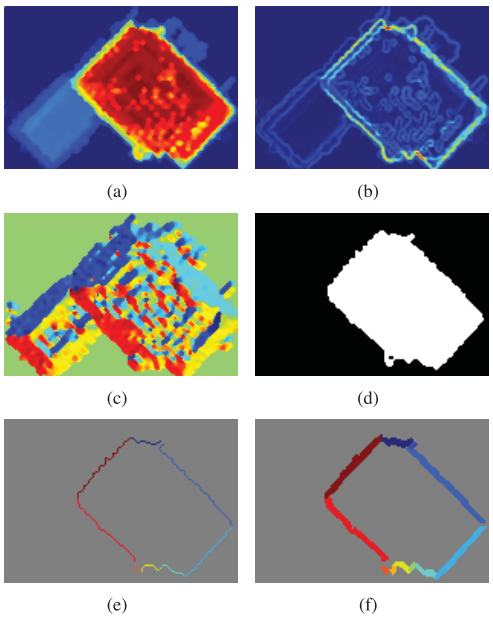

Fig. 9. Separation of building walls (DSM parts) for an individual building: (a) building extent in DSM, (b) gradient magnitude map, (c) gradient direction map, (d) building model after applying the height threshold, (e) separated building boundary segments, (f) extracted wall segments, different colors indicate different wall masks.

value of the maximal and minimal height. Third, after applying the height threshold (Fig. 9(d)), the building boundaries (with width of 1 pixel) are generated and separated according to the corresponding gradient direction values. Fourth, the separated boundary segments (Fig. 9(e)) are enlarged using the information of the neighborhood geometry and similar gradient direction, which yields separate wall masks (Fig. 9(f)). Finally, the simulation of the wall models provides the respective wall layover masks. A gradient direction difference is used as a threshold for separating the boundary in the third step. Low values lead to oversegmentation, for high values several building wall segments may be considered as one wall segment in the result. The suggested value is 30 degrees, which works for most of the rectangular buildings.

Regarding the façade characterization, SAR pixels located within the wall layover masks are extracted for identifying signature patterns. Dominant signatures in the layover area are likely to be related to façade structures, e.g., reflections at window corners [85]. Point signatures representing façades with regular structures tend to be distributed in range and wall direction, indicating the windows arrangement in vertical and horizontal direction, respectively. The analysis of the pattern topology may help convert pixel-based to object-based representations for identifying changes. Initial attempts in this direction are indicated as follows. First, the local maxima of the SAR amplitude image are extracted in the layover area (set of point signatures). Then, a weighted Hough transform, which emphasizes pixels identified as local maxima, is used to identify linear organized signatures (along the orientation direction of the façade and in range direction; see [88] for

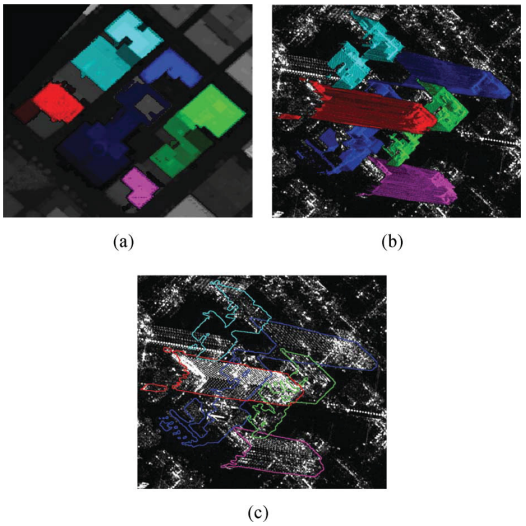

Fig. 10. Interpretation of SAR image in dense urban area: (a) individual building models; (b) simulated layover areas and (c) layover contours imposed on TerraSAR-X image. Different colors indicate different building models in the images.

further details). An object based representation of layover areas may be of great importance, because SAR images captured from different imaging geometries become comparable by analyzing differences of the pattern topology (for positive and negative changes).

B. Results and Discussion

In order to assess the functionality of the proposed approach, the SAR simulation is combined with the LiDAR data and two TerraSAR-X images on a dense area with tall buildings in the northern part of the scene for SAR image interpretation and façade pattern recognition, and on the harbor area for change detection between LiDAR and SAR data.

In the first experiment, 203 building models with more than 1500 pixels are extracted from the DSM. As an example, five building models are shown in Fig. 10(a). The contours of the corresponding simulated layover, overlapped on the geocoded TerraSAR-X image, are depicted in Fig. 10(c). Different colors indicate different building models. The red model is the same building model as shown in Fig. 9. Parts of its layover area are overlapped with signal responses from the green and blue buildings. It is clearly seen which layover parts and, hence, signature patterns can be assigned exclusively to the red building. This helps understand why the façade of this red building in the real SAR image has an abnormal grammar in the overlapped area (see detailed view in Fig. 13).

For the harbor area, the simulated image, the geocoded TerraSAR-X image, the separate layers, and the detected positive changes in the shadow and ground layers are shown in Fig. 11. For a better representation, a rectangular area (visualized by a yellow frame) is extracted and shown in Fig. 12(a)–(d). Compared visually to the given LiDAR data (Fig. 12(e)) and the WorldView-2 image (Fig. 12(f)), the detected positive change can be confirmed. Due to the speckle effect of the SAR

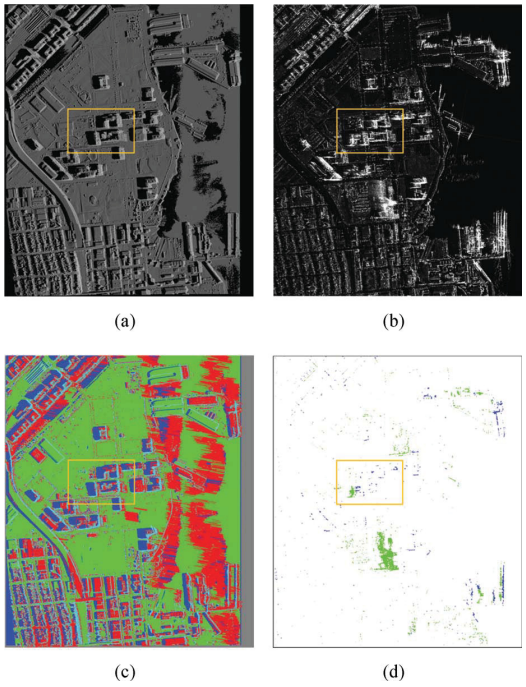

Fig. 11. Change detection between LiDAR and TerraSAR-X data: (a) geocoded simulated image from DSM, (b) geocoded TerraSAR-X image acquired on October 13, 2011, (c) separate layers (blue: shadow; green: ground; red: layover; cyan: double bounce; grey: background), (d) detected positive changes in shadow (blue) and ground (green) layer.

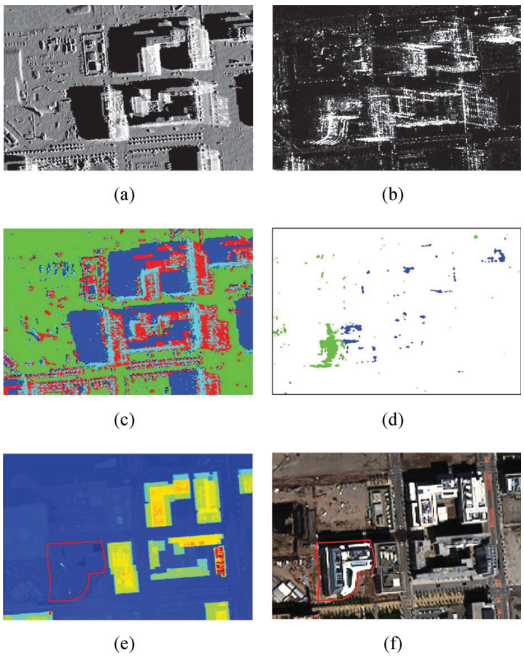

Fig. 12. Change detection between LiDAR and TerraSAR-X data (zoom in to rectangle marked area in Fig. 11), (a)–(d) images corresponding to those of Fig. 11, (e) LiDAR DSM with marked change, (f) WorldView-2 image showing a new building (marked in red).

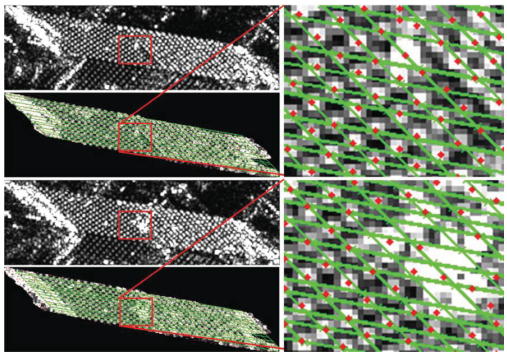

Fig. 13. Extracted signature pattern for the red building model in Fig. 10. Building layover in SAR image imposed with detected Hough lines. Red points: local intensity maxima. Acquisition dates: December 16, 2007 (upper two images), October 13, 2011 (lower two images).

sensor, which is not considered in the simulator, some small false alarms can be seen in the right upper corner.

As a change detection example, the red building model in Fig. 10 is chosen in order to analyze the appearance of point signatures. Among the 11 separated wall parts of the building model, two are chosen for façade pattern analysis according to their length and gradient direction (with respect to the SAR range direction). Fig. 13 shows the TerraSAR-X image and the imposed set of linearly organized signatures for the two image acquisition dates. Signature patterns extracted from layover areas provide the following information: the regularity of the pattern gives strong hints for the existence of buildings; distances between point signatures indicate distances between windows and floor heights; the number of floors and window columns can be counted in order to characterize the building topology. Although the signatures in the two TerraSAR-X images are not exactly the same, the topology of the pertinent patterns gives a strong hint that no significant changes are present.

IV. Radiosity Technique for Reflectance Retrieval in Complex Illumination Environments

Remote sensing exploitation using spectral sensors in the visible through shortwave infrared relies on the ability to determine the reflectance of surface materials. Atmospheric compensation methods calculate the solar illumination, both direct from the sun and indirect from scattered sunlight. However, many targets of interest are in complex illumination environments where the surface is in shadows and, even in sunlit areas, nearby objects can block some of the downwelling sky radiance. In addition, the nearby objects such as building walls or trees may reflect radiation, providing their own source of illumination onto the target of interest. Current atmospheric compensation algorithms do not account for these illumination conditions that are more complex than a clear, hemispherical sky overhead for an object parallel to flat ground.

Many spectral processing techniques require an accurate retrieval of the surface reflectance from the measured radiance data. Some material detection techniques, in particular, compare

the retrieved reflectance to reflectance spectra from a spectral library [89]. To obtain a better estimate of surface reflectance, more accurate estimates of the illumination on the surface is needed. In addition, retrieval of material reflectance in shadow regions depends solely on the indirect illumination from downwelling scattered radiance and reflections from nearby surfaces.

This section presents a radiosity-based method to improve reflectance retrieval under complex illumination conditions by taking into account surface tilt, solar obscuration, and surface to surface interaction within the scene. The background and implementation of the radiosity method to solve for surface reflectivity is discussed in [90]. Improvements to reflectance retrieval are shown through application of the radiosity technique to multi-spectral WorldView-2 data.

A. Proposed Method

Radiosity was first used to analyze heat transfer between surfaces [91]. While computationally intensive, the technique provided methods for computing radiant interchange between surfaces for many different applications. Computer graphics began to use radiosity as a way to calculate realistic looking scenes under specified lighting conditions. As computational capabilities have increased, radiosity has become a more capable method to create simulated scenes that are physically accurate.

The radiosity approach uses the energy balance of the surfaces in a scene to create a system of equations to solve for illumination [92]. Radiosity, which is equivalent to the radiant exitance, is related to the radiance of a surface by:

$$B(x) = \int_{\Omega} L(x, \theta, \phi) \cos\theta \, \partial\omega \tag{1}$$

where $L(x, \theta, \phi)$ is the outgoing radiance at a point defined by the location x in the direction defined by θ and ϕ. For ideal diffuse surfaces, the outgoing radiance is a function of the position and the radiosity can be simplified to:

$$B(x) = \pi L(x) \tag{2}$$

The general global illumination equation describes the energy equilibrium for a set of radiating surfaces where the radiance leaving point x in direction (θ_0, ϕ_0) is given by:

$$L(x, \theta, \phi) = L_e(x, \theta_0, \phi_0) + \int_{\Omega} \rho_{\mathrm{bd}}(x, \theta_0, \phi_0, \theta, \phi) + L_i(x, \theta, \phi) \cos\theta \, \partial\omega \tag{3}$$

where the first term, L_e, is the emitted radiance in the direction (θ_0, ϕ_0) at point x, and the integral term is the reflected radiance due to light incident at x from all other directions in the hemisphere Ω with the bidirectional reflectance distribution function of the surface at point x, y given by ρ_{bd}.

Using the definition of radiosity and discretizing the problem leads to the discrete radiosity equation [93]–[95] which is:

$$B_i = E_i + \rho_i \cdot \sum_{j=1}^{N} F_{ji} B_j \tag{4}$$

where E_i is the emitted radiance for a small patch i (set to zero for visible through shortwave infrared wavelengths), ρ_i is the diffuse reflectance at patch i (unknown to be solved for), F_{ji} is the form factor giving the solid angle subtended by the patch j onto patch i (solved for using scene geometry), B_j is the radiosity of patch j (retrieved from sensor data), and N is the total number of surfaces in the scene (obtained during scene and sky facetization).

The discrete radiosity equation solves for radiosity given a surface's known reflectivity and illumination. The problem in remote sensing is to solve the inverse problem: given a scene with known radiosity of each surface, solve for the surface illumination to estimate reflectivity. This procedure is known as the inverse global illumination [91]. Equation (4) can be rearranged to solve for reflectivity. Setting the emitted radiance to zero, we obtain the radiosity equation for reflective surfaces:

$$\rho_i = \frac{B_i}{\sum_{j=1}^{N} F_{ji} B_j} \tag{5}$$

This is equivalent to the ratio of the outgoing radiance to the incoming radiance $(\varphi_{\mathrm{out}}/\varphi_{\mathrm{in}})$. To use the radiosity equation to estimate surface reflectance, a 3-dimensional model of the scene needs to be developed to determine which surfaces see each other and to calculate the form factors, F_{ji}. This is achieved by dividing the geometry into discrete facets including both the objects in the scene as well as the hemispherical skydome. The discrete facets in the 3-dimensional model are generated using both the geometry of the scene and the measured radiance to obtain surface facets with near uniform radiance. In addition, the geometric model can be used to determine which sections of the sky illuminate each facet through the form factor calculation. The illumination on each surface can be calculated using the radiosity equation taking into account the radiance from other surface and sky facets that are visible from that surface.

In this research, the process to determine the surface reflectance using radiosity combines processing the geometry data from LiDAR and the spectral data. Fig. 14 shows the process flow.

The first step in the processing chain is to estimate the surface-leaving radiance by removing the atmospheric effects on the collected imagery. During this step, the data is converted from at-sensor radiance to surface-leaving radiance, which equate to the B_i terms in the radiosity equation. For radiometrically calibrated spectral data, such as that from WorldView-2, atmospheric parameters are retrieved using the radiative transfer code MODTRAN [96]. During this step, path radiance is estimated and then subtracted from the sensor radiance. The remaining signal is radiance from the target itself that reaches the sensor. The sensor-to-ground transmission losses are accounted for by dividing the at sensor target radiance by a MODTRAN-derived transmission estimate to produce the signal that would be observed from placing the sensor at the ground, which equates to the surface leaving radiance.

During the atmospheric retrieval step, MODTRAN is also used to estimate downwelling radiance at various azimuth and elevation angles. This allows for an accurate representation of the directional spectral radiance contributions from the sky. Fig. 15 shows a true-color composite of an upward-looking fisheye view of the MODTRAN-created skydome radiance, generated using uniform sampling across the sky.

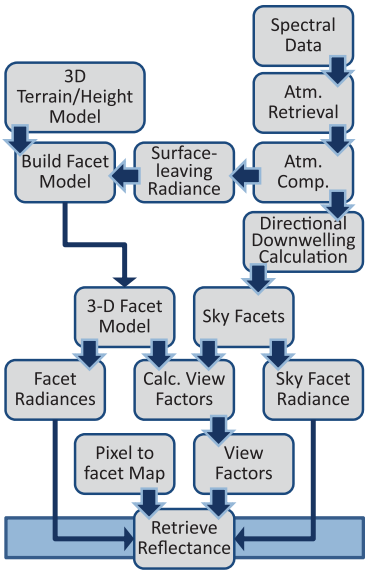

Fig. 14. The Radiosity reflectance retrieval workflow uses a series of operations to estimate reflectance using a 3-d spatial model and radiance data.

Fig. 15. True-color composite of an upward-looking fisheye view of the MODTRAN-created skydome radiance, generated using uniform sampling across the sky.

The directional sky data is interpolated to create a facetized skydome consisting of approximately 25,000 facets, which model changes in brightness across the skydome. The use of a facetized skydome with directional radiance contributions allows for more accurate illumination prediction in shadow, where the brightest portion of the sky (nearby the sun) is generally blocked by raised surface geometry in the scene and a Lambertian sky assumption would provide incorrect results. The facetized skydome is modeled at a sufficient distance such that, when traversing from one spatial location of a scene to another, the observer's perspective of the skydome does not change.

The next step in the processing chain is to facetize the scene into discrete patches that have uniform radiance and are on the same surface. An initial scene facetization is created using the set of *XYZ* coordinates from the LiDAR point cloud or other rasterized elevation data. This surface is registered with the radiance data, and then the facets are iteratively divided until each facet is radiometrically uniform across its surface. This division breaks the scene into facets that are sunlit or in shadow and minimizes any issues that are caused by nonuniform intensity across the surface as it interacts with other surfaces within the scene.

The pixel to facet map is generated by using the facetized elevation data and the registered ground-leaving radiance data. Then, radiosity values are assigned to each facet equal to the average surface-leaving radiance of pixels within that facet. Each facet is also tested to determine if it is shaded or in direct solar illumination. The sun is treated as a point source using the direct solar MODTRAN output term, retrieved during the initial atmospheric characterization step as the radiant intensity. The test examines whether the center (*x,y,z*) location of each facet either points away from the sun, or is obscured by other objects in the scene that block the line of sight between the facet's center and the solar location. If either test is true, that facet is flagged as being in shadow.

For facets not seen by the sensor, such as the sides of a building, radiosity is estimated using either the average scene radiance or separate averages from the visible sun-lit and shaded facets. Even though a surface may be hidden from the sensor, it may have a significant impact on the illumination of objects observed within the scene, such as a potential target of interest in shadow adjacent to a large building. Therefore, an accurate representation of the unseen surface's radiosity is important to estimate.

The last unknown in the radiosity equation is the form factor between scene facets and other scene/sky facets, F_{ji}. An OpenGL implementation of the hemi-cube algorithm [97] has been integrated into the MATLAB code to efficiently calculate the form factors between each facet to all the other facets.

The sensor data can then be converted to reflectance by dividing the retrieved ground-leaving radiance at the pixel level by the illumination estimate of the pixel's assigned facet. The proposed method is validated using scenes generated from DIRSIG [98].

B. Results and Discussion

The proposed technique is applied to the WorldView-2 image, as well as co-located LiDAR data on a 128 by 128 pixel subset that includes a large shadow area as shown in Fig. 16. The use of a subset of the full data reduced run-times and memory requirements.

The digital surface model (DSM) generated from the data orthorectified to a 0.5 m *x-y* grid is used to create the geometry model. Fig. 17 shows the DSM of the area processed.

MODTRAN and the WorldView-2 relative spectral response functions are used to calculate the transmission and path radiance for each band in order to convert the WorldView-2 data to surface-leaving radiance. Then, an in-scene correction is used to further refine the values. The in-scene techniques rely on the atmospheric effects' invariability between nearby pixels and the presence of two pixels of the same material in sunlight and shade. Within this step, the user manually selects two background pixels of the same apparent material, one in sun and the other in shadow. The path radiance and transmission estimates

Fig. 16. The image subset used for the calculations has a large shadow cast by the building in the middle of the image.

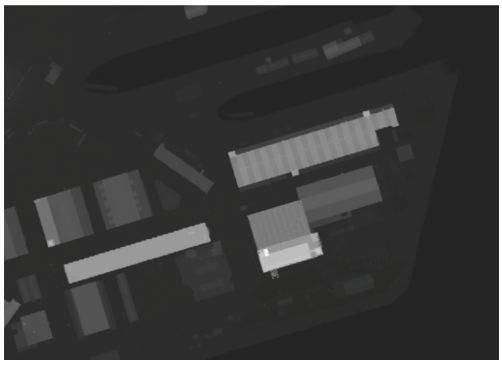

Fig. 17. A DSM model created from the LiDAR data provides the basis for the geometry model.

are modified until the radiosity retrieval for those two pixels results in the same reflectance being retrieved for both pixels. The fundamental basis of this approach is the fact that when the proper atmosphere and scene geometry is applied, the same reflectance should be obtained for a given material using the radiosity approach, regardless of whether it is sunlit or in shadow. Lambertian reflectance is assumed for all in-scene surfaces.

Once the data is converted to surface-leaving radiance, the radiosity technique is applied to the WorldView-2 subset selected for analysis. The facetization of the chip from the LiDAR data and surface-leaving radiance resulted in 3001 facets. Fig. 18 shows a wire-frame representation of the facets. A pixel to facet map is then created, which is used to assign radiosity values to the various scene surfaces, as well as determine the illumination on a per-pixel basis for the reflectance retrieval.

A reflectance retrieval using the radiosity equation is then performed. A true-color (RGB bands 5,3,2) composite of reflectance output obtained by the radiosity process (Fig. 19) shows the increased detail revealed in the shaded area. Relative spectral color and intensity of the road matches well between sunlit and shaded areas, but issues in reflectance retrieval persist at the shadow edges where pixels may be partially sunlit.

To further demonstrate the improvements, Figs. 20 and 21 show principal component (PC) transforms of the radiance data and the retrieved reflectance, respectively. The transform of the

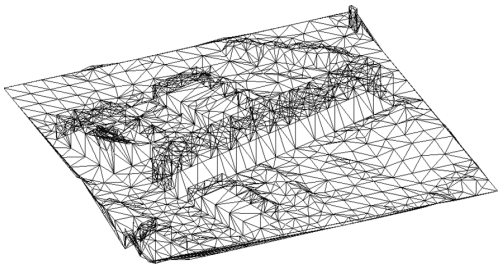

Fig. 18. The facetization process creates a new geometry model that accounts for surface orientation and the measured radiance differences.

Fig. 19. The image subset after applying the radiosity reflectance retrieval shows detail in the shaded region with structure similar to the adjacent sunlit region. Edge effects show up as dark pixels on the transitions between sunlit and shaded areas.

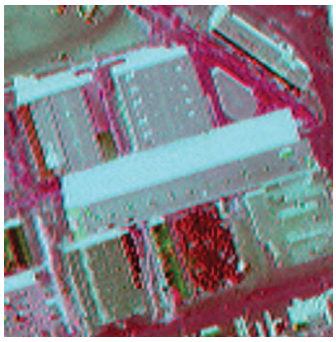

Fig. 20. A color composite from the first three principle components of the radiance transform shows the similar materials in the scene. The shaded region shows up as a different material than the surrounding surfaces.

radiance data shows little detail in the shaded region and appears as a different material class than the adjacent roads. After the radiosity reflectance retrieval, the PC transform shows the shaded region to more closely match the adjacent roads.

V. Conclusion

This paper summarized the outcome of the 2012 IEEE GRSS Data Fusion Contest, including the contributions of the three winning teams:

1) In Section II, a new metric to assess urban density that takes into account all three spatial dimensions of an urban area was proposed. Due to the 3-dimensional nature of human

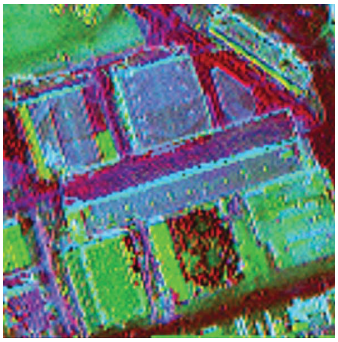

Fig. 21. A color composite from the first three principle components of the retrieved reflectance shows improved detail in the shaded region. The area now appears similar to the adjacent roads rather than a different material.

settlements, urban planning and decision making should be based on information sources that account for both the horizontal and vertical dimensions of a city to enable an integrated and more holistic assessment of the *builtscape* [21]. The derived UD map and statistics highlight the validity and suitability of the proposed metric as a useful measure to evaluate human settlement density and its distinct spatial patterns for different types of urban LU.

2) Section III illustrated a simulation based method for image interpretation and change detection, jointly using LiDAR and SAR data. To this end, the LiDAR data was decomposed into DSM, DEM, nDSM as well as individual building and wall models. Exploiting the simulated images of all these models, different layers (double reflections, layover, shadow, ground and background) are generated for the whole scene as well as for single buildings. Analyzing the TerraSAR-X image in the shadow and ground layer, positive changes were detected with respect to the LiDAR data. Analyzing building wall layover in TerraSAR-X images, signature patterns were identified, serving an object based description of façades. The results indicated that simulation techniques can support SAR image interpretation as well as change detection for local scenes and individual urban objects.
3) In Section IV, the radiosity technique was applied to retrieve reflectance for a subset of the WorldView-2 and LiDAR data. The results showed an improved capability to characterize shaded regions, demonstrating the utility of modeling illumination from nearby objects to improve the results for shaded regions.

As a final remark on the Contest, even though several different research topics were investigated by the various teams, none of the manuscripts exploited the three provided data sets in full synergy. In fact, the bulk of contributions either used multi-spectral and LiDAR or SAR and LiDAR data only. This may demonstrate the great difficulties encountered when fusing VHR multi-spectral and SAR data or fusing the three modalities together.

One possible explanation for this is that the information content in SAR data is typically characterized by three types of geometric effects, namely layover, shadow, and foreshortening [99]. These effects are more evident in VHR SAR imagery covering urban areas because human settlements are characterized by distinct and very individual 3-dimensional structures that comprise regularly and irregularly arranged LC objects of different shape, size and/or orientation [100]–[102]. Only when the viewing direction of the SAR and optical sensor is orthogonal [103], the fusion of these two data is possible and reasonable. However, this configuration is not the usual case. In contrast, the fusion of SAR and LiDAR does not suffer from such problems as the geometric projection is already considered in the SAR simulation procedure.

In the context of urban mapping with optical and LiDAR data, the additional information provided by VHR SAR systems (e.g., intensity, texture, coherence, etc.) can actually be of little help if geometric distortions predominate. This is because these effects hold the potential to hamper nearly every stage of the analysis task, including precise coregistration of the different data types, data fusion at different levels, and most importantly, feature extraction and classification.

It is also noteworthy that the fusion of all three data sources is application driven and may not be of interest for all possible studies. For instance, for the adjoint radiosity processing, SAR data was not considered as it does not add any useful information to improve surface reflectance retrieval.

Acknowledgment

The authors and IEEE GRSS DFTC would like to express their great appreciation to DigitalGlobe, Astrium Services, and USGS for providing the data sets used in this study. The DFTC is also particularly thankful to Mr. Ed Locher from DigitalGlobe, Dr. Oliver Lang and Dr. Parivash Lumsdon from Astrium Services, and Dr. Karl Heidemann from USGS, for their continuous support throughout the 2012 Data Fusion Contest.

References

[1] IEEE GRSS data fusion technical committee, 2012 [Online]. Available: http://www.grss-ieee.org/community/technical-committees/data-fusion/

[2] L. Alparone, L. Wald, J. Chanussot, C. Thomas, P. Gamba, and L. Bruce, "Comparison of pansharpening algorithms: Outcome of the 2006 GRS-S data-fusion contest," *IEEE Trans. Geosci. Remote Sens.*, vol. 45, no. 10, pp. 3012–3021, Oct. 2007.

[3] F. Pacifici, F. Del Frate, W. Emery, P. Gamba, and J. Chanussot, "Urban mapping using coarse SAR and optical data: Outcome of the 2007 GRSS data fusion contest," *IEEE Geosci. Remote Sens. Lett.*, vol. 5, no. 3, pp. 331–335, Jul. 2008.

[4] G. Licciardi, F. Pacifici, D. Tuia, S. Prasad, T. West, F. Giacco, C. Thiel, J. Inglada, E. Christophe, J. Chanussot, and P. Gamba, "Decision fusion for the classification of hyperspectral data: Outcome of the 2008 GRS-S data fusion contest," *IEEE Trans. Geosci. Remote Sens.*, vol. 47, no. 11, pp. 3857–3865, Nov. 2009.

[5] N. Longbotham, F. Pacifici, T. Glenn, A. Zare, M. Volpi, D. Tuia, E. Christophe, J. Michel, J. Inglada, J. Chanussot, and Q. Du, "Multi-modal change detection, application to the detection of flooded areas: Outcome of the 2009–2010 data fusion contest," *IEEE J. Sel. Topics Appl. Earth Observ. Remote Sens.*, vol. 5, no. 1, pp. 331–342, Feb. 2012.

[6] F. Pacifici and Q. Du, "Foreword to the special issue on optical multi-angular data exploitation and outcome of the 2011 GRSS data fusion contest," *IEEE J. Sel. Topics Appl. Earth Observ. Remote Sens.*, vol. 5, no. 1, pp. 3–7, Feb. 2012.

[7] J. Zhang, "Multi-source remote sensing fusion: status and trends," *Int. J. Image and Data Fusion*, vol. 1, no. 1, pp. 5–24, Mar. 2012.

[8] P. Hyde, R. Dubayah, W. Walker, J. B. Blair, M. Hofton, and C. Hunsaker, "Mapping forest structure for wildlife habitat analysis using multi-sensor (LiDAR, SAR/InSAR, ETM+, QuickBird) synergy," *Remote Sens. Environ.*, vol. 102, pp. 63–73, 2006.

[9] D. Goodenough, H. Chen, A. Dyk, G. Hobart, and A. Richardson, "Data fusion study between polarimetric SAR, hyperspectral and LiDAR data for forest information," in *Proc. IEEE Int. Geoscience and Remote Sensing Symp., IGARSS 2008*, Jul. 2008, vol. 2, pp. II-281–II-284.

[10] M. Benson, L. Pierce, K. Bergen, K. Sarabandi, K. Zhang, and C. Ryan, "Extrapolation of LiDAR for forest structure estimation using SAR, InSAR, and optical data," in *Proc. IEEE Int. Geoscience and Remote Sensing Symp., IGARSS 2010*, Jul. 2010, pp. 1633–1636.

[11] J. M. Kellndorfer, W. S. Walker, E. LaPoint, K. Kirsch, J. Bishop, and G. Fiske, "Statistical fusion of LiDAR, InSAR, and optical remote sensing data for forest stand height characterization: A regional-scale method based on LVIS, SRTM, Landsat ETM plus, and ancillary data sets," *J. Geophysical Research*, vol. 115, Jan. 2010.

[12] M. Benson, L. Pierce, K. Bergen, K. Sarabandi, K. Zhang, and C. Ryan, "Forest structure estimation using SAR, LiDAR, and optical data in the Canadian boreal forest," in *Proc. IEEE Int. Geoscience and Remote Sensing Symp., IGARSS 2011*, Jul. 2011, pp. 2609–2612.

[13] M. Lennon, N. Thomas, V. Mariette, S. Babichenko, and G. Mercier, "Oil slick detection and characterization by satellite and airborne sensors: Experimental results with SAR, hyperspectral and LiDAR data," in *Proc. IEEE Int. Geoscience and Remote Sensing Symp., IGARSS 2005*, Jul. 2005, vol. 1.

[14] M. Dalponte, L. Bruzzone, and D. Gianelle, "Fusion of hyperspectral and LiDAR remote sensing data for classification of complex forest areas," *IEEE Trans. Geosci. Remote Sens.*, vol. 46, no. 5, pp. 1416–1427, May 2008.

[15] T. Kurz, S. Buckley, J. Howell, and D. Schneider, "Close range hyperspectral and LiDAR data integration for geological outcrop analysis," in *1st Workshop Hyperspectral Image and Signal Processing: Evolution in Remote Sensing, WHISPERS'09*, Aug. 2009, pp. 1–4.

[16] K. Niemann, G. Frazer, R. Loos, and F. Visintini, "LiDAR-guided analysis of airborne hyperspectral data," in *1st Workshop Hyperspectral Image and Signal Processing: Evolution in Remote Sensing, WHISPERS'09*, Aug. 2009, pp. 1–4.

[17] M. Frank, Z. Pan, B. Raber, and C. Lenart, "Vegetation management of utility corridors using high-resolution hyperspectral imaging and LiDAR," in *2nd Workshop Hyperspectral Image and Signal Processing: Evolution in Remote Sensing (WHISPERS)*, Jun. 2010, pp. 1–4.

[18] A. Brook, E. Ben-Dor, and R. Richter, "Fusion of hyperspectral images and LiDAR data for civil engineering structure monitoring," in *2nd Workshop Hyperspectral Image and Signal Processing: Evolution in Remote Sensing (WHISPERS)*, Jun. 2010, pp. 1–5.

[19] C. Lenart, P. Burai, A. Smailbegovic, T. Biro, Z. Katona, and R. Andricevic, "Multi-sensor integration and mapping strategies for the detection and remediation of the red mud spill in Kolontar, Hungary: Estimating the thickness of the spill layer using hyperspectral imaging and LiDAR," in *3rd Workshop on Hyperspectral Image and Signal Processing: Evolution in Remote Sensing (WHISPERS)*, Jun. 2011, pp. 1–4.

[20] M. Shimoni, G. Tolt, C. Perneel, and J. Ahlberg, "Detection of vehicles in shadow areas using combined hyperspectral and LiDAR data," in *Proc. IEEE Int. Geoscience and Remote Sensing Symp., IGARSS 2011*, Jul. 2011, pp. 4427–4430.

[21] P. Gamba, F. Dell'Acqua, F. Cisotta, and G. Lisini, "High resolution InSAR "builtscape" improvement using LIDAR as ancillary data," in *Proc. IEEE Int. Geoscience and Remote Sensing Symp., IGARSS 2004*, Anchorage, AK, USA, Sep. 20–24, 2004, vol. 3, pp. 1808–1811.

[22] H. Taubenböck, M. Wegmann, A. Roth, H. Mehl, and S. Dech, "Urbanization in India—Spatiotemporal analysis using remote sensing data," *Computers, Environment and Urban Systems*, vol. 33, no. 3, pp. 179–188, May 2009.

[23] M. Pesaresi, M. Halkia, and G. Ouzounis, "Quantitative estimation of settlement density and limits based on textural measurements," in *Proc. Joint Urban Remote Sensing Event (JURSE)*, Apr. 2011, pp. 89–92.

[24] P. Tompalski and P. Wezyk, "LiDAR and VHRS data for assessing living quality in cities—An approach based on 3D indices," *ISPRS Int. Archives of the Photogrammetry, Remote Sensing and Spatial Information Sciences*, vol. XXXIX-B6, pp. 173–176, 2012.

[25] X.-Z. Pan, Q.-G. Zhao, J. Chen, Y. Liang, and B. Sun, "Analyzing the variation of building density using high spatial resolution satellite images: The example of Shanghai city," *Sensors*, vol. 8, no. 4, pp. 2541–2550, 2008.

[26] B. Yu, H. Liu, J. Wu, Y. Hu, and L. Zhang, "Automated derivation of urban building density information using airborne LiDAR data and object-based method," *Landscape and Urban Planning*, vol. 98, no. 3–4, pp. 210–219, Dec. 2010.

[27] T. Esch, V. Himmler, G. Schorcht, M. Thiel, T. Wehrmann, F. Bachofer, C. Conrad, M. Schmidt, and S. Dech, "Large-area assessment of impervious surface based on integrated analysis of single-date Landsat-7 images and geospatial vector data," *Remote Sens. Environ.*, vol. 113, no. 8, pp. 1678–1690, Aug. 2009.

[28] P. Leinenkugel, T. Esch, and M. Gähler, "Settlement detection and impervious surface estimation in the Mekong Delta using optical and SAR remote sensing data," *Remote Sens. Environ.*, vol. 115, no. 12, pp. 3007–3019, Dec. 2011.

[29] G. Xian and M. Crane, "An analysis of urban thermal characteristics and associated land cover in Tampa Bay and Las Vegas using Landsat satellite data," *Remote Sens. Environ.*, vol. 104, no. 2, pp. 147–156, Sept. 2006.

[30] F. Yuan and M. Bauer, "Comparison of impervious surface area and normalized difference vegetation index as indicators of surface urban heat island effects in Landsat imagery," *Remote Sens. Environ.*, vol. 106, no. 3, pp. 375–386, Feb. 2007.

[31] Q. Weng, "Remote sensing of impervious surfaces in the urban areas: Requirements, methods, and trends," *Remote Sens. Environ.*, vol. 117, pp. 34–49, Feb. 2012.

[32] D. Haase, "Effects of urbanisation on the water balance—A long-term trajectory," *Environmental Impact Assessment Review*, vol. 29, no. 4, pp. 211–219, Jul. 2009.

[33] K. Sawaya, L. Olmanson, N. Heinert, P. Brezonik, and M. Bauer, "Extending satellite remote sensing to local scales: Land and water resource monitoring using high-resolution imagery," *Remote Sens. Environ.*, vol. 88, no. 1–2, pp. 144–156, Nov. 2003.

[34] M. B. Pont and P. Haupt, , M. B. Pont and P. Haupt, Eds.*, Spacematrix: Space, Density and Urban Form*. Rotterdam, The Netherlands: NAi Publishers, 2010.

[35] E. Salomons and M. B. Pont, "Urban traffic noise and the relation to urban density, form, and traffic elasticity," *Landscape and Urban Planning*, vol. 108, no. 1, pp. 2–16, Oct. 2012.

[36] R. Gluch and K. Ridd, , T. Rashed and C. Jürgens, Eds., "The V-I-S model: Quantifying the urban environment," in *Remote Sensing of Urban and Suburban Areas*. Dordrecht, The Netherlands: Springer, 2010, pp. 85–116.

[37] S. Faryadi and S. Taheri, "Interconnections of urban green spaces and environmental quality of Tehran," *Int. J. Environmental Research*, vol. 3, no. 2, pp. 199–208, 2009.

[38] M. Hur, J. Nasar, and B. Chun, "Neighborhood satisfaction, physical and perceived naturalness and openness," *J. Environ. Psychol.*, vol. 30, no. 1, pp. 52–59, Mar. 2010.

[39] E. Leslie, T. Sugiyama, D. Ierodiaconou, and P. Kremer, "Perceived and objectively measured greenness of neighborhoods: Are they measuring the same thing," *Landscape and Urban Planning*, vol. 95, no. 1–2, pp. 28–33, Mar. 2010.

[40] J. Tilt, T. Unfried, and B. Roca, "Using objective and subjective measures of neighborhood greenness and accessible destinations for understanding walking trips and BMI in Seattle, Washington," *Amer. J. Health Promotion*, vol. 21, no. 4, pp. 371–379, 2007.

[41] E. Schöpfer, S. Lang, and T. Blaschke, "A Green index incorporating remote sensing and citizen's perception of green space," in *Proc. ISPRS Joint Conf. 3rd Int. Symp. Remote Sensing and Data Fusion Over Urban Areas (URBAN 2005) and the 5th Int. Symp. Remote Sensing of Urban Areas (URS 2005)*, M. Moeller and E. Wentz, Eds., Tempe, AZ, USA, Mar. 14–16, 2005, vol. 37, pp. 1–6, Part 5/W1.

[42] B. Ong, "Green plot ratio: An ecological measure for architecture and urban planning," *Landscape and Urban Planning*, vol. 63, no. 4, pp. 197–211, May 2003.

[43] C. Pohl and J. van Genderen, "Multisensor image fusion in remote sensing: Concepts, methods and applications," *Int. J. Remote Sens.*, vol. 19, no. 5, pp. 823–854, May 1998.

[44] R. Richter, D. Schläpfer, and A. Müller, "An automatic atmospheric correction algorithm for visible/NIR imagery," *Int. J. Remote Sens.*, vol. 27, no. 10, pp. 2077–2085, May 2006.

[45] U. Gangkofner, P. Pradhan, and D. Holcomb, "Optimizing the highpass filter addition technique for image fusion," *Photogramm. Eng. Remote Sens.*, vol. 74, no. 9, pp. 1107–1118, Sept. 2008.

[46] C. Tucker, "Red and photographic infrared linear combinations for monitoring vegetation," *Remote Sens. Environ.*, vol. 8, no. 2, pp. 127–150, May 1979.

[47] L. Zevenbergen and C. Thorne, "Quantitative analysis of land surface topography," *Earth Surface Processes and Landforms*, vol. 12, no. 1, pp. 12–56, Jan./Feb. 1987.

[48] G. Priestnall, J. Jafaar, and A. Duncan, "Extracting urban features from LiDAR digital surface models," *Computers, Environment and Urban Systems*, vol. 24, no. 2, pp. 65–78, Mar. 2000.

[49] U. Benz, P. Hofmann, G. Willhauck, I. Lingenfelder, and M. Heynen, "Multi-resolution, object-oriented fuzzy analysis of remote sensing data for GIS-ready information," *ISPRS J. Photogramm. Remote Sens.*, vol. 58, no. 3–4, pp. 239–258, Jan. 2004.

[50] T. Blaschke, S. Lang, and G. Hay, , T. Blaschke, S. Lang, and G. Hay, Eds., *Object-Based Image Analysis for Remote Sensing. Spatial Concepts for Knowledge-Driven Remote Sensing Applications*. Berlin, Germany: Springer, 2008.

[51] T. Blaschke, "Object-based image analysis for remote sensing," *ISPRS J. Photogramm. Remote Sens.*, vol. 65, no. 1, pp. 2–16, Jan. 2010.

[52] G. Hay and G. Castilla, , T. Blaschke, S. Lang, and G. Hay, Eds., "Geographic object-based image analysis (GEOBIA): A new name for a new discipline," in *Object-Based Image Analysis. Spatial Concepts for Knowledge-Driven Remote Sensing Applications*. Berlin, Germany: Springer, 2008, pp. 75–89.

[53] W. Zhou and A. Troy, "An object-oriented approach for analyzing and characterizing urban landscape at the parcel level," *Int. J. Remote Sens.*, vol. 29, no. 11, pp. 3119–3135, Jun. 2008.

[54] W. Zhou, G. Huang, A. Troy, and M. Cadenasso, "Object-based land cover classification of shaded areas in high spatial resolution imagery of urban areas: A comparison study," *Remote Sens. Environ.*, vol. 113, no. 8, pp. 1769–1777, Aug. 2009.

[55] M. Kim, M. Madden, and B. Xu, "GEOBIA vegetation mapping in Great Smoky Mountains National Park with spectral and non-spectral ancillary information," *Photogramm. Eng. Remote Sens.*, vol. 76, no. 2, pp. 137–149, Feb. 2010.

[56] B. Salehi, Y. Zhang, M. Zhong, and V. Dey, "Object-based classification of urban areas using VHR imagery and height points ancillary data," *Remote Sens.*, vol. 4, no. 8, pp. 2256–2276, Aug. 2012.

[57] C. Berger, M. Voltersen, I. Walde, S. Hese, and C. Schmullius, "Robust extraction of urban land cover information from HSR multi-spectral and LiDAR data," *IEEE J. Sel. Topics Appl. Earth Observ. Remote Sens.*, accepted for publication.

[58] *eCognition Developer 8.7.1. Reference Book*. Munich, Germany: Trimble Documentation, 2012.

[59] C. Burnett and T. Blaschke, "A multi-scale segmentation/object relationship modelling methodology for landscape analysis," *Ecological Modelling*, vol. 168, no. 3, pp. 233–249, Oct. 2003.

[60] B. Koch, M. Jochum, E. Ivitis, and M. Dees, "Pixelbasierte klassifizierung im Vergleich und zur Ergänzung zum objektbasierten Verfahren," *Photogrammetrie, Fernerkundung, Geoinformation*, vol. 3, pp. 195–204, 2003.

[61] M. Baatz, C. Hoffmann, and G. Willhauck, , T. Blaschke, S. Lang, and G. Hay, Eds., "Progressing from object-based to object-oriented image analysis," in *Object-Based Image Analysis. Spatial Concepts for Knowledge-Driven Remote Sensing Applications*. Berlin, Germany: Springer, 2008, pp. 29–42.

[62] J. Johnson, "Building footprints as of June 2011," 2012 [Online]. Available: https://data.sfgov.org/Facilities-and-Structures/Building-Footprints-Zipped-Shapefile-Format-/jezr-5bxm

[63] S. Stehman and R. Czaplewski, "Design and analysis for thematic map accuracy assessment: Fundamental principles," *Remote Sens. Environ.*, vol. 64, no. 3, pp. 331–344, Jun. 1998.

[64] J. Cohen, "A coefficient of agreement for nominal scales," *Educational and Psychological Measurement*, vol. 20, no. 1, pp. 37–46, Apr. 1960.

[65] M. Bauer, B. Loeffelholz, and B. Wilson, , Q. Weng, Ed., "Estimating and mapping impervious surface area by regression analysis of Landsat imagery," in *Remote Sensing of Impervious Surfaces*. Boca Raton, FL, USA: CRC Press, 2008, pp. 3–19.

[66] A. Elmore and S. Guinn, "Synergistic use of Landsat multispectral scanner with GIRAS land-cover data to retrieve impervious surface area for the Potomac River Basin in 1975," *Remote Sens. Environ.*, vol. 114, no. 10, pp. 2384–2391, Oct. 2010.

[67] L. Luo and G. Mountrakis, "Integrating intermediate inputs from partially classified images within a hybrid classification framework: An impervious surface estimation example," *Remote Sens. Environ.*, vol. 114, no. 6, pp. 1220–1229, Jun. 2010.

[68] Q. Weng, , Q. Weng, Ed., "Remote sensing of impervious surfaces," in *Remote Sensing of Impervious Surfaces*. Boca Raton, FL, USA: CRC Press, 2008, pp. XV–XXVI.

[69] L. Yang, C. Huang, C. Homer, B. Wylie, and M. Coan, "An approach for mapping large-area impervious surfaces: Synergistic use of Landsat-7 ETM+ and high spatial resolution imagery," *Can. J. Remote Sens.*, vol. 29, no. 2, pp. 230–240, Apr. 2003.

[70] M. Wynne, "Zoning use districts," 2012 [Online]. Available: https://data.sfgov.org/Geography/Zoning-Districts/mici-sct2

[71] J. Eberle and C. Berger, "Urban density (UD) mapping results for the city of San Francisco," 2012 [Online]. Available: http://www.sf.maps.essi-blog.org

[72] G. Franceschetti, A. Iodice, D. Riccio, and G. Ruello, "SAR raw signal simulation for urban structures," *IEEE Trans. Geosci. Remote Sens.*, vol. 41, no. 9, pp. 1986–1995, Sep. 2003.

[73] S. Auer, S. Hinz, and R. Bamler, "Ray-tracing simulation techniques for understanding high-resolution SAR images," *IEEE Trans. Geosci. Remote Sens.*, vol. 48, no. 3, pp. 1445–1456, Mar. 2010.

[74] T. Balz and U. Stilla, "Hybrid GPU-based single-and double-bounce SAR simulation," *IEEE Trans. Geosci. Remote Sens.*, vol. 47, no. 10, pp. 3519–3529, Oct. 2009.

[75] D. Brunner, G. Lemoine, H. Greidanus, and L. Bruzzone, "Radar imaging simulation for urban structures," *IEEE Geosci. Remote Sens. Lett.*, vol. 8, no. 1, pp. 68–72, Jan. 2011.

[76] H. Hammer and K. Schulz, "SAR-simulation of large urban scenes using an extended ray tracing approach," in *2011 Joint Urban Remote Sensing Event (JURSE)*, Apr. 2011, pp. 289–292.

[77] R. Guida, A. Iodice, D. Riccio, and U. Stilla, "Model-based interpretation of high-resolution SAR images of buildings," *IEEE J. Sel. Topics Appl. Earth Observ. Remote Sens.*, vol. 1, no. 2, pp. 107–119, Jun. 2008.

[78] T. Balz, , U. Soergel, Ed., "SAR simulation of urban areas: Techniques and applications," in *Radar Remote Sensing of Urban Areas*, ser. Remote Sensing and Digital Image Processing. Heidelberg, Germany: Springer, 2010, pp. 215–231.

[79] D. Brunner, G. Lemoine, and L. Bruzzone, "Earthquake damage assessment of buildings using VHR optical and SAR imagery," *IEEE Trans. Geosci. Remote Sens.*, vol. 48, no. 5, pp. 2403–2420, May 2010.

[80] F. Bovolo and L. Bruzzone, "A detail-preserving scale-driven approach to change detection in multitemporal SAR images," *IEEE Trans. Geosci. Remote Sens.*, vol. 43, no. 12, pp. 2963–2972, Dec. 2005.

[81] F. Bovolo and L. Bruzzone, "A split-based approach to unsupervised change detection in large-size multitemporal images: Application to tsunami-damage assessment," *IEEE Trans. Geosci. Remote Sens.*, vol. 45, no. 6, pp. 1658–1670, Jun. 2007.

[82] A. Schmitt, B. Wessel, and A. Roth, "Curvelet approach for SAR image denoising, structure enhancement, and change detection," in *Proc. CMRT09*, Sep. 2009, vol. 38, pp. 151–156.

[83] F. Bovolo, C. Martin, and L. Bruzzone, "A novel hierarchical approach to change detection with very high resolution SAR images for surveillance applications," in *Proc. IEEE Int. Geoscience and Remote Sensing Symp., IGARSS 2012*, Jul. 2012.

[84] H. Arefi, P. d'Angelo, H. Mayer, and P. Reinartz, "Iterative approach for efficient digital terrain model production from CARTOSAT-1 stereo images," *J. Appl. Remote Sens.*, vol. 5, no. 1, Jun. 2001.

[85] S. Auer, "3D Synthetic Aperture Radar Simulation for Interpreting Complex Urban Reflection Scenarios," Ph.D. dissertation, Technische Universität München, Munich, Germany, 2011.

[86] J. Tao, G. Palubinskas, P. Reinartz, and S. Auer, "Interpretation of SAR images in urban areas using simulated optical and radar images," in *2011 Joint Urban Remote Sensing Event (JURSE)*, Apr. 2011, pp. 41–44.

[87] J. Tao, S. Auer, and P. Reinartz, "Detecting changes between a DSM and a high resolution SAR image with the support of simulation based separation of urban scenes," in *Proc. 9th Eur. Conf. Synthetic Aperture Radar, EUSAR 2012*, Apr. 2012, pp. 95–98.

[88] S. Auer, C. Gisinger, and R. Bamler, "Characterization of SAR image patterns pertinent to individual façades," in *Proc. IEEE Int. Geoscience and Remote Sensing Symp., IGARSS 2012*, Jul. 2012.

[89] D. Manolakis, D. Marden, and G. Shaw, "Hyperspectral image processing for automatic target detection applications," *Lincoln Lab. J.*, vol. 14, no. 1, pp. 79–114, 2003.

[90] C. Borel, K. Ewald, M. Manzardo, C. Wamsley, and J. Jacobson, "Adjoint radiosity based algorithms for retrieving target reflectances in urban area shadows," in *Proc. 6th EARSeL Imaging Spectroscopy SIG Workshop*, Mar. 2009, pp. 16–19.

[91] M. F. Cohen and J. R. Wallace, *Radiosity and Realisitc Image Synthesis*. New York: Academic Press Professional, 2003.
[92] F. X. Sillion and C. Puech, *Radiosity and Global Illumination*. San Diego, CA: Morgan Kaufmann, 1994.
[93] C. M. Goral, K. E. Torrance, D. P. Greenberg, Greenberg, and B. Battaile, "Modeling the interaction of light between diffuse surfaces," *Computer Graphics*, vol. 18, no. 3, pp. 215–224, 1999.
[94] Y. Yu, P. Debevec, J. Malik, and T. Hawkins, "Inverse global illumination: Recovering reflectance models of real scenes from photographs," in *Proc. 26th Annu. Conf. Computer Graphics and Interactive Techniques, SIGGRAPH'99*, 1999, pp. 215–224, ACM Press/Addison-Wesley Publishing Co..
[95] S. N. Pattanaik and S. P. Mudur, "The potential equation and importance in illumination computations," *Computer Graphics*, vol. 12, pp. 131–136, 1993.
[96] A. Berk, L. W. Bernstein, and D. C. Robertson, "Modtran: A Moderate Resolution Model for Lowtran7," Air Force Geophysical Laboratory, Hanscom Air Force Base, MA, Tech. Rep. aFGL-TR-83-0187, 1983.
[97] M. Cohen and D. Greenberg, "The hemi-cube: A radiosity solution for complex environments," *Computer Graphics*, vol. 19, no. 3, pp. 31–40, 1985.
[98] J. R. Schott, S. D. Brown, R. V. Raqueno, H. N. Gross, and G. Robinson, "An advanced synthetic image generation model and its application to multi/hyperspectral algorithm development," *Can. J. Remote Sens.*, vol. 25, no. 2, pp. 99–111, 1999.
[99] R. Raney, , F. Henderson and A. Lewis, Eds., "Radar fundamentals: Technical perspective," in *Principles and Applications of Imaging Radar. Manual of Remote Sensing*, 3rd ed. New York, NY, USA: Wiley, 1998, vol. 2, pp. 9–130.
[100] Y. Dong, B. Forster, and C. Ticehurst, "Radar backscatter analysis for urban environments," *Int. J. Remote Sens.*, vol. 18, no. 6, pp. 1351–1364, 1997.
[101] A. Brenner and L. Roessing, "Radar imaging of urban areas by means of very high-resolution SAR and interferometric SAR," *IEEE Trans. Geosci. Remote Sens.*, vol. 46, no. 10, pp. 2971–2982, Oct. 2008.
[102] *Radar Remote Sensing of Urban Areas*, U. Soergel, Ed. Heidelberg, Germany: Springer, 2010, pp. 277–1.
[103] G. Palubinskas, P. Reinartz, and R. Bamler, "Image acquisition geometry analysis for the fusion of optical and radar remote sensing data," *Int. J. Image and Data Fusion*, vol. 1, no. 3, pp. 271–282, 2010.

4.3 Automated derivation of UST maps

This section is based on the manuscript entitled
"Object-based land cover mapping and comprehensive feature calculation for an automated derivation of urban structure types at block level".

The manuscript was authored by
Voltersen M, Berger C, Hese S & Schmullius C (2014)

and published in
Remote Sens Environ 154: 192–201;
doi: 10.1016/j.rse.2014.08.024.

Remote Sensing of Environment 154 (2014) 192–201

Contents lists available at ScienceDirect

Remote Sensing of Environment

journal homepage: www.elsevier.com/locate/rse

Object-based land cover mapping and comprehensive feature calculation for an automated derivation of urban structure types at block level

Michael Voltersen *, Christian Berger, Sören Hese, Christiane Schmullius

Department of Earth Observation, Institute of Geography, Friedrich-Schiller-University Jena, Loebdergraben 32, 07743 Jena, Germany

ARTICLE INFO

Article history:
Received 6 February 2014
Received in revised form 18 August 2014
Accepted 19 August 2014
Available online xxxx

Keywords:
Urban areas
Object-based image analysis
Airborne
Land cover mapping
Urban structure types

ABSTRACT

Cities have evolved under manifold geographical, economical, historical, and cultural criteria, resulting in various sizes and shapes. Each city exhibits individual features and unique characteristics, despite that structural similarities appear. The separation into individual patterns, commonly named urban structure types (USTs), supports the characterization of physical, functional, and energetic factors of settlement structures, enabling associated environmental and socio-economic investigations as well as the comparison between the patterns of different cities. This study presents an automated approach for the classification of USTs based on remote sensing data in order to analyze the links between settlement structures and environmental issues, such as air pollution or urban heat islands, in a later stage of the project. Initially, an object-based classification routine is implemented to identify the land cover for the city of Berlin, utilizing spatially very high resolution aerial images and object height information. UST classes are defined based on the occurrence within the study area and are delimited by block boundaries. Afterwards, indicators for the derivation of USTs are generated based on the previously derived land cover information and the most valuable features are selected with the help of Random Forests. Finally, structural units are classified, involving common and new land cover based parameters. The focus is on the generation of an automated and transferable routine for a comprehensive UST classification covering the entire city. Comparing the results with reference data, good classification accuracies for both land cover and USTs indicate the suitability of the proposed method.

1. Introduction

Between one-third and one-half of the land surface has already been affected by humans (Vitousek, Mooney, Lubchenco, & Melillo, 1997). Hence, various changes in the ecosystem, e.g., modified energy exchange, altered hydrological regime, and increasing urban heat island (UHI) effect occur by replacing natural surface cover with man-made structures (Bridgman, Warner, & Dodson, 1995). Decision-makers and city planners need efficient methods for large-scale monitoring of urban areas in order to achieve sustainable urban growth. Consequently, it is important to understand the links between settlement structures and socio-economic as well as environmental issues (Pauleit & Duhme, 2000). The basis for this comprehension can be established by dividing cities into a variety of urban patterns, commonly named urban morphology types (UMT) (Gill et al., 2008), urban structural units (USU) (Osmond, 2011; Pauleit & Duhme, 1998), or urban structure types (UST) (Banzhaf & Höfer, 2008; Heiden et al., 2012; Wurm, Taubenböck & Dech, 2010). USTs describe the composition of a city with all its artificial and natural surfaces based on the assumption that settlements consist of distinct spatial units with similar building structures, open spaces, and land use forms composing delimitable patterns (Pauleit & Burkhardt, 2004). As a consequence, environmentally relevant issues like stormwater management, landscape planning, and urban heat island mitigation can be addressed holistically, improving the quality of life of city residents by understanding the link between urban microclimate and city structures (Erell, Pearlmutter, & Williamson, 2010; Osmond, 2011). Soil sealing and its consequences for the environment are said to be almost irreversible (Blum, 2013); for that reason a well-conceived city management on the basis of USTs becomes an important tool for urban planners. While research has intensively focused on subdividing distinct urban classes such as infrastructure or building types, the UST approach presents a comprehensive, consistent, and transferable classification framework for the total area of cities (Osmond, 2011).

UST classification for large urban areas is dependent upon remote sensing data and methods. The use of images acquired by airborne and spaceborne sensors offers a high degree of objectivity, transferability, and automation. Up-to-date consistent and extensive information about urban land use structures are provided. A few studies have already addressed the UST classification from remotely sensed data, showing differences in many respects.

* Corresponding author. Tel.: +49 3641 94 89 69; fax: +49 3641 94 88 82.
E-mail addresses: michael.voltersen@uni-jena.de (M. Voltersen), christian.berger@uni-jena.de (C. Berger), soeren.hese@uni-jena.de (S. Hese), c.schmullius@uni-jena.de (C. Schmullius).

http://dx.doi.org/10.1016/j.rse.2014.08.024
0034-4257/

The classification depth varies between coarse class arrangements distinguishing only open spaces and three different intensities of built-up areas (Taubenböck, Esch, & Roth, 2006) and detailed class hierarchies of 15 or more classes (Banzhaf & Höfer, 2008; Gill et al., 2008; Hermosilla, Ruiz, Recio, & Balsa-Barreiro, 2012). Additionally, the boundaries delimiting homogeneous city blocks are either derived manually based on the evaluation of aerial photographs (Herold, Liu, & Clarke, 2003) or with the help of auxiliary data provided by municipalities or calculated from OpenStreetMap data (Bochow, Taubenböck, Segl, & Kaufmann, 2010). Likewise, the applied methods range from visual interpretation of aerial photographs (Gill et al., 2008) to the analysis of spatial metrics, image texture, and neighborhood graphs (Herold et al., 2003; Walde, Hese, Berger, & Schmullius, 2014). Related to that, the feature selection, a crucial step for a proper UST classification, exhibits major differences. On the one hand, features are selected based on the assumed characteristics of the previously defined typology of urban structures, underlying a subjective view (Banzhaf & Höfer, 2008; Lindner, Hese, Berger, & Schmullius, 2011; Wurm, Taubenböck, Roth & Dech, 2009). On the other hand, feature selection is performed utilizing statistical methods such as Random Forests or Sequential Forward Selection (Bochow et al., 2010; Walde et al., 2014). Furthermore, in most of the studies, the USTs of one city are analyzed whereas only some projects comprise a comparison of the transferability of the implemented methods to other region (Bochow et al., 2010; Puissant, Zhang, & Skupinski, 2012).

Examining the mentioned studies, some shortcomings become apparent. In many cases, the classification of city blocks is restricted to certain USTs, covering only parts of the city. As a consequence thereof, the classification depths prove to be insufficient. There is a lack of systematic extraction, calculation, and selection of suitable descriptive features for UST delineation. Descriptive features are often treated isolated, neglecting potential synergies of the combination of two or more parameters. In contrast, other studies need improvement regarding the achieved classification accuracies as well as strategies ensuring the transferability of the proposed methods in order to be qualified for operational applications. Considering the stated deficiencies, this study comprises an accurate object-based land cover classification, making use of multispectral data and height information, combined with an in-depth UST analysis. The detailed classification hierarchy contains several built-up classes as well as areas of natural surface cover, involving the entire area of the city. A comprehensive feature calculation of common parameters, landscape metrics, and rarely used features is performed. The most important features are selected knowledge-based and statistically with the help of Random Forests. Emphasis is put on an automated data processing in order to ensure the transferability of the methods, which will be tested for at least two other test sites in a further stage of the project. Finally, this study aims at the generation of highly accurate classification results compared to a reference map.

2. Materials

2.1. Study area

The city of Berlin is located in the north-east of Germany (52°31′ N, 13°24′ E). With more than 3.3 million inhabitants and an area of 891.7 km^2 it is the largest city and the capital of Germany (Destatis, 2013). Shaped by many historical events (e.g. industrialization, destruction during world war, separation into East and West Berlin) various structure types have evolved. Very densely developed areas can be found in the core area, featuring high amounts of impervious surface areas (ISA), whereas surrounding regions are characterized by large vegetation fractions. There is also an intensive variation of building types, even within the same block, and a great number of water bodies exist all over the city. The terrain features differences of 81 m in height.

2.2. Data basis

Multispectral raster data and height information were provided by DLR Berlin-Adlershof. The high spatial resolution airborne data was acquired by the UltraCamX sensor featuring 12 bit radiometric resolution with 1 m^2 pixel size. Four channels provide spectral characteristics in visible range and near infrared (Gruber, Ponticelli, Bernögger, & Leberl, 2008). Acquisition took place on September 23, 2010 during the morning hours. Thus, the small incidence angle of the sunlight causes major areas covered by shadows. Additionally, a digital surface model (DSM) computed by the stereoscopic interpretation of multiple overlapping UltraCamX scenes was also delivered by DLR Berlin-Adlershof, featuring the same high spatial resolution of 1 m pixel size.

Vector data was kindly provided by the Senate Department for Urban Development and the Environment Berlin (Senate Department for Urban Development & the Environment Berlin, 2010). Included block boundaries and information about manually derived urban structure types provide a basis for an automated UST delineation and serve as reference data for validation purposes.

3. Methods

The workflow of this study is subdivided into three parts: normalized digital surface model (nDSM) derivation, land cover mapping, and UST mapping. After the initial creation of an nDSM, a ruleset for land cover mapping is created and accuracy is assessed for each LC-class. Subsequently, land cover information is used to create descriptive features for all blocks within the study area. After designing a UST class hierarchy, a synergetic approach of knowledge-based and statistical feature selection is utilized in order to derive the defined urban structure types. Finally, an accuracy assessment of the generated UST map with the help of the reference dataset is connected.

3.1. nDSM derivation

Accurate land cover classification and UST mapping require area-wide height information. In order to generate object heights, an essential pre-processing step is the calculation of an nDSM. For this purpose, the Diff2Min approach has been developed using the Trimble eCognition software and its cognition network language (CNL) (Trimble, 2013). At first, a layer is created displaying the differences between the central pixel and the pixel with the lowest value of the DSM data within a moving window. A window size of 99 m edge length is chosen in order to take reference ground points of larger buildings or forested areas into account, but simultaneously preserving reasonable processing times. The resulting layer shows low values for every ground pixel and larger DSM-differences for elevated objects. A second layer is created containing only height information of the DSM for pixels with differences smaller than 1 m height in the first layer. This leads to a digital terrain model (DTM) with data gaps for elevated objects which are then filled by interpolation. Finally, after a slight smoothing of the DTM layer in order to remove edge effects, the nDSM is created by subtracting the values of the computed DTM from the given DSM. Accuracy of the generated nDSM is assessed for 250 randomly distributed reference points for elevated objects as well as ground pixels. A ground pixel is treated as correct if the nDSM value amounts to zero. The reference height of pixels of elevated objects is calculated by the difference between the measured DSM value of the respective pixel and adjacent ground pixels. Afterwards, deviations between heights of the reference points and the created nDSM are analyzed.

3.2. Land cover mapping

A detailed and accurate land cover mapping provides the basis for UST classifications. Errors in the derived land cover map are reflected in the accuracy of the USTs. The methodology presented in this paper

follows to a great extent the LC classification presented in Berger, Voltersen, Hese, Walde, and Schmullius (2013), which has proved to be robust and transferable. Six land cover classes are extracted utilizing multispectral data and nDSM: bare soil, buildings, grass/shrubs, impervious, trees, and water bodies. An object-based approach (Baatz & Schäpe, 1999; Blaschke, 2010; Schiewe, 2002) is chosen due to the known advantages concerning high spatial resolution land cover classification in contrast to pixel-based methods (Hay & Castilla, 2008; Lang, 2008; Tzotsos, Iosifidis, & Argialas, 2008) and an area of 18,000 × 18,000 pixels (324 km^2) is selected for classification. Initially, a normalization of the four multispectral input layers is performed. Furthermore, additional layers like the Normalized Difference Vegetation Index (NDVI) (Tucker, 1979), slope, brightness, and standard deviation of brightness within a moving window are calculated. Fig. 1 gives an overview of the LC classification scheme, which consciously avoids highly sophisticated analyses for the purpose of a quick and generic data processing. The image is processed using the very fast multi-threshold segmentation within eCognition, which simultaneously segments and classifies the image into elevated and non-elevated objects based on a fixed threshold of the nDSM values. Thereafter, elevated objects are segmented again using only the NDVI layer as input parameter. Tree seed-objects with high NDVI values are now assigned and grown into adjacent pixels of elevated objects with lower but still distinctive NDVI values. Hence, remaining unclassified elevated objects represent building segments. Subsequently, the segmentation of non-elevated objects is performed taking into account the four spectral bands as well as the brightness layer and the standard deviation of the brightness layer. The classification of ground objects follows a similar approach like the described methodology for elevated objects. First, the NDVI is used to separate seed-objects of the grass/shrubs class which are then grown into objects with slightly lower mean NDVI. Afterwards, remaining unclassified ground objects are allocated to water bodies, bare soil, and impervious depending on brightness, slope, NDVI, area, and the standard deviation of the brightness within a moving window. Completing the land cover classification, some obvious misclassifications are treated separately. For example, ships only surrounded by water and classified as buildings are assigned to the water class. Likewise, incorrect classified water bodies due to their similarity to shadowed areas are rectified considering differences in object area and their relative border to building or impervious. An accuracy assessment is performed applying a random stratified sampling routine and evaluating 100 pixels per class. Making use of an error matrix, errors of commission and omission, kappa coefficient and overall classification accuracy are calculated.

3.3. Urban structure type mapping

An essential task in urban structure type mapping is the definition of UST classes. As there are no compulsory and consistent urban structure types, the classification scheme depends on the study area and the objective of the respective analysis (Banzhaf & Höfer, 2008). Based on class hierarchies of several studies (Breuste, Wächter, & Bauer, 2001; Heiden et al., 2012; Pauleit & Duhme, 2000) and visual interpretation of the remote sensing data of the city of Berlin, a classification scheme is designed covering 15 USTs which can be summarized to six main classes. The defined USTs are shown in Fig. 2. Residential and office blocks are subdivided into seven classes depending on the dominating building type. Different combinations of development intensity and vegetation fraction are significant. Commercial and industrial areas are often characterized by different building types, ranging from small structures to huge industrial halls within one block, and exhibit only little or no vegetation. Unvegetated open spaces cover sealed areas like transport infrastructures, airports, parking lots, and town squares, but also areas of bare soil whereas the green spaces class comprises blocks with predominant recreational purposes and large fractions of vegetation. Additionally, classes relating to agricultural areas and water bodies complete the observed urban land uses. The level of detail of the presented UST class hierarchy is selected to cover the requirements of a holistic description of the city's structure but being transferable as well.

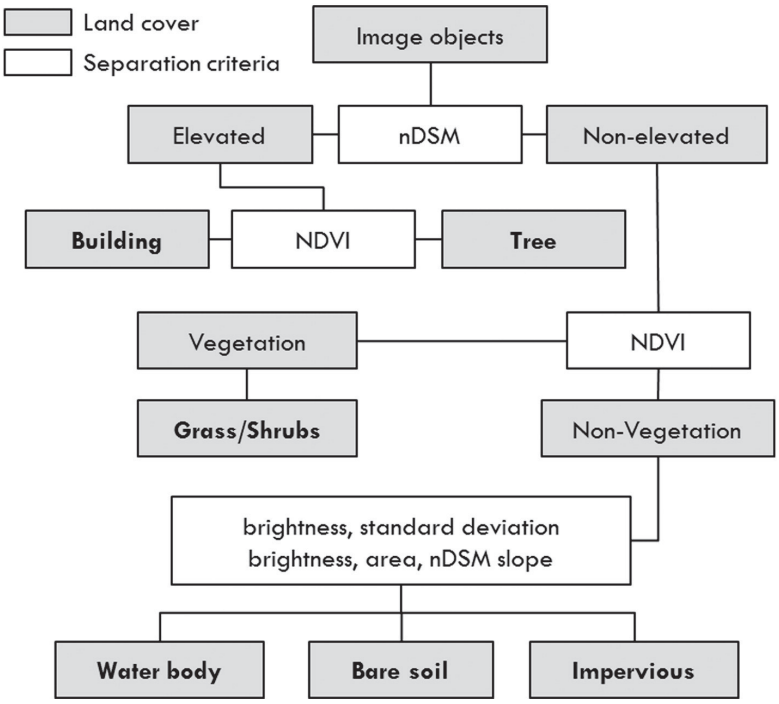

Fig. 1. Mapping scheme of the implemented land cover classification.

Fig. 2. The designed urban structure type class hierarchy.

USTs are derived in relation to a reference area which varies in size and shape with regard to the objective of the analysis. Some studies are based on a regular grid, others use block boundaries or administrative borders. Region-based strategies, which are commonly based on blocks or districts delineated by major road networks, are capable of representing the physical land cover structures. Furthermore, the morphological properties of regions (such as size, shape, and spatial relations) provide additional information for the designation of USTs (Barnsley & Barr, 2000). In this study, the block boundaries of the reference data provided by the Senate Department for Urban Development and the Environment Berlin are used for delimitation. Like the nDSM derivation and land cover mapping, UST mapping is performed utilizing the Trimble eCognition software. For this purpose, a subset of the study area has been selected covering 111.82 km^2. This is done in order to test the transferability of the developed methods for the entire image in a later stage of the project. A ruleset is developed looping through every block within the study area, applying a sequence of loops and if/else queries, making use of a number of object and scene variables for different levels and maps. More precisely, a unique object ID is allocated to every block. Thereafter, a region variable containing the coordinates of the particular block is used to create a second map, comprising the previously derived objects and land cover information only for the extent of this block. Descriptive parameters based on the land cover information are then calculated within the second map, thus the computing speed increases in contrast to computation on the entire image. The set of parameters includes building and vegetation features as well as landscape metrics (Herold, Scepan, & Clarke, 2002; McGarigal & Marks, 1995; Spellerberg & Fedor, 2003), 3D density metrics like urban density (UD) (Berger, Voltersen, Eckardt, et al., 2013) or urban vegetation index (UVI) (Tompalski & Wezyk, 2012) and additional block characteristics, shown in Table 1. Furthermore, mean, median, minimum, maximum, standard deviation, and sum (where meaningful) of the parameters are computed, resulting in overall 163 features. Finally, the second map is synchronized to an empty third map with the extent of the entire subset, including all the calculated parameters as object variables. This is done sequentially for every block. Using this approach, a large number of blocks can be processed and troubles related to computational costs can be circumvented.

Table 1
The derived block parameters.

Building	Vegetation	3D density metrics
• Volume	• Vegetation fraction	• Urban density
• Footprint	• Tree height	• Vegetation volume to Built-up volume
• Height	• Tree volume	• Urban vegetation index
• Gross floor area		
• Inverted floor area ratio	Landscape metrics	Other
• Distance between buildings		
• Number of buildings	• Fractal dimension	• Impervious surface area
• Roof type	• Relative patch richness	• Relative area of land cover per block
• Building coverage ratio	• Patch density	• Block perimeter
• Building aggregation	• Landscape shape index	• Block area
• Length/width ratio of buildings	• Shannon diversity index	• Common border index
• Frequency of building direction deviations		• Common border of class and block
		• Brightness

In order to handle the challenge of an optimal feature selection, a synergetic two-stage mapping approach is developed. First, UST prototypes for the six main UST classes are assigned by knowledge based assessment of the most suitable parameters. Beginning with the apparently more simple classes, prototypes for agricultural blocks are, for example, classified based on huge block areas, large amounts of bare soil or grass/shrubs, and non-existent building coverage ratios. Followed by the classification of water blocks (more than 60% of a block covered by water), green spaces (thresholds regarding vegetation fraction), unvegetated open spaces (only sparse vegetation fraction and building coverage ratio combined with a brightness threshold), commercial and industrial areas (huge blocks with high amounts of ISA and flat roofs as dominating roof type), and residential and office blocks (blocks with either more than 60% building coverage ratio or 10% building coverage ratio in combination with pitched roofs as dominating roof type) prototypes for every main UST class are assigned. Subsequently, a file is exported containing a list of the values of all 163 calculated parameters for each classified prototype-block. Utilizing the R software for statistical computing (R Core Team, 2014), use is made of Random Forests (Breiman, 2001), a combination of several classification and regression trees, to extract the most important variables for UST discrimination. For the generation of 200 decision trees, a certain number of variables are selected for the split decision at each node, which in this case refers to the square root of the number of all parameters, as it is recommended by Breiman (2002). The 30 most crucial features of the Random Forests analysis in R are then used within eCognition to train a second Random Forests classifier with regard to the objects classified as prototypes. After applying this classifier to the still unclassified blocks of the study area, the total area of the selected subset is classified into the six main USTs. Afterwards, the same processing sequence is individually applied to the sub-classes of residential and office blocks, unvegetated open spaces, and green spaces consisting again of (a) knowledge based prototype classification, (b) feature selection via Random Forests in R based on the knowledge based classified blocks, (c) training of a Random Forests classifier in eCognition utilizing the most important features derived in the previous step, and (d) applying the trained classifier to the unclassified block objects. As blocks of the mixed development class actually consist of several other UST classes, its classification causes difficulties and affects the proper separation of all other classes. Therefore, this class is assigned on the basis of the reference data and will be in the focus of future analyses. Like for the accuracy assessment of the land cover classification, the USTs are evaluated with the help of an error matrix which is derived assessing all blocks by the comparison of the produced classification map and the reference UST map provided by the Senate Department for Urban Development and the Environment Berlin.

4. Results

4.1. nDSM derivation

The applied Diff2Min approach was able to rapidly produce a normalized digital surface model for the large dataset of the entire study area. Assessing the accuracy of 250 manually selected ground samples based on the high resolution airborne UltraCamX DSM, 96.4% have the correct height of 0 m. For seven sample points of the assessed ground pixels, the interpolated nDSM height ranges between 1 and 3 m. In two cases, the calculation reveals major errors with 8.73 m and 47.17 m, respectively. Additionally, 250 samples within elevated objects have been assessed showing reasonable results with a median deviation of 0.3 m between reference data and calculated heights. As it is shown in Fig. 3, for most of the samples the deviation of calculated and actual height is less than 1 m (90.4%), almost 50% of the calculated heights are derived with an error of 0.3 m or lower. Only a small amount (3.6%) of the selected samples show discrepancies of more than 2 m, whereby in one case the Diff2Min approach failed to calculate the height with a deviation of 49.6 m.

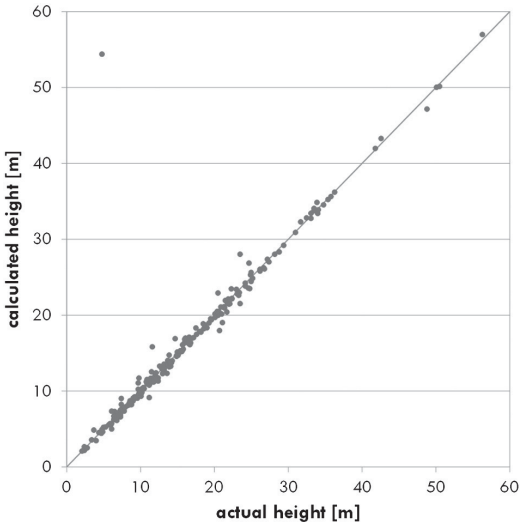

Fig. 3. Calculated heights of the nDSM versus manually derived heights.

4.2. Land cover mapping

The classified area of 324 km^2 covers the city center of Berlin as well as surrounding regions. All six land cover classes occur frequently in the selected study area. However, only 1.5% of the region is covered by water bodies and bare soil, respectively. Large amounts of the classified land cover belong to buildings (21%) and ISA (24.6%), but with more than half of the area, vegetated regions represent the largest parts of the classified image (17.5% for grass/shrubs and 33.9% for trees). An overview of the generated land cover classification is presented in Fig. 4, revealing a lot of ISA in the central districts whereas forests, grass, and shrubs are located mainly in the outer areas. Overall, 104,582 objects are classified as buildings.

The accuracy of the classified land cover is assessed via error matrix evaluating 100 randomly arranged samples per class (Congalton & Green, 2009). An overall accuracy (OA) of 92.2% and a kappa coefficient (Cohen, 1960) of 0.91 demonstrate very good classification results and prove the suitability of the proposed methods. In Table 2 the accuracy is assessed for each class, illustrating producer's accuracy (PA) for the columns (inversely correlated to commission error) and user's accuracy (UA) for the rows (inversely correlated to omission error) (Paine & Kiser, 2003). Table 2 demonstrates that, in most cases, the accuracies amount to 90% or higher. Water bodies (96.1%/98%) and trees (97.9%/93%) feature highest agreements between classification and reference data. By contrast, the classification of impervious areas succeeded with the lowest producer's (83%) and user's (88%) accuracies due to misclassifications regarding bare soil, buildings and grass/shrubs. Good classification results for buildings and trees indicate the benefit of implementing height information into land cover analyses.

4.3. Urban structure type mapping

As it is described in Section 3, the urban structure type mapping is based on a synergetic two-stage mapping approach, where the UST prototypes are initially separated knowledge-driven. Afterwards, the best features for UST delineation are calculated based on the classified prototypes using R and finally the classification of the overall study area is performed. At first, the results of the feature selection via Random

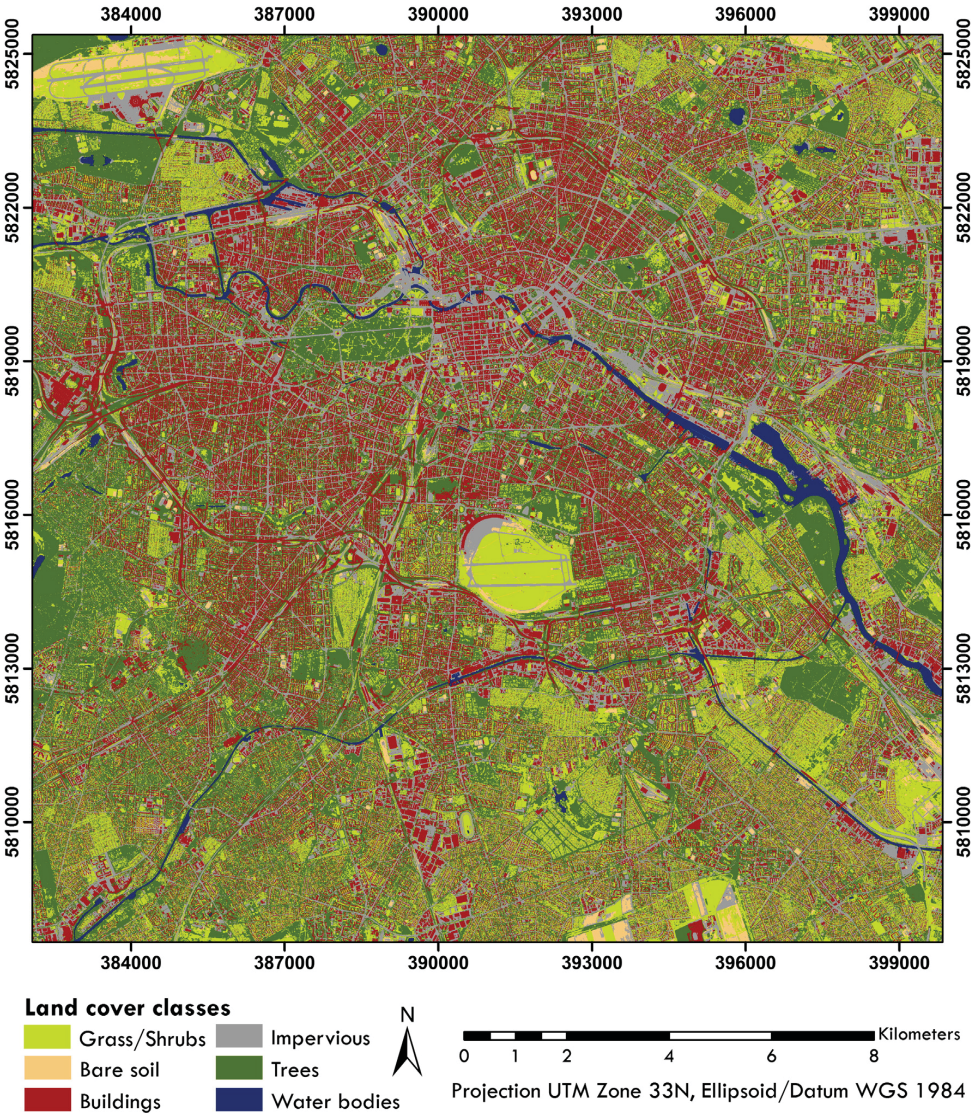

Fig. 4. The derived land cover classification for the city of Berlin.

Forests are illustrated, focusing exemplarily on the sub-classes of residential and office blocks. Table 3 shows the parameter importance of the five most valuable features for separating the six residential classes (skipping mixed development) based on the Mean Decrease Accuracy information given by the analysis in R. This indicator measures the decrease of accuracy when the values for a specific feature are randomly

Table 2
Accuracy assessment of the generated land cover map (bold values signify the amount of correctly classified samples).

		Reference							
		BA	BU	GR	IM	TR	WA	Total	UA [%]
Classification	Bare soil	**91**	0	5	3	0	1	100	**91**
	Buildings	2	**89**	0	8	0	1	100	**89**
	Grass/shrubs	0	1	**94**	4	1	0	100	**94**
	Impervious	3	1	5	**88**	1	2	100	**88**
	Trees	1	3	1	2	**93**	0	100	**93**
	Water bodies	0	0	1	1	0	**98**	100	**98**
Total		97	94	106	106	95	102	**600**	
PA [%]		**93.81**	**94.68**	**88.68**	**83.02**	**97.89**	**96.08**	**OA [%] 92.17**	

Table 3
Parameter importance of the five most valuable features indicated by the Mean Decrease Accuracy (MDA) index for the characterization of the sub classes of residential and office blocks.

Block development		Perimeter block development		Row development	
Feature	MDA	Feature	MDA	Feature	MDA
Impervious surface area	32.6	Common border of class and block	140.3	Frequency of building direction deviations 85°–90°	23.9
Urban density mean	32.5	Landscape shape index	64.3	Frequency of building direction deviations 0°–5°	21.2
Urban density median	11.4	Relative area of buildings per block	15.8	Length/width ratio of buildings mean	14.8
Vegetation fraction	10.4	Building coverage ratio	13.9	Length/width ratio of buildings median	7.5
Building aggregation	10.3	Common border index bare soil/impervious	3.7	Length/width ratio of buildings maximum	6.5
Apartment blocks		**High rise buildings**		**Detached and semi-detached houses**	
Feature	MDA	Feature	MDA	Feature	MDA
Building height mean	20.9	Inverted floor area ratio minimum	10.1	Inverted floor area ratio mean	26.6
Vegetation fraction	17.4	Inverted floor area ratio median	10.1	Building footprint mean	18.5
Inverted floor area ratio median	9.6	Inverted floor area ratio mean	8.5	Urban density maximum	9.8
Dominant roof type	7.8	Building height median	6.9	Gross floor area mean	9.3
Roof type percentage of pitched	7.7	Tree height median	5.3	Landscape shape index of trees	7.9

permuted. The higher the Mean Decrease Accuracy values the more important are the features.

In respect of the calculated feature importance, block developments are optimally separated from other USTs utilizing ISA and UD. In contrast to the simple ISA ratio, the UD index describes the intensity of urban development linking horizontal and vertical settlement characteristics (Berger, Voltersen, Eckardt, et al., 2013). The UD calculation in this study is slightly adapted concerning the area of interest, which relates to the city blocks instead of circles around the buildings. As expected, the commonly very densely developed block development class features very high UD values in contrast to other USTs, which is similar to the findings by Berger, Voltersen, Hese, et al. (2013). The most important feature for the description of perimeter block developments is the novel common border of class and block index, which in this case refers to the common border of buildings and block boundaries. Additionally, the landscape shape index (LSI) (McGarigal & Marks, 1995), belonging to the group of landscape metrics, plays a prominent role, indicating the degree of aggregation of buildings within a block. Table 3 also illustrates the feature importance for row developments. In addition to the established length to width ratio of buildings, especially the innovative measure of the frequency of building direction deviations is suitable to characterize this UST. It represents the deviation of the main direction of two buildings, calculated for all unique building pairs within a block, categorized into 5° intervals. Values of 0° to 5° indicate parallel buildings whereas 85° to 90° indicate orthogonal structures. Values in between signify a random arrangement of buildings. Apartment blocks are optimally separated using a set of different features like building height, vegetation fraction, inverted floor area ratio, and roof type. With the help of this combination, the complex structures of these USTs are described best as they vary regarding the appearance of buildings (height, number) and the composition of buildings and vegetation. The inverted floor area ratio (IFAR) dominates the feature importance for high rise buildings. By means of this indicator, the ratio between the footprint and the gross floor area (GFA) of a building is described (Berger, Voltersen, Eckardt, et al., 2013). It ranges between 0 (huge multi-level buildings) and 1 (single-level buildings) and is capable to characterize USTs featuring very tall buildings. Likewise, detached and semi-detached houses exhibit high values of IFAR associated with small building footprints and UD values. Thus, these parameters are used to separate the corresponding urban structure type.

The most valuable features are utilized to perform the UST classification of the entire subset. The resulting map of the UST analysis for the city of Berlin is shown in Fig. 5, where white areas imply excluded regions like roads, small traffic islands, and blocks cut by the image border, representing 23.8% of the image. Most of the USTs belong to mixed developments which will be treated separately in further analyses. Among the more homogeneous USTs, parks account for the largest amount covering 14.2 km^2 (12.7%) of the image, followed by block developments (12%) and commercial and industrial areas (11.5%). In contrast, only 0.5 km^2 is composed of high rise buildings blocks and woodland, respectively. Similar to this, 0.4% (0.44 km^2) of the image is covered by agricultural areas. Among the residential areas, in addition to the block development class, major regions are classified as perimeter block development (7%) and apartment blocks (5.2%). Only smaller regions belong to detached and semi-detached houses (3.1%), row developments (2.7%), and blocks with high rise buildings. The resulting UST map reveals some obvious patterns composed by clusters of the same UST, whereby surrounding regions are dominated by parks and loose built-up blocks and the city center features small-scaled UST variations.

The UST classification resulted in an overall accuracy of 82.1% and a kappa index of 0.79, signifying reasonable mapping results, whereby classification errors in the first level (main USTs) propagate to the sub-classes. As stated before, the mixed development class and areas outside the regions of interest are excluded from the accuracy assessment. Looking at Table 4, significant accuracy differences occur, ranging from 60.6% producers accuracy for unvegetated open spaces to 100% producer's accuracy for woodland and agriculture as well as 58.4% user's accuracy for high rise buildings to 100% user's accuracy for water bodies. Table 4 illustrates that especially the USTs dominated by natural surface cover feature greater similarities between classification result and reference data than USTs characterized by major building coverage ratios. However, the differentiation between residential/office blocks and commercial/industrial areas succeeded properly for most of the blocks. The results of the UST classification will be discussed in the following section and reasons for misclassifications are adduced.

5. Discussion

In this section, the implemented methods, the classification results, and major sources of errors are discussed. Initially, the derivation of the nDSM is addressed. The constructed Diff2Min approach generated plausible results within a very short processing time with regard to the huge number of pixels which had to be processed (457,599,488 pixels). However, in some situations the approach fails to perform correctly. For huge buildings or forested areas with no ground pixels within the size of the moving window (99 m edge length) a height of 0 m is assigned to the central pixel because no pixel with a lower DSM height is located in the area of the moving window. On the other hand, small-scaled changes in the terrain without building or tree coverage, such as hills situated completely within the moving window, receive nDSM heights larger than 0 m although the pixels belong to ground pixels. Therefore, the Diff2Min approach is suitable to calculate the height of urban objects precisely, but it is not qualified for nDSM creation over large woodlands or areas with very small-scaled

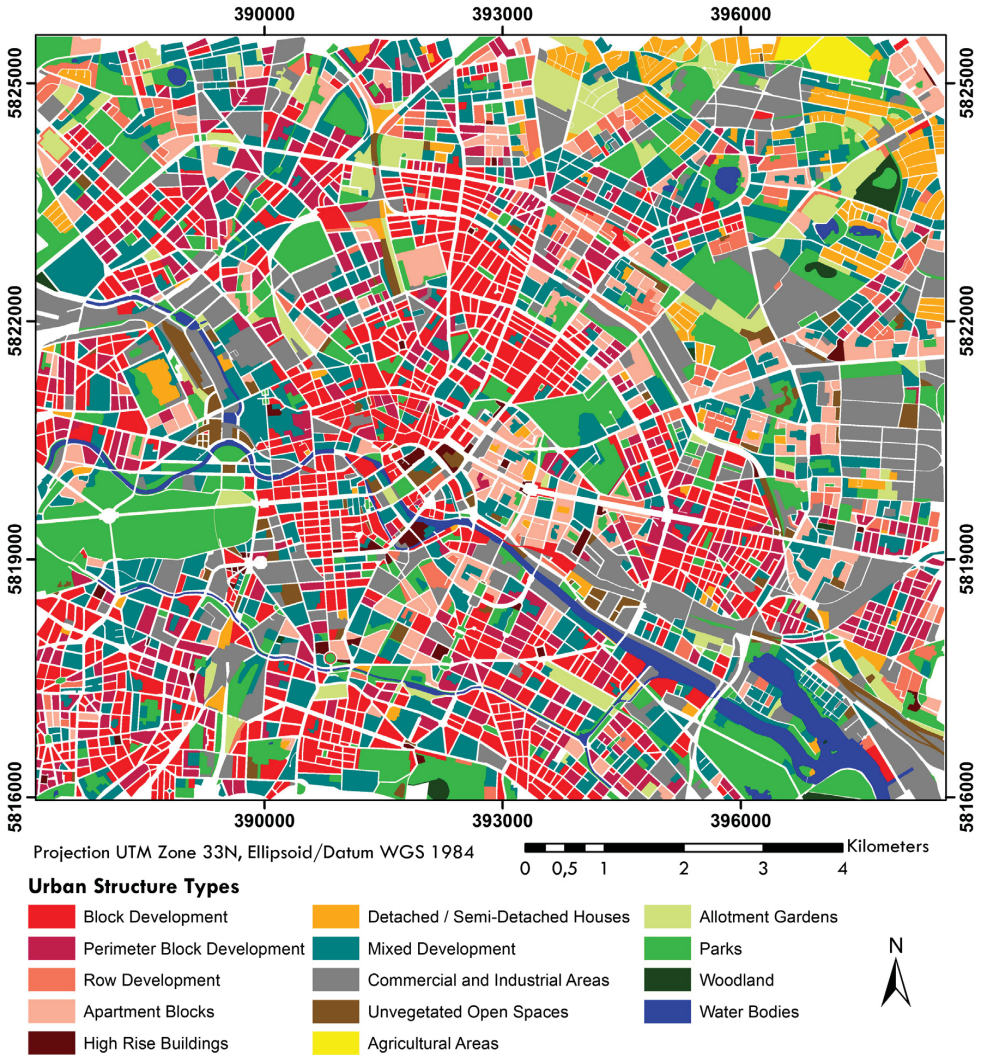

Fig. 5. The derived urban structure type classification for the city of Berlin.

Table 4
Accuracy assessment of the generated urban structure type map (areas in square kilometer, bold values signify the amount of correctly classified areas).

		Reference														
		11	12	13	14	15	16	2	3	41	42	43	5	6	Total	UA [%]
Classification	11	**12.35**	0.44	0	0.01	0.02	0	0.67	0.04	0	0	0	0	0	13.52	**91.37**
	12	2.33	**4.33**	0.12	0.23	0.02	0.07	0.03	0	0	0.01	0	0	0	7.14	**60.72**
	13	0.09	0.22	**2.55**	0.18	0.01	0.03	0.11	0.09	0	0.06	0	0	0	3.34	**76.20**
	14	0.51	0.59	0.28	**3.97**	0.02	0.01	0.03	0	0	0.51	0	0	0	5.93	**67.01**
	15	0.04	0.03	0	0.16	**0.33**	0	0.01	0	0	0.01	0	0	0	0.57	**58.44**
	16	0.03	0	0.04	0.04	0.02	**2.65**	0.17	0.05	0.01	0.29	0	0	0	3.29	**80.38**
	2	0.65	0.05	0.04	0.26	0.02	0.10	**10.75**	0.69	0	0.11	0	0	0.04	12.69	**84.68**
	3	0	0	0.01	0	0.04	0.01	0.17	**1.60**	0	0.34	0	0	0.03	2.20	**72.80**
	41	0.02	0.01	0	0.00	0	0.10	0.02	0.04	**2.24**	0.98	0	0	0	3.41	**65.81**
	42	0.01	0.01	0.11	0.12	0.02	0.30	0.11	0.11	0.25	**13.29**	0	0	0	14.32	**92.81**
	43	0	0	0	0.06	0	0.02	0	0	0.04	0.02	**0.44**	0	0	0.58	**75.88**
	5	0	0	0	0	0	0	0	0.03	0	0.02	0	**0.44**	0	0.49	**89.61**
	6	0	0	0	0	0	0	0	0	0	0	0	0	**2.57**	2.57	**100**
Total		16.03	5.68	3.14	5.02	0.49	3.28	12.05	2.64	2.54	15.66	0.44	0.44	2.63	**70.05**	
PA [%]		**77.05**	**76.29**	**81.14**	**79.13**	**68.88**	**80.63**	**89.18**	**60.65**	**88.18**	**84.87**	**100**	**100**	**97.42**	**OA [%] 82.11**	

changes in terrain heights. An automated adaptation of the window size with respect to the landform configuration would increase the precision of the approach.

Using an object-based approach for land cover mapping, the requirements of the processing of high spatial resolution remote sensing data are met. The achieved accuracies for all classes indicate the quality of the methodology. Misclassifications are mainly caused by known difficulties associated with urban land cover analysis. Due to an acquisition time in the morning hours, the small incidence angle of the sunlight causes major areas covered by shadows, which can especially impede the proper classification of dark surfaces like water bodies, but also affect the classification of other areas within the city located adjacent to buildings. In addition, narrow river segments separated by bridges within the city center are often confused with impervious surface areas. Likewise, the correct separation of impervious surfaces and bare soil proves difficult for data with low spectral resolution as both land cover types are characterized by manifold surface materials and overlapping spectral and spatial properties. The described errors of the land cover classification negatively affect the urban structure type mapping, especially for USTs which are characterized mainly based on the existence of one land cover class such as water bodies. However, the errors in classification represent only a small amount of the created land cover map. Hence, the land cover mapping approach produced reasonable results very efficiently, especially with respect to the relation of processing time and accuracy. Emphasis is put on fast image segmentation, simple class descriptions, and preceded layer normalization. In combination with the detection and growing of seed-objects based on relative thresholds, the created sequence aims at being robust and transferable. As the transferability has not been tested yet, further analyses will focus on this issue, but due to the similarity of the methods proposed by Berger, Voltersen, Hese, et al. (2013), equivalent classification results are to be expected for other study areas.

In order to create a transferable UST mapping approach, the combination of knowledge-based prototype assignment and Random Forests classification enables the automated execution of the ruleset for different study areas. However, a drawback concerning transferability is caused by the inclusion of block boundary data which is not available for every city. This issue has to be addressed either by the attempt to derive block boundaries based on homogeneous building clusters and additional land cover information or by utilizing the major road network of freely accessible data like OpenStreetMap.

Considering the most important features calculated by the Random Forests analysis, very plausible results have been generated. Block developments are commonly very densely developed and typically feature a lot more sealed areas than natural surface covers. This is proved by the two most important features for this UST, namely ISA and UD. Both indicators are able to characterize very compact city structures such as the city center, which exhibits the highest ISA and UD values. The characterization of perimeter block developments by utilizing the common border of buildings and block index seems comprehensible as these blocks are constituted by buildings adjacent to roads, which in turn shape the block edges. Likewise, the LSI is very useful for the delineation of this UST. It is calculated by the ratio of the total edge length of all building objects and the perimeter of a maximally aggregated object with the same area of all buildings. As the buildings of this UST are located on the outermost regions of the block, they are maximally disaggregated and therefore feature high LSIs. Similar to this, the features important for row developments fit very well to the assumptions made for these USTs as they are composed of elongated buildings in parallel or rectangular to each other. Therefore, optimal UST description is achieved by taking account of the buildings' main directions in combination with the length to width ratio. With an increasing building height, and thus an increasing number of floors, the inverted floor area ratio tends to zero. Therefore, it is capable to characterize blocks with single high rise buildings, given that no small misclassified building objects occur in the block area. The mentioned examples of the feature selection prove the suitability of the implemented methods. In particular, Random Forests analysis generates adequate results regarding feature importance.

The accuracy assessment demonstrates benefits and limitations of the UST classification. While the overall accuracy reveals good mapping results, particular classes are derived inadequately. Sports areas covered by artificial turf, e.g., are often misclassified as unvegetated open spaces due to missing significant NDVI values in contrast to natural lawns. By removing artificial turf sports grounds, the user's accuracy of unvegetated open spaces would increase from 72.8% to 80%. On the other hand, bare soil areas, slightly overgrown with grass, feature characteristics close to parks. Additionally, traffic areas are similar to small industrial areas, causing further errors in classification. For that reason, the planned subdivision of unvegetated open spaces into sealed areas and bare soil is postponed. Although this UST represents only 1.5% of the study area, the separation of both classes is considered to be important since an accurate derivation of bare soil areas might be helpful to identify regions for settlement densification in order to counteract urban sprawl. Most of the errors regarding the derivation of residential and office blocks are caused by two central issues: errors in land cover classification (like incorrect building objects or the confusion of impervious and bare soil) and the frequent occurrence of several building types within one block. Especially for the city of Berlin, the abundance of mixed developments (not only in the eponymous UST) impedes a proper classification. A possible approach to address this problem is to automatically derive block boundaries; thus blocks featuring only homogeneous structures would appear.

In summary, it can be stated that the accuracy strongly depends on the quality of the land cover classification and the reference data. In this case, the adaptation of the UST class hierarchy of the Senate Department for Urban Development and the Environment Berlin to the defined classes of this study proved to be difficult due to divergent classification depths. An accuracy assessment based on unmistakable attributed manually selected samples would very likely produce better results. Nevertheless, an overall accuracy of 82.1% for 15 different USTs verifies the suitability of the methodology.

6. Conclusion

The separation of cities into areas with homogeneous urban structures and similar land use provides the basis for an effective city management. For that reason, the urban structure type approach has been established, enabling holistic descriptions of a city and its interactions. Remote sensing data and methods offer objectivity, transferability and automation regarding the widespread analysis of USTs. However, previous studies lack comprehensive feature calculation, systematic extraction of the most suitable parameters, appropriate classification accuracy, and transferability. The known issues are addressed by implementing a sequence of processes which can be executed automatically on different data sets and regions. With 163 generated parameters, a comprehensive characterization of urban blocks is performed. As the manual evaluation of the most suitable features underlies subjective assumptions and possibly ignores valuable parameters, the feature selection via Random Forests based on prototypes presents an automated approach for selecting the best parameters. Satisfying UST classification results have been produced through a precise nDSM generation, land cover mapping, and feature extraction, resulting in 82.1% overall accuracy for the defined USTs. Analyzing the individual classes, distinct accuracy differences are apparent, mainly caused by difficulties in land cover classification and the existence of different structures within one block. The separation of unvegetated open spaces as well as the automated processing of mixed development blocks has to be addressed in further analyses. Furthermore, transferability of the approach will be tested for the complete city region of Berlin and for additional study areas located in Germany.

Acknowledgments

The authors would like to thank the DLR Berlin-Adlershof for providing multispectral data and the DSM of the UltraCamX sensor for the city of Berlin. We also want to express our thanks to the Senate Department for Urban Development and the Environment Berlin for the provision of auxiliary data including block boundaries and the UST reference map. This research is funded by the Graduate Academy of the Friedrich Schiller University Jena.

References

Baatz, M., & Schäpe, A. (1999). Object-oriented and multi-scale image analysis in semantic networks. *Proc. of the 2nd International Symposium on Operationalization of Remote Sensing*. Enschede: ITC.

Banzhaf, E., & Höfer, R. (2008). Monitoring urban structure types as spatial indicators with CIR aerial photographs for a more effective urban environmental management. *IEEE Journal of Selected Topics in Applied Earth Observations and Remote Sensing, 1*(2), 129–138.

Barnsley, M. J., & Barr, S. L. (2000). Monitoring urban land use by earth observation. *Surveys in Geophysics*, *21*(2), 269–289, http://dx.doi.org/10.1023/A:1006798328429.

Berger, C., Voltersen, M., Eckardt, R., Eberle, J., Heyer, T., Salepci, N., et al. (2013). Multi-modal and multi-temporal data fusion: Outcome of the 2012 GRSS data fusion contest. *IEEE Journal of Selected Topics in Applied Earth Observations and Remote Sensing, 6*(3), 1324–1340.

Berger, C., Voltersen, M., Hese, S., Walde, I., & Schmullius, C. (2013). Robust extraction of urban land cover information from HSR multi-spectral and LiDAR data. *IEEE Journal of Selected Topics in Applied Earth Observations and Remote Sensing*, *6*(5), 2196–2211, http://dx.doi.org/10.1109/JSTARS.2013.2252329.

Blaschke, T. (2010). Object-based image analysis for remote sensing. *ISPRS Journal of Photogrammetry and Remote Sensing, 65*(1), 2–16.

Blum, W. E. H. (2013). Land use planning and policy implication: Bridging between science, politics and decision making. In S. A. Shahid, F. K. Taha, & M.A. Abdelfattah (Eds.), *Developments in soil classification, land use planning and policy implications* (pp. 469–481). Springer Netherlands, http://dx.doi.org/10.1007/978-94-007-5332-7_25.

Bochow, M., Taubenböck, H., Segl, K., & Kaufmann, H. (2010). An automated and adaptable approach for characterizing and partitioning cities into urban structure types. *Geoscience and Remote Sensing Symposium (IGARSS) 2010 IEEE International* (pp. 1796–1799). Honolulu: IEEE, http://dx.doi.org/10.1109/IGARSS.2010.5652972.

Breiman, L. (2001). Random forests. *Machine Learning, 45*(1), 5–32, http://dx.doi.org/10.1023/A:1010933404324.

Breiman, L. (2002). Manual on setting up, using, and understanding random forests v3.1. Retrieved from. http://www.stat.berkeley.edu/~breiman/Using_random_forests_V3.1.pdf

Breuste, J., Wächter, M., & Bauer, B. (2001). *Beiträge zur umwelt-und sozialverträglichen Entwicklung von Stadtregionen*. Leipzig: Umweltforschungszentrum Leipzig-Halle.

Bridgman, H. A., Warner, R. F., & Dodson, J. R. (1995). *Urban biophysical environments. Meridian Australian geographical perspectives*. Oxford University Press, 152.

Cohen, J. (1960). A coefficient of agreement of nominal scales. *Educational and Psychological Measurement*, *20*(1), 37–46, http://dx.doi.org/10.1177/001316446002000104.

Congalton, R. G., & Green, K. (2009). *Assessing the accuracy of remotely sensed data—Principles and practices* (2nd ed.). Boca Raton: CRC Press, 183.

Destatis (2013). German cities sorted by area, population, and population density (31.12.2012). Retrieved November 04, 2013, from. https://www.destatis.de/DE/ZahlenFakten/LaenderRegionen/Regionales/Gemeindeverzeichnis/Administrativ/Aktuell/05Staedte.html

Erell, E., Pearlmutter, D., & Williamson, T. (2010). *Urban microclimate—Designing the spaces between buildings*. London: Earthscan.

Gill, S. E., Handley, J. F., Ennos, A.R., Pauleit, S., Theuray, N., & Lindley, S. J. (2008). Characterising the urban environment of UK cities and towns: A template for landscape planning. *Landscape and Urban Planning*, *87*(3), 210–222, http://dx.doi.org/10.1016/j.landurbplan.2008.06.008.

Gruber, M., Ponticelli, M., Bernögger, S., & Leberl, F. (2008). UltraCamX, the large format digital aerial camera system by Vexcel Imaging/Microsoft. *International Archives of the Photogrammetry, Remote Sensing and Spatial Information Sciences*, *37*, 665–670.

Hay, G., & Castilla, G. (2008). Geographic object-based image analysis (GEOBIA): A new name for a new discipline. In T. Blaschke, S. Lang, & G. Hay (Eds.), *Object-based image analysis. Spatial concepts for knowledge-driven remote sensing applications* (pp. 75–89). Berlin: Springer.

Heiden, U., Heldens, W., Roessner, S., Segl, K., Esch, T., & Mueller, A. (2012). Urban structure type characterization using hyperspectral remote sensing and height information. *Landscape and Urban Planning*, *105*(4), 361–375, http://dx.doi.org/10.1016/j.landurbplan.2012.01.001.

Hermosilla, T., Ruiz, L. A., Recio, J. A., & Balsa-Barreiro, J. (2012). Land-use mapping of Valencia City area from aerial images and LiDAR data. *GEOProcessing 2012: The Fourth International Conference on Advanced Geographic Information Systems, Applications, and Services* (pp. 232–237). Valencia: IARIA.

Herold, M., Liu, X., & Clarke, K. C. (2003). Spatial metrics and image texture for mapping urban land use. *Photogrammetric Engineering Remote Sensing, 69*(9), 991–1001.

Herold, M., Scepan, J., & Clarke, K. C. (2002). The use of remote sensing and landscape metrics to describe structures and changes in urban land uses. *Environment and Planning - Part A*, *34*(8), 1443–1458, http://dx.doi.org/10.1068/a3496.

Lang, S. (2008). Object-based image analysis for remote sensing applications: modeling reality—Dealing with complexity. In T. Blaschke, S. Lang, & G. Hay (Eds.), *Object-based image analysis* (pp. 3–27). Springer Berlin Heidelberg, http://dx.doi.org/10.1007/978-3-540-77058-9_1.

Lindner, M., Hese, S., Berger, C., & Schmullius, C. (2011). An object-based multisensoral approach for the derivation of urban land use structures in the city of Rostock, Germany. *Earth Resources and Environmental Remote Sensing/gis Applications II*, *Vol. 8181*, http://dx.doi.org/10.1117/12.898134.

McGarigal, K., & Marks, B. J. (1995). FRAGSTATS: Spatial pattern analysis program for quantifying landscape structure. *General Technical Report PNW-GTR-351*.

Osmond, P. (2011). Application of the urban structural unit method to inform post-carbon planning and design. *International Seminar on Urban Form: Urban Morphology and the Post-Carbon City*. Montreal: ISUF.

Paine, D. P., & Kiser, J.D. (2003). *Aerial photography and image interpretation* (2nd ed.). Hoboken: John Wiley & Sons.

Pauleit, S., & Burkhardt, I. (2004). Umweltqualität und Stadtentwicklung. Landschaftsökologische Projekte von Friedrich Duhme für die Landeshauptstadt München. *Landschaftsökologie in Forschung, Planung und Anwendung* (pp. 89–116).

Pauleit, S., & Duhme, F. (1998). Assessing the metabolism of urban systems for urban planning. In J. Breuste, H. Feldmann, & O. Uhlmann (Eds.), *Urban ecology* (pp. 65–69).

Pauleit, S., & Duhme, F. (2000). Assessing the environmental performance of land cover types for urban planning. *Landscape and Urban Planning*, *52*(1), 1–20, http://dx.doi.org/10.1016/S0169-2046(00)00109-2.

Puissant, A., Zhang, W., & Skupinski, G. (2012). Urban morphology analysis by high and very high spatial resolution remote sensing. *4th GEOBIA* (pp. 524–529). Rio de Janeiro: INPE.

R Core Team (2014). *R: A language and environment for statistical computing*. Vienna: R Foundation for Statistical Computing (Retrieved from http://www.r-project.org/).

Schiewe, J. (2002). Segmentation of high-resolution remotely sensed data—Concepts, applications and problems. *International Archives of Photogrammetry and Remote Sensing, 34*(4), 380–385.

Senate Department for Urban Development and the Environment Berlin. (2010). Geoportal-Berlin.

Spellerberg, I. F., & Fedor, P. J. (2003). A tribute to Claude Shannon (1916-2001) and a plea for more rigorous use of species richness, species diversity and the "Shannon–Wiener" Index. *Global Ecology and Biogeography*, *12*(3), 177–179, http://dx.doi.org/10.1046/j.1466-822X.2003.00015.x.

Taubenböck, H., Esch, T., & Roth, A. (2006). An urban classification approach based on an object-oriented analysis of high resolution satellite imagery for a spatial structuring within urban areas. *1st EARSeL Workshop of the SIG Urban Remote Sensing* (pp. 8). Berlin: EARSel.

Tompalski, P., & Wezyk, P. (2012). LiDAR and VHRS data for assessing living quality in cities—An approach based on 3D indices. *ISPRS International Archives of the Photogrammetry, Remote Sensing and Spatial Information Sciences*, *XXXIX-B6*. (pp. 173–176).

Trimble (2013). *eCognition Developer 8.9 reference book*. Munich: Trimble Germany GmbH.

Tucker, C. (1979). Red and photographic infrared linear combinations for monitoring vegetation. *Remote Sensing of Environment, 8*(2), 127–150.

Tzotsos, A., Iosifidis, C., & Argialas, D. (2008). A hybrid texture-based and region-based multi-scale image segmentation algorithm. In T. Blaschke, S. Lang, & G. Hay (Eds.), *Object-based image analysis* (pp. 221–236). Springer Berlin Heidelberg, http://dx.doi.org/10.1007/978-3-540-77058-9_12.

Vitousek, P.M., Mooney, H. A., Lubchenco, J., & Melillo, J. M. (1997). Human domination of Earth's ecosystems. *Science*, *277*(5325), 494–499, http://dx.doi.org/10.1126/science.277.5325.494.

Walde, I., Hese, S., Berger, C., & Schmullius, C. (2014). From land cover-graphs to urban structure types. *International Journal of Geographical Information Science*, *28*(3), 584–609, http://dx.doi.org/10.1080/13658816.2013.865189.

Wurm, M., Taubenböck, H., & Dech, S. (2010). Quantification of urban structure on building block level utilizing multisensoral remote sensing data. *Earth*, *7831*(1), 1–12, http://dx.doi.org/10.1117/12.864930.

Wurm, M., Taubenböck, H., Roth, A., & Dech, S. (2009). Urban structuring using multisensoral remote sensing data: By the example of the German cities Cologne and Dresden. *2009 Joint Urban Remote Sensing Event* (pp. 1–8). IEEE, http://dx.doi.org/10.1109/URS.2009.5137555.

4.4 Detailed analysis of USC–LST links

This section is based on the manuscript entitled
"Spatio-temporal analysis of the relationship between 2D/3D urban site characteristics and land surface temperature".

The manuscript was authored by
Berger C, Rosentreter J, Voltersen M, Baumgart C, Schmullius C & Hese S (2017)

and published in
Remote Sens Environ 193C: 225–243;
doi: 10.1016/j.rse.2017.02.020.

Remote Sensing of Environment 193 (2017) 225–243

Contents lists available at ScienceDirect

Remote Sensing of Environment

journal homepage: www.elsevier.com/locate/rse

Spatio-temporal analysis of the relationship between 2D/3D urban site characteristics and land surface temperature

C. Berger[a,*], J. Rosentreter[b], M. Voltersen[c], C. Baumgart[d], C. Schmullius[a], S. Hese[a]

[a] Department of Earth Observation, Friedrich-Schiller-Universität Jena, Löbdergraben 32, 07743 Jena, Germany
[b] Institute of Geographical Sciences, Freie Universität Berlin, Malteserstraße 74–100, 12249 Berlin, Germany
[c] Tama Group GmbH, Fraunhofer Straße 22, 82152 Martinsried, Germany
[d] Institut für Landes- und Stadtentwicklungsforschung, Brüderweg 22–24, 44135 Dortmund, Germany

ARTICLE INFO

Article history:
Received 2 December 2014
Received in revised form 2 February 2017
Accepted 25 February 2017

Keywords:
Human settlements
Urban site characteristics
Land surface temperature
Urban heat island
Correlation analysis
Landsat
ETM+

ABSTRACT

This paper focuses on the relationship between remotely-sensed urban site characteristics (USCs) and land surface temperature (LST). Particular emphasis is put on an extensive comparison of two-dimensional (2D) *and* three-dimensional (3D) USCs as potential indicators of the surface urban heat island (UHI) effect and as potential predictors for thermal sharpening applications. Both widely-used as well as more recently proposed metrics of the urban remote sensing literature are investigated within a single experiment. While some of these USCs have already been used earlier, others have never been analyzed before in the context of urban temperature studies. In addition to the comparison of 2D and 3D USCs, the spatio-temporal dependencies of their relation to LST are examined. To this end, the experimental setup of this work includes two study areas, 26 USCs, and 16 LST scenes covering four seasons. Use is made of a comprehensive database compiled for the cities of Berlin and Cologne, Germany. After data preparation, very high resolution (VHR) multi-spectral and height data are employed to map fine-scale urban land cover (LC). The resulting LC maps are then used in conjunction with the height information to compute 2D and 3D USCs. Subsequently, multi-temporal LST images are retrieved from Landsat Enhanced Thematic Mapper Plus (ETM+) scenes. The spatio-temporal investigation of the USC–LST connection constitutes the final stage of the workflow and is achieved in the framework of a dedicated correlation analysis. The results of this study highlight that the linkage between USCs and LST sensed at small scan angles is not stronger when 3D parameters are considered. Even though they may offer more holistic representations of the urban landscape, 3D USCs are consistently outperformed by some of the most widely-used 2D metrics. The analysis of spatial dependencies reveals that the USC–LST interplay does not only differ between, but also within the two test sites. This is due to their distinct geographies, with urban form and compactness, green spaces and street trees, and the structural composition of LC elements being some of the determining factors. The examination of temporal dependencies yielded that the association between USCs and LST is fairly stable over time but can be subject to larger inter- and intra-season variations for different reasons, including the season of acquisition, vegetation phenology, and meteorological conditions. Since previous research was based on the analysis of a single study area, a limited number of (mainly 2D) USCs, and/or only a few LST scenes acquired in specific seasons, it is concluded that the findings of this study provide researchers and practitioners with a more complete picture of the USC–LST relationship.

1. Introduction

It has long been recognized that urbanization can have a profound impact on the Earth's climate at the local and regional scale (Landsberg, 1981; Grimmond, 2007). One of the most well-documented examples of this human-induced climate modification is a phenomenon called the urban heat island (UHI) (Oke, 1973, 1982). It refers to the observation that cities often feature higher air and surface temperatures than their surroundings. The first scientific record of an UHI dates back to Howard (1833) and, since their discovery, UHIs have been studied extensively (Arnfield, 2003; Gago et al., 2013; Rizwan et al., 2008; Stewart, 2010). The environmental and socio-economic implications of the UHI effect are diverse and range from changes in precipitation patterns (Changnon, 1992; Lowry, 1998) to increases in air pollution (Sarrat et al., 2006; Weng and Yang, 2006), water use (Gober et al., 2009; Guhathakurta and Gober, 2007),

* Corresponding author.
E-mail address: christian.berger@uni-jena.de (C. Berger).

http://dx.doi.org/10.1016/j.rse.2017.02.020
0034-4257/

energy consumption (Ewing and Rong, 2008; Ko, 2013), and mortality rates (Basu and Samet, 2002; Curriero et al., 2002). Considering that the magnitude of UHIs is expected to increase in many places (Grimmond, 2007; McCarthy et al., 2010; Rizwan et al., 2008) while, at the same time, more and more people will be exposed to the living conditions in the cities of tomorrow (United Nations, 2008), there is an urgent need for information on urban site characteristics (USCs) enabling scientists and city planners to gain a better understanding of the driving forces behind the UHI phenomenon and, thus, to make more informed decisions about the future of urban environments.

Satellite and airborne remote sensing technology is capable of providing up-to-date, spatially explicit, and area-wide information that are well-suited to study UHIs (Ngie et al., 2014; Tomlinson et al., 2011; Voogt and Oke, 2003; Weng, 2009). By capturing the reflectance and height of urban elements, optical and light detection and ranging (LiDAR) remote sensing allows for the extraction of various USCs. These include, but are not limited to, biophysical descriptors (Ridd, 1995; Deng and Wu, 2012), land cover (LC) types (Berger et al., 2013b; O'Neil-Dunne et al., 2013), surface materials (Franke et al., 2009; Heiden et al., 2007), land use (LU) structures (Heiden et al., 2012; Voltersen et al., 2014), landscape patterns (Herold et al., 2003; Huang et al., 2007), and settlement density (Berger et al., 2013a; Yu et al., 2010). Through measuring the upwelling longwave radiation emitted by an urban area, thermal infrared remote sensing can be used to retrieve land surface temperature (LST) (Kuenzer and Dech, 2013; Li et al., 2013), an indicator of the so-called surface UHI (Roth et al., 1989). Once USCs and LST have been derived, it is straightforward to compare these sets of information as part of subsequent analyses (Voogt and Oke, 2003).

Given its high versatility, numerous studies have employed remote sensing to investigate the linkage between USCs and LST. In general, the scientific literature can be grouped into several categories according to the USCs considered. Biophysical descriptors of human settlements, like surface albedo, vegetation fraction (VF), and impervious surface area (ISA), are among the most frequently used USCs. They are usually obtained from spectral indices (Chen et al., 2006; Liu and Zhang, 2011; Ogashawara and da Silva Brum Bastos, 2012; Xian, 2008), spectral unmixing (Small, 2006; Weng et al., 2004; Yuan and Bauer, 2007), or subpixel classification techniques (Lazzarini et al., 2013; Xian and Crane, 2006; Zhang et al., 2009b). Discrete representations of urban LC and LU are of similar popularity as biophysical descriptors. They are often utilized to study intra-urban temperature differences, the magnitude of surface UHIs, and their changes over space and time (Chen et al., 2006; Lazzarini et al., 2013; Li et al., 2011; Mallick et al., 2013; Weng, 2001, 2003; Xiao et al., 2008). A special form of LC representations are urban surface material maps, which have been compared to LST patterns as part of some studies (Ben-Dor and Saaroni, 1997; Heldens et al., 2013; Quattrochi and Ridd, 1994). On the basis of LC and LU products, it is possible to extract further USCs, including landscape and settlement density metrics. Respective research has demonstrated that the composition and configuration of LC elements as well as the intensity of urban development can be closely connected to the thermal characteristics within cities (Li et al., 2011; Liu and Weng, 2008; Maimaitiyiming et al., 2014; Myint et al., 2013; Ren et al., 2013; Weng et al., 2008; Xiao et al., 2008; Yue et al., 2012; Zhang et al., 2009a; Zhou et al., 2011). Besides remotely-sensed USCs, ancillary geospatial data are sometimes used to analyze the origins of surface UHI formation. Typical layers of information are socioeconomic attributes, with population density being a quite common one (Buyantuyev and Wu, 2010; Huang et al., 2011; Weng et al., 2008; Xiao et al., 2008; Yue et al., 2012).

The above compilation of papers shows that a considerable amount of research has already been directed towards understanding the interactions between USCs and LST by means of Earth observation. Most notably, a lot of emphasis has been placed on the two-dimensional (2D) features of a city. In contrast to that, three-dimensional (3D) USCs, such as the height or volume of buildings, still remain largely unexplored although their impact on the urban climate is unquestioned (Oke, 1981; Unger, 2004) and their area-wide calculation has become feasible thanks to the increased availability of appropriate remote sensing data (Berger et al., 2013b; Cook et al., 2013; O'Neil-Dunne et al., 2013; Ehlers, 2009; Gamba et al., 2005; LiDAR Online, 2014; OpenTopography, 2014). Exceptions to this observation are rare. For instance, Chun and Guldmann (2014) examine the main determinants of the UHI of Columbus, OH, by feeding a set of remotely-sensed urban parameters (2D and 3D) into spatial regression models. They find that, among others, 3D USCs strongly impact urban LST. After evaluating 12 different indicators of urban composition (2D) and geometry (3D), Srivanit and Kazunori (2011) come to a similar conclusion. They report that the 3D characteristics of Bangkok, Thailand, are able to explain most of the variations in measurements of LST and air temperature. Apart from these exceptions, there is still a lack of studies relating 2D *and* 3D USCs to LST (Chun and Guldmann, 2014; Mallick et al., 2013; Ngie et al., 2014; Voogt and Oke, 2003). Moreover, previous research findings are based on the analysis of a single study area, a limited number of (mainly 2D) USCs, and/or only a few LST scenes acquired in specific seasons (e.g., Huang et al., 2011; Liu and Zhang, 2011; Maimaitiyiming et al., 2014; Myint et al., 2013; Ogashawara and da Silva Brum Bastos, 2012; Ren et al., 2013; Xiao et al., 2008; Weng et al., 2004; Yue et al., 2012; Zhang et al., 2009a,b). In order to obtain a more complete picture of the connection between USCs and LST, more comprehensive investigations still need to be undertaken. The present study aims to address this need.

This paper focuses on the relationship between USCs and LST. Particular emphasis is put on an extensive comparison of 2D *and* 3D USCs as potential indicators of the surface UHI effect and as potential predictors for thermal sharpening applications (cf. Zhan et al., 2013). Both widely-used as well as more recently proposed metrics of the urban remote sensing literature are investigated within a single experiment. While some of these USCs have already been used earlier (e.g., ISA and VF), others, like the vegetation volume to built-up volume (VV2BV) and urban density (UD), have never been analyzed before in the context of urban temperature studies. In addition to the comparison of 2D and 3D USCs, the spatio-temporal dependencies of their relation to LST are examined. To this end, the experimental setup of this work includes two study areas, 26 USCs, and 16 LST scenes covering four seasons. The remainder of this paper is structured as follows. In Sections 2 and 3, the data and methods used to achieve the above goal are presented. Sections 4 and 5 follow with the description and discussion of the study results. Section 6 concludes the findings of this investigation and provides an outlook on future research needs.

2. Materials

The analyses described in this paper are based on very high resolution (VHR) multi-spectral and height data, multi-temporal Landsat Enhanced Thematic Mapper Plus (ETM+) imagery, as well as additional geospatial information. The data sets used were acquired over the cities of Berlin and Cologne, Germany. An overview of the study areas and database is provided in the following.

2.1. Study areas

The federal city state of Berlin is located in north-eastern Germany (52° 31′ 06″N, 13° 24′ 30″E). It has more than 3.3 million residents and comprises an administrative area of about 892 km^2, making it the largest city of the country in terms of both population and size (Destatis, 2014). Berlin features a gentle topography. Elevation values range from 34 m a.s.l. in the valley of the HavelRiver to 115 m a.s.l. on the plateaus and hills surrounding the Spree river valley (Meng, 2014). According to the Köppen-Geiger classification

scheme (Köppen, 1936; Peel et al., 2007), the city is characterized by a humid continental climate (Dfb). Its mean annual temperature is 9.9 °C, with the coldest month being January (average: 0.8 °C) and the warmest month being July (average: 19.8 °C). On average, Berlin experiences 576 mm of precipitation per year (Deutscher Wetterdienst, 2014).

The City of Cologne is situated in western Germany (50° 56′ 33″N, 06° 57′ 32″E) and belongs to the federal state of North Rhine-Westphalia. With 1.02 million people living on an official area of roughly 405 km^2, it is the fourth most populous and seventh largest city of Germany (Destatis, 2014). Cologne lies about 49 m a.s.l. and, due to its location on both sides of the Rhine river, it does not feature significant topography (Müllenberg, 2010). The city's climate can be described as temperate oceanic (Cfb) (Köppen, 1936; Peel et al., 2007). Mild winters (average: 3.6 °C in January) and relatively warm summers (average: 20.1 °C in July) all contribute to a mean annual temperature that is higher than for Berlin (11.5 °C). Precipitation is evenly spread throughout the year and adds up to an annual average of 817 mm (Deutscher Wetterdienst, 2014).

2.2. Data

The data for this study consist of VHR multi-spectral and height data, multi-temporal Landsat ETM+ imagery, as well as additional geospatial information for both test sites. In total, the data sets cover 360 and 144 km^2 of Berlin and Cologne, respectively. The VHR data are employed to map urban LC and to compute 2D and 3D USCs. Some basic information about them are compiled in Table 1. The multi-spectral imagery comprises airborne UltraCamX and satellite-borne Ikonos-2 scenes acquired at different dates and spatial resolutions (denoted as ground sampling distance (GSD) in Table 1), but with the same spectral resolution. For each study area, the multi-spectral imagery is complemented by terrain and/or object height information. These are available in the form of digital elevation models (DEMs) and digital surface models (DSMs) derived from either UltraCamX stereo pairs or airborne LiDAR data (i.e., Riegl LMS-Q560). While DEMs represent the elevation of the bare ground surface without any objects like buildings or vegetation, DSMs contain information on both the Earth's surface as well as all objects on it (Maune, 2007).

The Landsat scenes are used to retrieve multi-temporal LST maps. As shown in Table 2, an overall number of 16 ETM+ images is considered. Each image was visually inspected to exclude scenes affected by clouds, cloud shadows, noise, or other unwanted artifacts. All data were recorded between July 1999 and April 2003, i.e., prior to the failure of the scan line corrector (SLC). Apart from a few exceptions, the acquisitions took place under largely favorable environmental conditions with clear skies, light winds, and only few precipitation events several days earlier (Table 2). The data were processed to Level 1T (precision and terrain corrected) by the United States Geological Survey (USGS) and both, the reflectance and thermal bands of each image acquisition take were provided at 30 m spatial resolution (USGS, 2014). To study the temporal dependencies of the relationship between USCs and LST, the time series covers all meteorological seasons. Moreover, five summer scenes per study area are selected to analyze potential intra-season differences in the USC–LST connection.

The ancillary data can be grouped into climatological and LU information. Climate records are needed to atmospherically correct the thermal bands of the Landsat scenes. They include hourly values of near-surface air temperature measured at the climate stations Berlin-Tempelhof and Köln-Bonn (Deutscher Wetterdienst, 2014) as well as atmospheric soundings of total precipitable water (TPW) captured within a 6-hour interval by the stations Lindenberg and Essen (University of Wyoming, 2014). LU information are required to identify potential intra-urban dependencies of the linkage between USCs and LST. They were made available as vector files by the cities of Berlin and Cologne. Each LU map contains a number of functional classes and the area of reference for both maps is the building block, i.e., the smallest inner-urban area surrounded by public streets.

3. Methods

The overall workflow of this study is displayed in Fig. 1. It consists of five consecutive steps, including (1) data preprocessing, (2) LC mapping, (3) USC calculation, (4) LST retrieval, and (5) correlation analysis. After data preparation, the VHR multi-spectral and height data are employed to map fine-scale urban LC. The resulting LC maps are then used in conjunction with the height information to compute 2D and 3D USCs. In a subsequent step, multi-temporal LST images are retrieved from the available Landsat ETM+ scenes. The spatio-temporal investigation of the USC–LST relationship constitutes the final stage of the workflow. It is achieved in the framework of a dedicated correlation analysis and by incorporating the LU maps of Berlin and Cologne. In the following paragraphs, the five steps are described in more detail.

3.1. Data preprocessing

An almost uniform sequence of preprocessing steps is applied to the database, with an exception being the VHR data. While the multi-spectral UltraCamX imagery of Berlin requires no further preprocessing, the Ikonos-2 scene over Cologne is atmospherically corrected using ATCOR (Richter and Schläpfer, 2014), panfused using the high-pass filter (HPF) resolution merge (Gangkofner et al., 2008), and coregistered to the LiDAR data using manually selected ground control points (GCPs). VHR height information for Berlin are only available in the form of a DSM. However, to obtain a normalized digital surface model (nDSM), a DEM is needed. The latter is created by applying the Diff2Min approach to the DSM (Voltersen et al., 2014). Subtraction of the generated DEM from the given DSM yields the final nDSM. It contains the height of urban objects relative to the ground. In contrast to Berlin, a DSM and DEM were provided by the city of Cologne. Accordingly, it is straightforward to compute the nDSM from the available data sources (Fig. 2).

In preparation for the subsequent LC classification, additional features are derived from the VHR inputs. Those are brightness, computed as the average reflectance of the blue, green, red, and near infrared (NIR) bands within a multi-spectral data set, the standard deviation of brightness, the normalized difference vegetation index (NDVI) (Tucker, 1979), and the slope (in percent) of the nDSMs (Zevenbergen and Thorne, 1987). The latter is useful for identifying

Table 1
The VHR data used to extract urban LC and to calculate USCs (date format: DDMonYY; time format: UTC).

	Multi-spectral imagery				Height information			
City	Sensor	Date/Time	Spectral bands	GSD	Sensor	Period	Products	GSD
Berlin	UltraCamX	23Sep10, 07:45Z	Blue, green, red, NIR	1.0 m	UltraCamX (stereo)	Sep10	DSM	1.0 m
Cologne	Ikonos-2	20Sep05, 11:07Z	Blue, green, red, NIR, pan	4.0 m (MS), 1.0 m (pan)	Riegl LMS-Q560	Mar10	DSM, DEM	1.0 m

Table 2
The Landsat ETM+ scenes used to retrieve LST and accompanying meteorological observations (date format: DDMonYY; time format: UTC). Except for precipitation and solar elevation, all values represent daily means measured at the climate stations of Berlin-Tempelhof and Köln-Bonn (Deutscher Wetterdienst, 2014). Precipitation is reported as sum that has accumulated three days prior to the acquisitions. Solar elevation information is taken from the metadata of the corresponding Landsat scenes.

				Meteorological observations[a]								
City	Season	Date	Time	AT	ST	RH	PR	WS	WD	SD	CC	SE
Berlin	Spring	17Apr03	09:51Z	12.7	11.5	46	0.0	3.5	71	12.7	0.8	44
	Summer	20Jun00	09:48Z	28.6	27.2	32	0.0	2.2	187	15.2	1.0	58
		11Jul99	09:55Z	24.3	24.3	49	0.0	4.5	78	8.9	5.7	55
		28Jul02	09:45Z	23.3	22.6	60	2.2	3.2	105	14.5	0.2	53
		14Aug00	09:53Z	24.0	22.5	47	0.1	1.8	119	13.4	0.3	48
		20Aug02	09:50Z	22.4	21.8	54	0.0	3.4	88	12.9	0.0	46
	Fall	24Sep00	09:47Z	10.5	9.5	69	0.0	4.1	90	11.3	0.0	35
	Winter	15Feb01	09:47Z	3.3	2.6	79	0.6	3.0	263	8.0	2.7	22
Cologne	Spring	03Apr02	10:10Z	14.9	14.3	41	1.4	6.0	91	11.8	0.9	41
	Summer	26Jun01	10:17Z	21.6	22.7	60	0.0	2.8	278	14.7	2.3	57
		05Jul01	10:11Z	24.1	24.7	52	0.0	4.4	90	13.4	3.0	58
		16Aug02	10:15Z	22.0	22.6	62	0.0	1.8	294	13.1	1.0	48
		22Aug01	10:10Z	22.8	23.7	58	0.9	2.7	90	11.8	1.7	47
		29Aug01	10:16Z	15.7	16.4	63	1.0	2.3	238	12.1	4.1	44
	Fall	22Oct00	10:12Z	14.5	13.0	78	1.3	3.2	155	9.5	1.7	27
	Winter	17Feb03	10:10Z	−2.6	−4.5	60	0.0	2.5	250	9.5	1.7	24

[a] AT = Air temperature [°C]; ST = Surface temperature [°C]; RH = Relative humidity [%]; PR = Precipitation [mm]; WS = Wind speed [m/s]; WD = Wind direction [degree]; SD = Sunshine duration [hours]; CC = Cloud cover [oktas]; SE = Solar elevation [°].

transitions between flat areas and elevated objects, such as buildings and trees (Priestnall et al., 2000).

Preprocessing of the ETM+ scenes involves two steps. First, to spatially match the imagery to the VHR data, coregistration is performed using GCPs and the DEMs. Second, the time series is clipped to the spatial extent of the VHR data. The climate records are prepared in a way that they correspond to the exact time of each Landsat acquisition. This is realized by means of linear interpolation between the individual measurements of both air temperature and TPW.

Since the LU maps of Berlin and Cologne comprise a different number of similar classes, it is necessary to harmonize them. Map harmonization is based on visual interpretation, expert knowledge, and experiences from previous studies (Heiden et al., 2012; Meinel et al., 2008; Pauleit and Duhme, 2000; Voltersen et al., 2014; Walde et al., 2014). Two of the major criteria applied are representativeness and simplicity. While the former means that the harmonized map classes should be typical for both study areas, the latter implies that they ought to be easily comprehensible. For this purpose, only those LU blocks with distinct physical and functional characteristics are selected to avoid the incorporation of mixed classes. The described aggregation procedure results in five final LU categories that are common to each map. These are block development, industrial/commercial areas, row development, detached housing, and allotment gardens (Fig. 2). The harmonized map categories are very close to the classification system proposed by Stewart and Oke (2012)

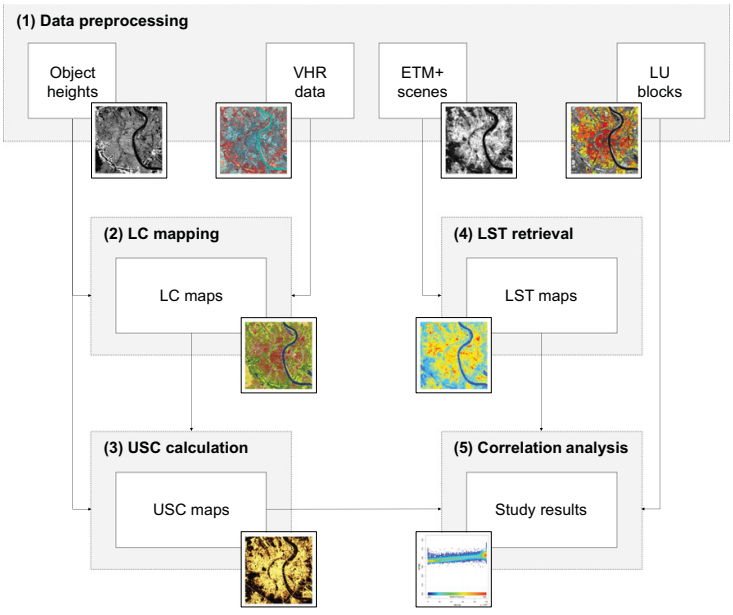

Fig. 1. The conceptual workflow of this study.

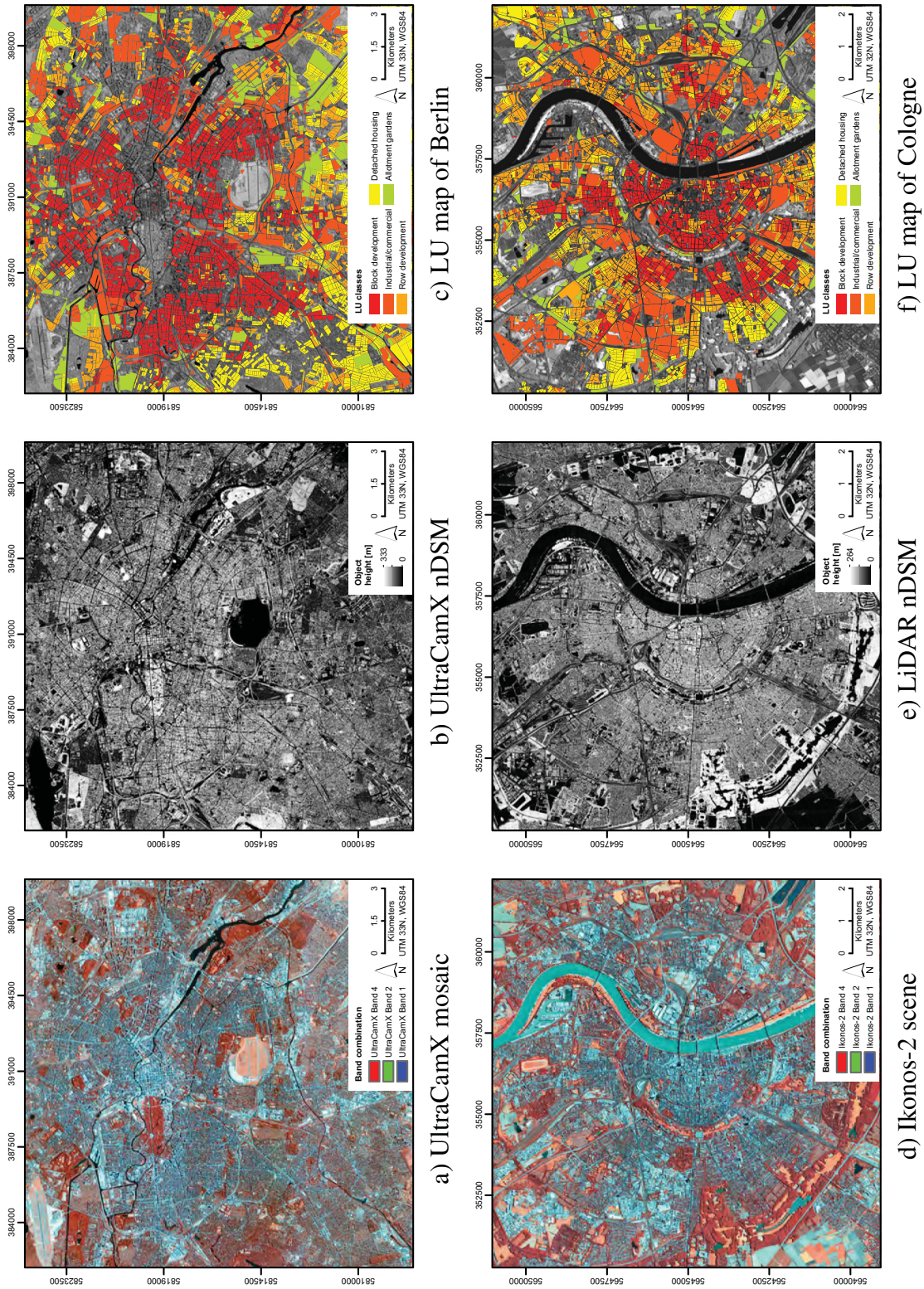

Fig. 2. Overview of the preprocessed VHR data and LU maps.

and correspond to the local climate zones (LCZs) of 'compact midrise' (block development), 'heavy industry' and 'large low-rise' (industrial/commercial areas), 'open midrise' (row development), 'open lowrise' (detached housing), and 'sparsely built' (allotment gardens). A visual impression of the classes in the final LU maps of Berlin and Cologne can be obtained in Voltersen et al. (2014).

3.2. LC mapping

Detailed LC maps provide the basis for the later computation of USCs. Since errors in these maps also determine the quality of the USCs to be derived, accurate classifications of urban LC are an important prerequisite for all further analyses. The methodology applied here is mainly based on the transferable classification scheme developed by Berger et al. (2013b) and refined by Voltersen et al. (2014). Six urban LC classes are extracted from the VHR data sets: Buildings, impervious surfaces, bare soil areas, tree canopy, grass/shrubs, and water bodies. To this end, a geographic object-based image analysis (GEOBIA) approach is chosen (Blaschke et al., 2008,2014) because of its distinct advantages over traditional, pixel-based classification techniques with respect to feature extraction from VHR multi-source imagery (Kim et al., 2010; Myint et al., 2011; Platt and Rapoza, 2008; Salehi et al., 2012; Yan et al., 2006; Zhou and Troy, 2008; Zhou et al., 2009). The mapping procedure is implemented as a single ruleset in Trimble eCognition Developer and its cognition network language (CNL) (Trimble Ltd., 2014).

In a first step, the input data are processed using the multi-threshold segmentation. This routine simultaneously segments and classifies the image into elevated and non-elevated objects according to a fixed nDSM threshold. Next, elevated objects are segmented again based on the NDVI. Tree seed objects with high NDVI values are now assigned and grown into adjacent pixels of elevated objects with a lower, but still distinctive NDVI. After the completion of the tree canopy class, the remaining elevated objects are labeled as buildings. The segmentation of non-elevated objects is performed by taking into account all spectral bands, image brightness, and the standard deviation of the brightness layer. The differentiation of ground objects is similar to the scheme outlined for elevated ones. Initially, the NDVI is employed to isolate seed objects belonging to the class grass/shrubs. These seeds are then grown into objects with a slightly lower NDVI. Subsequently, the remaining ground objects are ascribed to impervious surfaces, bare soil areas, or water bodies depending on their brightness, NDVI, slope, size, and standard deviation of brightness. In the last stage, some obvious misclassifications are corrected and a few reshaping algorithms are applied to the thematic objects for the purpose of border optimization. In this way, the original object primitives are successively transformed into more meaningful objects of interest that better correspond to the visual perception of humans (Baatz et al., 2008; Benz et al., 2004; Burnett and Blaschke, 2003). For an illustration of the described workflow, the reader is referred to Fig. 1 in Voltersen et al. (2014).

The final LC maps of Berlin and Cologne are displayed in Fig. 3. To assess mapping accuracy, VHR ortho imagery and Google products (Google Inc., 2014a,b) are used. A random sampling design is selected for validation comprising 100 sample points per class and map. The actual LC at each sample point location is then extracted from the reference data and compared to the maps. Finally, the numeric results of the comparison are transferred to an error matrix to determine classification accuracies and the kappa coefficient of agreement (Congalton and Green, 2009). Apart from some minor classification errors, the assessment confirms the high quality of the generated LC maps. While their overall accuracy is 92.2% for Berlin and 91.3% for Cologne, the kappa coefficient amounts to 0.91 and 0.89, respectively. Hence, the mapping results can be considered as very good and suitable for the calculation of USCs.

3.3. USC calculation

The obtained LC maps and the preprocessed nDSMs enable the calculation of various USCs. For the sake of brevity, an overview of the indicators featured in this study is compiled in Tables 3 and 4. As can be seen, 26 absolute and relative 2D/3D USCs are extracted from the VHR input data and products. Unlike absolute USCs, relative USCs represent normalized quantities and are therefore dimensionless. Note that all metrics are summarized at the Landsat pixel level (i.e., 30 m spatial resolution) as the basis for later comparisons with LST. For instance, the relative area of buildings (i.e., RA (B)) within each Landsat pixel is defined as the ratio of building area (taken from the VHR LC maps) and the total area of the respective resolution cell (i.e., 900 m^2). The effort of processing an overall number of 15,540,060 ETM+ pixels is rather high and takes about1000 working hours using a Windows desktop PC equipped with a 3.4 GHz quad-core processor and 8 GB of RAM. To provide an example of the USCs under consideration, the widely-used ISA (Lazzarini et al., 2013; Li et al., 2011; Myint et al., 2013; Weng et al., 2008; Xian, 2008; Xian and Crane, 2006; Yuan and Bauer, 2007; Yue et al., 2012; Zhang et al., 2009b) is illustrated in Fig. 3.

The selection of USCs is not based on any specific hypotheses. This means that, even though assumptions could be made on the basis of earlier works, there are no particular expectations with regard to the linkage between the chosen USCs and LST. Instead of hypotheses, the USC selection stems from existing research needs (cf. Section 1). There is a lack of comprehensive investigations relating 2D *and* 3D USCs to LST. The present study addresses this need by incorporating an extensive set of USCs as potential indicators of the surface UHI effect and as potential predictors for thermal sharpening applications. To this end, focus is put on both widely-used as well as more recently proposed metrics of the urban remote sensing literature (e.g., McGarigal, 2014; Meinel et al., 2008; Pan et al., 2008; Salomons and Berghauser Pont, 2012; Shannon and Weaver, 1949; Tompalski and Wezyk, 2012; Yu et al., 2010; Yuan and Bauer, 2007). While some of these USCs have already been used (e.g., ISA and VF), others, like VV2BV and UD, have never been analyzed before in the context of surface UHI studies. Accordingly, and in contrast to previous publications, the selection based on research needs enables novel, comprehensive, and consistent comparisons between 2D *and* 3D USCs within a single experiment.

3.4. LST retrieval

The retrieval of LST from the selected Landsat ETM+ scenes is accomplished by applying the mono-window algorithm (Qin et al., 2001) to the high gain thermal band of each image. The method is available as a C++ program (Zhang et al., 2006) and consists of three essential steps. First, the quantized calibrated pixel values (Q_{cal} in digital numbers, DNs) of the thermal band are converted to at-sensor spectral radiance (L_λ in W/(m^2 sr μm)) using

$$L_\lambda = \left(\frac{LMAX_\lambda - LMIN_\lambda}{Q_{calmax} - Q_{calmin}} \right) (Q_{cal} - Q_{calmin}) + LMIN_\lambda \quad (1)$$

where Q_{calmin} and Q_{calmax} are the minimum and maximum quantized calibrated pixel values in DN, and $LMIN_\lambda$ and $LMAX_\lambda$ are the at-sensor spectral radiances that are scaled to Q_{calmin} (=0) and Q_{calmax} (=255) in W/(m^2 sr μm) (Chander et al., 2009). Second, L_λ is converted to at-sensor brightness temperature (T_b in K) by

$$T_b = \frac{K2}{\ln\left(\frac{K1}{L_\lambda} + 1\right)} \quad (2)$$

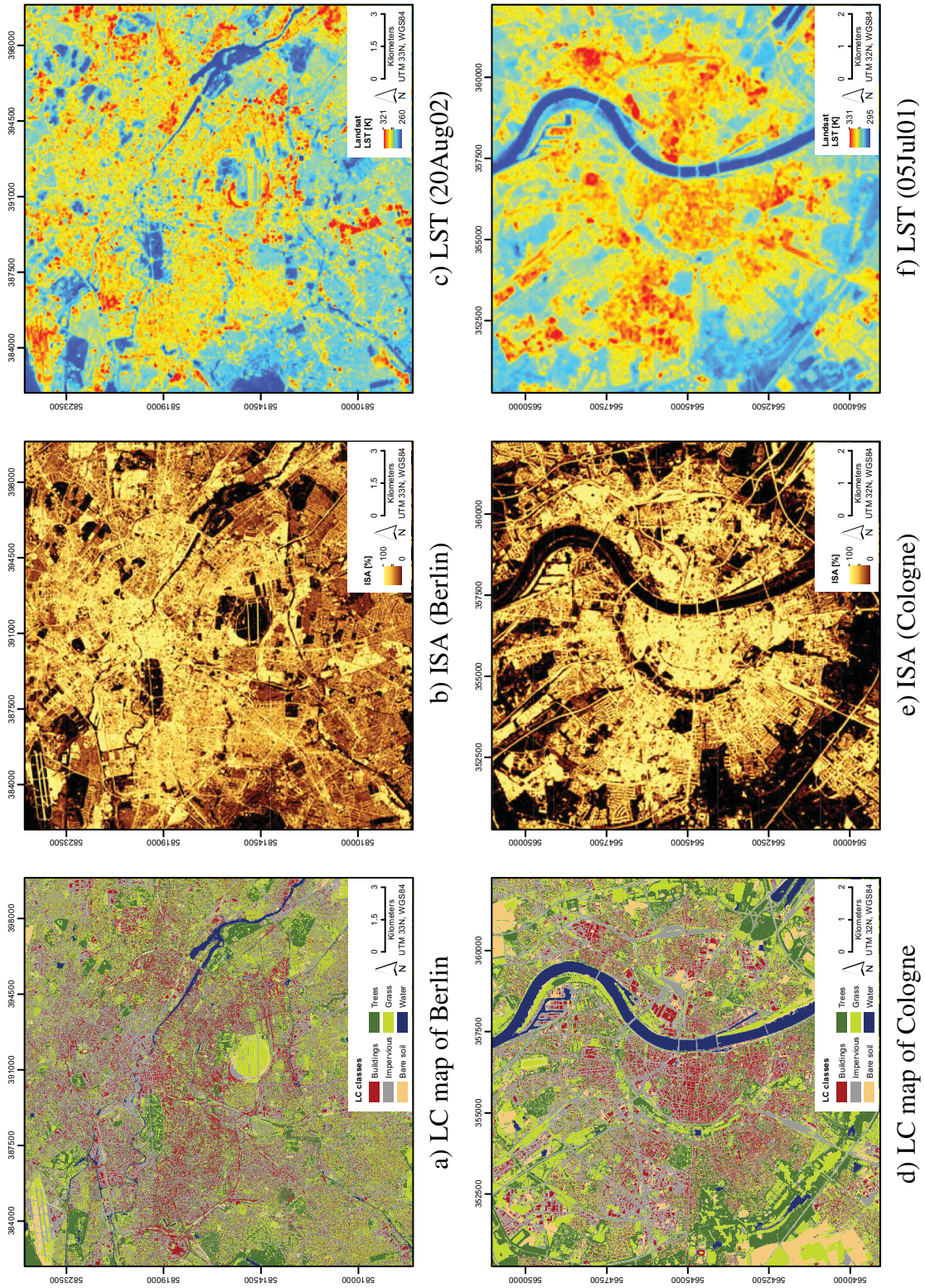

Fig. 3. Examples of the intermediate products of this study.

Table 3
Summary of the 2D USCs considered in this study.

Short form	Description	Range	Unit
2D (absolute)[a]			
BF	Mean area covered by buildings	$\pm 0 \ldots + \infty$	m^2
D2B	Mean distance between buildings and their nearest neighbor	$\pm 0 \ldots + \infty$	m
2D (relative)[b]			
FD (B)	Mean complexity of buildings as expressed by a perimeter–area ratio	$+1 \ldots + 2$	–
ISA	Ratio of area covered by buildings/impervious surfaces and total block area	$\pm 0 \ldots + 1$	–
LW (B)	Mean ratio of length and width of buildings	$+1 \ldots + \infty$	–
RA (B)	Ratio of area covered by buildings and total block area	$\pm 0 \ldots + 1$	–
RA (I)	Ratio of area covered by impervious surfaces and total block area	$\pm 0 \ldots + 1$	–
#B/A	Normalized number of buildings per block area	$-\infty \ldots + 1$	–
RA (G)	Ratio of area covered by grass/shrubs and total block area	$\pm 0 \ldots + 1$	–
RA (T)	Ratio of area covered by trees and total block area	$\pm 0 \ldots + 1$	–
VF	Ratio of area covered by trees and grass/shrubs and total block area	$\pm 0 \ldots + 1$	–
RA (S)	Ratio of area covered by bare soil and total block area	$\pm 0 \ldots + 1$	–
SDI	Measure quantifying the proportional abundance of each LC class	$\pm 0 \ldots + \infty$	–

[a] BF = Building footprint; D2B = Distance to buildings.
[b] FD (B) = Fractal dimension of buildings (McGarigal, 2014) ; ISA = Impervious surface area; LW (B) = Length to width ratio of buildings; RA (B) = Relative area of buildings; RA (I) = Relative area of impervious surfaces; #B/A = Number of buildings per block (Meinel et al., 2008) ; RA (G) = Relative area of grass/shrubs; RA (T) = Relative area of trees; VF = Vegetation fraction; RA (S) = Relative area of bare soil areas; SDI = Shannon's diversity (Shannon and Weaver, 1949) .

where $K2$ and $K1$ are calibration constants in K and W/(m^2 sr μm), respectively (Chander et al., 2009). Third, T_b is corrected for land surface emissivity and atmospheric effects to finally retrieve LST (T_s in K):

$$T_s = \frac{a(1 - C - D) + T_b\,(b(1 - C - D) + C + D) - DT_a}{C} \tag{3}$$

where a and b are dimensionless calibration constants and T_a is the effective mean atmospheric temperature in K (Qin et al., 2001). The parameters C and D are obtained from

$$C = \varepsilon\tau \tag{4}$$

$$D = (1 - \tau)(1 + (1 - \varepsilon)\tau) \tag{5}$$

where ε is the emissivity of the ground and τ is the atmospheric transmittance. Hence, the three unknowns needed to compute T_s from T_b are T_a, ε, and τ. T_a is approximated by a pair of linear equations corresponding to the two standard atmospheric profiles mid-latitude summer and mid-latitude winter (Cole et al., 1965; Qin et al., 2001). Its calculation only requires knowledge about the near-surface air temperature during the satellite overpass. This information is taken from the climate records available to this study (Deutscher Wetterdienst, 2014). Another set of empirical functions allows for the derivation of τ from the TPW observations at hand (Qin et al., 2001; University of Wyoming, 2014). Finally, ε is estimated using the ratio method proposed by Valor and Caselles (1996). This technique adaptively assigns emissivity values depending on the percentage of vegetation within each Landsat pixel and some user-defined thresholds. To quantify vegetation abundance, the NDVI (Tucker, 1979) is employed (Zhang et al., 2006). The ratio method is chosen because it is well-established and straightforward to implement. Moreover, it is able to estimate ε and its spatial variability not only for vegetated, but also for non-vegetated surfaces. This is because the abundance of impervious surfaces is inversely related to the abundance of vegetation within a city (Gluch and Ridd, 2010; Weng, 2012). Accordingly, the NDVI-based approach is suitable to map the spatial variability of ε in the context of this study because it enables a differentiation between vegetated and urban areas on the basis of continuous values of vegetation abundance.

Table 4
Summary of the 3D USCs considered in this study.

Short form	Description	Range	Unit
3D (absolute)[a]			
BH	Mean height of buildings	$\pm 0 \ldots + \infty$	m
BV	Mean volume of buildings	$\pm 0 \ldots + \infty$	m^3
BV/F	Mean volume of buildings per floor	$\pm 0 \ldots + \infty$	m^3
GFA	Mean area of all floors of a building	$\pm 0 \ldots + \infty$	m^2
TH	Mean height of trees	$\pm 0 \ldots + \infty$	m
TV	Mean volume of trees	$\pm 0 \ldots + \infty$	m^3
3D (relative)[b]			
BA	Aggregation of buildings as expressed by a combination of two ratios	$\pm 0 \ldots + 1$	–
CI	Ratio of building volume and total block area	$\pm 0 \ldots + \infty$	–
FAR	Ratio of sum of gross floor area and total block area	$\pm 0 \ldots + \infty$	–
UD	Intensity of urban development as expressed by a combination of four USCs	$-2 \ldots + 2$	–
SVF	Ratio of the radiation received (or emitted) by a planar surface to the radiation emitted (or received) by the entire sky hemisphere	$\pm 0 \ldots + 1$	–
UVI	Combined ratio quantifying the relation between vegetation and buildings	$\pm 0 \ldots + 1$	–
VV2BV	Ratio of tree volume and building volume	$\pm 0 \ldots + 1$	–

[a] BH = Building height; BV = Building volume; BV/F = Building volume per floor; GFA = Gross floor area; TH = Tree height; TV = Tree volume.
[b] BA = Building aggregation (Berger et al., 2013a); CI = Cubic index; FAR = Floor area ratio; UD = Urban density (Berger et al., 2013a); SVF = Sky view factor (Zakšek et al., 2011); UVI = Universal vegetation index (Tompalski and Wezyk, 2012); VV2BV = Vegetation volume to built-up volume (Tompalski and Wezyk, 2012).

Two examples of the resulting LST maps are shown in Fig. 3. The validation of these maps is a challenging task because the scales probed by satellite and field sensors are very different from each other. Moreover, LST is highly dynamic over space and time (Li et al., 2013), which makes it difficult to collect appropriate reference data for this study. In order to provide a rough estimate of the retrieval errors to be expected, the scientific literature can be consulted. Qin et al. (2001) assess the accuracy of the mono-window algorithm by means of the radiance-based method (Li et al., 2013). They find that the differences between retrieved and simulated Landsat LST range from 0.02 to 0.52 K under varying conditions. Sobrino et al. (2004) evaluate three methods to retrieve LST from Landsat Thematic Mapper (TM) imagery. With a root mean square error (RMSE) of 0.9 K, their results suggest that the mono-window algorithm performs best when atmospheric sounding data are available. Drawing from the experiences of the above studies, it is estimated that the LST maps considered in this paper feature uncertainties not higher than 1–2 K.

3.5. Correlation analysis

In the final stage of the presented workflow, the calculated USC maps are compared to the retrieved LST images to assess their spatio-temporal relationship. This is achieved by the use of Spearman's rank correlation coefficient, also known as Spearman's rho or simply ρ (Spearman, 1904, 1907). Other than the product–moment correlation after Pearson (1896, 1920), ρ is a nonparametric measure of statistical dependence between two given streams of data. It estimates how well the connection between these variables can be described by a monotonic function without making any assumptions about their frequency distribution (Hauke and Kossowski, 2011). Therefore, it is a suitable estimator when the distributions of the input data are non-Gaussian (Kowalski, 1972), as is the case for the USCs selected in this study. Furthermore, ρ does not require a linear relationship between the statistical series of interest (Hauke and Kossowski, 2011). The strength of association is quantified by correlating the ranks of observations, which has the additional advantage of being more robust against outliers (Croux and Dehon, 2010).

In principle, Spearman's ρ is a special form of the Pearson coefficient. For a sample size of n, it is formulated as

$$\rho = \frac{\sum_{i=1}^{n}(x_i - \bar{x})(y_i - \bar{y})}{\sqrt{\sum_{i=1}^{n}(x_i - \bar{x})^2 \sum_{i=1}^{n}(y_i - \bar{y})^2}} = \frac{cov(x,y)}{s_x s_y} \tag{6}$$

where x_i and y_i are the ranks of the variables X_i and Y_i, $\bar{x}$ and $\bar{y}$ are the mean ranks of X and Y, $cov(x,y)$ is the covariance of x and y, and $s_x s_y$ is the product of their standard deviations, respectively. It is a dimensionless quantity that ranges between −1 and +1, thereby indicating either a perfect negative or positive correlation. When ρ becomes 0, no statistical dependence exists. The significance of the resulting ρ-values can be determined via

$$t = \rho\sqrt{\frac{n-2}{1-\rho^2}} \tag{7}$$

which corresponds to an asymptotic approximation of the Student's t-distribution with $n-2$ degrees of freedom under the null hypothesis (Press et al., 1992).

It is worth noting that the mutual relationship between USCs and LST is assessed at the spatial resolution of the Landsat data (i.e., 30 m). To facilitate the comparisons, image pixels covering water bodies are masked out (cf. Xian and Crane, 2006; Yuan and Bauer, 2007). Moreover, NoData values occurring in the north-western parts of two ETM+ scenes over Berlin are excluded from any calculation. As part of the correlation analyses, the LU maps of both study areas (Table 2) are employed to identify potential intra-urban dependencies of the USC–LST connection. In this context, only those Landsat pixels that completely fall within a single LU block are regarded.

4. Results

The main result of this study is presented in Table 5. It quantifies the relationship between the selected USCs and the LST scenes under consideration. The observed relations are expressed by means of Spearman's rank correlation coefficient (ρ). All displayed correlation values are significant at the 0.01 level. To facilitate data interpretation, a color coding scheme is applied to the figures. While lower correlations are indicated by white color, tones of blue and orange suggest higher negative and positive correlations, respectively. There are two ways to comprehend the table. When read from top to bottom, the correlation differences between the individual USCs become obvious. When read from left to right, the spatio-temporal dependencies of the USC–LST connection are revealed. In particular, any potential effects of the study area as well as both the season and date of the Landsat acquisitions are emphasized. Based on these results, some general observations of the linkage between USCs and LST can be made.

First, no matter which city, season or acquisition date is regarded, the performances of the USCs are, relative to each other, fairly consistent. With values of up to ±0.79, VF and ISA yield the highest correlations within the comparison. Stronger positive and negative relationships are also found for UVI, VV2BV, RA (T), and UD. Depending on the framework conditions, the maximum scores obtained from these indicators range between −0.77 (UVI) and 0.65 (UD). In contrast to the aforementioned observations, most of the USCs perform only moderately. Typical representatives of the top end, the mid-range, and the bottom end of this group of parameters are BF, SVF, LW (B), and RA (G), reaching ρ-values of up to 0.62, −0.58, 0.52, and −0.39, respectively. There are only two USCs that show almost no statistical connection to LST. Under favorable conditions, these metrics produce correlation scores as high as 0.29 (SDI) and 0.22 (RA (S)).

Second, the relationship between USCs and LST varies over space and remains about the same over time. From a spatial viewpoint, the strength of correlation differs in dependence of the test site. On average, the Spearman coefficients reported for Cologne are about ±0.16 higher than those measured in Berlin. From a temporal viewpoint, the observed rank correlations do not change much when thermal data from different seasons and dates are used to retrieve LST. This is supported by the mean standard deviations of the ρ-values, which are comparatively low for both Berlin (0.06) and Cologne (0.07). Nevertheless, there are a few exceptions suggesting that at least some larger inter- and intra-season fluctuations exist. For example, the winter scene acquired over Berlin (15Feb01) and one of the summer scenes of Cologne (29Aug01) feature correlation coefficients that are on average 0.1 lower than those listed for the other ETM+ images.

In addition to the above differences in correlation between Berlin and Cologne, Fig. 4 deals with the intra-urban dependencies of the linkage between USCs and LST. More specifically, it displays the relationship between four selected USCs and the multi-temporal average of LST as a function of the predominant type of LU in both cities. Each USC belongs to one of the subcategories defined in Table 5 (i.e., absolute/relative, 2D/3D) and, at the same time, represents the best performing indicator of this particular group. The spider charts make clear that the USC–LST connection does not only differ between, but also within the two study areas, no matter which of the four USCs is examined. In Berlin, the highest absolute values of Spearman's ρ are reported for detached housing. On average, they amount to 0.42. Row development, allotment gardens, and block development form a group of use types with similar mean

Table 5
Spatio-temporal relationship between the selected USCs and LST as expressed by Spearman's rank correlation coefficient (date format: DDMonYY).

	Berlin								Cologne							
	Spr	Sum	Sum	Sum	Sum	Sum	Fall	Win	Spr	Sum	Sum	Sum	Sum	Sum	Fall	Win
USC	17Apr03	20Jun00	11Jul99	28Jul02	14Aug00	20Aug02	24Sep00	15Feb01	03Apr02	26Jun01	05Jul01	16Aug02	22Aug01	29Aug01	22Oct00	17Feb03
2D (absolute)																
• BF	+0.35	+0.38	+0.35	+0.47	+0.37	+0.43	+0.44	+0.31	+0.55	+0.60	+0.62	+0.59	+0.51	+0.39	+0.61	+0.52
• D2B	+0.20	+0.22	+0.19	+0.31	+0.22	+0.28	+0.29	+0.22	+0.48	+0.53	+0.54	+0.51	+0.43	+0.33	+0.53	+0.43
2D (relative)																
• FD (B)	+0.11	+0.12	+0.09	+0.20	+0.12	+0.18	+0.18	+0.13	+0.45	+0.48	+0.50	+0.47	+0.38	+0.29	+0.49	+0.38
• ISA	+0.57	+0.56	+0.62	+0.66	+0.58	+0.66	+0.62	+0.40	+0.73	+0.77	+0.79	+0.75	+0.67	+0.57	+0.72	+0.66
• LW (B)	+0.17	+0.20	+0.16	+0.28	+0.19	+0.26	+0.26	+0.21	+0.47	+0.51	+0.52	+0.49	+0.41	+0.31	+0.52	+0.41
• RA (B)	+0.35	+0.38	+0.36	+0.48	+0.38	+0.45	+0.45	+0.31	+0.56	+0.61	+0.63	+0.60	+0.52	+0.40	+0.62	+0.53
• RA (I)	+0.40	+0.39	+0.44	+0.45	+0.40	+0.47	+0.42	+0.29	+0.59	+0.62	+0.64	+0.59	+0.52	+0.46	+0.56	+0.50
• #B/A	−0.19	−0.22	−0.19	−0.32	−0.22	−0.29	−0.29	−0.20	−0.52	−0.56	−0.57	−0.54	−0.46	−0.35	−0.57	−0.46
• RA (G)	−0.30	−0.21	−0.27	−0.34	−0.24	−0.33	−0.31	−0.18	−0.36	−0.32	−0.33	−0.39	−0.29	−0.21	−0.37	−0.34
• RA (T)	−0.48	−0.52	−0.58	−0.51	−0.56	−0.52	−0.50	−0.28	−0.42	−0.55	−0.53	−0.60	−0.65	−0.67	−0.49	−0.54
• VF	−0.59	−0.57	−0.64	−0.67	−0.62	−0.68	−0.65	−0.40	−0.65	−0.72	−0.72	−0.79	−0.72	−0.66	−0.70	−0.67
• RA (S)	+0.14	+0.12	+0.15	+0.09	+0.18	+0.13	+0.14	+0.07	−0.01	+0.04	+0.01	+0.15	+0.17	+0.22	+0.04	+0.09
• SDI	+0.06	+0.13	+0.04	+0.16	+0.10	+0.15	+0.17	+0.18	+0.26	+0.26	+0.29	+0.22	+0.16	+0.09	+0.25	+0.15
3D (absolute)																
• BH	+0.27	+0.31	+0.28	+0.41	+0.30	+0.38	+0.39	+0.28	+0.50	+0.55	+0.57	+0.54	+0.45	+0.33	+0.57	+0.49
• BV	+0.33	+0.37	+0.34	+0.46	+0.36	+0.43	+0.43	+0.31	+0.54	+0.59	+0.61	+0.58	+0.50	+0.38	+0.60	+0.52
• BV/F	+0.35	+0.37	+0.35	+0.47	+0.37	+0.43	+0.44	+0.31	+0.55	+0.60	+0.61	+0.59	+0.51	+0.39	+0.61	+0.52
• GFA	+0.33	+0.37	+0.34	+0.46	+0.36	+0.43	+0.43	+0.31	+0.55	+0.59	+0.61	+0.58	+0.50	+0.38	+0.60	+0.52
• TH	−0.27	−0.30	−0.35	−0.26	−0.34	−0.28	−0.26	−0.13	−0.34	−0.46	−0.43	−0.51	−0.56	−0.59	−0.39	−0.42
• TV	−0.37	−0.42	−0.47	−0.40	−0.46	−0.41	−0.39	−0.21	−0.40	−0.53	−0.50	−0.58	−0.62	−0.65	−0.46	−0.50
3D (relative)																
• BA	+0.31	+0.35	+0.32	+0.45	+0.35	+0.42	+0.42	+0.29	+0.55	+0.60	+0.62	+0.59	+0.50	+0.38	+0.61	+0.53
• CI	+0.34	+0.37	+0.34	+0.47	+0.36	+0.43	+0.44	+0.31	+0.55	+0.60	+0.61	+0.59	+0.50	+0.38	+0.61	+0.53
• FAR	+0.34	+0.37	+0.34	+0.47	+0.36	+0.43	+0.44	+0.31	+0.55	+0.60	+0.62	+0.59	+0.50	+0.38	+0.61	+0.53
• UD	+0.40	+0.43	+0.43	+0.53	+0.43	+0.50	+0.49	+0.32	+0.58	+0.64	+0.65	+0.63	+0.54	+0.43	+0.64	+0.56
• SVF	−0.32	−0.36	−0.33	−0.43	−0.34	−0.41	−0.41	−0.31	−0.52	−0.56	−0.58	−0.55	−0.48	−0.41	−0.56	−0.49
• UVI	−0.44	−0.49	−0.50	−0.56	−0.51	−0.54	−0.53	−0.34	−0.67	−0.75	−0.75	−0.77	−0.71	−0.62	−0.72	−0.66
• VV2BV	−0.43	−0.48	−0.49	−0.55	−0.50	−0.53	−0.52	−0.33	−0.66	−0.74	−0.74	−0.76	−0.71	−0.62	−0.71	−0.64
Spearman's ρ	−1							0								+1

scores ranging from 0.31 to 0.28. The lowest mean rank correlation (0.24) is found in areas characterized by industrial and commercial LU. For Cologne, the numbers obtained are quite different. Judged by the mean absolute values of Spearman's ρ in descending order, block development (0.52) leads the ranking. In between lie the performances of row development, detached housing (both 0.41), and industrial/commercial areas (0.35). Allotment gardens (0.07) provide the lowest correlations.

Another prominent feature of the spider charts is that the highest overall rank correlations are always achieved when all LU blocks or even all Landsat pixels enter the calculations. The corresponding correlation coefficients are significantly higher than those of the individual LU classes. For Berlin and Cologne, they reach mean values of 0.54 and 0.65 in case all LU blocks are investigated as well as 0.46 and 0.63 in case all Landsat pixels are analyzed.

5. Discussion

In the following paragraphs, the performances of 2D and 3D USCs are compared and the spatio-temporal dependencies of the USC–LST connection are debated on the basis of the obtained correlation statistics. A discussion of some methodological considerations concludes the section.

5.1. Comparison of 2D and 3D USCs

From the numbers in Table 5, it becomes clear that ISA and VF, some of the most widely-used 2D metrics (Chen et al., 2006; Lazzarini et al., 2013; Liu and Zhang, 2011; Ogashawara and da Silva Brum Bastos, 2012; Small, 2006; Weng et al., 2004; Xian, 2008; Xian and Crane, 2006; Yuan and Bauer, 2007; Zhang et al., 2009b), are most strongly correlated with LST. The only 3D USCs showing similar, but not as high overall performances are UVI and VV2BV. Apart from this, the general tendency is that ISA and VF outperform all other USCs, including 2D and 3D indicators. Considering that the presence of buildings and trees adds a third spatial dimension to the urban landscape, one might not expect the 3D USCs to have a lower discriminative power than simple 2D measures like ISA and VF. The explanation for this observation is linked to the way LST is determined with remote sensing technology (Roth et al., 1989; Voogt and Oke, 1997).

In this study, thermal data provided by the Landsat-7 satellite mission are employed to retrieve LST. Since the onboard ETM+ sensor has a nadir-pointing viewing geometry, cities are observed from a bird's eye view with maximum "off-nadir" angles of 7.4° towards the edges of a scene (Hodgson and Kar, 2008). This means that horizontal urban surfaces (e.g., roofs, tree tops, and roads) are oversampled while vertical urban surfaces (e.g., building walls) are underrepresented in ETM+ based retrievals of LST. The inherent oversampling of plane areas is likely to be the reason why certain 2D USCs are more closely related to LST than 3D ones. It follows that the correlation statistics presented above are only valid for LST measurements derived from satellite remote sensing with nadir-pointing imaging systems. A more objective comparison between 2D and 3D USCs would only be possible if the temperature of the true active surface, i.e., the entire 3D urban surface with which the atmosphere is in contact (Roth et al., 1989; Voogt and Oke, 1997), was known.

Subject to data availability, an alternative approach could be to link 2D and 3D USCs to city-wide maps of both LST as well as (near-surface or rooftop level) air temperature and to compare the obtained correlation statistics. In the framework of such an experiment, it is expected that 2D USCs (e.g., ISA) will have a stronger

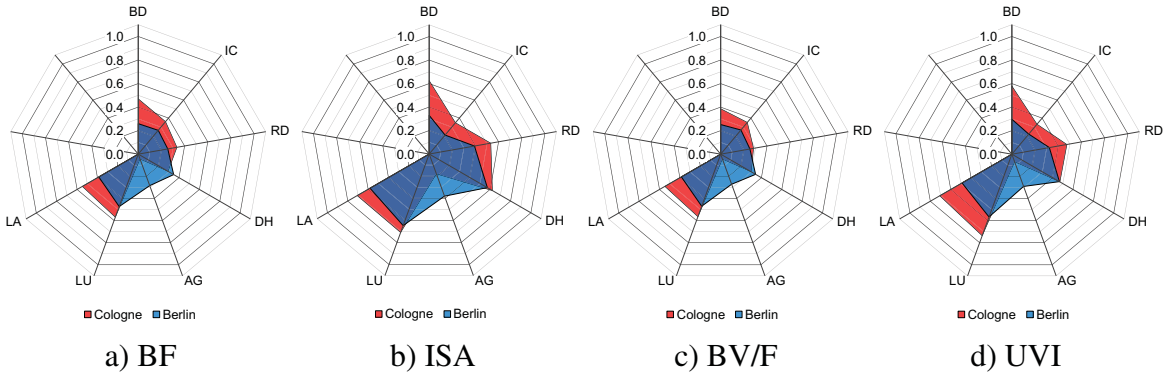

Fig. 4. Correlation between four selected USCs and the multi-temporal average of LST as a function of urban LU. The strength of association is quantified by absolute values of Spearman's ρ. BD = Block development; IC = Industrial/commercial areas; RD = Row development; DH = Detached housing; AG = Allotment gardens; LU = All LU blocks; LA = All Landsat pixels.

relationship to surface UHIs (i.e., the LST maps) while 3D USCs (e.g., the SVF) will be more closely connected to the canopy layer UHI (i.e., the air temperature maps). This assumption would be supported by UHI theory (e.g., Oke, 1981, 1982) and would be in line with the results of this study as well as the findings of related works (e.g., Srivanit and Kazunori, 2011).

5.2. Spatial dependencies of the USC–LST relationship

The study results enable the identification of inter- and intra-urban differences in the USC–LST connection. With respect to the former, Table 5 suggests that the statistical dependence between USCs and LST is much higher for Cologne than it is for Berlin. There are several factors causing this phenomenon, and all of them are related to the geography of the cities. To facilitate the comparison, Fig. 2 can be consulted. When compared to each other, the most noticeable differences between Cologne and Berlin are their spatial forms and structures. Over the centuries, Cologne has grown radially around its historic center. It therefore features a very compact structure that can be described by the concentric ring model (Burgess, 1925). In contrast, Berlin represents a consolidation of early settlements that has spread extensively throughout the years. Accordingly, it is a decentralized city spanning a much larger area and resembling the multiple nuclei model (Harris and Ullman, 1945).

The less compact structure of Berlin can be quantified by the ratio of mean building height (i.e., BH) to the mean distance between buildings (i.e., D2B). This geometric measure provides an estimate of the canyon aspect ratio (CAR) (Oke, 1988) for an entire city. While CAR amounts to 1.53 for Cologne, it only reaches a score of 0.84 for Berlin. Considering that regular and deep street canyons generally feature CAR values of around 1 and 2, respectively (Vardoulakis et al., 2003), this comparison shows that Berlin is structurally much less compact than Cologne. The above observation is also reflected by a higher number of evenly distributed and variably sized parks and other urban green spaces in Berlin (cf. Fig. 2). As a result, the average ratio of vegetation volume to building volume (i.e., VV2BV) is 21% higher for the capital city. Moreover, the LC maps extracted from the VHR data indicate a 5 and 7% higher share of grass (i.e., RA (G)) and tree canopy cover (i.e., RA (T)) in Berlin. The latter estimation seems reasonable given that alone more than 400,000 trees line its streets while Cologne only hosts 76,000 street trees (Berlin Senate Department for Urban Development and the Environment, 2013; Stadt Köln, 2013). When normalized by the administrative area of the cities, these numbers correspond to 448 (Berlin) and 188 (Cologne) street trees per km^2. Another important characteristic of Berlin is its more regular arrangement of building blocks as well as the occasionally grid-like network of streets (cf. Fig. 2).

Individually and in their entirety, these factors, be it urban form and compactness, urban green spaces and street trees, or the configuration of LC elements (cf. Arnfield, 2003; Gago et al., 2013; Grimmond, 2007; Li et al., 2011; Loughner et al., 2012; Ngie et al., 2014; Ren et al., 2013; Rizwan et al., 2008; Unger, 2004; Zhang et al., 2009a; Zhou et al., 2011), essentially contribute to a much less pronounced surface UHI of Berlin and a much more pronounced surface UHI of Cologne (cf. Fig. 3). Fig. 5 supports this statement by quantifying the intensity of the surface UHIs for the ETM+ scenes investigated. After Xian (2008), surface UHI intensity can be defined as the mean temperature difference (ΔLST in K) between four classes of urban land and the rural background (ISA$<$10%). As can be seen, the surface UHI intensity of Berlin is often significantly smaller than the one of Cologne, especially in the warm season. It is deduced that the distinct geographies of Berlin and Cologne do not only affect their thermal properties, but that they also determine the differences in correlation found for both test sites.

With respect to intra-urban differences, Fig. 4 highlights that the linkage between USCs and LST varies within the boundaries of a city. In particular, the spider charts contain two striking features. First, the observed relationships depend on the inner-urban region that is analyzed. Second, the LU-specific correlation statistics are different for Berlin and Cologne. A closer examination of these issues reveals that the strength of association is often driven by intra-class variability. That is, for a given type of urban LU, Spearman's ρ generally increases when both the USC and LST scene considered span a broader range of values. This is typically the case for LU classes composed of thermally distinct LC elements. For example, blocks dominated by detached housing usually feature a mixture of buildings, impervious surfaces, trees, short vegetation, and sometimes even water bodies. All of these LC types exhibit individual radiative properties and thus contribute to a strong within-class variability of the LST signal. At the same time, the composition of these LC units is different from block to block, leading to a simultaneous spread of USC values found for detached housing. To illustrate this causality, Fig. 6 compares the ISA–LST scatterplots for detached housing and allotment gardens. It is demonstrated that higher ρ scores are achieved for larger ranges of the two variables, especially in the case of Cologne. This tendency is substantiated by the fact that the highest overall performances of any USC are obtained when all LU blocks or even all Landsat pixels enter the calculations (Fig. 4). Hence, it seems reasonable to assume that, within a particular LU category, wider ranges of USC and LST are frequently accompanied by higher rank

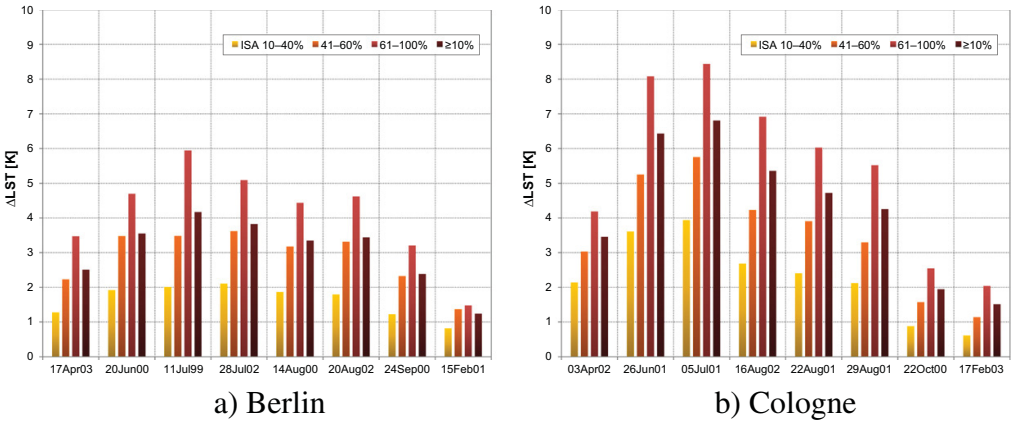

Fig. 5. Surface UHI intensities (ΔLST) of Berlin and Cologne.

correlation coefficients. The implications of these findings are threefold. First, LU-dependent correlation analyses allow for the detection of areas within a city that are more or less connected to LST. Second, they provide a means to better understand the higher overall correlations reported for an entire test site. And finally, they emphasize that a single correlation value only represents an integrated estimate of the USC–LST relationship which might not be sufficient for certain types of studies.

5.3. Temporal dependencies of the USC–LST relationship

Table 5 indicates that the linkage between USCs and LST is fairly consistent over time. In fact, many USCs, including ISA and VF, exhibit a quite stable behavior across all LST images. Nevertheless, there are a few exceptions suggesting that at least some larger inter- and intra-season variations exist. The most prominent examples are provided by the winter scene acquired over Berlin (15Feb01) and one of the summer scenes of Cologne (29Aug01). On average, the absolute ρ scores yielded for these LST measurements are 0.1 lower than those gained for the remaining ETM+ acquisitions. Closer inspection reveals that the observations are not the result of an individual cause. The above tendencies rather stem from an interplay of factors known to affect LST and its relation to USCs, including the season of acquisition, vegetation phenology, meteorological settings, and others (e.g., Chen et al., 2006; Li et al., 2011; Liu and Weng, 2008; Ren et al., 2013; Roth et al., 1989; Weng et al., 2008; Yuan and Bauer, 2007; Zhang et al., 2009b).

In the case of Berlin, the winter scene (15Feb01) was acquired at a much smaller, season-specific solar altitude (22.9°) than the other images (average: 48.9°). This circumstance is accompanied by a significant decrease in solar radiation and a substantial increase in surface shadowing before and during the time of acquisition. Due to the lack of area-wide insolation, the heating of the urban landscape is partly halted (e.g., Theeuwes et al., 2014). While being closely linked to the season of acquisition, vegetation phenology constitutes another important aspect. Since the rate of plant transpiration is greatly reduced during the cold (leaf-off) season, the effect of vegetation cooling is barely evident in winter LST imagery. Another reason is that temperatures of the surrounding man-made surfaces are already low due to the decreased insolation and/or increased shading.

By comparing the correlation values obtained for the winter images of Berlin (15Feb01) and Cologne (17Feb03), it can be derived that further factors need to be considered. Otherwise, it would not be possible to explain the observed differences in correlation. In this regard, a number of climate variables come into question (Table 2). The most notable disparity between the winter acquisitions is cloud cover, which is known to mitigate surface UHI intensity (Oke et al., 1991). It amounts to 2.7 and 0 oktas for Berlin and Cologne, respectively. Other causes for the weaker relationship between USCs and winter LST in Berlin (i.e., as compared to Cologne) are indicated by a lower sunshine duration (8 h) and solar elevation (22.9°) as well as higher values of wind speed (3 m/s) and precipitation (0.6 mm) for Berlin (Table 2). Besides these meteorological differences, and as detailed in Section 5.2, the distinct geographies of both cities have to be taken into account.

For understanding the USC–LST relationships found in Cologne (29Aug01), the meteorological context of the respective ETM+ scene has to considered. The normalized graphs and statistics in Table 6 show that climatic conditions have changed significantly over the three days prior to the acquisition (i.e., starting at t (−3d)). More specifically, an increase in cloud cover (by 3.1 oktas), wind speed (by 2.1 m/s), and peak wind speed (by 5.6 m/s) as well as a decrease in sunshine duration (by 6.1 h) were recorded at the observing station of Köln-Bonn at t (−2d). These atmospheric changes were associated with a smaller precipitation event (1 mm) and led to a sudden and steep drop in near-surface air temperature of 12 ° C by t (−1d). On the date of acquisition (t (−0d)), the air temperature was 1.4 K lower than the long-term mean for the international reference period (1981–2010). This is in stark contrast to the other four summer scenes, which were on average 5.3 K warmer than the 30-year mean (Deutscher Wetterdienst, 2014). Moreover, cloud cover was comparably high and amounted to 4.1 oktas (cf. Table 2). This indicates that the weather on that day was characterized by a mix of sun and clouds, even though the exact timing and spatial distribution of cloud cover remains unknown. Given these meteorological circumstances, it can be expected that Cologne's ability to generate a surface UHI was considerably reduced on 29Aug01.

Taken together, all of the above factors contribute to the perceptibly weaker correlations for scenes 15Feb01 and 29Aug01 when compared to the other thermal images used within the experiment. In other words, the temperature gradients between rural and urban areas as well as between individual urban LC/LU structures are less pronounced under certain conditions. This is also reflected by the relatively low surface UHI intensities reported for the acquisitions in question (Fig. 5). The provided examples demonstrate that the association between USCs and LST can be subject to larger inter-

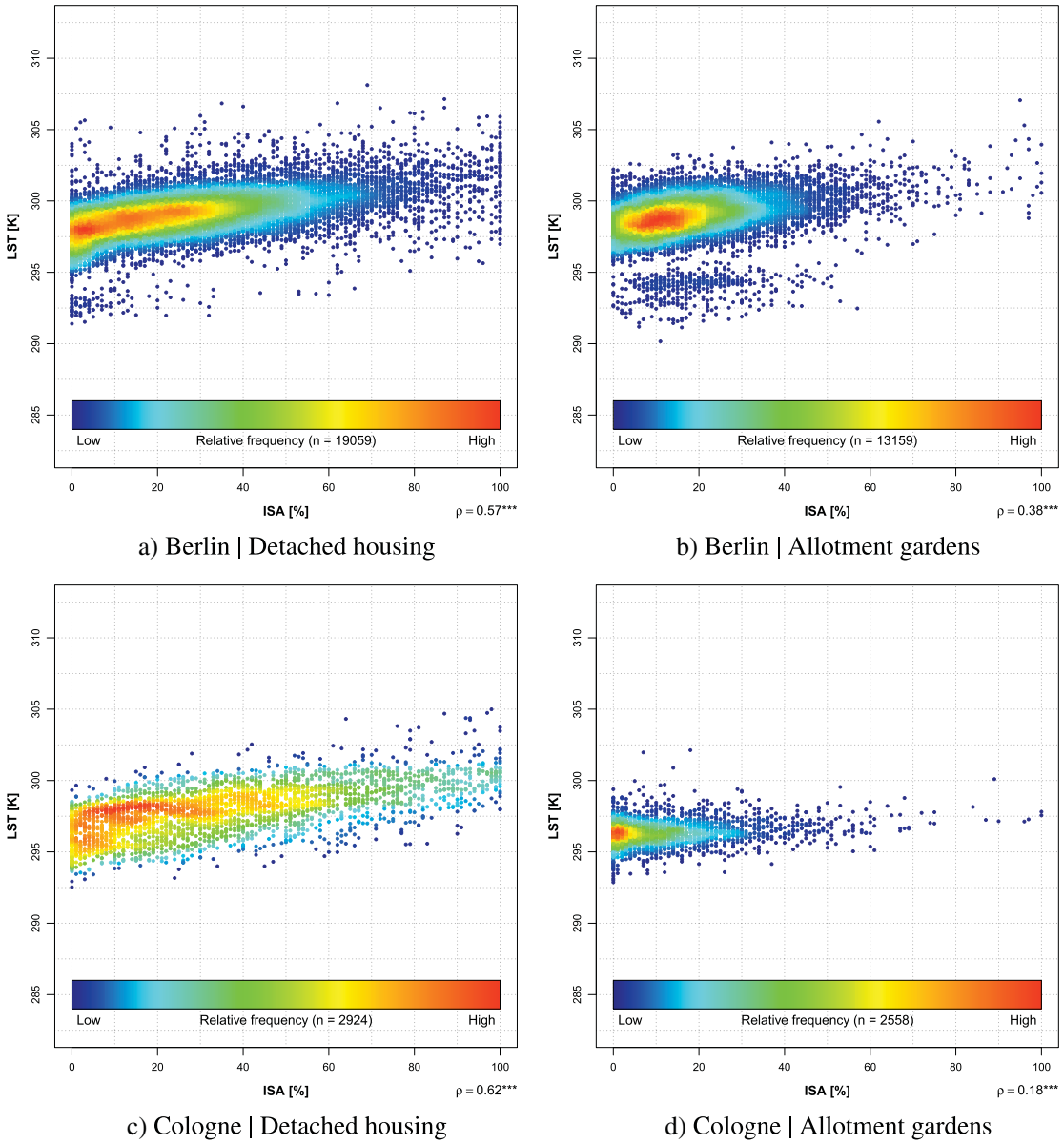

Fig. 6. Scatterplots of ISA versus the multi-temporal average of LST for two selected LU types.

and intra-season fluctuations for different reasons. This highlights the importance of and need for careful data selection and interpretation when studying surface UHIs and their determining factors with mono-temporal remote sensing. At the same time, it is emphasized that the increased empirical evidence gained from LST time series allows for the deduction of general data trends at higher levels of confidence. Thus, investigating thermal infrared measurements from multiple dates represents an adequate means to obtain a more complete picture of the USC–LST connection.

5.4. Methodological considerations

For a better interpretation of the study results, it is important to highlight potential issues and errors resulting from the workflow presented (Section 3). Therefore, the main sources of uncertainties related to the data and methods used in this work are summarized and discussed in the following. In general, they can be grouped according to the individual stages of the overall methodology (Fig. 1).

Table 6
Meteorological context of the ETM+ scene acquired over Cologne on 29Aug01. The reported climate parameters were measured at the observing station of Köln-Bonn (Deutscher Wetterdienst, 2014). The statistics provided for each parameter (avg, min, max) are based on daily mean values and refer to the time period 14 days prior to the Landsat acquisition. The graphs show the normalized signal of each parameter for this time period, with the blue line representing the temporal mean and the red dots corresponding to the minimum and maximum values observed.

Climate parameter	Unit	Avg	Min	Max	Normalized temporal signal
Air temperature	°C	20.9	14.4	25.7	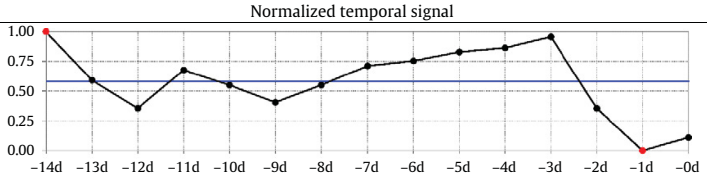
Precipitation	mm	0.4	0.0	2.3	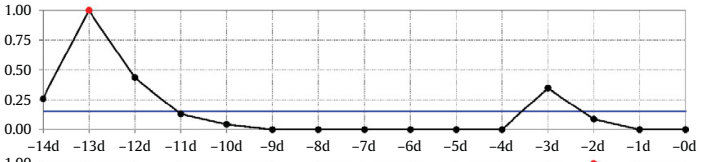
Wind speed	m/s	2.7	1.6	4.4	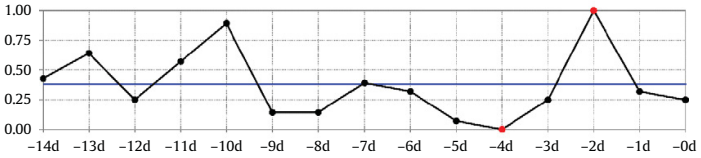
Peak wind speed	m/s	8.3	5.4	12.9	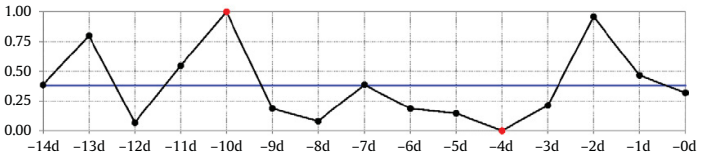
Cloud cover	Oktas	3.9	0.7	7.1	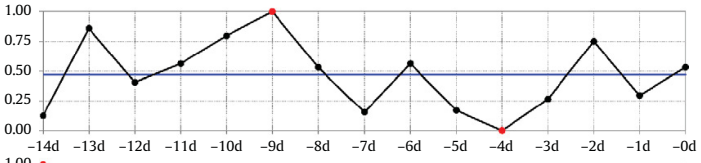
Sunshine duration	Hours	8.9	1.8	12.4	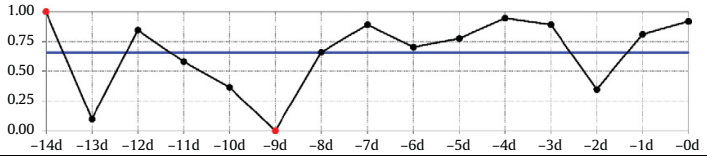

5.4.1. Data preprocessing

The thermal bands of all ETM+ scenes were not provided at their original spatial resolution of 60 m. Upon delivery, the data had already been oversampled to a pixel size of 30 m using the cubic convolution interpolation method (USGS, 2014). Since this process creates artificial and redundant image information, it also introduces a bias to the observed correlations.

5.4.2. LC mapping and USC calculation

Even though the LC maps were found to be suitable for the calculation of USCs, there are two issues to be considered. First, mapping assessment revealed that the LC classifications of Berlin and Cologne have an overall accuracy of 92.2% and 91.3%, respectively. Hence, they feature some misclassifications. Given that these mapping errors are passed to the USCs computed, it is inferred that they also have an impact on the study results.

Second, while the LC maps and USCs are extracted from more recent VHR input data, LST is retrieved from Landsat-7 SLC-on imagery acquired between July 1999 and April 2003 (cf. Tables 1 and 2). It follows that the temporal mismatch between these types of data causes further uncertainties as cities in general (Angel et al., 2011; Taubenböck et al., 2012; United Nations, 2008) and the two test sites in particular (Diermayer and Hostert, 2007; Taubenböck and Thiel, 2010) are subject to continuous LC change. However, the impact of LC change on the study results should not be overrated. This is because, according to the German monitor of settlement and open space development, Berlin and Cologne have experienced a change in built-up settlement area and transport space of only −1.2 and 2.9% for the years 2000–2010 and 2000–2006, respectively (Leibniz Institute of Ecological Urban and Regional Development, 2016). The effect of urban LC change on the statistics presented in this paper can therefore be considered as negligible. Apart from this, it has to be kept in mind that a time series of VHR multi-spectral and object height data is not available for the two study areas. Such data would enable the computation of 2D and 3D USCs for each of the ETM+ acquisitions employed and help removing the statistical uncertainties related to urban LC change.

5.4.3. LST retrieval

The uncertainties of the derived LST maps are expected to be not higher than 1–2 K (cf. Section 3.4). However, this number should be regarded as a rough estimate only since it is purely based on experiences from the scientific literature (Qin et al., 2001; Sobrino et al., 2004). For this reason, a direct and more reliable assessment of the actual retrieval errors and their effects on the USC–LST relationship deserves further investigation.

Another point to consider is that the correlation statistics presented in Table 5 are likely to be biased in favor of 2D USCs. This is because of the nadir-pointing viewing geometry of the Landsat-7 satellite and the resulting oversampling of horizontal urban surfaces in ETM+ based retrievals of LST. While these sensor characteristics are not optimal for comparing 2D and 3D USCs as well as their relation to LST, there is a lack of alternative and more suitable thermal infrared data or LST data products that could be used instead. For example, the thermal infrared subsystem of the Advanced Spaceborne Thermal Emission and Reflection Radiometer (ASTER) instrument has a scan angle (±8.54°) that is comparable to that of Landsat ETM+ (Abrams et al., 2002; Hodgson and Kar, 2008). Accordingly, the usage of ASTER imagery would not help overcoming the above-described limitation. In contrast to ASTER, the MODIS sensor features enhanced off-nadir viewing capabilities (±55°). However, it provides LST data products at a much coarser spatial resolution (1 km) than ETM+ (30 m) and ASTER (90 m) (Abrams et al., 2002; Wan, 1999). The list of potential thermal infrared imaging systems could be extended here (cf. Tomlinson et al., 2011). But none of the data these sensors deliver would enable making more objective comparisons between 2D and 3D USCs. The latter would only be possible if the temperature of the complete urban surface area (cf. Voogt and Oke, 1997) as well as its dynamics over time were known — city-wide and spatially-explicit. As such an exercise is beyond the scope of this paper, there is no appropriate alternative to the use of ETM+ data for producing detailed, multi-temporal LST maps of Berlin and Cologne.

5.4.4. Correlation analysis

In the study at hand, comparisons between USCs and LST are made at the Landsat pixel level (i.e., 30 m spatial resolution). But under certain conditions, the individual pixel constitutes a less appropriate area of reference for computing USCs. This is frequently the case when urban objects extracted from VHR data are too large to be represented by a single resolution cell. For example, if an industrial building consists of five pixels, it enters the calculation of each USC five separate times. Thus, the statistics obtained for those indicators quantifying the number or form of urban LC elements (cf. Tables 3 and 4) are likely to be impacted by this effect.

Drawing from the above considerations, it is without doubt that at least some of the obtained correlation statistics are affected by single or multiple components of the applied processing chain. Nevertheless, bearing in mind the efforts made to ensure a sound data analysis, it is reasonable to assume the results of this study to be valid.

6. Conclusions

Over the past decades, a considerable amount of remote sensing research has been directed towards a better understanding of the relationship between USCs and LST. However, while a lot of emphasis has been placed on the 2D characteristics of a city, 3D USCs have remained largely unexplored. In addition, previous findings are based on the analysis of a single study area, a limited number of (mainly 2D) USCs, and/or only a few LST scenes acquired in specific seasons. The present study aimed at addressing these deficits. It made extensive comparisons between 2D *and* 3D USCs to identify potential indicators of LST and the surface UHI effect as well as potential predictors for thermal sharpening applications (cf. Zhan et al., 2013). Both widely-used as well as more recently proposed metrics of the urban remote sensing literature were investigated within a single experiment. While some of these USCs have already been used earlier (e.g., ISA and VF), others, like VV2BV and UD, have never been analyzed before in the context of urban temperature studies. In addition to the comparison of 2D and 3D USCs, the spatio-temporal dependencies of their relation to LST were examined. To this end, the experimental setup of this work included two study areas, 26 USCs, and 16 LST scenes covering four meteorological seasons. Use was made of a comprehensive database compiled for the cities of Berlin and Cologne, Germany.

The results of this study highlight that the linkage between USCs and LST is not stronger when 3D parameters are considered instead of 2D ones. Even though they may offer more holistic representations of the urban landscape, correlation statistics suggest that 3D USCs are consistently outperformed by ISA and/or VF, i.e., some of the most widely-used 2D metrics. The analysis of spatial dependencies reveals that the USC–LST connection is different for the two study areas. This is due to their specific geographies, with urban form and compactness, urban green spaces and street trees, and the configuration of urban LC elements being some of the determining factors. Moreover, the USC–LST connection varies within the boundaries of a city, whereas the strength of association is often driven by structural composition. That is, urban LU structures composed of thermally distinct LC objects and patches are in general more closely related to LST. The existing intra-urban differences emphasize that a single correlation value reported for an entire test site only represents an integrated estimate which might not be sufficient for certain types of investigation.

The examination of temporal dependencies yielded that the relationship between USCs and LST is fairly consistent over time. Nonetheless, there are a few exceptions indicating some larger inter- and intra-season variations. Closer inspection shows that the observations arise from an interplay of drivers known to impact LST and its relation to USCs, including the season of acquisition, vegetation phenology, and meteorology. This underscores the importance of careful data selection and interpretation when studying surface UHIs and their driving forces with mono-temporal remote sensing. At the same time, it is stressed that the increased empirical evidence gained from LST time series allows for the deduction of general data trends at higher levels of confidence.

Despite the comprehensive experimental setup of this study, there are some open research aspects that should be addressed in the future. First, it would be worth extending the presented correlation analyses to other thermal infrared data or LST data products. This is because the present work exclusively focuses on Landsat ETM+ imagery and its findings therefore only apply to medium spatial resolution, small scan angle, and daytime thermal infrared measurements. For this reason, the inclusion of additional thermal data that have been acquired at different sensing schemes (i.e., in terms of spatial resolution, scan angle, and/or overpass time) would be a logical next step. These data could stem from airborne campaigns (if available), satellite sensors (e.g., ASTER and MODIS) or even modeling (cf. Voogt and Oke, 1997). They would enable the further characterization of the USC–LST relationship and its dependencies on spatial scale, sensor viewing geometry, and the diurnal cycle of urban surface temperatures.

Second, and as the presented workflow contains a number of variable components, future research should concentrate on the methodological dependencies of the reported correlations. Among others, the effect of different pixel sampling strategies, i.e., the procedure of selecting those pixels that enter the calculations, has to be addressed. For example, it could be worth exploring whether or not a random or a systematic sampling of pixels leads to the same results as those obtained when all pixels are considered (as is the

case in this study). In- or exclusions of water bodies, areas of LC change, and statistical outliers might also make a notable difference. Finally, it would be interesting to see if changes in the scales of comparison (e.g., pixels versus blocks) or the spatial extent of a study area have a significant impact. The identification of crucial components within the applied processing chain would be a sensible complement to the findings of this study and would further advance the search for the big picture of the USC–LST relationship.

7. List of abbreviations

2D	two-dimensional
3D	three-dimensional
#B/A	number of buildings per block
a.s.l.	above sea level
ASTER	Advanced Spaceborne Thermal Emission and Reflection Radiometer
BA	building aggregation
BF	building footprint
BH	building height
BV	building volume
BV/F	building volume per floor
CAR	canyon aspect ratio
Cfb	temperate oceanic climate
CI	cubic index
CNL	cognition network language
D2B	distance to buildings
DEM	digital elevation model
Dfb	humid continental climate
DLM	digital landscape model
DN	digital number
DSM	digital surface model
ETM+	Enhanced Thematic Mapper Plus
FAR	floor area ratio
FD (B)	fractal dimension of buildings
GCP	ground control point
GEOBIA	geographic object-based image analysis
GFA	gross floor area
GSD	ground sampling distance
HPF	high-pass filter
ISA	impervious surface area
LC	land cover
LCZ	local climate zone
LiDAR	light detection and ranging
LMS	laser measurement system
LSE	land surface emissivity
LST	land surface temperature
LU	land use
LW (B)	length to width ratio of buildings
MODIS	Moderate Resolution Imaging Spectroradiometer
NDVI	normalized difference vegetation index
NIR	near infrared
nDSM	normalized digital surface model
PC	personal computer
RA (B)	relative area of buildings
RA (G)	relative area of grass/shrubs
RA (I)	relative area of impervious surfaces
RA (S)	relative area of bare soil areas
RA (T)	relative area of trees
RAM	random access memory
RMSE	root mean square error
SDI	Shannon's diversity index
SLC	scan line corrector
SVF	sky view factor
TH	tree height
TM	Thematic Mapper
TV	tree volume
TPW	total precipitable water
UD	urban density
UHI	urban heat island
USC	urban site characteristic
USGS	United States Geological Survey
UST	urban structure type
UTC	coordinated universal time
UVI	universal vegetation index
VF	vegetation fraction
VHR	very high resolution
VV2BV	vegetation volume to built-up volume

Acknowledgments

The authors would like to thank the three anonymous reviewers, whose constructive criticism helped to substantially improve the quality of the manuscript. Moreover, they are grateful to the Berlin Senate Department for Urban Development and the Environment as well as the Cologne District Government (Department 7–Geobasis NRW) and the City of Cologne for the provision of LiDAR point clouds, digital orthophotos, and urban LU maps. The UltraCamX data of Berlin is courtesy of Frank Lehmann, Institute of Optical Sensor Systems, German Aerospace Center (DLR) Berlin-Adlershof. The Ikonos scene was acquired within the framework of the Enviland-2 research project, which was funded by the Space Agency of the DLRand theGerman Federal Ministry of Economics and Technology (BMWi) on the basis of legislation by the German Parliament grant no. 50EE0844–50EE0847.

Appendix A. Supplementary data

Supplementary data to this article can be found online at http://dx.doi.org/10.1016/j.rse.2017.02.020. These data include the boundaries of the two study areas described in this article.

References

Abrams, M., Hook, S., Ramachandran, B., 2002. ASTER User Handbook, Version 2. Jet Propulsion Laboratory (JPL), Pasadena, CA.

Angel, S., Parent, J., Civco, D., Biel, A., 2011. Making room for a planet of cities. Policy Focus Report, ID PF027. Lincoln Institute of Land Policy, Cambridge, MA.

Arnfield, A., 2003. Two decades of urban climate research: a review of turbulence, exchanges of energy and water, and the urban heat island. Int. J. Climatol. 23, 1–26.

Baatz, M., Hoffmann, C., Willhauck, G., 2008. Progressing from object-based to object-oriented image analysis. In: Blaschke, T., Lang, S., Hay, G. (Eds.), Object-based image analysis. Spatial concepts for knowledge-driven remote sensing applications. Springer, Berlin, Germany, pp. 29–42.

Basu, R., Samet, J., 2002. Relation between elevated ambient temperature and mortality: A review of the epidemiologic evidence. Epidemiol. Rev. 24, 190–202.

Ben-Dor, E., Saaroni, H., 1997. Airborne video thermal radiometry as a tool for monitoring microscale structures of the urban heat island. Int. J. Remote Sens. 18, 3039–3053.

Benz, U., Hofmann, P., Willhauck, G., Lingenfelder, I., Heynen, M., 2004. Multi-resolution, object-oriented fuzzy analysis of remote sensing data for GIS-ready information. ISPRS J. Photogramm. Remote Sens. 58, 239–258.

Berger, C., Voltersen, M., Eckardt, R., Eberle, J., Heyer, T., Salepci, N., Hese, S., Schmullius, C., Tao, J., Auer, S., Bamler, R., Ewald, K., Gartley, M., Jacobson, J., Buswell, A., Du, Q., Pacifici, F., 2013a. Multi-modal and multi-temporal data fusion: outcome of the 2012 GRSS data fusion contest. IEEE J. Sel. Top. Appl. Earth Obs. Remote Sens. 6, 1324–1340.

Berger, C., Voltersen, M., Hese, S., Walde, I., Schmullius, C., 2013b. Robust extraction of urban land cover information from HSR multi-spectral and LiDAR data. IEEE J. Sel. Top. Appl. Earth Obs. Remote Sens. 6, 2196–2211.

Berlin Senate Department for Urban Development and the Environment, 2013. Straßenbäume in Berlin — Anzahl je Kilometer Stadtstraße (Bestandsdichte) in Berlin und den Bezirken. http://www.stadtentwicklung.berlin.de/umwelt/stadtgruen/stadtbaeume/de/daten_fakten/downloads/ausw_137.pdf.

Blaschke, T., Hay, G., Kelly, M., Lang, S., Hofmann, P., Addink, E., Queiroz Feitosa, R., van der Meer, F., van der Werff, H., van Coillie, F., Tiede, D., 2014. Geographic object-based image analysis — towards a new paradigm. ISPRS J. Photogramm. Remote Sens. 87, 180–191.
Blaschke, T., Lang, S., Hay, G. (Eds.), 2008. Object-based image analysis for remote sensing. Spatial concepts for knowledge-driven remote sensing applications. Springer, Berlin, Germany.
Burgess, E., 1925. The growth of the city: an introduction to a research project. In: Park, R., Burgess, E., McKenzie, R. (Eds.), The City. University of Chicago Press, Chicago, IL, pp. 47–62.
Burnett, C., Blaschke, T., 2003. A multi-scale segmentation/object relationship modelling methodology for landscape analysis. Ecol. Model. 168, 233–249.
Buyantuyev, A., Wu, J., 2010. Urban heat islands and landscape heterogeneity: linking spatiotemporal variations in surface temperatures to land-cover and socioeconomic patterns. Landsc. Ecol. 25, 17–33.
Chander, G., Markham, B., Helder, D., 2009. Summary of current radiometric calibration coefficients for Landsat MSS, TM, ETM+, and EO-1 ALI sensors. Remote Sens. Environ. 113, 893–903.
Changnon, S., 1992. Inadvertent weather modification in urban areas: lessons for global climate change. Bull. Am. Meteorol. Soc. 73, 619–627.
Chen, X.-L., Zhao, H.-M., Li, P.-X., Yin, Z.-Y., 2006. Remote sensing image-based analysis of the relationship between urban heat island and land use/cover changes. Remote Sens. Environ. 104, 133–146.
Chun, B., Guldmann, J.-M., 2014. Spatial statistical analysis and simulation of the urban heat island in high-density central cities. Landsc. Urban Plan. 125, 76–88.
Cole, A., Court, A., Cantor, A., 1965. Model atmospheres. In: Valley, S. (Ed.), Handbook of Geophysics and Space Environments. McGraw-Hill, New York, NY, pp. 1–22.
Congalton, R., Green, K. (Eds.), 2009. Assessing the accuracy of remotely sensed data. Principles and practices. 2nd ed. CRC Press, Boca Raton, FL.
Cook, B., Corp, L., Nelson, R., Middleton, E., Morton, D., McCorkel, J., Masek, J., Ranson, K.J., Ly, V., Montesano, P., 2013. NASA Goddard's LiDAR, Hyperspectral and Thermal (G-LiHT) airborne imager. Remote Sens. 5, 4045–4066.
Croux, C., Dehon, C., 2010. Influence functions of the Spearman and Kendall correlation measures. Stat. Methods Appl. 19, 497–515.
Curriero, F., Heiner, K., Samet, J., Zeger, S., Strug, L., Patz, J., 2002. Temperature and mortality in 11 cities of the eastern United States. Epidemiology 155, 80–87.
Deng, C., Wu, C., 2012. BCI: A biophysical composition index for remote sensing of urban environments. Remote Sens. Environ. 127, 247–259.
Destatis, 2014. Städte (Alle Gemeinden mit Stadtrecht) nach Fläche, Bevölkerung und Bevölkerungsdichte am 31.12.2012. Statistisches Bundesamt. https://www.destatis.de/DE/ZahlenFakten/LaenderRegionen/Regionales/Gemeindeverzeichnis/Administrativ/Aktuell/05Staedte.html.
Deutscher Wetterdienst, 2014. WebWerdis: Weather request and distribution system. https://werdis.dwd.de/werdis/start_js_JSP.do.
Diermayer, E., Hostert, P., 2007. Assessing post-socialist urban change with Landsat data; case study Berlin, Germany. Urban remote sensing joint event, 11–13 April 2007, Paris, France. pp. 1–4.
Ehlers, M., 2009. Future EO sensors of relevance — integrated perspective for global urban monitoring. In: Gamba, P., Herold, M. (Eds.), Global Mapping of Human Settlement. CRC Press, Boca Raton, FL, pp. 321–337.
Ewing, R., Rong, F., 2008. The impact of urban form on U.S. residential energy use. Hous. Policy Debate 19, 1–30.
Franke, J., Roberts, D., Halligan, K., Menz, G., 2009. Hierarchical Multiple Endmember Spectral Mixture Analysis (MESMA) of hyperspectral imagery for urban environments. Remote Sens. Environ. 113, 1712–1723.
Gago, E., Roldan, J., Pacheco-Torres, R., Ordóñez, J., 2013. The city and urban heat islands: a review of strategies to mitigate adverse effects. Renew. Sustain. Energy Rev. 25, 749–758.
Gamba, P., Dell'Acqua, F., Dasarathy, B., 2005. Urban remote sensing using multiple data sets: past, present, and future. Inf. Fusion 6, 319–326.
Gangkofner, U., Pradhan, P., Holcomb, D., 2008. Optimizing the high-pass filter addition technique for image fusion. Photogramm. Eng. Remote Sens. 74, 1107–1118.
Gluch, R., Ridd, K., 2010. The V-I-S model: quantifying the urban environment. In: Rashed, T., Juergens, C. (Eds.), Remote Sensing of Urban and Suburban Areas. Springer, Dordrecht, The Netherlands, pp. 85–116.
Gober, P., Brazel, A., Quay, R., Myint, S., Grossman-Clarke, S., Miller, A., Rossi, S., 2009. Using watered landscapes to manipulate urban heat island effects: how much water will it take to cool Phoenix? J. Am. Plan. Assoc. 76, 109–121.
Google Inc., 2014a. Google Earth. https://earth.google.com/.
Google Inc., 2014b. Google Maps. https://www.google.de/maps.
Grimmond, S., 2007. Urbanization and global environmental change: local effects of urban warming. Geogr. J. 173, 83–88.
Guhathakurta, S., Gober, P., 2007. The impact of the Phoenix urban heat island on residential water use. J. Am. Plan. Assoc. 73, 317–329.
Harris, C., Ullman, E., 1945. The nature of cities. Ann. Am. Acad. Pol. Soc. Sci. 242, 7–17.
Hauke, J., Kossowski, T., 2011. Comparison of values of Pearson's and Spearman's correlation coefficients on the same sets of data. Quaestiones Geographicae. 30, 87–93.
Heiden, U., Heldens, W., Roessner, S., Segl, K., Esch, T., Mueller, A., 2012. Urban structure type characterization using hyperspectral remote sensing and height information. Landsc. Urban Plan. 105, 361–375.
Heiden, U., Segl, K., Roessner, S., Kaufmann, H., 2007. Determination of robust spectral features for identification of urban surface materials in hyperspectral remote sensing data. Remote Sens. Environ. 111, 537–552.
Heldens, W., Taubenböck, H., Esch, T., Heiden, U., Wurm, M., 2013. Analysis of surface thermal patterns in relation to urban structure types: a case study for the City of Munich. In: Kuenzer, C., Dech, S. (Eds.), Thermal Infrared Remote Sensing: Sensors, Methods, Applications. Springer, Dordrecht, The Netherlands, pp. 475–493.
Herold, M., Liu, X., Clarke, K., 2003. Spatial metrics and image texture for mapping urban land use. Photogramm. Eng. Remote Sens. 69, 991–1001.
Hodgson, M., Kar, B., 2008. Modeling the potential swath coverage of nadir and off–nadir pointable remote sensing satellite-sensor systems. Cartogr. Geogr. Inf. Sci. 35, 147–156.
Howard, L., 1833. The Climate of London Deduced from Meteorological Observations Made in the Metropolis and at Various Places Around It. 2nd ed., vol. 1–3. J. Rickerby, London, UK.
Huang, G., Zhou, W., Cadenasso, M., 2011. Is everyone hot in the city? Spatial pattern of land surface temperatures, land cover and neighborhood socioeconomic characteristics in Baltimore, MD. J. Environ. Manag. 92, 1753–1759.
Huang, J., Lu, X., Sellers, J., 2007. A global comparative analysis of urban form: applying spatial metrics and remote sensing. Landsc. Urban Plan. 82, 184–197.
Kim, M., Madden, M., Xu, B., 2010. GEOBIA vegetation mapping in Great Smoky Mountains National Park with spectral and non-spectral ancillary information. Photogramm. Eng. Remote Sens. 76, 137–149.
Ko, Y., 2013. Urban form and residential energy use: a review of design principles and research findings. J. Plan. Lit. 28, 327–351.
Kowalski, C., 1972. On the effects of non-normality on the distribution of the sample product–moment correlation coefficient. J. R. Stat. Soc. Ser. C. Appl. Stat. 21, 1–12.
Kuenzer, C., Dech, S. (Eds.), 2013. Thermal infrared remote sensing: Sensors, methods, applications. Springer, Dordrecht, The Netherlands.
Köppen, W., 1936. Das geographische System der Klimate. In: Köppen, W., Geiger, R. (Eds.), Handbuch der klimatologie. vol. 1, part C. Gebrüder Borntraeger, Berlin, Germany, pp. 1–44.
Landsberg, H., 1981. The Urban Climate. . Int. Geophys. Ser.. vol. 28. Academic Press, New York City, NY.
Lazzarini, M., Marpu, P., Ghedira, H., 2013. Temperature–land cover interactions: the inversion of urban heat island phenomenon in desert city areas. Remote Sens. Environ. 130, 136–152.
Leibniz Institute of Ecological Urban and Regional Development, 2016. Monitor of settlement and open space development. http://www.ioer-monitor.de/maps/.
Li, J., Song, C., Cao, L., Zhu, F., Meng, X., Wu, J., 2011. Impacts of landscape structure on surface urban heat islands: a case study of Shanghai, China. Remote Sens. Environ. 115, 3249–3263.
Li, Z., Tang, B., Wu, H., Ren, H., Yan, G., Wan, Z., Trigo, I., Sobrino, J., 2013. Satellite-derived land surface temperature: current status and perspectives. Remote Sens. Environ. 131, 14–37.
LiDAR Online, 2014. LiDAR Online — Worldwide LiDAR Data and Geoservices. https://www.lidar-online.com/.
Liu, H., Weng, Q., 2008. Seasonal variations in the relationship between landscape pattern and land surface temperature in Indianapolis, USA. Environ. Monit. Assess. 144, 199–219.
Liu, L., Zhang, Y., 2011. Urban heat island analysis using the Landsat TM data and ASTER data: a case study in Hong Kong. Remote Sens. 3, 1535–1552.
Loughner, C., Allen, D., Zhang, D.-L, Pickering, K., Dickerson, R., Landry, L., 2012. Roles of urban tree canopy and buildings in urban heat island effects: parameterization and preliminary results. J. Appl. Meteorol. Climatol. 51, 1775–1793.
Lowry, W., 1998. Urban effects on precipitation amount. Prog. Phys. Geogr. 22, 477–520.
Maimaitiyiming, M., Ghulam, A., Tiyip, T., Pla, F., Latorre-Carmona, P., Halik, Ü., Sawut, M., Caetano, M., 2014. Effects of green space spatial pattern on land surface temperature: implications for sustainable urban planning and climate change adaptation. ISPRS J. Photogramm. Remote Sens. 89, 59–66.
Mallick, J., Rahman, A., Singh, C., 2013. Modeling urban heat islands in heterogeneous land surface and its correlation with impervious surface area by using night-time ASTER satellite data in highly urbanizing city, Delhi-India. Adv. Space Res. 52, 639–655.
Maune, D. (Ed.), 2007. Digital elevation model technologies and applications: The DEM users manual. 2nd ed. ASPRS, Bethesda, MD.
McCarthy, M., Best, M., Betts, R., 2010. Climate change in cities due to global warming and urban effects. Geophys. Res. Lett. 37, 1–5.
McGarigal, K., 2014. FRAGSTATS Help. Version 4. University of Massachusetts, Amherst, MA. http://www.umass.edu/landeco/research/fragstats/documents/fragstats.help.4.2.pdf.
Meinel, G., Hecht, R., Herold, H., Schiller, G., Spangenberg, M., Burgdorf, M., Kawka, R., Müller, H., Schmitt, G., Selle, K., 2008. Automatische Ableitung von stadtstrukturellen Grundlagendaten und Integration in einem Geographischen Informationssystem. Bundesamt für Bauwesen und Raumordnung (BBR), Bonn, Germany. Forschungen Heft 134.
Meng, R., 2014. Berlin im Überblick. Zahlen und Fakten. http://www.berlin.de/berlin-im-ueberblick/zahlenfakten/index.de.html.
Myint, S., Gober, P., Brazel, A., Grossman-Clarke, S., Weng, Q., 2011. Per-pixel vs. object-based classification of urban land cover extraction using high spatial resolution imagery. Remote Sens. Environ. 115, 1145–1161.
Myint, S., Wentz, E., Brazel, A., Quattrochi, D., 2013. The impact of distinct anthropogenic and vegetation features on urban warming. Landsc. Ecol. 28, 959–978.
Müllenberg, J., 2010. Wie hoch liegt eigentlich Köln. http://www.stadt-koeln.de/politik-und-verwaltung/presse/wie-hoch-liegt-eigentlich-koeln.
Ngie, A., Abutaleb, K., Ahmed, F., Darwish, A., Ahmed, M., 2014. Assessment of urban heat island using satellite remotely sensed imagery: a review. S. Afr. Geogr. J. 96,

1–17.
Ogashawara, I., da Silva Brum Bastos, V., 2012. A quantitative approach for analyzing the relationship between urban heat islands and land cover. Remote Sens. 4, 3596–3618.
Oke, T., 1973. City size and the urban heat island. Atmos. Environ. 7, 769–779.
Oke, T., 1981. Canyon geometry and the nocturnal urban heat island: comparison of scale model and field observations. J. Climatol. 1, 237–254.
Oke, T., 1982. The energetic basis of the urban heat island. Q. J. R. Meteorol. Soc. 108, 1–24.
Oke, T., 1988. Street design and urban canopy layer climate. Energy Build. 11, 103–113.
Oke, T., Johnson, G., Steyn, D., Watson, I., 1991. Simulation of surface urban heat islands under 'ideal' conditions at night. Part 2: diagnosis of causation. Bound.-Layer Meteorol. 56, 339–358.
O'Neil-Dunne, J., MacFaden, S., Royar, A., Pelletier, K., 2013. An object-based system for LiDAR data fusion and feature extraction. Geocarto Int. 28, 1–16.
OpenTopography, 2014. OpenTopography — a portal to high-resolution topography data and tools. http://www.opentopography.org/.
Pan, X.-Z., Zhao, Q.-G., Chen, J., Liang, Y., Sun, B., 2008. Analyzing the variation of building density using high spatial resolution satellite images: the example of Shanghai City. Sensors 8, 2541–2550.
Pauleit, S., Duhme, F., 2000. Assessing the environmental performance of land cover types for urban planning. Landsc. Urban Plan. 52, 1–20.
Pearson, K., 1896. Mathematical contributions to the theory of evolution. III. Regression, heredity, and panmixia. Philos. Trans. R. Soc. Lond. A 187, 253–318.
Pearson, K., 1920. Notes on the history of correlation. Biometrika 13, 25–45.
Peel, M., Finlayson, B., McMahon, T., 2007. Updated world map of the Köppen-Geiger climate classification. Hydrol. Earth Syst. Sci. 11, 1633–1644.
Platt, R., Rapoza, L., 2008. An evaluation of an object-oriented paradigm for land use/land cover classification. Prof. Geogr. 60, 87–100.
Press, W., Teukolsky, S., Vetterling, W., Flannery, B., 1992. Numerical Recipes in C. The Art of Scientific Computing. 2nd ed., Cambridge University Press, Cambridge, UK., pp. 994.
Priestnall, G., Jafaar, J., Duncan, A., 2000. Extracting urban features from LiDAR digital surface models. Comput. Environ. Urban. Syst. 24, 65–78.
Qin, Z., Karnieli, A., Berliner, P., 2001. A mono-window algorithm for retrieving land surface temperature from Landsat TM data and its application to the Israel–Egypt border region. Int. J. Remote Sens. 22, 3719–3746.
Quattrochi, D., Ridd, M., 1994. Measurement and analysis of thermal energy responses from discrete urban surfaces using remote sensing data. Int. J. Remote Sens. 15, 1991–2022.
Ren, Z., He, X., Zheng, H., Zhang, D., Yu, X., Shen, G., Guo, R., 2013. Estimation of the relationship between urban park characteristics and Park Cool Island intensity by remote sensing data and field measurement. Forests 4, 868–886.
Richter, R., Schläpfer, D., 2014. Atmospheric/Topographic Correction for Satellite Imagery. ATCOR-2/3 User Guide, version 8.3.1. Deutsches Zentrum für Luft- und Raumfahrt (DLR), Wessling, Germany.
Ridd, M., 1995. Exploring a V-I-S (vegetation-impervious surface-soil) model for urban ecosystem analysis through remote sensing: comparative anatomy for cities. Int. J. Remote Sens. 16, 2165–2185.
Rizwan, A., Dennis, L., Liu, C., 2008. A review on the generation, determination and mitigation of urban heat island. J. Environ. Sci. 20, 120–128.
Roth, M., Oke, T., Emery, W., 1989. Satellite-derived urban heat island from three coastal cities and the utilization of such data in urban climatology. Int. J. Remote Sens. 10, 1699–1720.
Salehi, B., Zhang, Y., Zhong, M., Dey, V., 2012. Object-based classification of urban areas using VHR imagery and height points ancillary data. Remote Sens. 4, 2256–2276.
Salomons, E., Berghauser Pont, M., 2012. Urban traffic noise and the relation to urban density, form, and traffic elasticity. Landsc. Urban Plan. 108, 2–16.
Sarrat, C., Lemonsu, A., Masson, V., Guedalia, D., 2006. Impact of urban heat island on regional atmospheric pollution. Atmos. Environ. 40, 1743–1758.
Shannon, C., Weaver, W., 1949. The Mathematical Theory of Communication. The University of Illinois Press, Urbana, Illinois.
Small, C., 2006. Comparative analysis of urban reflectance and surface temperature. Remote Sens. Environ. 104, 168–189.
Sobrino, J., Jiménez-Muñoz, J., Paolini, L., 2004. Land surface temperature retrieval from LANDSAT TM 5. Remote Sens. Environ. 90, 434–440.
Spearman, C., 1904. The proof and measurement of association between two things. Am. J. Psychol. 15, 72–101.
Spearman, C., 1907. Demonstration of formulæ for true measurement of correlation. Am. J. Psychol. 18, 161–169.
Srivanit, M., Kazunori, H., 2011. The influence of urban morphology indicators on summer diurnal range of urban climate in Bangkok Metropolitan Area, Thailand. Int. J. Civ. Environ. Eng. 11, 34.
Stadt Köln, 2013. Kölner Grün Stiftung - Amt für Landschaftspflege und Grünflächen. http://www.stadt-koeln.de/leben-in-koeln/freizeit-natur-sport/wald/spenden-sie-fuer-ihren-strassenbaum
Stewart, I.D., 2010, February. A systematic review and scientific critique of methodology in modern urban heat island literature. Int. J. Climatol. 31, 200–217.
Stewart, I., Oke, T., 2012. Local climate zones for urban temperature studies. Bull. Am. Meteorol. Soc. 93, 1879–1900.
Taubenböck, H., Esch, T., Felbier, A., Wiesner, M., Roth, A., Dech, S., 2012. Monitoring urbanization in mega cities from space. Remote Sens. Environ. 117, 162–176.
Taubenböck, H., Thiel, M., 2010. Landbedeckungsklassifikation der Stadt-Umland-Region München und Analyse ihrer raumzeitlichen Entwicklung. In: Taubenböck, H., Dech, S. (Eds.), Fernerkundung im urbanen raum. Erdbeobachtung auf dem weg zur planungspraxis. Wissenschaftliche Buchgesellschaft, Darmstadt, Germany, pp. 45–51.
Theeuwes, N., Steenefeld, G., Ronda, J., Heusinkveld, B., van Hove, L., Holtslag, A., 2014. Seasonal dependence of the urban heat island on the street canyon aspect ratio. Q. J. R. Meteorol. Soc. 140, 2197–2210.
Tomlinson, C., Chapman, L., Thornes, J., Baker, C., 2011. Remote sensing land surface temperature for meteorology and climatology: a review. Meteorol. Appl. 18, 296–306.
Tompalski, P., Wezyk, P., 2012. LiDAR and VHRS data for assessing living quality in cities — an approach based on 3D indices. ISPRS Int. Arch. Photogramm. Remote. Sens. Spat. Inf. Sci. XXXIX-B6, 173–176.
Trimble Ltd, 2014. eCognition Developer 9.0.1. Reference Book. Trimble Documentation, Munich, Germany.
Tucker, C., 1979. Red and photographic infrared linear combinations for monitoring vegetation. Remote Sens. Environ. 8, 127–150.
Unger, J., 2004. Intra-urban relationship between surface geometry and urban heat island: review and new approach. Clim. Res. 27, 253–264.
United Nations, 2008. World urbanization prospects. The 2007 revision. . Executive SummaryDepartment of Economic and Social Affairs/ Population Division, New York City, NY.
University of Wyoming, 2014. Atmospheric soundings. http://weather.uwyo.edu/upperair/sounding.html.
USGS, 2014. Landsat update — Volume 4, Issue 1, 2010. New Thermal Band resampling: 30-meter pixels. http://landsat.usgs.gov/documents/about_LU_Vol_4_Issue_Special_Edition.pdf.
Valor, E., Caselles, V., 1996. Mapping land surface emissivity from NDVI: application to European, African, and South American areas. Remote Sens. Environ. 57, 167–184.
Vardoulakis, S., Fisher, B., Pericleous, K., Gonzalez-Flesca, N., 2003. Modelling air quality in street canyons: a review. Atmos. Environ. 37, 155–182.
Voltersen, M., Berger, C., Hese, S., Schmullius, C., 2014. Object-based land cover mapping and comprehensive feature calculation for an automated derivation of urban structure types at block level. Remote Sens. Environ. 154, 192–201.
Voogt, J., Oke, T., 1997. Complete urban surface temperatures. J. Appl. Meteorol. 36, 1117–1132.
Voogt, J., Oke, T., 2003. Thermal remote sensing of urban climates. Remote Sens. Environ. 86, 370–384.
Walde, I., Hese, S., Berger, C., Schmullius, C., 2014. From land cover-graphs to urban structure types. Int. J. Geogr. Inf. Sci. 28, 584–609.
Wan, Z., 1999. MODIS Land-Surface Temperature Algorithm Theoretical Basis Document (LST ATBD), Version 3.3. Institute for Computational Earth System Science, University of California, Santa Barbara, CA.
Weng, Q., 2001. A remote sensingGIS evaluation of urban expansion and its impact on surface temperature in the Zhujiang Delta, China. Int. J. Remote Sens. 22, 1999–2014.
Weng, Q., 2003. Fractal analysis of satellite-detected urban heat island effect. Photogramm. Eng. Remote Sens. 69, 555–566.
Weng, Q., 2009. Thermal infrared remote sensing for urban climate and environmental studies: methods, applications, and trends. ISPRS J. Photogramm. Remote Sens. 64, 335–344.
Weng, Q., 2012. Remote sensing of impervious surfaces in the urban areas: requirements, methods, and trends. Remote Sens. Environ. 117, 34–49.
Weng, Q., Liu, H., Liang, B., Lu, D., 2008. The spatial variations of urban land surface temperatures: pertinent factors, zoning effect, and seasonal variability. IEEE J. Sel. Top. Appl. Earth Obs. Remote Sens. 1, 154–166.
Weng, Q., Lu, D., Schubring, J., 2004. Estimation of land surface temperature-vegetation abundance relationship for urban heat island studies. Remote Sens. Environ. 89, 467–483.
Weng, Q., Yang, S., 2006. Urban air pollution patterns, land use, and thermal landscape: an examination of the linkage using GIS. Environ. Monit. Assess. 117, 463–489.
Xian, G., 2008. Satellite remotely-sensed land surface parameters and their climatic effects for three metropolitan regions. Adv. Space Res. 41, 1861–1869.
Xian, G., Crane, M., 2006. An analysis of urban thermal characteristics and associated land cover in Tampa Bay and Las Vegas using Landsat satellite data. Remote Sens. Environ. 104, 147–156.
Xiao, R., Weng, Q., Ouyang, Z., Li, W., Schienke, E.W., Zhang, Z., 2008. Land surface temperature variation and major factors in Beijing, China. Photogramm. Eng. Remote Sens. 74, 451–461.
Yan, G., Mas, J.F., Maathuis, B., Xiangmin, Z., Van Dijk, P., 2006. Comparison of pixel-based and object-oriented image classification approaches — a case study in a coal fire area, Wuda, Inner Mongolia, China. Int. J. Remote Sens. 27, 4039–4055.
Yu, B., Liu, H., Wu, J., Hu, Y., Zhang, L., 2010. Automated derivation of urban building density information using airborne LiDAR data and object-based method. Landsc. Urban Plan. 98, 210–219.
Yuan, F., Bauer, M., 2007. Comparison of impervious surface area and normalized difference vegetation index as indicators of surface urban heat island effects in Landsat imagery. Remote Sens. Environ. 106, 375–386.
Yue, W., Liu, Y., Fan, P., Ye, X., Wu, C., 2012. Assessing spatial pattern of urban thermal environment in Shanghai, China. Stoch. Env. Res. Risk A. 26, 899–911.
Zakšek, K., Oštir, K., Kokalj, Z., 2011. Sky-view factor as a relief visualization technique. Remote Sens. 3, 398–415.
Zevenbergen, L., Thorne, C., 1987. Quantitative analysis of land surface topography. Earth Surf. Process. Landf. 12, 12–56.
Zhan, W., Chen, Y., Zhou, J., Wang, J., Liu, W., Voogt, J., Zhu, X., Quan, J., Li, J., 2013. Disaggregation of remotely sensed land surface temperature: literature survey, taxonomy, issues, and caveats. Remote Sens. Environ. 131, 119–139.

Zhang, J., Wang, Y., Li, Y., 2006. A C++ program for retrieving land surface temperature from the data of Landsat TM/ETM+ band6. Comput. Geosci. 32, 1796–1805.
Zhang, X., Zhong, T., Feng, X., Wang, K., 2009a. Estimation of the relationship between vegetation patches and urban land surface temperature with remote sensing. Int. J. Remote Sens. 30, 2105–2118.
Zhang, Y., Odeh, I., Han, C., 2009b. Bi-temporal characterization of land surface temperature in relation to impervious surface area, NDVI and NDBI, using a sub-pixel image analysis. Int. J. Appl. Earth Obs. Geoinf. 11, 256–264.
Zhou, W., Huang, G., Cadenasso, M.L., 2011. Does spatial configuration matter? Understanding the effects of land cover pattern on land surface temperature in urban landscapes. Landsc. Urban Plan. 102, 54–63.
Zhou, W., Huang, G., Troy, A., Cadenasso, M., 2009. Object-based land cover classification of shaded areas in high spatial resolution imagery of urban areas: a comparison study. Remote Sens. Environ. 113, 1769–1777.
Zhou, W., Troy, A., 2008. An object-oriented approach for analyzing and characterizing urban landscape at the parcel level. Int. J. Remote Sens. 29, 3119–3135.

Chapter 5

Synthesis

The overall goal of this dissertation was to develop methods for the fusion of HSR multispectral imagery and object height data as well as to showcase their utility in the context of different urban environmental mapping and monitoring applications. The thesis therefore intended to make both a technical and an applied research contribution to the field of urban remote sensing. Particular emphasis was put on mapping urban LC, USCs, and USTs, as well as the usage of USCs to study urban LST and the surface UHI phenomenon. These human settlement parameters were chosen because they are thematically connected, difficult to obtain from other data sources, and of high importance for urban planning and environmental management. In order to meet the above goal, a comprehensive literature review was conducted in advance. The review helped identifying current deficits within the chosen fields of research. Furthermore, it led to the formulation of four specific study objectives that, in turn, determined the practical research agenda. In the following, the achievements of this work with respect to each specific study objective are summarized, reflected and discussed, and employed to outline potential avenues for future research (Sect. 5.1ff.).

5.1 Summary

Study objective #1 — Robust extraction of urban LC information

In Section 4.1, a robust GEOBIA approach was developed to extract detailed and accurate urban LC information from HSR multispectral and object height data. Special attention was paid to the critical evaluation of the proposed method with regard its performance for and applicability to different test sites and various sets of HSR multisensor data. For this purpose, the experimental setup of the study included three cities featuring different physical structures, four sets of HSR optical and LiDAR data, as well as statistical measures to enable the assessment of classification accuracies and methodological transferability. The study results highlight the great potential of the described approach for accurate, robust, and large-area mapping of urban environments. User's and producer's accuracies observed for all maps were almost consistently above 80% and in many cases even above 90%. Only few larger class-specific errors occurred mainly due to the rather

simple (yet effective) assumptions on which the method is based. The presented feature extraction workflow can thus be used as a template for or starting point of future LC mapping efforts.

Study objective #2 — Integrated assessment of 2D and 3D USCs
In Section 4.2, a new spatial indicator was designed and implemented. The aim was to integratively assess urban density by taking into account the 2D and 3D key characteristics of a city. To this end, fusion of the WorldView-2 and LiDAR data provided in the framework of the 2012 IEEE GRSS Data Fusion Contest was performed. In a first step, basic urban LC information was extracted from the preprocessed input data sets using the GEOBIA approach developed in Section 4.1. The LC map was then utilized in combination with the object height information provided by the LiDAR data to infer urban density. The resulting map and statistics underscore the plausibility and qualification of the proposed metric as a useful measure to evaluate human settlement density and its distinct spatial patterns for different types of urban LU. By taking into account all three spatial dimensions of the urban environment, an integrated and more holistic assessment of the "builtscape" is enabled. To further enhance the transparency of the study, a dedicated geoportal was set up that visualizes all input data, final results, by-products, and ancillary information.

Study objective #3 — Automated derivation of UST maps
In Section 4.3, a generic GEOBIA system was developed for an area-wide, automated derivation of USTs. Synergistic use was made of HSR multispectral and object height data acquired by the airborne UltraCamX sensor over the city of Berlin, Germany. Initially, urban LC information was extracted from the preprocessed input data by means of the classification scheme presented in Section 4.1. The LC map was then employed together with the UltraCamX object heights to infer a comprehensive set of 2D, 3D, and integrated 2D/3D USCs. In a third step, the importance of the generated image features was evaluated by the random forests machine learning algorithm. Finally, the experiences gained from the assessment were used to build improved UST class descriptions. The latter were based on both well-established as well as more recently introduced USCs, such as the urban density metric proposed in Section 4.2. The analysis results and the produced map emphasize the suitability of the described method with regard to classification accuracy, workflow automation, and preparedness in the context of future UST mapping and monitoring tasks.

Study objective #4 — Detailed analysis of USC–LST links
In Section 4.4, the relationship between USCs and LST was studied. Focus was laid on an extensive comparison of 2D, 3D, and integrated 2D/3D USCs as potential predictors of urban LST as well as potential indicators of the surface UHI effect. In addition to the comparison of USCs, the spatio-temporal dependencies of their relation to LST were examined. For this purpose, the experimental setup included two study areas, 26 USCs, and 16 LST scenes covering four seasons. The results of the study demonstrate that the linkage between USCs and LST sensed at small scan angles is not

Tab. 5–1: Synthesis of the scientific contributions made by this work.

Field of research	Scientific contribution	Demonstrated in	Selected examples
Urban LC mapping over large areas	Robust extraction of fine-scale urban LC information	Section 4.1/ Berger et al. (2013b)	Section 4.1: Table 5; Section 4.3: Table 2
USC design and implementation	Integrated assessment of 2D/3D urban density patterns	Section 4.2/ Berger et al. (2013a)	Section 4.2: Figure 4; Section 4.3: Table 3
UST definition and characterization	Area-wide, automated, and robust derivation of USTs	Section 4.3/ Voltersen et al. (2014)	Section 4.3: Table 4; Voltersen et al. (2015)
Surface UHI and urban LST studies	Detailed analysis of 2D, 3D, and 2D/3D USCs vs LST	Section 4.4/ Berger et al. (2017)	Section 4.4: Table 5; Section 4.4: Figure 4

stronger when 3D or integrated 2D/3D parameters are considered. Even though they may offer more holistic representations of the urban landscape, they were consistently outperformed by some of the most widely-used 2D metrics. The analysis of spatial dependencies revealed that the USC–LST interplay does not only differ between, but also within the two test sites. This is due to their distinct geographies, with urban form and compactness, green spaces and street trees, and the structural composition of LC elements being some of the determining factors. The examination of temporal dependencies yielded that the association between USCs and LST is fairly stable over time, but can be subject to larger inter- and intra-season variations for different reasons, including the season of acquisition, vegetation phenology, and meteorological conditions. Since previous research was based on the analysis of a single study area, a limited number of (mainly 2D) USCs, and/or only few LST scenes acquired in specific seasons, the findings of the study provide researchers and practitioners with a more complete picture of the USC–LST relations.

5.2 Reflection

The achievements of this thesis are synthesized in Table 5–1. Motivated by a selection of existing research needs, four technical and applied scientific contributions were made in the field of HSR urban remote sensing (cf. Sect. 3.1 and 4.1ff.). At the core of these individual contributions are detailed urban environmental maps produced by the fusion techniques that have been developed and jointly employed within the framework of a predefined case study. The following paragraphs reflect on the proposed methodologies, obtained results, as well as their implications. A concise summary of the discussions on each scientific contribution is provided in Table 5–2.

Discussion of the research contribution in Section 4.1

In Berger et al. (2013b), study objective #1 was met. Prior to this work, there was a lack of robust GEOBIA approaches for extracting accurate urban LC information from HSR multispectral and object height data. In particular, previous object-based methods were frequently reported to work well on small spatial subsets (Lu et al. 2010; Salehi et al. 2012) or for one entire study

area (>100 km²) only (Platt & Rapoza 2008; Walker & Blaschke 2008). Moreover, these methods often relied on monosensor imagery (i.e., multispectral or 3D data; Taubenböck et al. 2010b) or even data acquired by one specific sensor (Schöpfer & Möller 2006; Platt & Rapoza 2008; Lu et al. 2010; Walker & Blaschke 2008). The present thesis has addressed these deficits by developing a dedicated mapping strategy and by demonstrating its performance for and transferability to different study areas and various sets of HSR multisensor data.

As opposed to other techniques that have been proposed before or afterwards (e.g., Li et al. 2014; Li & Shao 2014; O'Neil-Dunne et al. 2014; Walker & Blaschke 2008; Wurm et al. 2011), a unique characteristic of the GEOBIA system in Berger et al. (2013b) is its simplicity. That is, the rules for class discrimination are deliberately kept simple. For instance, a total number of only seven image features are employed to establish the decision tree, including spectral brightness, the NDVI, and the slope of the nDSM. Furthermore, the implemented routines mainly focus on the identification of seed objects belonging to a certain LC type and the successive growing of these segments on the basis of relative topological queries. It is thanks to this simplicity that an overfitting with regard to input data and test sites is avoided and the robustness of the rule set is ensured. At the same time, this basic approach to detailed urban LC extraction is easily comprehensible, quickly adjustable, and therefore features a high degree of reusability.

Despite its effective structure, there are two issues preventing the developed method from complete automation: Rule set initialization and simplicity. The first term refers to the necessity of parameterizing the rule set prior to its application. As part of this preparatory step, the minimum mapping unit is defined and several classification thresholds (e.g., for building and tree heights) need to be provided. They are specified in the form of project variables at the beginning of the ruleset and handed over to the corresponding mapping processes at a later stage. Even though such a system design enhances reusability, it always requires manual interaction. The second term is related to the usage of only few basic decision criteria and object features. While being conducive to transferability, this comes at the price of increased error margins for certain LC types, with a common example being the confusion between impervious surfaces and bare soil areas. Increasing the accuracy of these and other map categories would necessitate the implementation of more sophisticated, but less universal class descriptions. This emphasizes the trade-off between performance and robustness when building methods for operational urban environmental monitoring.

Depending on the properties of the available HSR data, additional changes may have to be made to the rule set in order to compensate for them. Accordingly, this can be regarded as a third potential issue entailing further manual interactions. To keep the number of necessary adaptions low, it is recommended to draw on a set of coregistered multispectral and object height data. The multispectral data should be radiometrically corrected and contain the four standard lower spatial resolution channels (i.e., blue, green, red, and NIR) for calculating image brightness and the NDVI. A higher spatial resolution monochromatic band is not mandatory, but would be ideal for the purpose of pansharpening. The object height data should be acquired after leaf emergence (i.e.,

Tab. 5–2: Summary of the discussions on each scientific contribution.

	Methodological		
Contribution	Strengths	Limitations	Requirements
Berger et al. (2013b)	• suitable for accurate and robust LC extraction • processing of different HSR multisource data • support of large data volumes acquired over different urban settings	• workflow setup hinders complete automation • rule set simplicity partly causes larger errors	• HSR multispectral data w/ 4 std. spectral bands • coregistered, leaf-on 3D data with ≥4 pts/m²
Berger et al. (2013a)	• holistic assessment of urban density patterns • mutual reinforcement of 2D/3D key city features • versatility of the new urban density index	• added value of the index depends on application • revaluation is necessary on a case-by-case basis	• LC information with ~90% overall accuracy • coregistered, leaf-on 3D data with ≥4 pts/m²
Voltersen et al. (2014)	• area-wide and automated derivation of UST maps • synthesis of existing UST legends and definitions • objective selection of the most descriptive USCs	• UST legend only valid for German study areas • dependence on urban block data properties	• LC information with ~90% overall accuracy • coregistered, leaf-on 3D data with ≥4 pts/m² • block boundaries w/o streets and mixed uses
Berger et al. (2017)	• detailed inspection of 2D/3D USCs vs LST • inclusion of widely-used and more recent USCs • analysis of two cities, 26 USCs, and 16 LST maps from 4 meteorol. seasons • multiscale investigation using all derived maps	• outcomes of the study only valid for daytime LST measurements acquired at medium spatial resolution and small scanning angles	• reliable and detailed information on urban LC, USCs, and USTs • multitemporal TIR imagery or LST maps

during the growing season) to enable the proper detection of tree canopies and taller shrubs. In addition, they should match the spatial resolution of the multispectral imagery and thus feature a density of at least 4 points/m². If these requirements are not met, a higher number of modifications may need to be undertaken in order to make up for any undesired data characteristics. Since the quality of 3D point cloud data is usually subject to larger variations than that of multispectral imagery, it represents the most important prerequisite for a successful mapping project.

Irrespective of the above limitations, the developed GEOBIA approach was thoroughly demonstrated in Section 4.1 and proved to be suitable in the context of several follow-up studies (Berger et al. 2013a; Berger et al. 2015; Berger et al. 2017; Voltersen et al. 2014; Voltersen et al. 2015). It facilitated the generation of detailed and reliable urban LC maps for five entire study areas, including Berlin, Cologne, Rostock, Erfurt, and San Francisco. The overall accuracies of the classification results ranged between 83 and 92% (average: 89%; median: 90%). From the validation statistics as well as from qualitative evaluation, it is found that the presented feature

extraction workflow is able to properly capture the characteristics of different German and US American cities. Moreover, it can integrate various sets of optical and 3D inputs, deal with changes in illumination and phenology, and process vast amounts of HSR data. Thus, the method fulfills some of the essential requirements for detailed, transferable, and large-area monitoring of urban environments, and it does so by exploiting the high synergistic potential between those HSR multisensor Earth observation data that are becoming increasingly available worldwide.

Discussion of the research contribution in Section 4.2

In Berger et al. (2013a), study objective #2 was met. Prior to this work, existing USCs only covered specific 2D or 3D aspects of settlement compactness, and the few notable exceptions to this observation were mainly related to urban green (Gupta et al. 2012; Liu et al. 2015; Tompalski & Wężyk 2012). Accordingly, there was a need for a spatial indicator that integratively assesses urban density by taking into account some of the 2D and 3D key characteristics of a city. The present thesis has closed this research gap by designing and implementing a corresponding USC and by evaluating its ability to estimate the intensity of development and its varying spatial patterns for different types of urban LU. The calculation of this measure requires accurate urban LC information as well as object height data acquired under leaf-on conditions with at least 4 points/m^2.

In contrast to conventional USCs, the proposed metric results from a logical combination of four parameters. These quantify vertical development (iFAR), urban vegetation (VF), soil sealing (ISA), and the clustering of urban structures (BA) within a predefined AOI. Since each input variable addresses a different and distinct aspect of the "builtscape" (Gamba et al. 2004), the index enables a more holistic assessment of local urban density patterns. Moreover, it is conceived in a way that the individual and unique contributions coming from the four above parameters are mutually reinforced. This is achieved by a mathematical expression consisting of two terms that are subtracted from each other (Figure 4 in Berger et al. 2013a). While the left term of the equation is proportional to urban density and becomes larger if ISA and/or BA increase, the right term is inversely proportional to urban density and increases with iFAR and/or VF.

In spite of its advantages over other USCs, it is important to note that the presented spatial indicator should be considered as one of many possible ways to combine 2D and 3D settlement characteristics. In other words, the index only represents one specific example. It is, however, not meant to be a universal solution for describing the intensity of urban development. Even though its suitability for reproducing the spatial distribution of human settlement density was demonstrated, the true value of the metric always depends on the application and its validity therefore has to be revaluated on a case-by-case basis. Subsequent investigations should therefore involve comparisons between the developed USC and a set of established and recently introduced indices.

With respect to the latter point, some first experiences were already made in the context of this dissertation. More precisely, the new urban density index was calculated together with a long list

of existing 2D and 3D USCs. Afterwards, its utility was proven for the characterization of USTs as well as for the analysis of surface UHIs (Voltersen et al. 2014; Voltersen et al. 2015; Berger et al. 2017). In the framework of the experiments conducted, the indicator belonged to the three most important features for deriving the UST classes "block development" and "detached/semi-detached housing". At the same time, it was among the top five predictors of urban LST. These findings are promising as they highlight the versatility of the proposed USC. They may encourage other researchers to integrate the parameter into future urban environmental analyses.

Discussion of the research contribution in Section 4.3

In Voltersen et al. (2014), study objective #3 was met. Prior to this work, there was a need for area-wide and automated GEOBIA approaches to derive USTs from HSR multispectral and object height data. One reason for this was that previous object-based methods were often restricted to only few (Hu & Wang 2013; Steiniger et al. 2008; Walde et al. 2014; Wurm & Taubenböck 2010c) or site-specific map categories (Banzhaf & Höfer 2008; Geiss et al. 2011) covering a small spatial subset of the city under consideration (Bochow et al. 2010b; Heiden et al. 2012; Hu & Wang 2013; Lackner & Conway 2008; Steiniger et al. 2008; Steinnocher et al. 2001; Wurm et al. 2009). Another reason was that these methods frequently relied on a qualitative description of all target classes. This resulted in the utilization of subjectively predefined decision rules and features that were assumed to be effective according to the conceptual model for each UST of interest (Banzhaf & Höfer 2008; Wurm et al. 2009; Wurm & Taubenböck 2010c). Since such approaches suffer from a lack of accuracy and/or robustness, the present thesis aimed at overcoming the above limitations by developing a more generic classification scheme.

In comparison to earlier studies, two major improvements were made in Voltersen et al. (2014). The first one refers to the harmonization and refinement of existing UST legends. In the course of the investigations, five main classes and 13 subclasses were defined and characterized. These classes represent a synthesis of map keys found in the scientific literature and structural units occurring in all German cities. Hence, they allow for an area-wide and transferable mapping. The second type of improvement is related to the integration of machine learning into object-based classification routines. In particular, a two-stage procedure was implemented. Initially, the versatile processing tools of GEOBIA environments were exploited to systematically compute an extended set of both widely-used and more recent USCs. Afterwards, the variable importance measure provided by the RF algorithm was utilized to statistically select the most suitable features for UST mapping. In this way, a comprehensive calculation and an objective assessment of potentially useful spatial indicators were accomplished. The statistics obtained from the importance measure turned out to be plausible and enabled a higher overall degree of workflow automation.

The success of the proposed GEOBIA approach mainly depends on the quality and character of the employed input data and products. In this context, four factors were found to be of crucial importance, including a sufficient accuracy of the urban LC map (ca. 90%), an appropriate density

and acquisition period of the 3D point cloud data (≥4 points/m²; growing season/after leaf emergence), and an adequate definition of urban block boundaries (exclusion of streets and mixed development). All of these classification inputs should be derived or selected with great care. This is because any error in or unwanted property of those information will have a negative impact on the later calculation and selection of USCs as well as on the final UST mapping result.

In conclusion, the harmonization of existing map keys and the integration of machine learning into a GEOBIA workflow constituted two essential steps towards an area-wide and automated characterization of USTs. With an overall accuracy of 82%, the hybrid classification scheme was successfully showcased for a large part of Berlin, Germany. In a follow-up study, an even higher degree of accuracy was achieved after transferring it to Berlin's entire administrative area (89%) and after applying it to the German cities of Cologne (86%) and Rostock (85%) (Voltersen 2016). Thanks to a computer-aided selection of the most descriptive USCs, only minor technical adaptations were necessary to produce reliable maps and statistics. Thus, if the above input data and product requirements are met, the approach is expected to work well for other German and, in a wider sense, European and Western culture cities. Even though the proposed UST legend exclusively draws on experiences from Germany, its extension to further classes found in different regions of the world is straightforward on the basis of the hybrid, two-stage methodology.

Discussion of the research contribution in Section 4.4

In Berger et al. (2017), study objective #4 was met. Prior to this work, the potential of 2D, 3D, and integrated 2D/3D USCs for predicting urban LST had never been jointly analyzed. Instead, the bulk of publications exclusively focused on the 2D features of a city and only a few non-exhaustive investigations existed incorporating 3D USCs as well (Chun & Guldmann 2014; Chun & Guhathakurta 2016; Nassar et al. 2016; Scarano & Sobrino 2015; Weber et al. 2014b; Wong & Nichol 2013). Moreover, previous research findings were often based on the examination of a single study area, a limited number of USCs, and/or only a few LST scenes acquired within specific seasons (e.g., Huang et al. 2011; Liu & Zhang 2011; Maimaitiyiming et al. 2014; Myint et al. 2013; Ogashawara & da Silva Brum Bastos 2012; Ren et al. 2013; Xiao et al. 2008; Zhang et al. 2009a; Zhang et al. 2009b). The present thesis picked up those flaws and eradicated them by designing and implementing a comprehensive experiment.

Unlike other methodological setups in the field, the experiment allowed for a detailed inspection of the spatio-temporal relationship between 2D/3D USCs and LST. Both well-established and recently introduced metrics of the urban remote sensing literature were taken into account within a single analysis. While some of these USCs had already been employed earlier, others had never been considered before in the context of urban temperature studies. In order to realize specific sub analyses (e.g., on inter- and intra-urban differences), use was made of all methods developed and maps produced within the preceding contributions of this dissertation. This underlines the close connection between the chosen topics of work (cf. Fig. 3–1), emphasizes that the generated data

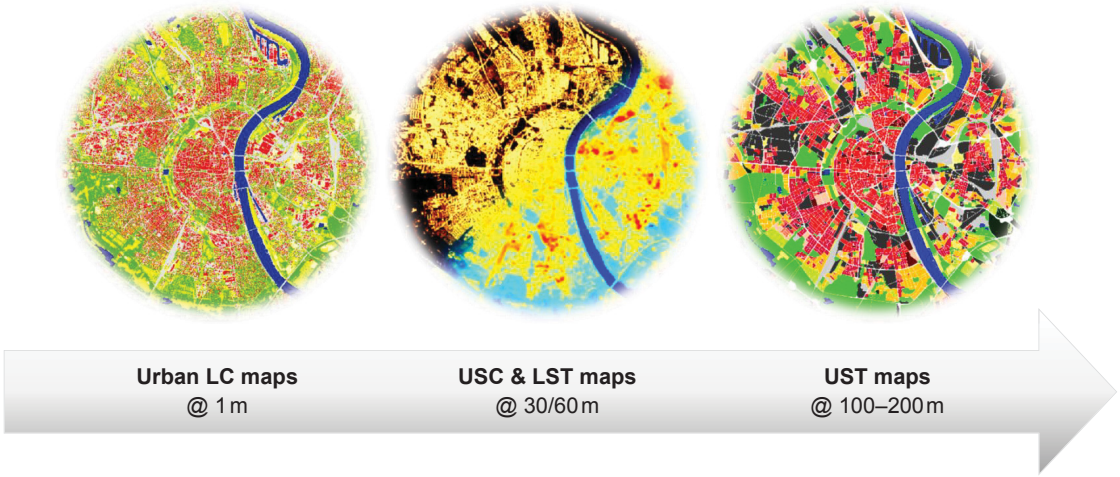

Fig. 5–1: Spatial resolution of the urban environmental maps produced. Note that the value range specified for the UST maps was estimated by calculating the square root of the average area of urban blocks in Berlin and Cologne.

products can be reused in the context of different follow-up applications, and highlights that their integration holds a considerable potential for advancing urban environmental research.

The results obtained for two entire test sites, 26 USCs, and 16 LST scenes covering four seasons offered a more complete picture of the complex USC–LST interplay and provided a scientifically sound basis for discussing some of the main drivers of the surface UHI effect (cf. Sect. 5.1). They may also be of value for the conception of improved thermal sharpening algorithms. However, due to the usage of Landsat ETM+ imagery, it always has to be kept in mind that the outcomes of the experiment are only valid for daytime LST measurements made at medium spatial resolution (i.e., 60 m) and small scan angles (i.e., ±7.4°). As a last point, it is noteworthy that the final study in this thesis involved the consecutive derivation and joint analysis of urban LC, USCs, USTs, and LST. This implies that it spanned across multiple spatial scales and therefore met one of the big challenges in urban remote sensing data processing and interpretation (Gamba 2013).

Closing thoughts

By accounting for existing research needs in the field of urban remote sensing, a suite of GEOBIA approaches was developed in the present thesis that build on top of each other. These methods exploit the synergistic potential among HSR multisource data and have been verified in the context of four selected urban environmental mapping and monitoring applications. From a geographical perspective, much of the work presented in this dissertation has concentrated on test sites located in Germany. However, the described classification and analysis schemes are expected to work well for any other Western culture city as long as the used multispectral imagery, object height data, and ancillary geospatial information are of a certain standard (cf. Tab. 5–2). Fortunately, these requirements are increasingly fulfilled thanks to a growing number of those HSR multisensor data becoming more and more available in the urbanized regions of the world (cf. Sect. 1.1).

All in all, the proposed set of procedures proved to be suitable for an accurate, yet robust characterization of different settlement parameters, including urban LC, USCs, and USTs. Moreover, its preparedness for (semi-) automated observation tasks was successfully demonstrated. It can therefore be considered as a useful complement to already operational monitoring applications running at the global scale (e.g., the extraction of urban footprints; Esch et al. 2013) as well as more experimental technical solutions operating at the local scale (e.g., the unmixing of urban surface materials; Heiden et al. 2007). In the final investigation of this work (cf. Sect. 4.4), the developed methods were effectively employed to produce thematic maps at three spatial scales (Fig. 5–1). These maps were then used to examine the complex spatio-temporal relationship between USCs and LST. This case study was exemplary for showing that the multilevel information products generated by the fusion of HSR multispectral and object height data are highly versatile and can be integrated, individually or jointly, into other analyses at comparable, coarser, or finer spatial scales. In this sense, the present thesis has provided a consistent and continuous methodological framework for local to regional mapping and monitoring of urban environmental phenomena.

5.3 Outlook

Instead of simply listing the open issues and unsolved problems arising from Chapter 4, this section proposes a concept for future research (Fig. 5–2). The concept directly builds upon the accomplished achievements and known limitations of the present thesis. For this purpose, a set of new, innovative, and interconnected work tasks is defined. These tasks aim at integrating and exploiting the developed methods and gained experiences. Moreover, they are designed to unify and address both unanswered questions and logical next steps within a single study framework.

Tasks #1/2 — Data compilation and urban environmental mapping
Similar to the scope of this thesis, the proposed research concept intends to make a contribution to the field of urban environmental mapping and monitoring using multisource data. To this end, an overall number of four main work tasks is necessary (Fig. 5–2). Task #1 deals with the acquisition and preparation of (primarily HSR) multisensor and -temporal remote sensing data and products as well as ancillary geospatial information. After the compilation of all required inputs, the methods developed in this dissertation are employed to map the status of urban LC, various USCs, and USTs (Task #2). Because the accuracy and robustness of the methods have already been demonstrated, classifications can be conducted for all major urban areas in Germany (e.g., those with more than 500 000 inhabitants). In a potential follow-up project, an extension to (mega-) cities and -settlement agglomerations located in different cultural regions of the world is also conceivable. Comparable efforts are already underway for US American cities and highlight the importance of open data policies and a close collaboration between researchers and practitioners for consistent and countrywide urban environmental mapping (O'Neil-Dunne et al. 2014).

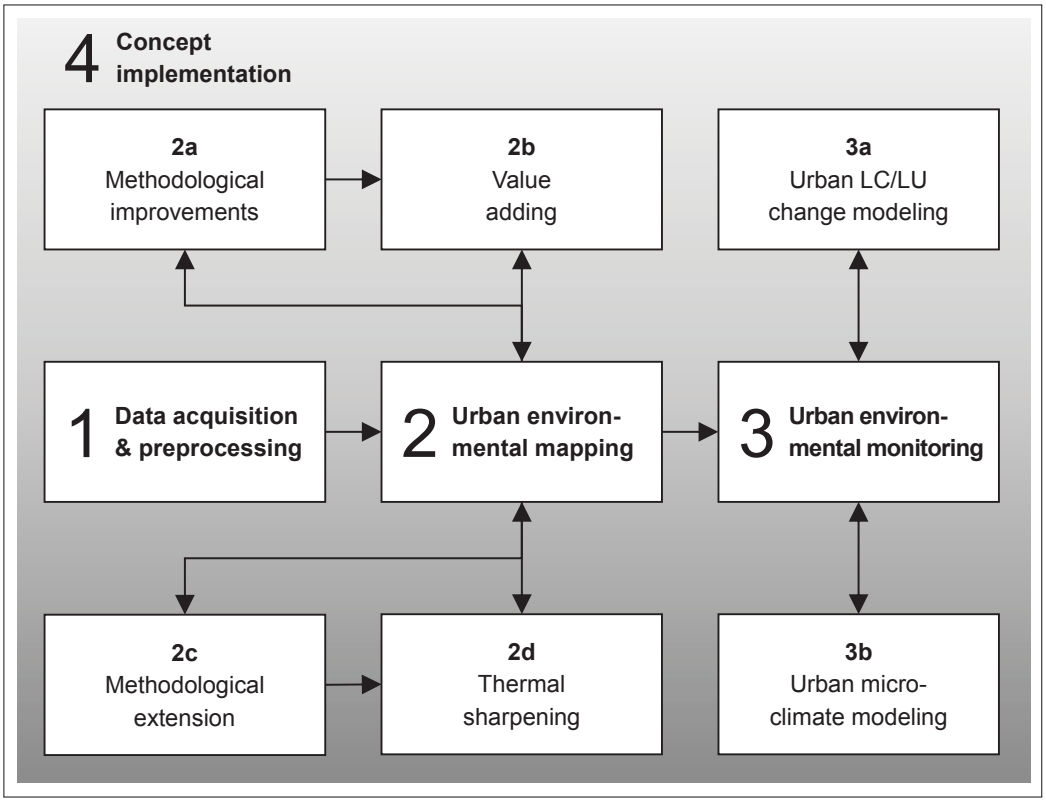

Fig. 5–2: Work tasks of the concept for future research.

Subtask #2a — Methodological improvements

Despite their suitability, the methods described in Chapter 4 revealed certain limitations (Tab. 5–2). For instance, the accuracy of the GEOBIA approaches for urban LC extraction and UST derivation partly suffered from too simplistic assumptions and the dependence on urban block data characteristics, respectively. The focus of Subtask #2a therefore lies on overcoming some of these flaws and improving the maps anticipated in the second project stage. One way to optimize the trade-off between performance and transferability would be to successively refine the decision rules, features, and thresholds of the methods and to compare their impact against the effort of implementation using the evaluation protocol suggested by Hofmann et al. (2011a). Since no map produced by digital classification routines is perfect, it might also be reasonable to develop a dedicated post processing and manual correction strategy that allows for eliminating obvious and non-systematic errors (cf. O'Neil-Dunne et al. 2014). Even though these misclassifications may have no bearing on total accuracy, they can compromise the visual quality of a map and thus reduce its acceptance among end users in a practical setting. To further increase the robustness of the described UST mapping procedure, a segmentation algorithm could be conceived that is independent of the properties of urban block boundary data. The realization of such an autonomous algorithm is clearly not a trivial task (cf. Lackner & Conway 2008), but it might be accomplished by relying on a priori knowledge of open source urban street networks (Geofabrik GmbH 2015).

Subtask #2b — Value adding

In a next step, the refined urban LC and UST classifications resulting from Subtask #2a are employed to infer a suite of value-added products and to assess their value within specific applications (Subtask #2b). When combined with other sources of data, the urban LC maps allow for the creation of different thematic information. Among others, these may include 3D city models (Wurm & Taubenböck 2010b) as well as maps on urban tree biomass (Raciti et al. 2014), urban tree canopies (Locke et al. 2010), solar potential (Jakubiec & Reinhart 2013), and signal obstruction (Lohani & Kumar 2008), to name only a few. By integrating 3D city models with HSR LST maps (cf. Subtask #2d), the estimation of complete urban surface temperatures in the sense of Voogt & Oke (1997) also seems possible. Even more opportunities arise from the available UST classifications as these provide a common spatial interface and can be linked to data from various fields of application. Potential derivatives of UST characterizations can be maps on various environmental and socio-economic variables like rain water infiltration and surface runoff (Pauleit & Duhme 2000), noise and air pollution (Weber et al. 2014a), heat risk and water contamination (Höfer 2013), energy efficiency and water demand (Geiss et al. 2011; Pauleit & Duhme 2000), CO_2 emissions (Baiocchi et al. 2015), population density (Meinel et al. 2008; Wurm & Taubenböck 2010a), and urban quality of life (Bhatti et al. 2016).

Subtask #2c — Methodological extension

Although the linkage between USCs and LST was comprehensively investigated, there is still a need for additional studies (Subtask #2c). As an example, the analyses in Berger et al. (2017) were restricted to daytime LST measurements made at medium spatial resolution (i.e., 60 m) and small scan angles (i.e., ±7.4°). An effective means to enhance their validity would be to extend the experimental setup to ASTER and MODIS data. In this way, examining the key determinants of nocturnal surface UHIs is possible. Moreover, the effect of TIR imagery acquired at coarser spatial resolution and larger off-nadir views can be inspected. The recent opening of the ASTER data archive is conducive to these types of investigation (Buis 2016). In Section 4.4, some methodological dependencies of the reported correlations have been discussed as well. Even though a part of these issues has been resolved in a subsequent study (Schmidt 2015), some of them (e.g., the impact of varying test site extents) remain open and deserve further attention within the proposed research concept. This enables obtaining a more complete picture of the USC–LST relationship.

Subtask #2d — Thermal sharpening

On the basis of the improved maps generated in Subtask #2a and the experiences gained in Subtask #2c, it is possible to design and evaluate a thermal sharpening algorithm, i.e., a method to increase the spatial resolution of TIR imagery. Thermal sharpening is a rapidly evolving field of research and of high relevance for a broad range of users and (urban) applications (Zhan et al. 2013).

Knowledge about the origins of urban LST and information on various settlement parameters are required to conceptualize and build an accurate and reliable technique. To synthesize fine-scale LST maps from lower spatial resolution data, a two-stage workflow is suggested. First, a comprehensive set of well-established and poorly-investigated surface UHI indicators is extracted from the repertoire of available data and derived environmental maps. It comprises, but is not limited to, controls like surface albedo, urban LC, the SVF, and topographic variables, such as elevation, slope, and aspect. Second, since the utility of RF machine learning has been demonstrated earlier (Sect. 4.3), it is proposed to make use of its distinct advantages for objectively selecting the most important features for predicting HSR urban LST. The prototype and final versions of the algorithm need to be assessed following an appropriate validation protocol (Zhan et al. 2013). They can be tested by experimenting with airborne TIR imagery as well as Landsat, ASTER, and/or MODIS data. The analysis of MODIS data might be of particular interest due to the relatively coarse spatial but high temporal resolution of the sensor. If the sharpening technique proves to be successful, it can be used to add a fourth parameter to the list of HSR urban environmental maps anticipated in Task #2.

Task #3 — Urban environmental monitoring

With the third main task, the research concept is extended by a temporal change monitoring and modeling component. The overall goal of this task is to gain a better understanding of past urban development patterns, processes, and their climatic impacts in order to predict future urbanization trends and prepare for the challenges associated with them. For this purpose, the urban LC, USC, and UST classifications produced for the selected test sites (Task #2) are used as temporal benchmarks (e.g., indicating the status for the year 2010) and analyzed in conjunction with a sequence of historical remote sensing data to detect the spatial changes of these settlement parameters over time. Ideally, a long and regularly-spaced time series (e.g., one acquisition per decade from 1960 to 2010) of declassified imagery, historical black and white, and/or CIR air photos is accessible for this task. From a methodological perspective, the major difficulty lies in developing an appropriate change detection and analysis framework that is independent of 3D point clouds. This is because such object height information are usually not available for the past decades. The framework could be built upon the GEOBIA approaches presented in Chapter 4 and should be able to deliver (change) maps of urban LC, USCs, and USTs for the individual acquisitions of the input data stack.

Subtask #3a— Urban LC/LU change modeling

The coupling of mapping and modeling is regarded to be crucial for advancing research on urban areas (Wentz et al. 2014). This is one reason why the proposed concept features two modeling components. In Subtask #3a, emphasis is put on a continuous simulation of past and future urban development (e.g., from 1960 to 2060). To ensure a realistic reproduction and prediction of patterns and processes, the urban environmental (benchmark) maps produced for each time step (i.e., between 1960 and 2010) are taken into account. This requires a model that can be

constrained by external information. A suitable candidate for this job is the widely-used slope, land use, exclusion, urban, transportation, hillshade (SLEUTH) model (Chaudhuri & Clarke 2013). The described experimental setup is expected to reveal the history and future of major urban areas in Germany at an unprecedented level of spatio-temporal detail. It therefore enables an improved identification and understanding of manifold urbanization mechanisms, from local-scale construction and demolition to regional diffusion and coalescence. A prime example for studying these processes as well as related climatic phenomena (cf. Subtask #3b) would be the Rhine-Ruhr metropolitan area, Germany's only "megacity" with almost 10 million residents (Destatis 2014).

Subtask #3b — Urban microclimate modeling

The second modeling component (Subtask #3b) constitutes a sensible and straightforward addition to Task #3. It focuses on the impact of long-term LC and LU changes (i.e., between 1960 and 2060) on the urban microclimate in general and urban temperatures in particular. To this end, use is made of ENVI-met, a 3D coupled flow-energy balance model to predict the interactions between urban surfaces, vegetation, and the atmosphere (Bruse & Fleer 1998). Analogous to SLEUTH, ENVI-met is highly flexible and can be parameterized with the urban environmental (change) maps derived in Task #3. However, it is recommended to define spatial subsets for modeling because the software makes complex predictions at fine scales and is thus computationally intensive. These subsets should represent "hot spots" of spatial change and may be in the form of inner-urban transects covering different types of LC and LU. For an improved data interpretation and modeling, it might also be advisable to reclassify the derived UST maps according to the LCZ scheme (Bechtel & Daneke 2012; Stewart & Oke 2012). This is because the LCZ scheme was explicitly designed for UHI studies and focuses on climatically relevant surface properties.

After subset definition, ENVI-met is prompted to simulate different urban climate parameters for the time steps before and after selected change events. In this way, recurring development patterns and processes that have contributed to urban warming in the past are recognized. By drawing on the results obtained from the SLEUTH model (Subtask #3a), it is also possible to study the future of urban microclimates. For instance, deliberate modifications, like the sealing of natural surfaces, the construction of buildings or the variation of their direction, height, and roofing, could be applied to those ENVI-met subsets corresponding to the most recent mapping products (cf. Task #2). In the framework of such what-if scenarios, imminent urbanization trends can be incorporated and their impact on UHI genesis can be investigated. Moreover, they enable the evaluation of different urban design choices for mitigating unwanted climatic effects in urban areas (cf. Berger et al. 2015). This ultimately helps deriving recommendations for planning and managing thermally balanced cityscapes. An ideal test site for implementing Subtask #3b would (again) be the urban heat archipelago (cf. Shepherd et al. 2013) of the Rhine-Ruhr metropolis.

Task #4 — Concept implementation

The final work task of the research concept is about implementation. This means that the methods developed, products generated, and the knowledge acquired have to be embedded into a larger practical context of urban planning and management. The rationale behind the implementation part is that mapping and monitoring strategies like the one presented above should always only represent one of several contributions from all kinds of disciplines with the aim to achieve sustainable urban development in both the environmental as well as the socio-economic dimension (cf. Sect. 1.1). Hence, in the framework of such holistic approaches, a close integration of inputs from various natural and social sciences is necessary (Simon 2007). To make progress towards sustainability in all of its facets, they also require concerted actions by stakeholders and interest groups from all levels, including policy makers, urban planners, resource managers, industry, science, and people (Solecki et al. 2013; Taubenböck 2011). Only through its implementation within real-world applications, it is granted that the proposed project retains its practical value and does not remain in the domain of research. At the same time, this lays the foundation for long-term collaborations bridging the gap between urban science and planning. On the basis of a common, holistic vision for turning sustainability concepts into reality, the previous, diagnostic work tasks become part of a larger endeavor to proactively address the challenges of urbanization in the 21st century.

Literature

Abrams M & Hook S (2013) NASA's Hyperspectral Infrared Imager (HyspIRI). In: Kuenzer C & Dech S (Eds) *Thermal infrared remote sensing: Sensors, methods, applications*. Dordrecht, The Netherlands: Springer, 117–130.

Abrams M, Hook S & Ramachandran B (2002) *ASTER user handbook. Version 2*. Technical report. Pasadena, CA: JPL.

Aguilar M, Saldaña M & Aguilar F (2013) GeoEye-1 and WorldView-2 pan-sharpened imagery for object-based classification in urban environments. *Int J Remote Sens* 34(7): 2583–2606.

Albertz J (2009[4]) *Einführung in die Fernerkundung. Grundlagen der Interpretation von Luft- und Satellitenbildern*. Darmstadt, Germany: Wissenschaftliche Buchgesellschaft, 254 pp.

Alexander C, Tansey K, Kaduk J, Holland D & Tate N (2011) An approach to classification of airborne laser scanning point cloud data in an urban environment. *Int J Remote Sens* 32(24): 9151–9169.

Angel S, Parent J, Civco D, Blei A & Potere D (2011a) The dimensions of global urban expansion: Estimates and projections for all countries, 2000–2050. *Prog Plann* 75(2): 53–107.

Angel S, Parent J, Civco D & Blei A (2011b) *Making room for a planet of cities*. Policy Focus Report PF027. Cambridge, MA: Lincoln Institute of Land Policy.

Arnfield A (2003) Two decades of urban climate research: A review of turbulence, exchanges of energy and water, and the urban heat island. *Int J Climatol* 23(1): 1–26.

Arnold C & Gibbons C (1996) Impervious surface coverage: The emergence of a key environmental indicator. *J Am Plann Assoc* 62(2): 243–258.

Artmann M (2014) Institutional efficiency of urban soil sealing management – From raising awareness to better implementation of sustainable development in Germany. *Landscape Urban Plan* 131: 83–95.

Arvidson T, Barsi J, Jhabvala M & Reuter D (2013) Landsat and thermal infrared imaging. In: Kuenzer C & Dech S (Eds) *Thermal infrared remote sensing: Sensors, methods, applications*. Dordrecht, The Netherlands: Springer, 177–196.

Assyakur A, Adnyana I, Arthana I & Nuarsa I (2012) Enhanced built-up and bareness index (EBBI) for mapping built-up and bare land in an urban area. *Remote Sens* 4(10): 2957–2970.

Aubrecht C, Steinnocher K, Hollaus M & Wagner W (2009) Integrating Earth observation and GIScience for high resolution spatial and functional modeling of urban land use. *Comput Environ Urban* 33(1): 15–25.

Baatz M, Hofmann C & Willhauck G (2008) Progressing from object-based to object-oriented image analysis. In: Blaschke T, Lang S & Hay G (Eds) *Object-based image analysis. Spatial concepts for knowledge-driven remote sensing applications*. Berlin, Germany: Springer, 29–42.

Baiocchi G, Creutzig F, Minx J & Pichler P.-P (2015) A spatial typology of human settlements and their CO_2 emissions in England. *Global Environ Chang* 34: 13–21.

Baltsavias E (1999) Airborne laser scanning: Basic relations and formulas. *ISPRS J Photogramm* 54(2–3): 199–214.

Banzhaf E & Höfer R (2008) Monitoring urban structure types as spatial indicators with CIR aerial photographs for a more effective urban environmental management. *IEEE J Sel Top Appl Earth Obs Remote Sens* 1(2): 129–138.

Baraldi A & Boschetti L (2012) Operational automatic remote sensing image understanding systems: Beyond geographic object-based and object-oriented image analysis (GEOBIA/GEOOIA). Part 1: Introduction. *Remote Sens* 4(9): 2694–2735.

Barnsley M & Barr S (1996) Inferring urban land use from satellite sensor images using kernel-based spatial reclassification. *Photogramm Eng Rem S* 62(8): 949–958.

Barnsley M, Møller-Jensen L & Barr S (2001) Inferring urban land use by spatial and structural pattern recognition. In: Donnay J, Barnsley M & Longley P (Eds) *Remote sensing and urban analysis*. GISDATA 9. Boca Raton, FL: CRC Press, 115–144.

Barnsley M & Barr S (2000) Monitoring urban land use by Earth observation. *Surv Geophys* 21(2–3): 269–289.

Barsi J, Schott J, Hook S, Raqueno N, Markham B & Radocinski R (2014) Landsat-8 Thermal Infrared Sensor (TIRS) vicarious radiometric calibration. *Remote Sens* 6(11): 11607–11626.

Baud I, Kuffer M, Pfeffer K, Sliuzas R & Karuppannan S (2010) Understanding heterogeneity in metropolitan India: The added value of remote sensing data for analyzing sub-standard residential areas. *Int J Appl Earth Obs* 12(5): 359–374.

Bechtel B (2011) Multisensorale Fernerkundungsdaten zur mikroklimatischen Beschreibung und Klassifikation urbaner Strukturen. *Photogramm Fernerkun* 5: 325–338.

Bechtel B (2012a) Downscaling land surface temperature in an urban area: A case study for Hamburg, Germany. *Remote Sens* 4(10): 3184–3200.

Bechtel B (2012b) Robustness of annual cycle parameters to characterize the urban thermal landscapes. *IEEE Geosci Remote S* 9(5): 876–880.

Bechtel B, Alexander P, Böhner J, Ching J, Conrad O, Feddema J, Mills G, See L & Stewart I (2015) Mapping local climate zones for a worldwide database of the form and function of cities. *ISPRS Int J Geo-Inf* 4(1): 199–219.

Bechtel B & Daneke C (2012) Classification of local urban climate zones based on multiple Earth observation data. *IEEE J Sel Top Appl Earth Obs Remote Sens* 5(4): 1191–1202.

Beck L, Lobitz B & Wood B (2000) Remote sensing and human health: New sensors and new opportunities. *Emerg Infect Dis* 6(3): 217–227.

Becker F & Li Z (1995) Surface temperature and emissivity at various scales: Definition, measurement and related problems. *Remote Sens Rev* 12(3–4): 225–253.

Belgiu M, Hofer B & Hofmann P (2014) Coupling formalized knowledge bases with object-based image analysis. *Remote Sens Lett* 5(6): 530–538.

Ben-Dor E & Saaroni H (1997) Airborne video thermal radiometry as a tool for monitoring microscale structures of the urban heat island. *Int J Remote Sens* 18(14): 3039–3053.

Benediktsson J, Chanussot J & Moon W (2012) Very high-resolution remote sensing: Challenges and opportunities. *P IEEE* 100(6): 1907–1910.

Benz U, Hofmann P, Willhauck G, Lingenfelder I & Heynen M (2004) Multi-resolution, object-oriented fuzzy analysis of remote sensing data for GIS-ready information. *ISPRS J Photogramm* 58(3–4): 239–258.

Bereitschaft B & Debbage K (2013) Urban form, air pollution, and CO_2 emissions in large U.S. metropolitan areas. *Prof Geogr* 65(4): 612–635.

Berger C, Riedel F, Rosentreter J, Stein E, Hese S & Schmullius C (2015) Fusion of airborne hyperspectral and LiDAR remote sensing data to study the thermal characteristics of urban environments. In: Helbich M, Arsanjani J & Leitner M (Eds) *Computational approaches for urban environments*. Geotechnologies and the environment 13. Heidelberg, Germany: Springer, 273–292.

Berger C, Rosentreter J, Voltersen M, Baumgart C, Schmullius C & Hese S (2017) Spatio-temporal analysis of the relationship between 2D/3D urban site characteristics and land surface temperature. *Remote Sens Environ* 193C: 225–243.

Berger C, Voltersen M, Eckardt R, Eberle J, Heyer T, Salepci N, Hese S, Schmullius C, Tao J, Auer S, Bamler R, Ewald K, Gartley M, Jacobson J, Buswell A, Du Q & Pacifici F (2013a) Multi-modal and multi-temporal data fusion: Outcome of the 2012 GRSS Data Fusion Contest. *IEEE J Sel Top Appl Earth Obs Remote Sens* 6(3): 1324–1340.

Berger C, Voltersen M, Hese S, Walde I & Schmullius C (2013b) Robust extraction of urban land cover information from HSR multi-spectral and LiDAR data. *IEEE J Sel Top Appl Earth Obs Remote Sens* 6(5): 2196–2211.

Berghauser Pont M & Haupt P (Eds) (2010) *Spacematrix: Space, density and urban form*. Rotterdam, The Netherlands: NAi Publishers, 280 pp.

Berlin Senate Department for Urban Development and the Environment (2015) *Urban structure*. <http://www.stadtentwicklung.berlin.de/umwelt/umweltatlas/edin_607.htm> (last accessed on 2015-05-12).

Berry B (2008) Urbanization. In: Marzluff J, Shulenberger E, Endlicher W, Alberti M, Bradley G, Ryan C, ZumBrunnen C & Simon U (Eds) *Urban ecology. An international perspective on the interaction between humans and nature*. New York, NY: Springer, 25–48.

Besussi E, Chin N, Batty M & Longley P (2010) The structure and form of urban settlements. In: Rashed T & Jürgens C (Eds) *Remote sensing of urban and suburban areas*. Remote sensing and digital image processing 10. Dordrecht, The Netherlands: Springer, 13–31.

Bhaskaran S, Paramananda S & Ramnarayan M (2010) Per-pixel and object-oriented classification methods for mapping urban features using Ikonos satellite data. *Appl Geogr* 30(4): 650–665.

Bhatta B (2010) *Analysis of urban growth and sprawl from remote sensing data*. Advances in geographic information science. Berlin, Germany: Springer, 172 pp.

Bhatta B, Saraswati S & Bandyopadhyay D (2010) Urban sprawl measurement from remote sensing data. *Appl Geogr* 30(4): 731–740.

Bhatti S, Tripathi N. Nagai M & Nitivattananon V (2016) Spatial interrelationships of quality of life with land use/land cover, demography and urbanization. *Soc Indic Res* n.v.(n.n.): 1–24.

Blaschke T (2000) Ohne Salz und Pfeffer. Objektorientierte Bildanalyse – Eine Revolution in der Fernerkundung. *GeoBIT* 2: 30–32.

Blaschke T (2010) Object based image analysis for remote sensing. *ISPRS J Photogramm* 65(1): 2–16.

Blaschke T, Hay G, Kelly M, Lang S, Hofmann P, Addink E, Queiroz Feitosa R, van der Meer F, van der Werff H, van Coillie F & Tiede D (2014) Geographic object-based image analysis – Towards a new paradigm. *ISPRS J Photogramm* 87: 180–191.

Blaschke T, Lang S & Hay G (Eds) (2008) *Object-based image analysis for remote sensing. Spatial concepts for knowledge-driven remote sensing applications*. Berlin, Germany: Springer, 818 pp.

Blaschke T & Strobl J (2001) What's wrong with pixels? Some recent developments interfacing remote sensing and GIS. *GIS* 14(6): 12–17.

Bochow M (2010) Automatisierungspotenzial von Stadtbiotopkartierungen durch Methoden der Fernerkundung. PhD thesis. Osnabrück, Germany: Fachbereich Mathematik/Informatik, Universität Osnabrück.

Bochow M, Peisker T, Roessner S, Segl K & Kaufmann H (2010a) Towards an automated update of urban biotope maps using remote sensing data: What is possible?. In: Müller N, Werner P & Kelcey J (Eds) *Urban biodiversity and design*. Conservation science and practice 7. Hoboken, NJ: Blackwell Publishing, 255–272.

Bochow M, Taubenböck H, Segl K & Kaufmann H (2010b) An automated and adaptable approach for characterizing and partitioning cities into urban structure types. *Proceedings of IGARSS*, 25–30 July, Honolulu, HI, 1796–1799.

Böhm P, Breuste J, Werheit M & Wickop E (2001a) Definition des verwendeten Stadtstrukturtypenansatzes. In: Breuste J, Wächter M & Bauer B (Eds) *Beiträge zur umwelt- und sozialverträglichen Entwicklung von Stadtregionen*. Leipzig, Germany: UFZ, CD–Rom.

Böhm P, Breuste J, Werheit M & Wickop E (2001b) Erläuterungen zur Stadtstrukturtypenkarte Leipzig. In: Breuste J, Wächter M & Bauer B (Eds) *Beiträge zur umwelt- und sozialverträglichen Entwicklung von Stadtregionen*. Leipzig, Germany: UFZ, CD–Rom.

Böhm P, Breuste J, Werheit M & Wickop E (2001c) Theoretische Grundlagen zum Stadtstrukturtypenansatzes. In: Breuste J, Wächter M & Bauer B (Eds) *Beiträge zur umwelt- und sozialverträglichen Entwicklung von Stadtregionen*. Leipzig, Germany: UFZ, CD–Rom.

Bolund P & Hunhammar S (1999) Ecosystem services in urban areas. *Ecol Econ* 29(2): 293–301.

Botkin D & Beveridge C (1997) Cities as environments. *Urban Ecosystems* 1(1): 3–19.

Brenner A & Roessing L (2008) Radar imaging of urban areas by means of very high-resolution SAR and interferometric SAR. *IEEE T Geosci Remote* 46(10): 2971–2982.

Breuste J (2010) Challenges and problems of implementing landscape ecological knowledge in practice – The case of urban development. *The Problems of Landscape Ecology* 28: 23–32.

Brown L (Ed) (2001) *Eco-economy: Building an economy for the Earth*. New York, NY: Norton & Company, 333 pp.

Bruse M & Fleer H (1998) Simulating surface–plant–air interactions inside urban environments with a three dimensional numerical model. *Environ Modell Softw* 13(3–4): 373–384.

Buis A (2016) *Japan make ASTER Earth data available at no cost*. <https://www.nasa.gov/feature/jpl/nasa-japan-make-aster-earth-data-available-at-no-cost> (last accessed on 2015-05-12).

Burnett C & Blaschke T (2003) A multi-scale segmentation/object relationship modelling methodology for landscape analysis. *Ecol Model* 168(3): 233–249.

Buyantuyev A & Wu J (2010) Urban heat islands and landscape heterogeneity: Linking spatiotemporal variations in surface temperatures to land-cover and socioeconomic patterns. *Landscape Ecol* 25(1): 17–33.

Cai S & Liu D (2013) A comparison of object-based and contextual pixel-based classifications using high and medium spatial resolution images. *Remote Sens Lett* 4(10): 998–1007.

Campbell J & Wynne R (2011[5]) *Introduction to remote sensing*. New York, NY: The Guilford Press, 667 pp.

Cao Y, Wei H, Zhao H & Li N (2012) An effective approach for land-cover classification from airborne LiDAR fused with co-registered data. *Int J Remote Sens* 33(18): 5927–5953.

Chander G, Markham B & Helder D (2009) Summary of current radiometric calibration coefficients for Landsat MSS, TM, ETM+, and EO-1 ALI sensors. *Remote Sens Environ* 113(5): 893–903.

Changnon S (1992) Inadvertent weather modification in urban areas: Lessons for global climate change. *Bull Amer Meteor Soc* 73(5): 619–627.

Chaudhuri G & Clarke K (2013) The SLEUTH land use change model: A review. *Int J Environ Resour Res* 1(1): 88–104.

Chen X & Nordhaus W (2011) Using luminosity data as a proxy for economic statistics. *P Natl Acad Sci USA* 108(21): 8589–8594.

Chen X, Zhao H, Li P & Yin Z (2006) Remote sensing image-based analysis of the relationship between urban heat island and land use/cover changes. *Remote Sens Environ* 104(2): 133–146.

Chen Y (2011) Derivation of the functional relations between fractal dimension of and shape indices of urban form. *Comput Environ Urban* 35(6): 442–451.

Chen Y, Su W, Li J & Sun Z (2009) Hierarchical object oriented classification using very high resolution imagery and LiDAR data over urban areas. *Adv Space Res* 43(7): 1101–1110.

Cheng J & Ren H (2012) Land-surface temperature and thermal infrared emissivity. In: Liang S, Li X & Wang J (Eds) *Advanced remote sensing. Terrestrial information extraction and applications*. Oxford, UK: Academic Press, 235–271.

Chrysoulakis N, Feigenwinter C, Triantakonstantis D, Penyevskiy I, Tal A, Parlow E, Fleishman G, Düzgün S, Esch T & Marconcini M (2014) A conceptual list of indicators for urban planning and management based on Earth observation. *ISPRS Int J Geo-Inf* 3(3): 980–1002.

Chun B & Guhathakurta S (2016) The impacts of three-dimensional surface characteristics on urban heat islands over the diurnal cycle. *Prof Geogr*, 1–12.

Chun B & Guldmann J (2014) Spatial statistical analysis and simulation of the urban heat island in high-density central cities. *Landscape Urban Plan* 125: 76–88.

CIESIN (Center for International Earth Science Information Network)/Columbia University, IFPRI (International Food Policy Research Institute), The World Bank & CIAT (Centro Internacional de Agricultura Tropical) (2011) *Global Rural-Urban Mapping Project, Version 1 (GRUMPv1): Urban extents grid*. Palisades, NY: NASA Socioeconomic Data & Applications Center (SEDAC). <http://sedac.ciesin.columbia.edu/data/set/grump-v1-urban-extents> (last accessed on 2015-05-12).

Comber A (2008) The separation of land cover from land use using data primitives. *J Land Use Sci* 3(4): 215–229.

Comber A, Wadsworth R & Fisher P (2008) Using semantics to clarify the conceptual confusion between land cover and land use: The example of 'forest'. *J Land Use Sci* 3(2–3): 185–198.

Cook B, Corp L, Nelson R, Middleton E, Morton D, McCorkel J, Masek J, Ranson K, Ly V & Montesano P (2013) NASA Goddard's LiDAR, Hyperspectral and Thermal (G-LiHT) Airborne Imager. *Remote Sens* 5(8): 4045–4066.

Coseo P & Larsen L (2014) How factors of land use/land cover, building configuration, and adjacent heat sources and sinks explain urban heat islands in Chicago. *Landscape Urban Plan* 125: 117–129.

Crooks A, Pfoser D, Jenkins A, Croitoru A, Stefanidis A, Smith D, Karagiorgou S, Efentakis A & Lamprianidis G (2014) Crowdsourcing urban form and function. *Int J Geogr Inf Sci* 29(5): 720–741.

Dahiya S, Garg P & Jat M (2013) A comparative study of various pixel-based image fusion techniques as applied to an urban environment. *Int J Image Data Fusion* 4(3): 197–213.

De Souza L & Giunta M (2011) Urban indices as environmental noise indicators. *Comput Environ Urban* 35(5): 421–430.

Dell'Acqua F (2009) The role of SAR sensors. In: Gamba P & Herold M (Eds) *Global mapping of human settlement*. Boca Raton, FL: CRC Press, 309–336.

Dell'Acqua F, Gamba P & Lisini G (2006) Semi-automatic choice of scale-dependent features for satellite SAR image classification. *Pattern Recogn Lett* 27(4): 244–251.

Deng C & Wu C (2012) BCI: A biophysical composition index for remote sensing of urban environments. *Remote Sens Environ* 127: 247–259.

Destatis (2014) *Städte (alle Gemeinden mit Stadtrecht) nach Fläche, Bevölkerung und Bevölkerungsdichte am 31.12.2012*. <www.destatis.de/DE/ZahlenFakten/LaenderRegionen/Regionales/Gemeindeverzeichnis/Administrativ/Aktuell/05Staedte.html> (last accessed on 2015-05-12).

Di Gregorio A (2005) *Land cover classification system (LCCS). Classification concepts and user manual. Software version 2*. FAO environment and natural resources service series 8. Rome, Italy: FAO, 208 pp.

DigitalGlobe (2013) *DigitalGlobe and GeoEye complete combination*. <http://investor.digitalglobe.com/phoenix.zhtml?c=70788&p=irol-newsArticle&ID=1780199> (last accessed on 2015-05-12).

Doll C, Muller J & Morley J (2006) Mapping regional economic activity from night-time light satellite imagery. *Ecol Econ* 57(1): 75–92.

Dong Y, Forster B & Ticehurst C (1997) Radar backscatter analysis for urban environments. *Int J Remote Sens* 18(6): 1351–1364.

Donnay J (1999) Use of remote sensing in planning. European perspectives. In: Stillwell J, Geertman S & Openshaw S (Eds) *Geographical information and planning*. Advances in spatial science. The regional science series. Berlin, Germany: Springer, 242–260.

Donnay J, Barnsley M & Longley P (Eds) (2001) *Remote sensing and urban analysis*. GISDATA 9. Boca Raton, FL: CRC Press, 272 pp.

Dousset B, Gourmelon F, Laaidi K, Zeghnoun A, Giraudet E, Bretin P, Mauri E & Vandentorren S (2011) Satellite monitoring of summer heat waves in the Paris metropolitan area. *Int J Climatol* 31(2): 313–323.

Du P, Liu P, Xia J, Feng L, Liu S, Tan K & Cheng L (2014) Remote sensing image interpretation for urban environment analysis: Methods, system and examples. *Remote Sens* 6(10): 9458–9474.

Ebert A, Kerle N & Stein A (2009) Urban social vulnerability assessment with physical proxies and spatial metrics derived from air- and spaceborne imagery and GIS data. *Nat Hazards* 48(2): 275–294.

EEA (European Environment Agency) (2002) *Environmental signals 2002. Benchmarking the millenium*. Environmental Assessment Report 9. Luxembourg: Office for Official Publications of the European Communities.

EEA (European Environment Agency) (2006) *Urban sprawl in Europe – The ignored challenge*. EEA Report 10/2006. Luxembourg: Office for Official Publications of the European Communities.

EEA (European Environment Agency) (2013) *Corine land cover 2006 seamless vector data. Version 17 (12/2013)*. <http://www.eea.europa.eu/data-and-maps> (last accessed on 2015-05-12).

Ehlers M (2009) Future EO sensors of relevance – Integrated perspective for global urban monitoring. In: Gamba P & Herold M (Eds) *Global mapping of human settlement*. Boca Raton, FL: CRC Press, 321–337.

Ehlers M, Klonus S & Åstrand P (2008) Quality assessment for multi-sensor multi-date image fusion. *Proceedings of the XXIth ISPRS congress*, July 03–11, Beijing, China, 499–506.

Eliasson I (1992) Infrared thermography and urban temperature patterns. *Int J Remote Sens* 13(5): 869–879.

eoPortal (2015a) *CBERS-3 and 4*. <https://directory.eoportal.org/web/eoportal/satellite-missions/c-missions/cbers-3-4> (last accessed on 2015-05-12).

eoPortal (2015b) *KOMPSAT-2*. <https://directory.eoportal.org/web/eoportal/satellite-missions/k/kompsat-2> (last accessed on 2015-05-12).

EPA (United States Environmental Protection Agency) (2008) *Reducing urban heat islands: Compendium of strategies. Urban heat island basics*. Technical report. Washington, DC: Office of Atmospheric Programs/Climate Protection Partnership Division.

Esch T, Himmler V, Schorcht G, Thiel M, Wehrmann T, Bachofer F, Conrad C, Schmidt M & Dech S (2009) Large-area assessment of impervious surface based on integrated analysis of single-date Landsat-7 images and geospatial vector data. *Remote Sens Environ* 113(8): 1678–1690.

Esch T, Marconcini M, Felbier A, Roth A, Heldens W, Huber M, Schwinger M, Taubenböck H, Müller A & Dech S (2013) Urban footprint processor – Fully automated processing chain generating settlement masks from global data of the TanDEM-X mission. *IEEE Geoscience and Remote Sensing Letters* 10(6): 1617–1621.

Esch T, Marconcini M, Felbier A, Roth A & Taubenböck H (2014) Mapping global human settlement pattern using SAR data acquired by the TanDEM-X mission. In: Weng Q (Ed) *Global urban monitoring and assessment through Earth observation*. Remote sensing applications. Boca Raton, FL: CRC Press, 83–96.

EUSI (European Space Imaging) (2015) *Satellites*. <http://www.euspaceimaging.com/satellites> (last accessed on 2015-05-12).

Evans T, Costa M, Telmer K & Silva T (2010) Using ALOS/PALSAR and Radarsat-2 to map land cover and seasonal inundation in the Brazilian Pantanal. *IEEE J Sel Top Appl Earth Obs Remote Sens* 3(4): 560–575.

Fauvel M, Chanussot J & Benediktsson J (2006) Decision fusion for the classification of urban remote sensing images. *IEEE T Geosci Remote* 44(10): 2828–2838.

Fina S, Krehl A, Siedentop S, Taubenböck H & Wurm M (2014) Dichter dran! Neue Möglichkeiten der Vernetzung von Geobasis-, Statistik- und Erdbeobachtungsdaten zur räumlichen Analyse und Visualisierung von Stadtstrukturen mit Dichteoberflächen und -profilen. *Raumforsch Raumordn* 72(3): 179–194.

Fisher P, Comber A & Wadsworth R (2005) Land use and land cover: Contradiction or complement. In: Fisher P & Unwin D (Eds) *Re-presenting GIS*. Hoboken, NJ: John Wiley & Sons, 85–98.

Flanders D, Hall-Beyer M & Pereverzoff J (2003) Preliminary evaluation of eCognition object-based software for cut block delineation and feature extraction. *Can J Remote Sens* 29(4): 441–452.

Foley J, DeFries R, Asner G, Barford C, Bonan G, Carpenter S, Chapin F, Coe M, Daily G, Gibbs H, Helkowski J, Holloway T, Howard E, Kucharik C, Monfreda C, Patz J, Prentice I, Ramankutty N & Snyder P (2005) Global consequences of land use. *Science* 309(5734): 570–574.

Forster B (1993) Coefficient of variation as a measure of urban spatial attributes using spot HRV and Landsat TM data. *Int J Remote Sens* 14(12): 2403–2409.

Forzieri G, Tanteri L, Moser G & Catani F (2013) Mapping natural and urban environments using airborne multi-sensor ADS40–MIVIS–LiDAR synergies. *Int J Appl Earth Obs* 23: 313–323.

Franke J, Roberts D, Halligan K & Menz G (2009) Hierarchical Multiple Endmember Spectral Mixture Analysis (MESMA) of hyperspectral imagery for urban environments. *Remote Sens Environ* 113(8): 1712–1723.

Gál T, Lindberg F & Unger J (2009) Computing continuous sky view factors using 3D urban raster and vector databases: Comparison and application to urban climate. *Theor Appl Climatol* 95(1): 111–123.

Gallo K, Tarpley J, McNab A & Karl T (1995) Assessment of urban heat islands: A satellite perspective. *Atmos Res* 37(1–3): 37–43.

Gamba P (2013) Global mapping of human settlement: A global challenge for EO data processing and interpretation. *P IEEE* 101(3): 570–581.

Gamba P (2014) Image and data fusion in remote sensing of urban areas: Status issues and research trends. *Int J Image Data Fusion* 5(1): 2–12.

Gamba P, Dell'Acqua F, Cisotta F & Lisini G (2004) High resolution InSAR "builtscape" improvement using LiDAR as ancillary data. *Proceedings of IGARSS*, 20–24 September, Anchorage, AK, 1808–1811.

Gamba P, Dell'Acqua F & Dasarathy B (2005) Urban remote sensing using multiple data sets: Past, present, and future. *Inform Fusion* 6(4): 319–326.

Gamba P & Herold M (Eds) (2009) *Global mapping of human settlement. Experiences, datasets, and prospects*. Remote sensing applications. Boca Raton, FL: CRC Press, 364 pp.

Gao B (1996) NDWI – A normalized difference water index for remote sensing of vegetation liquid water from space. *Remote Sens Environ* 58(3): 257–266.

Geiss C, Taubenböck H, Wurm M, Esch T, Nast M, Schillings C & Blaschke T (2011) Remote sensing-based characterization of settlement structures for assessing local potential of district heat. *Remote Sens* 3(7): 1447–1471.

Geofabrik GmbH (2015) *OpenStreetMap data extracts*. <http://download.geofabrik.de/> (last accessed on 2015-05-12).

Gibson C (1998) *Brownfield: Red data. The values artificial habitats have for uncommon invertebrates*. English Nature Research Reports 273. Peterborough, UK: English Nature.

Gill S, Handley J, Ennos A, Pauleit S, Theuray N & Lindley S (2008) Characterising the urban environment of UK cities and towns: A template for landscape planning. *Landscape Urban Plan* 87(3): 210–222.

Gillespie A (2014) Land surface temperature. In: Njoku E (Ed) *Encyclopedia of remote sensing*. Encyclopedia of Earth sciences series. New York City, NY: Springer, 314–319.

Gillespie A, Rokugawa S, Matsunaga T, Cothern J, Hook S & Kahle A (1998) A temperature and emissivity separation algorithm for Advanced Spaceborne Thermal Emission and Reflection Radiometer (ASTER) images. *IEEE T Geosci Remote* 36(4): 1113–1126.

Giri C (2012) Brief overview of remote sensing of land cover. In: Weng Q (Ed) *Remote sensing of land use and land cover*. Remote sensing applications. Boca Raton, FL: CRC Press, 3–12.

Giridharan R & Kolokotroni M (2009) Urban heat island characteristics in London during winter. *Sol Energy* 83(9): 1668–1682.

GLP (Global Land Project) (2005) *Science plan and implementation strategy*. IGBP Report No. 53/IHDP Report No. 19. Stockholm, Sweden: IGBP Secretariat.

González-Aguilera D, Crespo-Matellán E, Hernández-López D & Rodríguez-Gonzálvez P (2013) Automated urban analysis based on LiDAR-derived building models. *IEEE T Geosci Remote* 51(3): 1844–1851.

Gopal S, Tang X, Phillips N, Nomack M, Pasquarella V & Pitts J (2016) Characterizing urban landscapes using fuzzy sets. *Comput Environ Urban* 57: 212–223.

Graesser J, Cheriyadat A, Vatsavai R, Chandola V, Long J & Bright E (2012) Image based characterization of formal and informal neighborhoods in an urban landscape. *IEEE J Sel Top Appl Earth Obs Remote Sens* 5(4): 1164–1176.

Greenhill D, Ripke L, Hitchman A, Jones G & Wilkinson G (2003) Characterization of suburban areas for land use planning using landscape ecological indicators derived from Ikonos-2 multispectral imagery. *IEEE T Geosci Remote* 41(9): 2015–2021.

Griffiths P, Hostert P, Gruebner O & van der Linden S (2010) Mapping megacity growth with multi-sensor data. *Remote Sens Environ* 114(2): 426–439.

Grimm N, Faeth S, Golubiewski N, Redman C, Wu J, Bai X & Briggs J (2008) Global change and the ecology of cities. *Science* 319(5864): 756–760.

Grimmond S (2007) Urbanization and global environmental change: Local effects of urban warming. *Geogr J* 173(1): 83–88.

Guindon B (1997) Computer-based aerial image understanding: A review and assessment of its application to planimetric information extraction from very high resolution satellite images. *Can J Remote Sens* 23(1): 38–47.

Gupta K, Kumar P, Pathan S & Sharma K (2012) Urban Neighborhood Green Index – A measure of green spaces in urban areas. *Landscape Urban Plan* 105(3): 325–335.

Haala N & Brenner C (1999) Extraction of buildings and trees in urban environments. *ISPRS J Photogramm* 54(2–3): 130–137.

Haas J, Furberg D & Ban Y (2015) Satellite monitoring of urbanization and environmental impacts – A comparison of Stockholm and Shanghai. *Int J Appl Earth Obs* 38: 138–149.

Haase D & Nuissl H (2007) Does urban sprawl drive changes in the water balance and policy?: The case of Leipzig (Germany) 1870–2003. *Landscape Urban Plan* 80(1–2): 1–13.

Hahs A, McDonnell M, McCarthy M, Vesk P, Corlett R, Norton B, Clemants S, Duncan R, Thompson K, Schwartz M & Williams N (2009) A global synthesis of plant extinction rates in urban areas. *Ecol Lett* 12(11): 1165–1173.

Hamedianfar A, Shafri H, Mansor S & Ahmad N (2014) Improving detailed rule-based feature extraction of urban areas from WorldView-2 image and LiDAR data. *Int J Remote Sens* 35(5): 1876–1899.

Han Y, Kim H, Choi J & Kim Y (2012) A shape–size index extraction for classification of high resolution multispectral satellite images. *Int J Remote Sens* 33(6): 1682–1700.

Haralick R, Shanmugam K & Dinstein I (1973) Textural features for image classification. *IEEE T Syst Man Cyb* 3(6): 610–621.

Harrison C & Davies G (2002) Conserving biodiversity that matters: Practitioners' perspectives on brownfield development and urban nature conservation in London. *J Environ Manage* 65(1): 95–108.

Hay G & Castilla G (2008) Geographic Object-Based Image Analysis (GEOBIA): A new name for a new discipline. In: Blaschke T, Lang S & Hay G (Eds) *Object-based image analysis for remote sensing. Spatial concepts for knowledge-driven remote sensing applications*. Berlin, Germany: Springer, 75–89.

Hay G, Kyle C, Hemachandran B, Chen G, Rahman M, Fung T & Arvai J (2011) Geospatial technologies to improve urban energy efficiency. *Remote Sens* 3(7): 1380–1405.

Heiden U, Heldens W, Roessner S, Segl K, Esch T & Mueller A (2012) Urban structure type characterization using hyperspectral remote sensing and height information. *Landscape Urban Plan* 105(4): 361–375.

Heiden U, Segl K, Roessner S & Kaufmann H (2007) Determination of robust spectral features for identification of urban surface materials in hyperspectral remote sensing data. *Remote Sens Environ* 111(4): 537–552.

Heinonen J, Horvath A & Junnila S (2015) Environmental assessments in the built environment: Crucial yet underdeveloped. *Environ Res Lett* 10(3): 1–6.

Heinzel J & Kemper T (2015) Automated metric characterization of urban structure using building decomposition from very high resolution imagery. *Int J Appl Earth Obs* 35(B): 151–160.

Heldens W (2010) Use of airborne hyperspectral data and height information to support urban micro climate characterisation. PhD thesis. Würzburg, Germany: Julius-Maximilians-Universität Würzburg.

Heldens W, Heiden U, Esch T, Stein E & Müller A (2011) Can the future EnMAP mission contribute to urban applications? A literature survey. *Remote Sens* 3(9): 1817–1846.

Heldens W, Taubenböck H, Esch T, Heiden U & Wurm M (2013) Analysis of surface thermal patterns in relation to urban structure types: A case study for the City of Munich. In: Kuenzer C & Dech S (Eds) *Thermal infrared remote sensing: Sensors, methods, applications*. Dordrecht, The Netherlands: Springer, 475–493.

Henderson F & Xia Z (1997) SAR applications in human settlement detection, population estimation and urban land use pattern analysis: A status report. *IEEE T Geosci Remote* 35(1): 79–85.

Henderson J, Storeygard A & Weil D (2012) Measuring economic growth form outer space. *Am Econ Rev* 102(2): 994–1028.

Heritage G & Large A (Eds) (2009) *Laser scanning for the environmental sciences*. Hoboken, NJ: John Wiley & Sons, 278 pp.

Hermosilla T, Palomar-Vázquez J, Balaguer-Beser Á, Balsa-Barreiro J & Ruiz L (2014) Using street based metrics to characterize urban typologies. *Comput Environ Urban* 44: 68–79.

Hermosilla T, Ruiz L, Recio J & Cambra-López M (2012) Assessing contextual descriptive features for plot-based classification of urban areas. *Landscape Urban Plan* 106(1): 124–137.

Herold M, Gardner M & Roberts D (2003a) Spectral resolution requirements for mapping urban areas. *IEEE T Geosci Remote* 41(9): 1907–1919.

Herold M, Liu X & Clarke K (2003b) Spatial metrics and image texture for mapping urban land use. *Photogramm Eng Rem S* 69(9): 991–1001.

Herold M, Roberts D, Gardner M & Dennison P (2004) Spectrometry for urban area remote sensing – Development and analysis of a spectral library from 350 to 2400 nm. *Remote Sens Environ* 91(3–4): 304–319.

Herold M & Roberts D (2006) Multispectral satellites – Imaging spectrometry – LiDAR: Spectral-spatial tradeoffs in urban mapping. *Int J Geoinf* 2(1): 1–13.

Herold M, Scepan J & Clarke K (2002) The use of remote sensing and landscape metrics to describe structures and changes in urban land uses. *Environ Plann A* 34(8): 1443–1458.

Höfer R (2013) Remote sensing based derivation of urban structure types to assess hydro-meteorological impacts in highly dynamic urban agglomerations in Latin America. PhD thesis. Freiburg, Germany: Professur für physische Geographie/Fakultät für Umwelt und natürliche Ressourcen, Albert-Ludwigs-Universität Freiburg.

Hofmann P, Strobl J & Blaschke T (2011a) Quantifying the robustness of fuzzy rule sets in object-based image analysis. *Int J Remote Sens* 32(22): 7359–7381.

Hofmann P, Strobl J & Nazarkulova A (2011b) Mapping green spaces in Bishkek – How reliable can spatial analysis be?. *Remote Sens* 3(6): 1088–1103.

Hooke R & Martín-Duque J (2012) Land transformation by humans: A review. *GSA Today* 22(12): 4–10.

Howard L (1833[2]) *The climate of London deduced from meteorological observations made in the metropolis and at various places around it*. Vol. I–III. London, UK: J. Rickerby.

Hu S & Wang L (2013) Automated urban land-use classification with remote sensing. *Int J Remote Sens* 34(3): 790–803.

Huang B, Zhang H & Yu L (2012) Improving Landsat ETM+ urban area mapping via spatial and angular fusion with MISR multi-angle observations. *IEEE J Sel Top Appl Earth Obs Remote Sens* 5(1): 101–109.

Huang G, Zhou W & Cadenasso M (2011) Is everyone hot in the city? Spatial pattern of land surface temperatures, land cover and neighborhood socioeconomic characteristics in Baltimore, MD. *J Environ Manage* 92(7): 1753–1759.

Huang J, Lu X & Sellers J (2007) A global comparative analysis of urban form: Applying spatial metrics and remote sensing. *Landscape Urban Plan* 82(4): 184–197.

Huete A (1988) A soil-adjusted vegetation index (SAVI). *Remote Sens Environ* 25(3): 295–309.

Huizhi L, Jianguo S, Chan J, Cheng A & Heping L (2002) Influences of structures on urban ventilation: A numerical experiment. *Adv Atmos Sci* 19(6): 1045–1054.

IEA (International Energy Agency) (2008) *World Energy Outlook*. Paris, France: OECD/IEA, 569 pp.

IGN (Instituto Geográfico Nacional) (2015) *Fotogrametría y Teledetección. Plan Nacional de Ortofotografía Aérea (PNOA)*. <http://www.ign.es/ign/layoutIn/actividadesFotoTelePNOA.do> (last accessed on 2015-05-12).

Ivajnšič D, Kaligarič M & Žiberna I (2014) Geographically weighted regression of the urban heat island of a small city. *Appl Geogr* 53: 341–353.

Jakubiec J & Reinhart C (2013) A method for predicting city-wide electricity gains from photovoltaic panels based on LiDAR and GIS data combined with hourly Daysim simulations. *Sol Energy* 93: 127–143.

Jansen L & Di Gregorio A (2003) Land-use data collection using the "land cover classification system": Results from a case study in Kenya. *Land Use Policy* 20(2): 131–148.

Jensen J (2006[2]) *Remote sensing of the environment: An Earth resource perspective*. Upper Saddle River, NJ: Prentice Hall, 608 pp.

Jensen J & Cowen D (1999) Remote sensing of urban/suburban infrastructure and socio-economic attributes. *Photogramm Eng Rem S* 65(5): 611–622.

Jensen R, Gatrell J, Boulton J & Harper B (2004) Using remote sensing and geographic information systems to study urban quality of life and urban forest amenities. *Ecol Soc* 9(5): 1–10.

Jensen R, Gatrell J & McLean D (Eds) (2007[2]) *Geo-spatial technologies in urban environments. Policy, practice, and pixels*. Berlin, Germany: Springer, 240 pp.

Ji W, Ma J, Twibell R & Underhill K (2006) Characterizing urban sprawl using multi-stage remote sensing images and landscape metrics. *Comput Environ Urban* 30(6): 861–879.

Jiménez-Muñoz J & Sobrino J (2003) A generalized single-channel method for retrieving land surface temperature from remote sensing data. *J Geophys Res* 108(D22): 1–9.

Jochem A, Höfle B, Rutzinger M & Pfeifer N (2009) Automatic roof plane detection and analysis in airborne LiDAR point clouds for solar potential assessment. *Sensors* 9(7): 5241–5262.

Johnson B (2013) High-resolution urban land-cover classification using a competitive multi-scale object-based approach. *Remote Sens Lett* 4(2): 131–140.

JPL (Jet Propulsion Laboratory) (2015a) *AVIRIS data – Ordering free AVIRIS standard data products*. <http://aviris.jpl.nasa.gov/data/free_data.html> (last accessed on 2015-05-12).

JPL (Jet Propulsion Laboratory) (2015b) *HyspIRI*. Comprehensive development report. Pasadena, CA: Caltech.

Kawamura M, Jayamana S & Tsujiko Y (1996) Relation between social and environmental conditions in Colombo, Sri Lanka and the urban index estimated by satellite remote sensing data. *Int Arch Photogramm Remote Sens Spatial Inf Sci* XXXI-B7: 321–326.

Keramitsoglou I (2014) Investigations of the diurnal thermal behavior of Athens, Greece, by statistical downscaling of land surface temperature images and pattern analysis. In: Weng Q (Ed) *Global urban monitoring and assessment through Earth observation*. Remote sensing applications. Boca Raton, FL: CRC Press, 249–266.

Kim M, Madden M & Xu B (2010) GEOBIA vegetation mapping in Great Smoky Mountains National Park with spectral and non-spectral ancillary information. *Photogramm Eng Rem S* 76(2): 137–149.

Kim Y & Kim Y (2014) Improved classification accuracy based on the output-level fusion of high-resolution satellite images and airborne LiDAR data in urban area. *IEEE Geosci Remote S* 11(3): 636–640.

Kit O & Lüdeke M (2013) Automated detection of slum area change in Hyderabad, India using multitemporal satellite imagery. *ISPRS J Photogramm* 83: 130–137.

Koch B, Jochum M, Ivitis E & Dees M (2003) Pixelbasierte Klassifizierung im Vergleich und zur Ergänzung zum objektbasierten Verfahren. *Photogramm Fernerkun* 3: 195–204.

Konecny G, Schuhr W & Wu J (1982) Untersuchungen über die Interpretierbarkeit von Bildern unterschiedlicher Sensoren und Plattformen für die kleinmaßstäbige Kartierung. *Bildmessung und Luftbildwesen* 50: 187–200.

Kramer H (2002[4]) *Observation of the Earth and its environment. Survey of missions and sensors*. Berlin, Germany: Springer, 1509 pp.

Krehl A, Siedentop S, Taubenböck H & Wurm M (2016) A comprehensive view on urban spatial structure: Urban density patterns of German city regions. *ISPRS Int J Geo-Inf* 5(76): 1–21.

Kriegler F, Malila W, Nalepka R & Richardson W (1969) Preprocessing transformations and their effects on multispectral recognition. *Proceedings of the 6th International Symposium on Remote Sensing of Environment*, October 13–16, Ann Arbor, MI, 97–131.

Krüger E, Minella F & Rasia F (2011) Impact of urban geometry on outdoor thermal comfort and air quality from field measurements in Curitiba, Brazil. *Build Environ* 46(3): 621–634.

Kuenzer C & Dech S (Eds) (2013) *Thermal infrared remote sensing: Sensors, methods, applications*. Remote sensing and digital image processing 17. Dordrecht, The Netherlands: Springer, 537 pp.

Kuenzer C, Guo H, Ottinger M, Zhang J & Dech S (2013) Spaceborne thermal infrared observation – An overview of most frequently used sensors for applied research. In: Kuenzer C & Dech S (Eds) *Thermal infrared remote sensing: Sensors, methods, applications*. Dordrecht, The Netherlands: Springer, 131–148.

Kuttler W (2004) Stadtklima, Teil 1: Grundzüge und Ursachen. *UWSF* 16(3): 187–199.

Kuttler W (2008) The urban climate – Basic and applied aspects. In: Marzluff J, Shulenberger E, Endlicher W, Alberti M, Bradley G, Ryan C, ZumBrunnen C & Simon U (Eds) *Urban ecology. An international perspective on the interaction between humans and nature*. New York, NY: Springer, 233–248.

La Rosa D & Wiesmann D (2013) Land cover and impervious surface extraction using parametric and non-parametric algorithms from the open-source software R: An application to sustainable urban planning in Sicily. *GISci Remote Sens* 50(2): 231–250.

Lackner M & Conway T (2008) Determining land-use information from land cover through an object-oriented classification of Ikonos imagery. *Can J Remote Sens* 34(1–2): 77–92.

Lakes T & Kim H (2012) The urban environmental indicator "Biotope Area Ratio" – An enhanced approach to assess and manage the urban ecosystem services using high resolution remote-sensing. *Ecol Ind* 13(1): 93–103.

Landsberg H (1981) *The urban climate*. International geophysics series 28. New York, NY: Academic Press, 275 pp.

Lang S, Schöpfer E, Hölbling D, Blaschke T, Moeller M, Jekel T & Kloyber E (2008) Quantifying and qualifying urban green by integrating remote sensing, GIS, and social science methods. In: Petrosillo I,

Müller F, Jones K, Zurlini G, Krauze K, Victorov S, Li B & Kepner W (Eds) *Use of landscape sciences for the assessment of environmental security*. NATO science for peace and security series C: Environmental security. Dordrecht, The Netherlands: Springer, 93–105.

Lazzarini M, Marpu P & Ghedira H (2013) Temperature-land cover interactions: The inversion of urban heat island phenomenon in desert city areas. *Remote Sens Environ* 130: 136–152.

Leinenkugel P, Esch T & Kuenzer C (2011) Settlement detection and impervious surface estimation in the Mekong Delta using optical and SAR remote sensing data. *Remote Sens Environ* 115(12): 3007–3019.

Li G & Weng Q (2005) Using Landsat ETM+ imagery to measure population density in Indianapolis, Indiana, USA. *Photogramm Eng Rem S* 71(8): 947–958.

Li J, Song C, Cao L, Zhu F, Meng X & Wu J (2011) Impacts of landscape structure on surface urban heat islands: A case study of Shanghai, China. *Remote Sens Environ* 115(12): 3249–3263.

Li J, Taylor G, Kidner D & Ware M (2008) Prediction and visualization of GPS multipath signals in urban areas using LiDAR digital surface models and building footprints. *Int J Geogr Inf Sci* 22(11–12): 1197–1218.

Li X, Li W, Middel A, Harlan S, Brazel A & Turner II B (2016) Remote sensing of the surface urban heat island and land architecture in Phoenix, Arizona: Combined effects of land composition and configuration and cadastral–demographic–economic factors. *Remote Sens Environ* 174: 233–243.

Li X, Myint S, Zhang Y, Galletti C, Zhang X & Turner II B (2014) Object-based land-cover classification for metropolitan Phoenix, Arizona, using aerial photography. *Int J Appl Earth Obs* 33: 321–330.

Li X & Shao G (2014) Object-based land-cover mapping with high resolution aerial photography at a county scale in Midwestern USA. *Remote Sens* 6(11): 11372–11390.

Li Z, Tang B, Wu H, Ren H, Yan G, Wan Z, Trigo I & Sobrino J (2013) Satellite-derived land surface temperature: Current status and perspectives. *Remote Sens Environ* 131: 14–37.

Liao W, Pižurica A, Bellens R, Gautama S & Philips W (2015) Generalized graph-based fusion of hyperspectral and LiDAR data using morphological features. *IEEE Geosci Remote S* 12(3): 552–556.

Lidar Online (2014) *Lidar Online – Worldwide LiDAR data and geoservices*. <https://www.lidar-online.com/> (last accessed on 2014-05-12).

Lillesand T, Kiefer R & Chipman J (2008[6]) *Remote sensing and image interpretation*. Hoboken, NJ: John Wiley & Sons, 756 pp.

Linde L & Kirstein W (2004) Vergleich unterschiedlicher Klassifikationsansätze am Beispiel von hochauflösenden Satellitenbilddaten im Raum Leipzig. *Photogramm Fernerkun* 6: 519–526.

Lindner M, Hese S, Berger C & Schmullius C (2011) An object-based multisensoral approach for the derivation of urban land use structures in the City of Rostock, Germany. *Proceedings of SPIE 8181*, September 19–22, Prague, Czech Republic, 1–8.

Ling Y, Ehlers M, Usery E & Madden M (2008) Effects of spatial resolution ratio in image fusion. *Int J Remote Sens* 29(7): 2157–2167.

Liu H & Weng Q (2008) Seasonal variations in the relationship between landscape pattern and land surface temperature in Indianapolis, USA. *Environ Monit Assess* 144(1–3): 199–219.

Liu H & Weng Q (2009) An examination of the effect of landscape pattern, land surface temperature, and socioeconomic conditions on WNV dissemination in Chicago. *Environ Monit Assess* 159(1–4): 143–161.

Liu K, Su H, Li X, Wang W, Yang L & Liang H (2016) Quantifying spatial-temporal pattern of urban heat island in Beijing: An improved assessment using land surface temperature (LST) time series observations from Landsat, MODIS, and Chinese new satellite GaoFen-1. *IEEE J Sel Top Appl Earth Obs Remote Sens* 9(5): 2028–2042.

Liu L & Zhang Y (2011) Urban heat island analysis using the Landsat TM data and ASTER data: A case study in Hong Kong. *Remote Sens* 3(7): 1535–1552.

Liu X, Clarke K & Herold M (2006) Population density and image texture. A comparison study. *Photogramm Eng Rem S* 72(2): 187–196.

Liu Y, Meng Q, Zhang J, Zhang L, Jancso T & Vatseva R (2015) An effective Building Neighborhood Green Index model for measuring urban green space. *Int J Dig Earth* 9(4): 387–409.

Lo C (1995) Automated population and dwelling unit estimation from high-resolution satellite images: A GIS approach. *Int J Remote Sens* 16(1): 17–34.

Lo C (1997) Application of Landsat TM data for quality of life assessment in an urban environment. *Comput Environ Urban* 21(3–4): 259–276.

Locke D, Grove M, Lu J, Troy A, O'Neil-Dunne J & Beck B (2010) Prioritizing preferable locations for increasing urban tree canopy in New York City. *Cities Environ* 3(1): 1–18.

Lohani B & Kumar R (2008) A model for predicting GPS-GDOP and its probability using LiDAR data and ultra rapid product. *J Appl Geod* 2(4): 213–222.

Longley P (2002) Geographical information systems: Will developments in urban remote sensing and GIS lead to 'better' urban geography?. *Prog Hum Geog* 26(2): 231–239.

Longley P, Barnsley M & Donnay J (2001) Remote sensing and urban analysis: A research agenda. In: Donnay J, Barnsley M & Longley P (Eds) *Remote sensing and urban analysis*. GISDATA 9. Boca Raton, FL: CRC Press, 249–262.

Loveland T (2012) History of land-cover mapping. In: Weng Q (Ed) *Remote sensing of land use and land cover*. Remote sensing applications. Boca Raton, FL: CRC Press, 13–22.

Lowry W (1998) Urban effects on precipitation amount. *Prog Phys Geog* 22(4): 477–520.

Lu D, Hetrick S & Moran E (2010) Land cover classification in a complex urban-rural landscape with QuickBird imagery. *Photogramm Eng Rem S* 76(10): 1159–1168.

Luo B & Zhang L (2014) Robust autodual morphological profiles for the classification of high-resolution satellite images. *IEEE T Geosci Remote* 52(2): 1451–1462.

Lwin K & Murayama Y (2009) A GIS approach to estimation of building population for micro-spatial analysis. *T GIS* 13(4): 401–414.

MacFaden S, O'Neil-Dunne J, Royar A, Lu J & Rundle A (2012) High-resolution tree canopy mapping for New York City using LiDAR and object-based image analysis. *J Appl Remote Sens* 6(1): 1–23.

Maimaitiyiming M, Ghulam A, Tiyip T, Pla F, Latorre-Carmona P, Halik Ü, Sawut M & Caetano M (2014) Effects of green space spatial pattern on land surface temperature: Implications for sustainable urban planning and climate change adaptation. *ISPRS J Photogramm* 89: 59–66.

Mallet C & Bretar F (2009) Full-waveform topographic lidar: State-of-the-art. *ISPRS J Photogramm* 64(1): 1–16.

Mallick J, Rahman A & Singh C (2013) Modeling urban heat islands in heterogeneous land surface and its correlation with impervious surface area by using night-time ASTER satellite data in highly urbanizing city, Delhi-India. *Adv Space Res* 52(4): 639–655.

Mandal M (2006) Physiological changes in certain test plants under automobile exhaust pollution. *J Environ Biol* 27(1): 43–47.

Maune D (Ed) (2007[2]) *Digital elevation model technologies and applications: The DEM users manual*. Bethesda, MD: ASPRS, 655 pp.

McGarigal K (2014) *FRAGSTATS Help. Version 4*. <http://www.umass.edu/landeco/research/fragstats/documents/fragstats.help.4.2.pdf> (last accessed on 2015-05-12).

McKinney M (2008) Effects of urbanization on species richness: A review of plants and animals. *Urban Ecosyst* 11(2): 161–176.

Meinel G & Heber B (1998) *Strukturtypenkarte Dresden (1997)*. Unpublished report. Dresden, Germany: IÖR.

Meinel G, Hecht R, Herold H, Schiller G, Spangenberg M, Burgdorf M, Kawka R, Müller H, Schmitt G & Selle K (2008) *Automatische Ableitung von stadtstrukturellen Grundlagendaten und Integration in einem Geographischen Informationssystem*. In: Bundesministeriums für Verkehr, Bau und Stadtwicklung & Bundesamt für Bauwesen und Raumordnung (Eds) Forschungen 134. Bonn, Germany: Bundesamt für Bauwesen und Raumordnung, 98 pp.

Meinel G, Herold H & Hecht R (2007) Gebäudebasierte, vollautomatische Erhebung und Analyse der Siedlungsstruktur – Grundlage für Monitoring und Bewertung der Siedlungsentwicklung. *Proceedings of REAL CORP 007*, May 20–23, Vienna, Austria, 815–824.

Meinel G, Neubert M & Reder J (2001) Pixelorientierte versus segmentorientierte Klassifikation von Ikonos-Satellitenbilddaten – Ein Methodenvergleich. *Photogramm Fernerkun* 3: 157–170.

Meric S, Fayard F & Pottier E (2009) Radargrammetric SAR image processing. In: Ho P (Ed) *Geoscience and remote sensing*. Rijeka, Croatia: InTech, 421–454.

Mesev V (1997) Remote sensing of urban systems: Hierarchical integration with GIS. *Comput Environ Urban* 21(3–4): 175–187.

Mesev V (1998) The use of census data in urban image classification. *Photogramm Eng Rem S* 64(5): 431–438.

Mesev V (2007) Fusion of point-based postal data with IKONOS imagery. *Inform Fusion* 8(2): 157–167.

Mesev V (2010) Classification of urban areas: Inferring land use from the interpretation of land cover. In: Rashed T & Jürgens C (Eds) *Remote sensing of urban and suburban areas*. Remote sensing and digital image processing 10. Dordrecht, The Netherlands: Springer, 141–164.

Miller R & Small C (2003) Cities from space: Potential applications of remote sensing in urban environmental research and policy. *Environ Sci Policy* 6(2): 129–137.

Moeller M & Blaschke T (2006) GIS-gestützte Bildanalyse der städtischen Vegetation als Indikator urbaner Lebensqualität. *Photogramm Fernerkun* 1: 19–30.

Myint S, Wentz E, Brazel A & Quattrochi D (2013) The impact of distinct anthropogenic and vegetation features on urban warming. *Landscape Ecol* 28(5): 959–978.

Nassar A, Blackburn G & Whyatt J (2016) Dynamics and controls of urban heat sink and island phenomena in a desert city: Development of a local climate zone scheme using remotely-sensed inputs. *Int J Appl Earth Obs* 51: 76–90.

Neil K & Wu J (2006) Effects of urbanization on plant flowering phenology: A review. *Urban Ecosyst* 9(3): 243–257.

Ngie A, Abutaleb K, Ahmed F, Darwish A & Ahmed M (2014) Assessment of urban heat island using satellite remotely sensed imagery: A review. *S Afr Geogr J* 96: 1–17.

Nichol J (1994) A GIS-based approach to microclimate monitoring in Singapore's high-rise housing estates. *Photogramm Eng Rem S* 60(10): 1225–1232.

Nichol J, King B, Quattrochi D, Dowman I, Ehlers M & Ding X (2007) Earth observation for urban planning and management. State of the art and recommendations for application of Earth observation in urban planning. *Photogramm Eng Rem S* 73(9): 973–979.

Niemczynowicz J (1999) Urban hydrology and water management – Present and future challenges. *Urban Water* 1(1): 1–14.

Niemeyer J, Rottensteiner F & Soergel U (2014) Contextual classification of LiDAR data and building object detection in urban areas. *ISPRS J Photogramm* 87: 152–165.

NLS (National Land Survey of Finland) (2015) *File service of open data (avoimien aineistojen tiedostopalvelu)*. <https://tiedostopalvelu.maanmittauslaitos.fi/tp/kartta?lang=en> (last accessed on 2015-05-12).

NOAA (National Oceanic and Atmospheric Administration) (2012) *Lidar 101: An introduction to Lidar technology, data, and applications*. Technical report. Charleston, SC: Coastal Services Center.

NOAA (National Oceanic and Atmospheric Administration) Office for Coastal Management (2015) *Digital coast data access viewer*. <http://coast.noaa.gov/dataviewer/#> (last accessed on 2015-05-12).

Norman J & Becker F (1995) Terminology in thermal infrared remote sensing of natural surfaces. *Remote Sens Rev* 12(3–4): 159–173.

Novack T, Esch T, Kux H & Stilla U (2011) Machine learning comparison between WorldView-2 and QuickBird-2-simulated imagery regarding object-based urban land cover classification. *Remote Sens* 3(10): 2263–2282.

Nunez M & Oke T (1977) The energy balance of an urban canyon. *J Appl Meteorol* 16(1): 11–19.

Ogashawara I & da Silva Brum Bastos V (2012) A quantitative approach for analyzing the relationship between urban heat islands and land cover. *Remote Sens* 4(11): 3596–3618.

Oke T (1973) City size and the urban heat island. *Atmos Environ* 7(8): 769–779.

Oke T (1976) The distinction between canopy and boundary layer urban heat islands. *Atmosphere* 14(4): 268–277.

Oke T (1981) Canyon geometry and the nocturnal urban heat island: Comparison of scale model and field observations. *J Climatol* 1(3): 237–254.

Oke T (1982) The energetic basis of the urban heat island. *Q J Roy Meteor Soc* 108(455): 1–24.

Oke T (1987[2]) *Boundary layer climates*. London, UK: Routledge, 435 pp.

Oke T (1997) Urban climates and global environmental change. In: Thompson R & Perry A (Eds) *Applied climatology: Principles & practices*. London, UK: Routledge, 273–287.

Oke T & East C (1971) The urban boundary layer in Montreal. *Bound-Lay Meteorol* 1(4): 411–437.

Okujeni A, van der Linden S, Jakimow B, Rabe A, Verrelst J & Hostert P (2014) A comparison of advanced regression algorithms for quantifying urban land cover. *Remote Sens* 6(7): 6324–6346.

O'Neil-Dunne J, MacFaden S & Royar A (2014) A versatile, production-oriented approach to high-resolution tree canopy mapping in urban and suburban landscapes using GEOBIA and data fusion. *Remote Sens* 6(12): 12837–12865.

O'Neil-Dunne J, MacFaden S, Royar A & Pelletier K (2013) An object-based system for LiDAR data fusion and feature extraction. *Geocarto Int* 28(3): 227–242.

Ong B (2003) Green plot ratio: An ecological measure for architecture and urban planning. *Landscape Urban Plan* 63(4): 197–211.

OpenTopography (2014) *OpenTopography – A portal to high-resolution topography data and tools*. <http://www.opentopography.org/> (last accessed on 2014-05-12).

Ouma Y, Ngigi T & Tateishi R (2006) On the optimization and selection of wavelet texture for feature extraction from high-resolution satellite imagery with application towards urban-tree delineation. *Int J Remote Sens* 27(1): 73–104.

Pacifici F, Del Frate F, Emery W, Gamba P & Chanussot J (2008) Urban mapping using coarse SAR and optical data: Outcome of the 2007 GRSS Data Fusion Contest. *IEEE Geosci Remote S* 5(3): 331–335.

Pahlavani P, Amirkolaee H & Nahr S (2015) A new feature selection from LiDAR data and digital aerial images acquired for an urban/c environment using an ANFIS-based classification and a fuzzy rough set method. *Int J Remote Sens* 36(14): 3587–3615.

Pan X, Zhao Q, Chen J, Liang Y & Sun B (2008) Analyzing the variation of building density using high spatial resolution satellite images: The example of Shanghai city. *Sensors* 8(4): 2541–2550.

Paola J & Schowengerdt R (1995) A detailed comparison of backpropagation neural network and maximum-likelihood classifiers for urban land use classification. *IEEE T Geosci Remote* 33(4): 981–996.

Parrish C & Nowak R (2009) Improved approach to LIDAR airport obstruction surveying using full-waveform data. *J Surv Eng* 135(2): 72–82.

Patino J & Duque J (2013) A review of regional science applications of satellite remote sensing in urban settings. *Comput Environ Urban* 37: 1–17.

Pauleit S (2011) *Stadtstrukturtypen. Personal communication (2011-02-20)*.

Pauleit S & Breuste J (2011) Land-use and surface-cover as urban ecological indicators. In: Niemelä J, Breuste J, Elmqvist T, Guntenspergen G, James P & McIntyre N (Eds) *Urban ecology: Patterns, processes, and applications*. Oxford, UK: Oxford University Press, 19–30.

Pauleit S & Duhme F (2000) Assessing the environmental performance of land cover types for urban planning. *Landscape Urban Plan* 52(1): 1–20.

Pauleit S, Ennos R & Golding Y (2005) Modeling the environmental impacts of urban land use and land cover change – A study in Merseyside, UK. *Landscape Urban Plan* 71(2–4): 295–310.

Pesaresi M, Ehrlich D, Caravaggi I, Kauffmann M & Louvrier C (2011a) Toward global automatic built-up area recognition using optical VHR imagery. *IEEE J Sel Top Appl Earth Obs Remote Sens* 4(4): 923–934.

Pesaresi M, Halkia M & Ouzounis G (2011b) Quantitative estimation of settlement density and limits based on textural measurements. *Proceedings of the 2011 Joint Urban Remote Sensing Event*, April 11–13, Munich, Germany, 89–93.

Pickett S, Cadenasso M, Grove J, Boone C, Groffman P, Irwin E, Kaushal S, Marshall V, McGrath B, Nilon C, Pouyat R, Szlavecz K, Troy A & Warren P (2011) Urban ecological systems: Scientific foundations and a decade of progress. *J Environ Manage* 92(3): 331–362.

Platt R & Rapoza L (2008) An evaluation of an object-oriented paradigm for land use/land cover classification. *Prof Geogr* 60(1): 87–100.

Pohl C & Van Genderen J (1998) Multisensor image fusion in remote sensing: Concepts, methods and applications. *Int J Remote Sens* 19(5): 823–854.

Poznanska A, Bayer S & Bucher T (2013) Derivation of urban objects and their attributes for large-scale urban areas based on very high resolution UltraCam true orthophotos and nDSM: A case study Berlin, Germany. *Proceedings of SPIE 8893*, September 23–25, Dresden, Germany, 1–13.

Prashad L (2014) Urban heat island. In: Njoku E (Ed) *Encyclopedia of remote sensing*. Encyclopedia of Earth sciences series. New York City, NY: Springer, 878–881.

Price J (1979) Assessment of the urban heat island effect through the use of satellite data. *Mon Wea Rev* 107(11): 1554–1557.

Priestnall G, Jafaar J & Duncan A (2000) Extracting urban features from LiDAR digital surface models. *Comput Environ Urban* 24(2): 65–78.

Puissant A, Zhang W & Skupinski G (2012) Urban morphology analysis by high and very high resolution remote sensing. *Proceedings of the 2012 GEOBIA*, May 07–09, Rio de Janeiro, Brazil, 524–529.

Qian Y, Zhou W, Yan J, Li W & Han L (2015) Comparing machine learning classifiers for object-based land cover classification using very high resolution imagery. *Remote Sens* 7(1): 153–168.

Qin Z, Karnieli A & Berliner P (2001) A mono-window algorithm for retrieving land surface temperature from Landsat TM data and its application to the Israel–Egypt border region. *Int J Remote Sens* 22(18): 3719–3746.

Qiu F, Sridharan H & Chun Y (2010) Spatial autoregressive model for population estimation at the census block level using LiDAR-derived building volume information. *Cartogr Geogr Inform* 37(3): 239–257.

Quattrochi D & Ridd M (1994) Measurement and analysis of thermal energy responses from discrete urban surfaces using remote sensing data. *Int J Remote Sens* 15(10): 1991–2022.

Raber B & Cannistra J (2005) *LIDAR guidebook: Concepts, project design, and practical applications*. Park Ridge, IL: URISA, 63 pp.

Raciti S, Hutyra L & Newell J (2014) Mapping carbon storage in urban trees with multi-source remote sensing data: Relationships between biomass, land use, and demographics in Boston neighborhoods. *Sci Total Environ* 500–501: 72–83.

Rafiee A, Dias E & Koomen E (2016) Local impact of tree volume on nocturnal urban heat island: A case study in Amsterdam. *Urban For Urban Gree* 16: 50–61.

Raney R (1998[3]) Radar fundamentals: Technical perspective. In: Henderson F & Lewis A (Eds) *Principles & applications of imaging radar. Manual of remote sensing*. Vol. 2. New York City, NY: John Wiley & Sons, 9–130.

Rashed T & Jürgens C (Eds) (2010) *Remote sensing of urban and suburban areas*. Remote sensing and digital image processing 10. Dordrecht, The Netherlands: Springer, 352 pp.

Rashed T, Weeks J, Couclelis H & Herold M (2007) An integrative GIS and remote sensing model for place-based urban vulnerability analysis. In: Mesev V (Ed) *Integration of GIS and remote sensing*. Mastering GIS: Technology, applications and management. Hoboken, NJ: John Wiley & Sons, 199–233.

Reiss-Schmidt S (2010) München: "Wachstum nach Innen" – Nachhaltige Stadtentwicklung zwischen Wandel und Identität. In: Taubenböck H & Dech S (Eds) *Fernerkundung im urbanen Raum. Erdbeobachtung auf dem Weg zur Planungspraxis*. Darmstadt, Germany: Wissenschaftliche Buchgesellschaft, 15–30.

Ren Z, He X, Zheng H, Zhang D, Yu X, Shen G & Guo R (2013) Estimation of the relationship between urban park characteristics and park cool island intensity by remote sensing data and field measurement. *Forests* 4(4): 868–886.

Reuter D, Richardson C, Pellerano F, Irons J, Allen R, Anderson M, Jhabvala M, Lunsford A, Montanaro M, Smith R, Tesfaye Z & Thome K (2015) The Thermal Infrared Sensor (TIRS) on Landsat 8: Design overview and pre-launch characterization. *Remote Sens* 7(1): 1135–1153.

Richards J & Jia X (2008[4]) *Remote sensing digital image analysis*. Berlin, Germany: Springer, 439 pp.

Richter R & Schläpfer D (2014) *Atmospheric/topographic correction for satellite imagery. ATCOR-2/3 user guide, version 8.3.1*. Wessling, Germany: Deutsches Zentrum für Luft- und Raumfahrt (DLR).

Ridd M (1995) Exploring a V-I-S (vegetation-impervious surface-soil) model for urban ecosystem analysis through remote sensing: Comparative anatomy for cities. *Int J Remote Sens* 16(12): 2165–2185.

Rizwan A, Dennis L & Liu C (2008) A review on the generation, determination and mitigation of urban heat island. *J Environ Sci* 20(1): 120–128.

Roetzer T, Wittenzeller M, Haeckel H & Nekovar J (2000) Phenology in central Europe – Differences and trends of spring phenophases in urban and rural areas. *Int J Biometeorol* 44(2): 60–66.

Roth M, Oke T & Emery W (1989) Satellite-derived urban heat island from three coastal cities and the utilization of such data in urban climatology. *Int J Remote Sens* 10(11): 1699–1720.

Rouse J, Haas R, Scheel J & Deering D (1973) Monitoring vegetation systems in the Great Plains with ERTS. *Proceedings of the 3rd Earth Resource Technology Satellite (ERTS) Symposium*, December 10–14, Washington, DC, 48–62.

Salehi B, Zhang Y, Zhong M & Dey V (2012) Object-based classification of urban areas using VHR imagery and height points ancillary data. *Remote Sens* 4(8): 2256–2276.

Salomons E & Berghauser Pont M (2012) Urban traffic noise and the relation to urban density, form, and traffic elasticity. *Landscape Urban Plan* 108(1): 2–16.

Santos T, Rodrigues A & Tenedório J (2012) Characterizing urban volumetry using LiDAR data. *Proceedings of the 29th Urban Data Management Symposium*, 29–31 May, London, UK, 71–75.

Satellite Imaging Corporation (2015a) *GeoEye-2 (WorldView-4) satellite sensor (0.34m)*. <http://www.satimagingcorp.com/satellite-sensors/geoeye-2/> (last accessed on 2015-05-12).

Satellite Imaging Corporation (2015b) *KOMPSAT-3 satellite sensor (0.7m)*. <http://www.satimagingcorp.com/satellite-sensors/kompsat-3/> (last accessed on 2015-05-12).

Sawaya K, Olmanson L, Heinert N, Brezonik P & Bauer M (2003) Extending satellite remote sensing to local scales: Land and water resource monitoring using high-resolution imagery. *Remote Sens Environ* 88(1–2): 144–156.

Scalenghe R & Marsan F (2009) The anthropogenic sealing of soils in urban areas. *Landscape Urban Plan* 90(1): 1–10.

Scarano M & Sobrino J (2015) On the relationship between the sky view factor and the land surface temperature derived by Landsat-8 images in Bari, Italy. *Int J Remote Sens* 36(19–20): 4820–4835.

Schiewe J (2002) Segmentation of high-resolution remotely sensed data – Concepts, applications and problems. *Proceedings of the ISPRS technical commission IV symposium on geospatial theory, processings and applications*, July 9–12, Ottawa, Canada, 1–6.

Schiewe J & Ehlers M (2005) A novel method for generating 3D city models from high resolution and multi-sensor remote sensing data. *Int J Remote Sens* 26(4): 683–698.

Schiewe J, Tufte L & Ehlers M (2001) Potential and problems of multi-scale segmentation methods in remote sensing. *GeoBIT* 6: 34–39.

Schmidt A (2015) Städtische Versiegelung versus Landoberflächentemperatur: Identifizierung maßgeblicher Einflussfaktoren. MSc thesis. Jena, Germany: Lehrstuhl Fernerkundung/Institut für Geographie, Friedrich-Schiller-Universität Jena.

Schneider A, Friedl M & Potere D (2009) A new map of global urban extent from MODIS satellite data. *Environ Res Lett* 4(4): 1–11.

Schöpfer E, Lang S & Blaschke T (2005) A Green Index incorporating remote sensing and citizen's perception of green space. *Proceedings of the 2005 Joint Urban Remote Sensing Event*, 14–16 March, Tempe, AZ, 1–6.

Schöpfer E & Möller M (2006) Comparing metropolitan areas – A transferable object-based image analysis approach. *Photogramm Fernerkun* 10(4): 277–286.

Schowengerdt R (2007[3]) *Remote sensing. Models and methods for image processing*. London, UK: Academic Press, 515 pp.

Schulte W & Sukopp H (2000) Stadt- und Dorfbiotopkartierungen. Erfassung und Analyse ökologischer Grundlagen im besiedelten Bereich der Bundesrepublik Deutschland – ein Überblick. *Naturschutz und Landschaftsplanung* 32(5): 140–147.

Seto K, Fragkias M, Güneralp B & Reilly M (2011) A meta-analysis of global urban expansion. *PLoS ONE* 6(8): 1–9.

Seto K, Güneralp B & Hutyra L (2012) Global forecasts of urban expansion to 2030 and direct impacts on biodiversity and carbon pools. *P Natl Acad Sci USA* 109(40): 16083–16088.

Seto K, Kaufmann R & Woodcock C (2000) Landsat reveals China's farmland reserves, but they're vanishing fast. *Nature* 121: 121.

Shackelford A & Davis C (2003) A hierarchical fuzzy classification approach for high-resolution multispectral data over urban areas. *IEEE T Geosci Remote* 41(9): 1920–1932.

Shahmohamadi P, Che-Ani A, Ramly A, Maulud K & Mohd-Nor M (2010) Reducing urban heat island effects: A systematic review to achieve energy consumption balance. *Int J Phys Sci* 5(6): 626–636.

Shan J & Toth C (Eds) (2009) *Topographic laser ranging and scanning. Principles and processing*. Boca Raton, FL: CRC Press, 616 pp.

Shaver E, Horner R, Skupien J, May C & Ridley G (Eds) (2007[2]) *Fundamentals of urban runoff management: Technical and institutional issues*. Madison, WI: North American Lake Management Society, 327 pp.

Shepherd J, Anderson T, Strother C, Horst A, Bounoua L & Mitra C (2013) *Urban climate archipelagos: A new framework for urban impacts on climate*. <https://earthzine.org/2013/11/29/urban-climate-archipelagos-a-new-framework-for-urban-impacts-on-climate/> (last accessed on 2015-05-12).

Simon D (2007) Cities and global environmental change: Exploring the links. *Geogr J* 173(1): 75–92.

Slonecker E, Jennings D & Garofalo D (2001) Remote sensing of impervious surfaces: A review. *Remote Sens Rev* 20(3): 227–255.

Small C (2006) Comparative analysis of urban reflectance and surface temperature. *Remote Sens Environ* 104(2): 168–189.

Sobrino J, Jiménez-Muñoz J & Paolini L (2004) Land surface temperature retrieval from LANDSAT TM 5. *Remote Sens Environ* 90(4): 434–440.

Soergel U (Ed) (2010) *Radar remote sensing of urban areas*. Remote sensing and digital image processing 15. Berlin, Germany: Springer, 277 pp.

Soille P (2004[2]) *Morphological image analysis*. Berlin, Germany: Springer, 392 pp.

Solecki W, Seto K & Marcotullio P (2013) It's time for an urbanization science. *Environ Sci Policy Sust Dev* 55(1): 12–17.

Srivanit M & Kazunori H (2011) The influence of urban morphology indicators on summer diurnal range of urban climate in Bangkok Metropolitan Area, Thailand. *Int J Civil Environ Eng* 11(5): 34–46.

Stathopoulou M & Cartalis C (2007) Use of satellite remote sensing in support of urban heat island studies. *Adv Build Energy Res* 1(1): 203–212.

Steiniger S, Lange T, Burghardt D & Weibel R (2008) An approach for the classification of urban building structures based on discriminant analysis techniques. *T GIS* 12(1): 31–59.

Steinnocher K, Bauer T, Köstl M & Kressler F (2001) Beobachtung von Stadtentwicklung mit Fernerkundung. Applikationen und Innovationen. *Österreichische Zeitschrift für Vermessung und Geoinformation* 89(3): 145–148.

Stewart I (2010) A systematic review and scientific critique of methodology in modern urban heat island literature. *Int J Climatol* 31(2): 200–217.

Stewart I & Oke T (2012) Local climate zones for urban temperature studies. *Bull Amer Meteor Soc* 93(12): 1879–1900.

Sugarbaker L, Constance E, Heidemann H, Jason A, Lukas V, Saghy D & Stoker J (2014) *The 3D Elevation Program initiative – A call for action*. Circular 1399. Reston, VA: U.S. Geological Survey.

Sukopp H & Weiler S (1988) Biotope mapping and nature conservation strategies in urban areas of the Federal Republic of Germany. *Landscape Urban Plan* 15(1–2): 39–58.

Susaki J, Komiya Y & Takahashi K (2013) Calculation of enclosure index for assessing urban landscapes using digital surface models. *IEEE J Sel Top Appl Earth Obs Remote Sens* 7(10): 4038–4045.

Svensson M (2004) Sky view factor analysis – Implications for urban air temperature differences. *Meteorol Appl* 11(3): 201–211.

Svirejeva-Hopkins A, Schellnhuber H & Pomaz V (2004) Urbanised territories as a specific component of the global carbon cycle. *Ecol Model* 173(2–3): 295–312.

Tang Z, Engel B, Lim K, Pijanowski B & Harbor J (2005) Minimizing the impact of urbanization on long term runoff. *J Am Water Resour As* 41(6): 1347–1359.

Taubenböck H (2011) The global issue of "mega-urbanization": An unsolvable challenge for stakeholders, resresearch and residents?. *Int Arch Photogramm Remote Sens Spatial Inf Sci* XXXVIII-4/C21: 143–148.

Taubenböck H & Dech S (Eds) (2010) *Fernerkundung im urbanen Raum. Erdbeobachtung auf dem Weg in die Praxis*. Darmstadt, Germany: Wissenschaftliche Buchgesellschaft, 45–51 pp.

Taubenböck H, Esch T, Felbier A, Wiesner M, Roth A & Dech S (2012) Monitoring urbanization in mega cities from space. *Remote Sens Environ* 117: 162–176.

Taubenböck H, Esch T, Wurm M, Heldens W & Dech S (2010a) From Earth observation to urban planning in cities. *Proceedings of the PLUREL conference*, October 19–22, Copenhagen, Denmark, 1–6.

Taubenböck H, Esch T, Wurm M, Roth A & Dech S (2010b) Object-based feature extraction using high spatial resolution satellite data of urban areas. *J Spat Sci* 55(1): 117–132.

Taubenböck H, Habermeyer M, Roth A & Dech S (2006) Automated allocation of highly structured urban areas in homogeneous zones from remote sensing data by Savitzky-Golay filtering and curve sketching. *IEEE Geosci Remote S* 3(4): 532–536.

Taubenböck H & Kraff N (2014) The physical face of slums: a structural comparison of slums in Mumbai, India, based on remotely sensed data. *J Hous Built Environ* 29(1): 15–38.

Taubenböck H, Post J, Roth A, Zosseder K, Strunz G & Dech S (2008) A conceptual vulnerability and risk framework as outline to identify capabilities of remote sensing. *Nat Hazards Earth Syst Sci* 8: 409–420.

Taubenböck H, Wegmann M, Roth A, Mehl H & Dech S (2009a) Urbanization in India – Spatiotemporal analysis using remote sensing data. *Comput Environ Urban* 33(3): 179–188.

Taubenböck H, Wegmann M, Roth A, Schmidt M & Dech S (2009b) Urbanization: A global change issue. *Proceedings of the 33rd ISRSE*, May 04–08, Stresa, Italy, 1–4.

Thomas N, Hendrix C & Congalton R (2003) A comparison of urban mapping methods using high-resolution digital imagery. *Photogramm Eng Rem S* 69(9): 963–972.

Thoonen G, Mahmood Z, Peeters S & Scheunders P (2012) Multisource classification of color and hyperspectral images using color attribute profiles and composite decision fusion. *IEEE J Sel Top Appl Earth Obs Remote Sens* 5(2): 510–521.

Tomlinson C, Chapman L, Thornes J & Baker C (2011) Remote sensing land surface temperature for meteorology and climatology: A review. *Meteorol Appl* 18(3): 296–306.

Tompalski P & Wężyk P (2012) LiDAR and VHRS data for assessing living quality in cities – An approach based on 3D indices. *Int Arch Photogramm Remote Sens Spatial Inf Sci* XXXIX-B6: 173–176.

Townshend J, Huang C, Kalluri S, Defries R & Liang S (2000) Beware of per-pixel characterization of land cover. *Int J Remote Sens* 21(4): 839–843.

Townshend J, Justice C, Skole D, Malingreau J, Cihlar J, Teillet P, Sadowski F & Ruttenberg S (1994) The 1 km resolution global data set: Needs of the International Geosphere–Biosphere Programme. *Int J Remote Sens* 15(17): 3417–3441.

Tucker C (1979) Red and photographic infrared linear combinations for monitoring vegetation. *Remote Sens Environ* 8(2): 127–150.

Tuia D & Camps-Valls G (2011) Urban image classification with semisupervised multiscale cluster kernels. *IEEE J Sel Top Appl Earth Obs Remote Sens* 4(1): 65–74.

Tuyahov A, Davies C & Holz R (1973) Detection of urban blight using remote sensing techniques. *Remote Sens Earth Resour* 2: 213–226.

UBA (Umweltbundesamt) (2004) *Flächenverbrauch, ein Umweltproblem mit wirtschaftlichen Folgen*. Hintergrundpapier. Berlin, Germany: UBA.

UN (United Nations) (2014) *World urbanization prospects: The 2014 revision. Highlights*. ST/ESA/SER.A/352. New York, NY: Department of Economic & Social Affairs/Population Division.

Unger J (2004) Intra-urban relationship between surface geometry and urban heat island: Review and new approach. *Clim Res* 27(3): 253–264.

UN-Habitat (United Nations Human Settlements Programme) (2010) *State of the World's Cities 2010/2011. Bridging the urban divide. Overview and key findings*. Technical report. Nairobi, Kenya: UN-Habitat.

Ural S, Hussain E & Shan J (2011) Building population mapping with aerial imagery and GIS data. *Int J Appl Earth Obs* 13(6): 841–852.

USDA (United States Department of Agriculture) Natural Resources and Conservation Service (2015) *Geospatial data gateway*. <https://gdg.sc.egov.usda.gov/GDGOrder.aspx> (last accessed on 2015-05-12).

USGS (United States Geological Survey) (2010) *Landsat update. New thermal band resampling: 30-meter pixels*. <http://landsat.usgs.gov/documents/about_LU_Vol_4_Issue_Special_Edition.pdf> (last accessed on 2015-05-12).

USGS (United States Geological Survey) (2015) *EarthExplorer*. <http://earthexplorer.usgs.gov/> (last accessed on 2015-05-12).

Valor E & Caselles V (1996) Mapping land surface emissivity from NDVI: Application to European, African, and South American areas. *Remote Sens Environ* 57(3): 167–184.

Veldkamp A & Verburg P (2004) Modelling land use change and environmental impact. *J Environ Manage* 72(1–2): 1–3.

Vitousek P, Mooney H, Lubchenco J & Melillo J (1997) Human domination of Earth's ecosystems. *Science* 277(5325): 494–499.

Voegtle T, Steinle E & Tóvári D (2005) Airborne laserscanning data for determination of suitable areas for photovoltaics. *Int Arch Photogramm Remote Sens Spatial Inf Sci* XXXVI-3/W19: 215–220.

Voltersen M (2016) Integrated analysis of urban structure types and land surface temperatures utilizing remote sensing data and methods. PhD thesis. Jena, Germany: Lehrstuhl Fernerkundung/Institut für Geographie, Friedrich-Schiller-Universität Jena.

Voltersen M, Berger C, Hese S & Schmullius C (2014) Object-based land cover mapping and comprehensive feature calculation for an automated derivation of urban structure types at block level. *Remote Sens Environ* 154: 192–201.

Voltersen M, Berger C, Hese S & Schmullius C (2015) Expanding an urban structure type mapping approach from a subarea to the entire city of Berlin. *Proceedings of the 2015 Joint Urban Remote Sensing Event*, March 30–April 01, Lausanne, Switzerland, 1–4.

Voogt J (2002) Urban heat island. In: Munn T & Douglas I (Eds) *Encyclopedia of global environmental change. Causes and consequences of global environmental change*. Vol. 3. Chichester, UK: John Wiley & Sons, 660–666.

Voogt J & Oke T (1997) Complete urban surface temperatures. *J Appl Meteorol* 36(9): 1117–1132.

Voogt J & Oke T (2003) Thermal remote sensing of urban climates. *Remote Sens Environ* 86(3): 370–384.

Wald L (1999) Some terms of reference in data fusion. *IEEE T Geosci Remote* 37(3): 1190–1193.

Walde I, Hese S, Berger C & Schmullius C (2014) From land cover-graphs to urban structure types. *Int J Geogr Inf Sci* 28(3): 584–609.

Walker J & Blaschke T (2008) Object-based land-cover classification for the Phoenix metropolitan area: Optimization vs. transportability. *Int J Remote Sens* 29(7): 2021–2040.

Wang H, Lu S, Wu B & Li X (2013) Advances in remote sensing of impervious surfaces extraction and its applications. *Adv Earth Sci* 28(3): 327–336.

Wang R (2013) 3D building modeling using images and LiDAR: A review. *Int J Image Data Fusion* 4(4): 273–292.

Wang Z, Ziou D, Armenakis C, Li D & Li Q (2005) A comparative analysis of image fusion methods. *IEEE T Geosci Remote* 43(3): 1391–1402.

Ward D, Phinn S & Murray A (2000) Monitoring growth in rapidly urbanizing areas using remotely sensed data. *Prof Geogr* 52(3): 371–386.

Weber C & Hirsch J (1992) Some urban measurements from SPOT data: Urban life quality indices. *Int J Remote Sens* 13(17): 3251–3261.

Weber N, Haase D & Franck U (2014a) Assessing modelled outdoor traffic-induced noise and air pollution around urban structures using the concept of landscape metrics. *Landscape Urban Plan* 125: 105–116.

Weber N, Haase D & Franck U (2014b) Zooming into temperature conditions in the city of Leipzig: How do urban built and green structures influence Earth surface temperatures in the city?. *Sci Total Environ* 496: 289–298.

Wehr A & Lohr U (1999) Airborne laser scanning – An introduction and overview. *ISPRS J Photogramm* 54(2–3): 68–82.

Welch R (1982) Spatial resolution requirements for urban studies. *International Journal of Remote Sensing* 3(2): 139–146.

Weng Q (2001) A remote sensing–GIS evaluation of urban expansion and its impact on surface temperature in the Zhujiang Delta, China. *Int J Remote Sens* 22(10): 1999–2014.

Weng Q (Ed) (2008) *Remote sensing of impervious surfaces*. Remote sensing applications. Boca Raton, FL: CRC Press, 454 pp.

Weng Q (2009) Thermal infrared remote sensing for urban climate and environmental studies: Methods, applications, and trends. *ISPRS J Photogramm* 64(4): 335–344.

Weng Q (2012) Remote sensing of impervious surfaces in the urban areas: Requirements, methods, and trends. *Remote Sens Environ* 117: 34–49.

Weng Q (Ed) (2014) *Global urban monitoring and assessment through Earth observation*. Remote sensing applications. Boca Raton, FL: CRC Press, 386 pp.

Weng Q & Fu P (2014) Modeling annual parameters of clear-sky land surface temperature variations and evaluating the impact of cloud cover using time series of Landsat TIR data. *Remote Sens Environ* 140: 267–278.

Weng Q, Gamba P, Mountrakis G, Pesaresi M, Lu L, Kemper T, Heinzel J, Xian G, Jin H, Miyazaki H, Xu B, Quresh S, Keramitsoglou I, Ban Y, Esch T, Roth A & Elvidge C (2014) Urban observing sensors. In: Weng Q (Ed) *Global urban monitoring and assessment through Earth observation*. Remote sensing applications. Boca Raton, FL: CRC Press, 49–79.

Weng Q, Liu H, Liang B & Lu D (2008) The spatial variations of urban land surface temperatures: Pertinent factors, zoning effect, and seasonal variability. *IEEE J Sel Top Appl Earth Obs Remote Sens* 1(2): 154–166.

Weng Q & Lu D (2007) Subpixel analysis of urban landscapes. In: Weng Q & Quattrochi D (Eds) *Urban remote sensing*. Boca Raton, FL: CRC Press, 71–90.

Weng Q, Lu D & Schubring J (2004) Estimation of land surface temperature–vegetation abundance relationship for urban heat island studies. *Remote Sens Environ* 89(4): 467–483.

Weng Q & Quattrochi D (Eds) (2007) *Urban remote sensing*. Boca Raton, FL: CRC Press, 412 pp.

Wentz E (2012) Synthesizing urban remote sensing through application, scale, data and case studies. *Geocarto Int* 27(5): 425–442.

Wentz E, Anderson S, Fragkias M, Netzband M, Mesev V, Myint S, Quattrochi D, Rahman A & Seto K (2014) Supporting global environmental change research: A review of trends and knowledge gaps in urban remote sensing. *Remote Sens* 6(5): 3879–3905.

Wickop E, Böhm P, Eitner K & Breuste J (1998) *Ein Qualitätszielkonzept für Stadtstrukturtypen am Beispiel der Stadt Leipzig. Entwicklung einer Methodik zur Operationalisierung einer nachhaltigen Stadtentwicklung auf der Ebene von Stadtstrukturen*. Technical report 14. Leipzig, Germany: UFZ.

Wong M & Nichol J (2013) Spatial variability of frontal area index and its relationship with urban heat island intensity. *Int J Remote Sens* 34(3): 885–896.

Woodcock C & Strahler A (1987) The factor of scale in remote sensing. *Remote Sens Environ* 21(3): 311–332.

Woodcock C, Strahler A & Franklin J (1983) Remote sensing for land management and planning. *Environ Manage* 7(3): 223–238.

Wu C & Murray A (2005) A cokriging method for estimating population density in urban areas. *Comput Environ Urban* 29(5): 558–579.

Wu S, Silván-Cárdenas J & Wang L (2007) Per-field urban land use classification based on tax parcel boundaries. *Int J Remote Sens* 28(12): 2777–2801.

Wurm M & Taubenböck H (2010a) Abschätzung der Bevölkerungsverteilung mit Methoden der Fernerkundung. In: Taubenböck H & Dech S (Eds) *Fernerkundung im urbanen Raum. Erdbeobachtung auf dem Weg zur Planungspraxis*. Darmstadt, Germany: Wissenschaftliche Buchgesellschaft, 143–152.

Wurm M & Taubenböck H (2010b) Das 3D-Stadtmodell als planungsrelevante Grundlageninformation. In: Taubenböck H & Dech S (Eds) *Fernerkundung im urbanen Raum. Erdbeobachtung auf dem Weg zur Planungspraxis*. Darmstadt, Germany: Wissenschaftliche Buchgesellschaft, 66–75.

Wurm M & Taubenböck H (2010c) Fernerkundung als Grundlage zur Identifikation von Stadtstrukturtypen. In: Taubenböck H & Dech S (Eds) *Fernerkundung im urbanen Raum. Erdbeobachtung auf dem Weg zur Planungspraxis*. Darmstadt, Germany: Wissenschaftliche Buchgesellschaft, 94–103.

Wurm M, Taubenböck H, Roth A & Dech S (2009) Urban structuring using multisensoral remote sensing data: By the example of the German cities Cologne and Dresden. *Proceedings of the 2009 Joint Urban Remote Sensing Event*, 20–22 May, Shanghai, China, 1–8.

Wurm M, Taubenböck H, Schardt M, Esch T & Dech S (2011) Object-based image information fusion using multisensor Earth observation data over urban areas. *Int J Image Data Fusion* 2(2): 121–147.

Xian G (2008) Satellite remotely-sensed land surface parameters and their climatic effects for three metropolitan regions. *Adv Space Res* 41(11): 1861–1869.

Xian G & Crane M (2006) An analysis of urban thermal characteristics and associated land cover in Tampa Bay and Las Vegas using Landsat satellite data. *Remote Sens Environ* 104(2): 147–156.

Xiao R, Weng Q, Ouyang Z, Li W, Schienke E & Zhang Z (2008) Land surface temperature variation and major factors in Beijing, China. *Photogramm Eng Rem S* 74(4): 451–461.

Xu H (2008) A new index for delineating built-up land features in satellite imagery. *Int J Remote Sens* 29(14): 4269–4276.

Xu H (2010) Analysis of impervious surface and its impact on urban heat environment using the normalized difference impervious surface index (NDISI). *Photogramm Eng Rem S* 76(5): 557–565.

Xu S, Vosselman G & Oude Elberink S (2014) Multiple-entity based classification of airborne laser scanning data in urban areas. *ISPRS J Photogramm* 88: 1–15.

Yan W, Shaker A & El-Ashmawy N (2015) Urban land cover classification using airborne LiDAR data: A review. *Remote Sens Environ* 158: 295–310.

Yang X (Ed) (2011) *Urban remote sensing: Monitoring, synthesis and modeling in the urban environment*. Hoboken, NJ: John Wiley & Sons, 388 pp.

Yokoya N, Nakazawa S, Matsuki T & Iwasaki A (2014) Fusion of hyperspectral and LiDAR data for landscape visual quality assessment. *IEEE J Sel Top Appl Earth Obs Remote Sens* 7(6): 2419–2425.

Yoshida H & Omae M (2005) An approach for analysis of urban morphology: Methods to derive morphological properties of city blocks by using an urban landscape model and their interpretations. *Comput Environ Urban* 29(2): 223–247.

Yu B, Liu H, Wu J, Hu Y & Zhang L (2010) Automated derivation of urban building density information using airborne LiDAR data and object-based method. *Landscape Urban Plan* 98(3–4): 210–219.

Yu Q, Gong P, Clinton N, Biging G, Kelly M & Schirokauer D (2006) Object-based detailed vegetation classification with airborne high spatial resolution remote sensing imagery. *Photogramm Eng Rem S* 72(7): 799–811.

Yuan F & Bauer M (2007) Comparison of impervious surface area and normalized difference vegetation index as indicators of surface urban heat island effects in Landsat imagery. *Remote Sens Environ* 106(3): 375–386.

Yue A, Zhang C, Yang J, Su W, Yun W & Zhu D (2013) Texture extraction for object-oriented classification of high spatial resolution remotely sensed images using a semivariogram. *Int J Remote Sens* 34(11): 3736–3759.

Yue W, Liu Y, Fan P, Ye X & Wu C (2012) Assessing spatial pattern of urban thermal environment in Shanghai, China. *Stoch Env Res Risk A* 26(7): 899–911.

Zanoni V & Goward S (2003) A new direction in Earth observations from space: IKONOS. *Remote Sens Environ* 88(1–2): 1–2.

Zha Y, Gao J & Ni S (2003) Use of normalized difference built-up index in automatically mapping urban areas from TM imagery. *Int J Remote Sens* 24(3): 583–594.

Zhan W, Chen Y, Zhou J, Wang J, Liu W, Voogt J, Zhu X, Quan J & Li J (2013) Disaggregation of remotely sensed land surface temperature: Literature survey, taxonomy, issues, and caveats. *Remote Sens Environ* 131: 119–139.

Zhang H, Lin H, Li Y & Zhang Y (2013) Feature extraction for high-resolution imagery based on human visual perception. *Int J Remote Sens* 34(4): 1146–1163.

Zhang J (2010) Multi-source remote sensing data fusion: Status and trends. *Int J Image Data Fusion* 1(1): 5–24.

Zhang X, Zhong T, Feng X & Wang K (2009a) Estimation of the relationship between vegetation patches and urban land surface temperature with remote sensing. *Int J Remote Sens* 30(8): 2105–2118.

Zhang Y, Odeh I & Han C (2009b) Bi-temporal characterization of land surface temperature in relation to impervious surface area, NDVI and NDBI, using a sub-pixel image analysis. *Int J Appl Earth Obs* 11(4): 256–264.

Zhao H & Chen X (2005) Use of normalized difference bareness index in quickly mapping bare areas from TM/ETM+. *Proceedings of IGARSS*, 25–29 July, Seoul, South Korea, 1666–1668.

Zhong Y, Zhao B & Zhang L (2014a) Multiagent object-based classifier for high spatial resolution imagery. *IEEE T Geosci Remote* 52(2): 841–847.

Zhong Y, Zhao J & Zhang L (2014b) A hybrid object-oriented conditional random field classification framework for high spatial resolution remote sensing imagery. *IEEE T Geosci Remote* 52(11): 7023–7037.

Zhou W, Cadenasso M, Schwarz K & Pickett S (2014) Quantifying spatial heterogeneity in urban landscapes: Integrating visual interpretation and object-based classification. *Remote Sens* 6(4): 3369–3386.

Zhou W, Huang G & Cadenasso M (2011) Does spatial configuration matter? Understanding the effects of land cover pattern on land surface temperature in urban landscapes. *Landscape Urban Plan* 102(1): 54–63.

Zhou W, Huang G, Troy A & Cadenasso M (2009) Object-based land cover classification of shaded areas in high spatial resolution imagery of urban areas: A comparison study. *Remote Sens Environ* 113(8): 1769–1777.

Zhou W & Troy A (2008) An object-oriented approach for analyzing and characterizing urban landscape at the parcel level. *Int J Remote Sens* 29(11): 3119–3135.

Zhou W, Troy A & Grove M (2008) Object-based land cover classification and change analysis in the Baltimore Metropolitan Area using multitemporal high resolution remote sensing data. *Sensors* 8(3): 1613–1636.

Zhou Y, Weng Q, Gurney K, Shuai Y & Hu X (2012) Estimation of the relationship between remotely sensed anthropogenic heat discharge and building energy use. *ISPRS J Photogramm* 67: 65–72.

Zhu X & Toutin T (2013) Land cover classification using airborne LiDAR products in Beauport, Québec, Canada. *Int J Image Data Fusion* 4(3): 252–271.

Zierdt M & Dippmann S (1995) Ökologische Stadtstrukturen und Lufthygiene im Stadtgebiet von Halle. In: Eckart K (Ed) *Ökologische, ökonomische und raumstrukturelle Prozesse in den neuen Bundesländern. Das Beispiel Sachsen-Anhalt*. Schriftenreihe der Gesellschaft für Deutschlandforschung 46. Berlin, Germany: Duncker & Humblot, 143–160.

Manuskripte

Erklärungen

Für alle in dieser kumulativen Dissertation verwendeten Manuskripte liegen die notwendigen Genehmigungen der Verlage für die Zweitpublikation (»reprint permissions«) vor.

Die Koautoren der in dieser kumulativen Dissertation verwendeten Manuskripte sind sowohl über die Nutzung als auch über die unten angegebenen Eigenanteile informiert und stimmen dem zu.

Ich bin mit der Abfassung der Dissertation als publikationsbasiert, d.h. kumulativ, einverstanden und bestätige die vorstehenden Angaben. Eine entsprechend begründete Befürwortung mit Angabe des wissenschaftlichen Anteils des Doktoranden an den verwendeten Publikationen werde ich parallel an den Rat der Chemisch-Geowissenschaftlichen Fakultät richten.

.....	.....	.....
Name Promovend	Ort, Datum	Unterschrift

.....	.....	.....
Name Erstbetreuer	Ort, Datum	Unterschrift

.....	.....	.....
Name Zweitbetreuer	Ort, Datum	Unterschrift

Eigenanteile

Manuskript #1

Berger C, Voltersen M, Hese S, Walde I & Schmullius C (2013c) Robust extraction of urban land cover information from HSR multi-spectral and LiDAR data. *IEEE J Sel Top Appl Earth Obs Remote Sens* 6(5): 2196–2211.

	Berger, C.	Voltersen, M.	Hese, S.	Walde, I.	Schmullius, C.
Forschungskonzeption	☑		☑		☑
Untersuchungsplanung	☑	☑			
Datenerhebung & -verarbeitung	☑	☑		☑	
Datenanalyse & -interpretation	☑	☑			
Schreiben des Manuskripts	☑				
Publikationsäquivalent	1.0	n/s	n/s	n/s	n/s

Manuskript #2

Berger C, Voltersen M, Eckardt R, Eberle J, Heyer T, Salepci N, Hese S, Schmullius C, Tao J, Auer S, Bamler R, Ewald K, Gartley M, Jacobson J, Buswell A, Du Q & Pacifici F (2013b) Multi-modal and multi-temporal data fusion: Outcome of the 2012 GRSS Data Fusion Contest. *IEEE J Sel Top Appl Earth Obs Remote Sens* 6(3): 1324–1340.

	Berger, C.	Voltersen, M.	Eckardt, R.	Eberle, J.	Heyer, T.
Forschungskonzeption	☑				
Untersuchungsplanung	☑				
Datenerhebung & -verarbeitung	☑	☑		☑	☑
Datenanalyse & -interpretation	☑		☑		
Schreiben des Manuskripts	☑				
Publikationsäquivalent	0.5	n/s	n/s	n/s	n/s
	Salepci, N.	Hese, S.	Schmullius, C.	Tao, J.	Auer, S.
Forschungskonzeption		☑	☑	☑	☑
Untersuchungsplanung				☑	☑
Datenerhebung & -verarbeitung	☑			☑	
Datenanalyse & -interpretation				☑	
Schreiben des Manuskripts				☑	☑
Publikationsäquivalent	n/s	n/s	n/s	n/s	n/s
	Bamler, R.	Ewald, K.	Gartley, M.	Jacobson, J.	Buswell, A.
Forschungskonzeption	☑	☑	☑	☑	☑
Untersuchungsplanung	☑	☑			
Datenerhebung & -verarbeitung		☑			
Datenanalyse & -interpretation		☑			
Schreiben des Manuskripts	☑	☑			
Publikationsäquivalent	n/s	n/s	n/s	n/s	n/s
	Du, Q.	Pacifici, F.			
Forschungskonzeption					
Untersuchungsplanung					
Datenerhebung & -verarbeitung		☑			
Datenanalyse & -interpretation					
Schreiben des Manuskripts	☑	☑			
Publikationsäquivalent	n/s	n/s			

Manuskript #3

Voltersen M, Berger C, Hese S & Schmullius C (2014) Object-based land cover mapping and comprehensive feature calculation for an automated derivation of urban structure types at block level. *Remote Sens Environ* 154: 192–201.

	Voltersen, M.	Berger, C.	Hese, S.	Schmullius, C.
Forschungskonzeption	☑	☑	☑	☑
Untersuchungsplanung	☑	☑	☑	
Datenerhebung & -verarbeitung	☑	☑		
Datenanalyse & -interpretation	☑			
Schreiben des Manuskripts	☑			
Publikationsäquivalent	n/s	0.5	n/s	n/s

Manuskript #4

Berger C, Rosentreter J, Voltersen M, Baumgart C, Schmullius C & Hese S (2017) Spatio-temporal analysis of the relationship between 2D/3D urban site characteristics and land surface temperature. *Remote Sens Environ* 193C: 225–243.

	Berger, C.	Rosentreter, J.	Voltersen, M.	Baumgart, C.	Schmullius, C.
Forschungskonzeption	☑				☑
Untersuchungsplanung	☑	☑			
Datenerhebung & -verarbeitung	☑	☑	☑	☑	
Datenanalyse & -interpretation	☑	☑			
Schreiben des Manuskripts	☑				
Publikationsäquivalent	1.0	n/s	n/s	n/s	n/s

	Hese, S.
Forschungskonzeption	☑
Untersuchungsplanung	
Datenerhebung & -verarbeitung	
Datenanalyse & -interpretation	
Schreiben des Manuskripts	
Publikationsäquivalent	n/s

Selbstständigkeitserklärung

Ich erkläre, dass ich die vorliegende Arbeit selbstständig und unter Verwendung der angegebenen Hilfsmittel, persönlichen Mitteilungen und Quellen angefertigt habe.

.....	.....
Ort, Datum	Christian Berger

Curriculum Vitæ

Personal details

Name	Christian Berger
Birthday	May 3, 1985
Birthplace	Pößneck, Thuringia
Citizenship	German

Professional development

since 2009	Research associate at the Department for Earth Observation, Institute of Geography, Friedrich-Schiller-Universität Jena, Germany
	Activities: Synergistic usage of SAR/optical satellite data to estimate forest and savanna ecosystem parameters · Projects: ARS AfricaE & ForestBiomass
	Former activities: Analysis of high spatial resolution optical & SAR data for urban environmental monitoring applications · Project: Enviland-2
2009	Intern at Model–Data Integration Research Group, Max-Planck-Institute for Biogeochemistry (MPI-BGC), Jena, Germany (2 months)
	Activities: Investigating the spatio-temporal relationship between data sets of vegetation productivity and water availability at global scale
2008	Graduate assistant at Department for Earth Observation, Institute of Geography, Friedrich-Schiller-Universität Jena, Germany (10 months)
	Activities: Literature review; Assessment of forest cover change; Preparation of a field trip to Vanuatu · Project: Vanuatu Carbon Credits Project
2007	Intern at German Remote Sensing Data Center (DFD), German Aerospace Center (DLR), Oberpfaffenhofen, Germany (2 months)
	Activities: Atmospheric/topographic correction and object-based urban land cover classifcation of Landsat time series · Project: SHAKTI
2006	Student assistant at Department of Geoinformatics, Hydrology and Modeling, Friedrich-Schiller-Universität Jena, Germany (9 months)
	Activity: Literature review on dryland salinity · Project: DrySal

Schooling and university education

since 2011	PhD candidate at the Department for Earth Observation, Institute of Geography, Friedrich-Schiller-Universität Jena, Germany
	Research subject: Fusion of high spatial resolution multispectral and object height data for urban environmental mapping and monitoring

2010	Master thesis (⊘ 1.1) at the Department for Earth Observation, Institute of Geography, Friedrich-Schiller-Universität Jena, Germany Title: "Fusion of high resolution SAR data and multispectral imagery at pixel level – A comprehensive evaluation" · Project: Enviland-2
2007—2010	Study of Geoinformatics (M. Sc.) at Friedrich-Schiller-Universität Jena Master of Science in June 2010 (⊘ 1.1 · ECTS grade A) Advanced courses: Geographic object-based image analysis (GEOBIA) · Derivation of land surface parameters · Integrated landscape analysis
2007	Bachelor thesis (⊘ 1.0) at German Remote Sensing Data Center (DFD), German Aerospace Center (DLR), Oberpfaffenhofen, Germany Title: "Spatio-temporal analysis of Indian megacities using Landsat satellite time series" (in German) · Project: SHAKTI
2004—2007	Study of Geography (BSc) at Friedrich-Schiller-Universität Jena Bachelor of Science in September 2007 (⊘ 1.3 · ECTS grade A) Major subjects: Remote Sensing · Geoinformatics · Soil Science Minor subjects: Ecology · Cartography · Statistics · Hydrology
2003—2004	Alternative civilian service (Zivildienst)
2003	A level (Abitur) in June 2003 Advanced courses: Mathematics · English
1991—2003	Primary and grammar school in Neustadt an der Orla, Thuringia

Other qualifications

Awards	2012 IEEE GRSS Data Fusion Contest (1st place)
Field experience	Design and implementation of a forest inventory protocol for measuring diameter at breast height (DBH), tree height, and tree species on a 4900 ha test site in the Thuringian Forest, Germany · Project: ForestBiomass Design and implementation of a protocol to derive ASD field spectral measurements in the City of Rostock, Germany · Project: Enviland-2 Design and implementation of a protocol for validating a LC map used to support hydrological modeling in the Gera river basin, Thuringia
Advanced training	Workshop on interactive data language (IDL) programming, Jena, 2011 · Held by Dipl.-Inf. Martin Habermeyer, DLR Workshop on remote sensing and biogeochemical modeling, Jena, 2009 · Held by Dr. Markus Reichstein, MPI-BGC Workshop on theory and applications of imaging spectroscopy, Jena, 2008 · Held by Dipl.-Geol. Andreas Müller, DLR Workshop on interferometric data processing using Gamma, Jena, 2008 · Held by Dr. Maurizio Santoro, Gamma RS Workshop on polarimetric SAR interferometry (PolInSAR), Jena, 2007 · Held by Prof. Dr. Irena Hajnsek, ETH Zurich

Computer literacy	Digital image processing eCognition · Envi · Erdas Imagine · Geomatica SAR & LiDAR software Gamma · Nest · PolSARpro · TreesVis · LAStools · Surfer GIS & landscape analysis ArcGIS · ArcView · ArcInfo · Quantum GIS · Fragstats Scripting & typesetting IDL · Matlab · Gamma · R · Python · LaTeX
Fund raising	Enviland-2 add-on (DLR/BMWi, 6 months, ~25k €) · AutoStructure (GA–LGS, 3 years, ~75k €) · ForestBiomass (DLR/BMWi, 2.5 years, ~125k €)
Reviewer activities	IEEE Journal of Seleted Topics in Earth Observations and Remote Sensing · Information Fusion · International Journal of Digital Earth · International Journal of Remote Sensing
Linguistic proficiency	German: Native language English: Cambridge Certificate in Advanced English (C1) Russian: Basic knowledge
Driving license	Categories B · ML

Publications

Refereed articles

Berger C, Rosentreter J, Voltersen M, Baumgart C, Schmullius C & Hese S (2017) Spatio-temporal analysis of the relationship between 2D/3D urban site characteristics and land surface temperature. *Remote Sens Environ* 193C: 225–243.

Berger C, Voltersen M, Eckardt R, Eberle J, Heyer T, Salepci N, Hese S, Schmullius C, Tao J, Auer S, Bamler R, Ewald K, Gartley M, Jacobson J, Buswell A, Du Q & Pacifici F (2013b) Multi-modal and multi-temporal data fusion: Outcome of the 2012 GRSS Data Fusion Contest. *IEEE J Sel Top Appl Earth Obs Remote Sens* 6(3): 1324–1340.

Berger C, Voltersen M, Hese S, Walde I & Schmullius C (2013c) Robust extraction of urban land cover information from HSR multi-spectral and LiDAR data. *IEEE J Sel Top Appl Earth Obs Remote Sens* 6(5): 2196–2211.

Eckardt R, Berger C, Thiel C & Schmullius C (2013) Removal of optically thick clouds from multi-spectral satellite images using multi-frequency SAR data. *Remote Sens* 5(6): 2973–3006.

Fassnacht F, Hartig F, Latifi H, Berger C, Hernández J, Corvalán P & Koch B (2014) Importance of sample size, data type and prediction method for remote sensing-based estimations of aboveground forest biomass. *Remote Sens Environ* 154: 102–114.

Latifi H, Fassnacht F, Hartig F, Berger C, Hernández J, Corvalán P & Koch B (2015) Stratified aboveground forest biomass estimation by remote sensing data. *Int J Appl Earth Obs* 38: 229–241.

Odipo V, Nickless A, Berger C, Baade J, Urbazaev M, Walther C & Schmullius C (2016) Assessment of aboveground woody biomass dynamics using terrestrial laser scanner and L-band ALOS PALSAR data in South African savanna. *Remote Sens* 7(12): 294.

Voltersen M, Berger C, Hese S & Schmullius C (2014) Object-based land cover mapping and comprehensive feature calculation for an automated derivation of urban structure types at block level. *Remote Sens Environ* 154: 192–201.

Walde I, Hese S, Berger C & Schmullius C (2012) Graph-based urban land use mapping from high resolution satellite images. *ISPRS Ann* I-4: 119–124.

Walde I, Hese S, Berger C & Schmullius C (2013a) Graph based mapping of urban structure types from high resolution satellite image objects – A case study of the German cities of Rostock and Erfurt. *IEEE Geosci Remote S* 10(4): 932–936.

Walde I, Hese S, Berger C & Schmullius C (2014) From land cover-graphs to urban structure types. *Int J Geogr Inf Sci* 28(3): 584–609.

Book chapters

Ackermann N, Becker F, Berger C, Bindel M, Eberle J, Elbertzhagen I, Franke K.-H, Hecheltjen A, Koch T, Kubertschak T, Menz G, Riedel T, Schmullius C, Schwarz M, Thonfeld F, Weise K & Wolf B (2012) ENVILAND 2 – Von multisensoralen Satellitenbildern zu operationellen Produkten. In: Borg E, Daedelow H & Johnson, R. (Eds) *RapidEye Science Archive (RESA). Vom Algorithmus zum Produkt*. Berlin, Germany: GITO, 123–149.

Berger C, Riedel F, Rosentreter J, Stein E, Hese S & Schmullius C (2015a) Fusion of airborne hyperspectral and LiDAR remote sensing data to study the thermal characteristics of urban environments. In: Helbich M, Arsanjani J & Leitner M (Eds) *Computational approaches for urban environments*. Geotechnologies and the environment 13. Heidelberg, Germany: Springer, 273–292.

Walde I, Hese S, Berger C & Schmullius C (2013b) Vom Satellitenbild zu Stadtstrukturtypen: Wie Graphen die Flächennutzung charakterisieren. In: Meinel G, Schumacher U & Behnisch M (Eds) *Flächennutzungsmonitoring V: Methodik, Analyseergebnisse, Flächenmanagement*. IÖR-Schriften 61. Berlin, Germany: Rhombos, 179–187.

Conference papers

Berger C, Hese S & Schmullius C (2010) Fusion of high resolution SAR data and multispectral imagery at pixel level – A statistical comparison. *Proceedings of the 2nd Joint EARSeL SIG workshop*, September 22–24, Ghent, Belgium, 245–268.

Berger C, Urban M, Herold M & Sambale J (2009b) Accuracy assessment for estimating historical forest area changes – A REDD case study for the pacifc island state of Vanuatu. *Proceedings of the 33rd ISRSE*, May 04–08, Stresa, Italy, 1–6.

Berger C, Voltersen M, Hese S, Walde I & Schmullius C (2012) Using geographic object-based image analysis (GEOBIA) for land cover mapping and settlement density assessment. *Proceedings of the 2012 GEOBIA*, May 07–09, Rio de Janeiro, Brazil, 503–508.

Bindel M, Hese S, Berger C & Schmullius C (2011a) Evaluation of rededge spectral information for biotope mapping using RapidEye. *Proceedings of SPIE 8174*, September 19–22, Prague, Czech Republic, 1–9.

Bindel M, Hese S, Berger C & Schmullius C (2011b) Feature selection from high resolution remote sensing data for biotope mapping. *Proceedings of the 2011 ISPRS workshop on high-resolution Earth imaging for geospatial information*, June 14–17, Hannover, Germany, 39–44.

Fassnacht F, Hartig F, Latifi H, Berger C, Hernández J, Corvalán P & Koch B (2013) Combination of EO1-Hyperion and LiDAR data to estimate biomass in a highly complex second growth native forest in central Chile. *Proceedings of the 2013 LARS*, October 23–25, Santiago de Chile, Chile, 1–6.

Hese S, Lindner M, Voltersen M & Berger C (2011) TerraSAR-X and RapidEye data for the parameterisation of relational characteristics of urban ATKIS DLM objects. *Proceedings of the 2011 ISPRS workshop on high-resolution Earth imaging for geospatial information*, June 14–17, Hannover, Germany, 111–114.

Lindner M, Hese S, Berger C & Schmullius C (2011) An object-based multisensoral approach for the derivation of urban land use structures in the City of Rostock, Germany. *Proceedings of SPIE 8181*, September 19–22, Prague, Czech Republic, 1–8.

Taubenböck H, Wegmann M, Berger C, Breunig M, Roth A & Mehl H (2008) Spatio-temporal analysis of Indian megacities. *Proceedings of the XXIth ISPRS congress*, July 03–11, Beijing, China, 75–82.

Voltersen M, Berger C, Hese S & Schmullius C (2015) Expanding an urban structure type mapping approach from a subarea to the entire city of Berlin. *Proceedings of the 2015 Joint Urban Remote Sensing Event*, March 30–April 01, Lausanne, Switzerland, 1–4.

Selected presentations

Berger C, Baumgart C, Voltersen M, Walde I, Hese S & Schmullius C (2013a) Analysis of the relationship between settlement density & land surface temperature using multi-sensor RS data. *Poster presentation at the 2013 ESA Living Planet Symposium*, September 09–13, Edinburgh, UK.

Berger C, Engelhardt S, Truckenbrodt J, Thiel C, Enssle F, Fassnacht F, Schmullius C & Koch B (2014a) On the potential of multi-temporal TanDEM-X data to assess the aboveground biomass (AGB) of two temperate forests in Germany. *Oral presentation at the 2014 ForestSAT*, November 04–07, Riva del Garda (TN), Italy.

Berger C, Hese S & Schmullius C (2009a) Fusion of high resolution SAR data and multispectral imagery for improved urban land cover characterization. *Poster presentation at the 3rd EARSeL SIG workshop on LULC*, November 25–27, Bonn, Germany.

Berger C, Hese S & Schmullius C (2011a) A proposal for (semi-) automatic mapping of urban structure types (USTs) using remote sensing data and methods. *Oral presentation at the 3rd RSS*, September 7–8, Wageningen, The Netherlands.

Berger C, Hese S & Schmullius C (2011b) Evaluation of image fusion techniques to combine high resolution TerraSAR-X and multispectral RapidEye imagery. *Poster presentation at the 4th EARSeL SIG workshop on LULC*, June 1–3, Prague, Czech Republic.

Berger C, Hese S & Schmullius C (2011c) (Semi-) automatic mapping of urban structure types (USTs) using remote sensing data and methods. *Poster presentation at the 2011 AK Fernerkundung*, September 29–30, Würzburg, Germany.

Berger C, Rosentreter J, Voltersen M, Baumgart C, Hese S & Schmullius C (2014b) Analysis of the temporal relationship between settlement density metrics & land surface temperature. *Poster presentation at RAQRS IV*, September 22–26, Valencia, Spain.

Berger C, Truckenbrodt J, Engelhardt S, Thiel C, Enssle F, Fassnacht F, Schmullius C & Koch B (2015b) Fusion of Radarsat-2 and TanDEM-X satellite data to support the assessment of aboveground biomass (AGB) in temperate forests. *Oral presentation at the 36th ISRSE*, May 11–15, Berlin, Germany.

Eberle J & Berger C (2012) Urban density (UD) mapping results for the City of San Francisco (Geoportal). *Contribution to the 2012 IEEE GRSS Data Fusion Contest*. <http://sf.maps.essi-blog.org/> (last accessed on 2015-01-06).

. . . .

Ort, Datum | Christian Berger